Human peroxiredoxin 3: the shape-shifting peroxidase as a versatile protein tecton

A thesis submitted in partial fulfilment of

the requirements for the degree of

Doctor of Philosophy in Biochemistry

2017

N. Amy Yewdall

University of Canterbury

As the wind of time blows into the sails of space,
the unfolding of the universe nurtures the evolution of matter
under the pressure of information.

Jean-Marie Lehn, 2002

Acknowledgements

The last four years have been remarkable and for that I have many to sincerely thank. My biggest thank you is for my supervisor, Juliet 'the Boss' Gerrard for the invaluable mentoring, patience, and infectious enthusiasm. Your passion for bold science and cautious optimism is inspiring. I sincerely look forward to future occasions when we can share a carpet-friendly G&T. To my other boss, Grant Pearce, thank you for your interest, input and for being a calming presence during the storm of writing. Thanks to the protein nanotech team – Amy Phillips, Akshita Wason, and Helen Ashmead – for the great yarns about science and beyond, with a special mention to Amy1 for teaching me the ropes. Thanks to the rest of the Gerrard team, past and present, for an enjoyable time at the bench. To the Dobson-Gerrard-Pearce Lab triad – especially Rach, Katniss, Jenny, Sarah, Eric, Jezza, Rishi and Dylan – thank you all for catalysing so many memorable moments: from flash mobs and 'singing' in disused train carriages, to our ridiculous lunch-time discussions. You all certainly made lab life at Canterbury more vibrant. Cheers also to Ren for being so inspiringly passionate about science and never crossing the line. A very special thank you for the structural biology team at the University of Auckland, especially those in the main lab, for all the excellent advice, support and cake. In particular, thanks to David Goldstone for your beer banter and helpful guidance; and to Lia for teaching me about the 'c' word and B&D. To my Auckland science family – Mel, Karima, Lia, Anders, Ehab, and Smitha – cheers for the fun (and delicious) memories.

Various collaborations have enriched this work and I am grateful to all those who have assisted me including: Mark Hampton and Alexander Peskin from the Otago Medical School; Dave, Alok, Martin and Leo from the University of Auckland, and Carol Robinson and Tim Allison from the University of Oxford. With a special thanks for the members of the Robinson Lab for a splendid English summer! Also many thanks to the various organisations that have provided financial support for my overseas trip, including: New Zealand Federation of Graduate Women, Royal Society of New Zealand, Maurice and Phyllis Paykel Trust, MacDiarmid Emerging Scientist Association, New Zealand Institute of Chemistry, and The Company of Biologists.

My thanks also goes out to all of my friends outside of the lab for the pep talks and cheery encouragements. Finally, thank you to my family for their enduring belief in me: to Dad for inspiring me to pursue science, to Mum for making sure I stick with it, to May for going into banking so I don't have to worry about being in science (jokes), and to Eric for being the most supportive plus one I could ask for.

Table of Contents

List of Abbreviations

%	percentage
[θ]	mean residue ellipticity
-Cter	C-terminal histidine tag (used as suffix on protein names)
-Nter	N-terminal histidine tag (used as suffix on protein names)
°C	degree Celsius
1-Cys	a class of peroxiredoxin with one cysteine residue
2-Cys	a class of peroxiredoxin with two cysteine residues
Å	angstrom
A interface	monomer-monomer interface of peroxiredoxin
AhpE	a 2-Cys peroxiredoxin from *Mycobacterium tubercluosis*
ASK1	Apoptosis signal-regulating kinase 1
ATP	adenosine triphosphate
AUC	analytical ultracentrifugation
AvrII	restriction enzyme site
B interface	dimer-dimer interface of peroxiredoxin
B&D	buns & dumplings
BSA	bovine serum albumin
BtPrx3	*Bos taurus* (bovine) peroxiredoxin 3
CID	collision induced dissociation
Co^{2+}	cobalt ion
C_P (usually Cys_P)	peroxidatic cysteine
C_P^{FF}	peroxidatic cysteine with a fully folded active site
C_P^{LU}	peroxidatic cysteine with a locally unfolded active site
C_pS	peroxidatic cysteine mutated to serine
C_R (usually Cys_R)	resolving cysteine
CRP	cyclic AMP-activated global transcriptional regulator
cryo-EM	cryo-electron microscopy
CuAAC	copper-catalyzed azide-alkyne cycloaddition
CysP	peroxidatic cysteine
Cys_R	resolving cysteine
Cα	the backbone carbon atom of the amino acid residue
Da	Daltons
Dmax	maximal particle diameter
DNA	deoxyribonucleic acid
DPS	DNA-binding proteins from starved cells
DTT	dithiothreitol

E. coli	*Escherichia coli*
EDTA	ethylenediaminetetraacetic acid
F190*tag*	phenylalanine in amino acid position 190 mutated to amber stop codon
FF	fully folded
FT	flow through
G&T	gin and tonic
GGLG	conserved amino acid residue motif that confers resistance to hyperoxidation
GluC	a serine proteinase that cleaves peptide bonds
h	hour
H_2O_2	hydrogen peroxide
Hcp1	protein component of type IV secretion system in *P. aeruginosa*
HEPES	N-2-hydroxyethlpiperazine-N'-2-ethane sulfonic acid
His_6-tag	six histidine tag
HMW	high molecular weight
HRP	horse radish peroxidase
HsPrx3	human peroxiredoxin 3
IMAC	immobilised metal affinity chromatography
IPTG	isopropyl β-D-1-thiogalactopyranoside
kDa	kilo Daltons
L	litre
LB	Luria Bertani or Lysogeny Broth
LC-MS	liquid chromatography coupled mass spectrometry
LMW	low molecular weight
Lsm	Sm-like protein
LU	locally unfolded
M. jannaschii	*Methanococcus jannaschii*
m/z	mass-to-charge
MB	Magnificent Broth ™
MBP	maltose binding protein
MES	2-(N-morpholino)ethanesulfonic acid
Mg^{2+}	magnesium cation
MilliQ	ultrapure water
min	minute
MjaaRS	*Methanococcus jannaschii* aminoacyl-tRNA synthetase
mL	millilitre
MluI	restriction enzyme site
mM	millimolar
MOPS	3-morpholinopropanesulfonic acid
MPD	2-Methyl-2,4-pentanediol

mRNA	messenger RNA
MS	mass spectrometry
MS/MS	tandem mass spectrometry
MW	molecular weight
MWCO	molecular weight cut-off
Ni^{2+}	nickel ion
nm	nanometres
nMS	native mass spectrometry
NTA	nitrilotriacetic acid
OD_{600}	optical density at 600 nm
P(r)	electron distance distribution function
pAzF	p-azidophenylalanine
PDB	protein data bank
PDBePISA	an interactive tool for the exploration of macromolecular interfaces
PO_4^{3+}	phosphate ion
Prx	peroxiredoxin
PTEN	Phosphatase and tensin homolog
q	scattering vector
QTOF	quadrupole time-of-flight
R interface	ring interface of peroxiredoxin
RAD52	a protein encoded by the *RAD52* gene
Rg	radius of gyration
RMSD	root-mean-square deviation
RNA	ribonucleic acid
ROOH	hydroperoxides
rpm	revolutions per minute
rTEV protease	recombinant tobacco etch virus protease containing a histidine tag
S	Svedburg is a unit of time equal to 10^{-13} s
s	second
S75E	serine in amino acid position 75 mutated to glutamic acid
S78C	serine in amino acid position 78 mutated to cysteine
SAXS	small angle X-ray scattering
SDS	sodium dodecyl sulfate
SEC	size exclusion chromatography
SEC-SLS	size exclusion chromatography coupled with static light scattering
SmPrx1	*Schistosoma masoni* peroxiredoxin 1
SO_4^{2-}	sulfate ion
SPAAC	strain-promoted azide-alkyne cycloaddition
Srx	sulfiredoxin
StAhpC	Salmonella typhimurium AhpC, a bacterial 2-Cys peroxiredoxin

tag	nucleic acid sequence of the amber stop codon
TB	Terrific broth
TCEP	tris(2-carboxyethyl)phosphine
TEM	transmission electron microscopy
TMV	tobacco mosiac virus
TRAP	*trp* RNA-binding attenuation protein
Tris	tris(hydroxymethyl)aminoethane
tRNA	transfer RNA
Trx	thioredoxin
UAA	unnatural amino acid
UV	ultraviolet
v/v	unit volume per unit volume
w/v	unit weight per unit volume
WT	wild-type
Y10*tag*	tyrosine in amino acid position 10 mutated to amber stop codon
Y160*tag*	tyrosine in amino acid position 160 mutated to amber stop codon
YF	conserved amino acid residue motif that confers resistance to hyperoxidation
ε_{240}	extinction coefficient of H_2O_2 at 240 nm
ε_{403}	extinction coefficient of HRP at 403 nm
µg	micrograms
µL	microlitre
µM	micromolar

Abstract

The biological realm contains numerous examples of nano-scale molecules that can self-assemble into a diverse array of architectures, making them attractive building blocks (or tectons) for applications in bionanotechnology. Proteins are one such biological molecule able to assemble into various three-dimensional structures. Exploring the mechanism and conditions in which these protein structures form is not only useful for the understanding of its biological role, but is also a prerequisite for their use in rational materials design.

Human peroxiredoxin 3 (HsPrx3) are ubiquitous antioxidant proteins that can form a plethora of protein architectures: from homodimers that reversibly assemble into dodecameric rings (or toroids), and rings that can further associate into protein tubes. This thesis examines the high molecular weight protein tube structure of HsPrx3 (Chapter 2) and its assembly mechanism (Chapter 3). A 2.8 Å crystal structure of HsPrx3 was elucidated for the first time and was displayed as a short tube composed of three rings. This structure, together with a cryo-electron microscopy reconstruction obtained with collaborators, enabled a novel hypothesis for the biological role of these protein tubes as having a self-associating chaperone function. Using native mass spectrometry, protein tube formation was demonstrated to be formed *via a* non-commutative mechanism. Protein tube formation was also shown to be reversible, increasing the appeal of HsPrx3 proteins as tectons for bionanotechnology.

HsPrx3 proteins react with hydrogen peroxide and upon oxidation, the reduced dodecameric rings disassemble into oxidised homodimers. The relationship between this quaternary structural switch and peroxidase activity was investigated (Chapter 4). Point mutations at the dimer-dimer interface were generated, creating an obligate dimer (S75E HsPrx3) and a stabilised toroid (S78C HsPrx3). Intriguingly, the obligate dimer was minimally active, suggesting that the ring structure is important, but not vital, for active site positioning. This raises interesting questions as to the biological function of this redox-induced structural change. On the other hand, the stabilised toroid was crystallised and the 2.4 Å structure provided a detailed understanding of the interactions that stabilise the dimer-dimer interface. S78C HsPrx3 will be a useful tecton as componentry for future applications.

Having gained a deeper understanding of HsPrx3 self-assembly, functionalisation of the protein surface with novel chemistries was explored (Chapter 5). An unnatural amino acid, p-azidophenylalanine, was chosen for *in vivo* incorporation into HsPrx3 *via* an *E. coli* expression system. Although, not entirely successful, this marks a promising initial venture at functionalising HsPrx3.

Chapter 1: Introduction

1.1 Self-assembly: an intrinsic phenomenon of life

Self-assembly refers to the spontaneous, and usually reversible, organisation of components into ordered structures (Lehn, 2007). It is an equilibrium process driven by the minimisation of the free energy of the system (Halley and Winkler, 2008). This phenomenon emerges for an array of matters, including inorganic materials (Fang *et al*, 2016), and it is a vital intrinsic feature of biomolecules, which enables their self-assembly into the organised structures necessary for life (Furst, 2013). From nano-scale biological components, to the macroscopic cellular organisms, self-assembly generates order over magnitudes of size and complexity. The hierarchical self-assembling organisation enables the precise control of the resulting structures, where small sections of such structures can be easily repaired, or unit components modified to embellish the self assembled structure with new function, without altering the entire assembly (Furst, 2013). The forces responsible for self-assembly vary depending on the particular system and its size (Whitesides and Grzybowski, 2002). In particular, molecular self-assembly involves the organisation of biological components at the nano-scale and occurs via non-covalent interactions, such as van der Waals forces, electrostatics, hydrophobic interactions, hydrogen bonds and coordination bonds (Furst, 2013; Fang *et al*, 2016). Such self-assembling biological components can be harnessed for applications in the nano-scale realm, and this field of research is called bionanotechnology.

1.2 Biological matters in bionanotechnology

1.2.1 Introduction to bionanotechnology

Biological molecules exist in the nano-scale and have an inherent ability to self-assemble, making these molecules appealing tectons (or building blocks) for the creation of sophisticated structures for applications in bionanotechnology. Such tectons include the four major classes of biomolecules that constitute life (Figure 1.1): nucleic acids (Zhang *et al*, 2014), amino acids (Gerrard, 2013), lipids (Mashaghi *et al*, 2013), and carbohydrates (Han *et al*, 2015). Each class of biomolecule features different properties related to its natural function, which can favour certain applications beyond their original biological roles (Section 1.2.2). Functionalisation of these tectons or the structures

they form allows for useful applications to be realised. These applications can range from tissue engineering (Tamerler and Sarikaya, 2009; Subramani *et al*, 2008) and drug delivery (Farokhzad and Langer, 2009; Ravichandran, 2009; Rother *et al*, 2016) to the development of biosensors (Gilardi *et al*, 2002), molecular machines (Konstas *et al*, 2010) or nano-pore technology (Venkatesan and Bashir, 2011; Wendell *et al*, 2009).

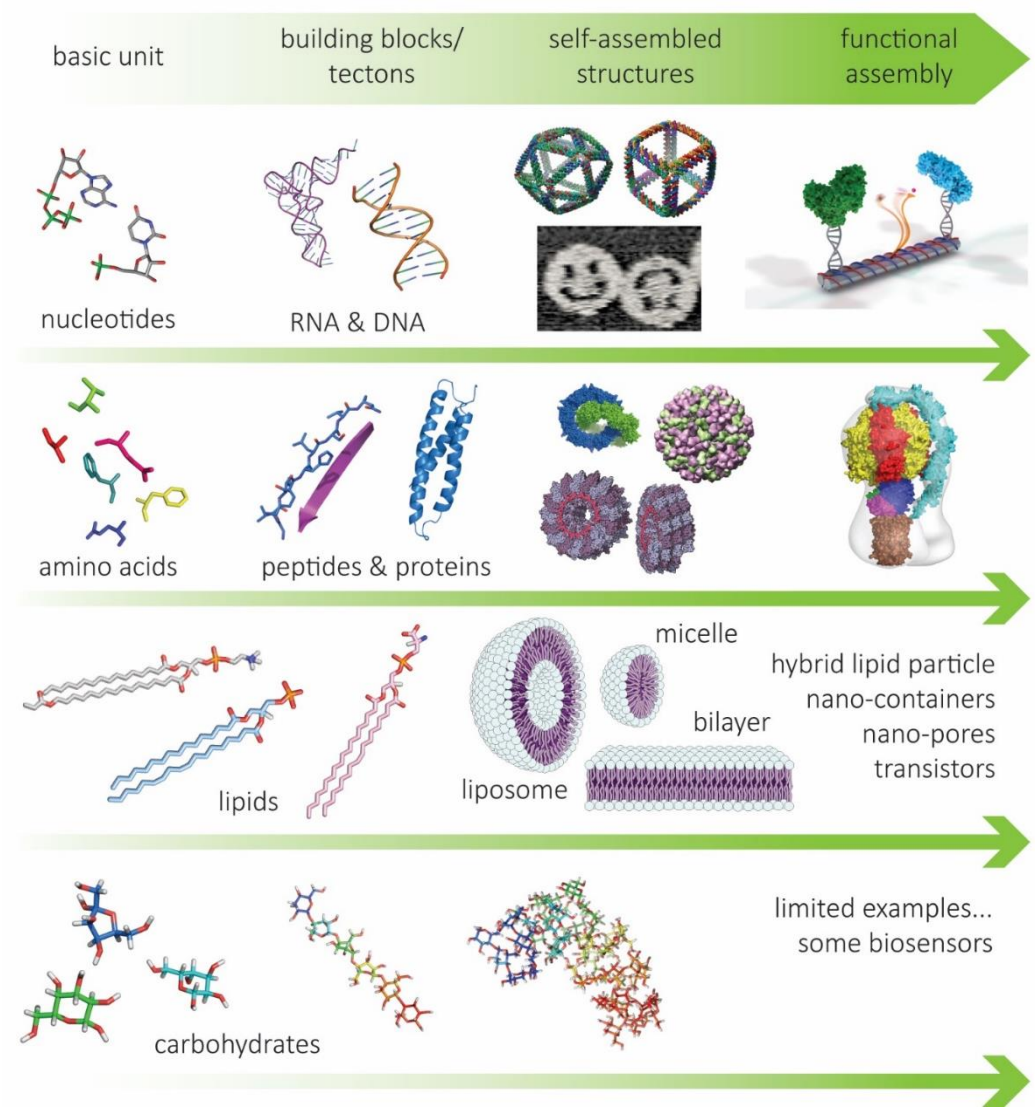

Figure 1.1: Self-assembly of the four major classes of biomolecules

Basic units of biological molecules can self-assemble into a wide variety of structures. Studying how these biomolecules self-assemble can not only reveal insights into their biological function as most of these structures have a purpose in cellular life, but also provides clues as to how these materials can be harnessed for bionanotechnology. In fact, completely novel nanostructures have been engineered based on all of these biomolecules. The basic units of nucleotides and amino acids assemble into chains that can fold into 2D or 3D tectons, which are able to further associate to form more complex 2D or 3D structures. Lipids are basic units as well as the starting tecton for which complex liposome, micelle or bilayer structures can be created. These lipids structures are an essential part of compartmentalisation involved in life processes, but have also been used as nano-carriers for drug delivery applications. Carbohydrates can form very complex networks of polysaccharides which can adopt 3D morphologies; however, the structure prediction for carbohydrates is still in its infancy, but promises to expand as a field of research.

1.2.2 Bio-inspired building blocks

1.2.2.1 Lipids

The unique properties of lipids, such as amphiphilicity, as well as the diversity in chemistry of head and tail groups, makes them appealing for many applications in bionanotechnology (Mashaghi *et al*, 2013). Lipids can self-assemble into a diverse array of structures from bilayers, nano-films, micelles and liposomes (Israelachvili, 2011). Some of these lipid structures form crucial barriers for compartmentalisation inside cells (Alberts *et al*, 2002), and have been harnessed for use as nano-containers and hybrid lipid particles that can hold an array of cargo for purposes in drug delivery (Zhou *et al*, 2010a; Schäfer *et al*, 2010). Lipid bilayers are also transparent to light (Mashaghi *et al*, 2008) and can conduct heat (Mashaghi *et al*, 2013), features which also make them useful for nanotechnology (Backus *et al*, 2011). Lipids have also been integral components of nano-pores (Jonsson *et al*, 2010; Yusko *et al*, 2011; Hernandez-Ainsa *et al*, 2013) and graphene-based transistors (Noy *et al*, 2011). Computational tools have been recently developed to further enhance novel lipid architecture designs (Mashaghi *et al*, 2013).

1.2.2.2 Nucleic acids

Deoxyribonucleic acid (DNA) and ribonucleic acid (RNA) are bio-polymers responsible for storage of cellular information. They are composed of four nucleotide bases that base-pair in a predictable manner, allowing computer algorithms to predict sequences that interact to form specific DNA 2D or 3D architectures (Seeman, 2005). Nucleic acid structures are often compatible with organic or inorganic materials, but run the risk of not being biocompatible with cells and organisms as they require high magnesium concentrations to fold, and could be readily degraded by DNases as part of cellular antiviral defence (Chen *et al*, 2015).

Numerous examples of DNA architectures have been developed: from simple 2D tiles (Fu and Seeman, 1993; Winfree *et al*, 1998; Seeman, 2003; Park *et al*, 2006) to folding up 2D DNA arrays to any desired pattern (Rothemund, 2006). More complex structures such as cage polyhedras (Zhang and Seeman, 1994; Shih *et al*, 2004), tubes (Aldaye and Sleiman, 2007; Yin *et al*, 2008; Rothemund *et al*, 2004) and Borromean rings (Mao *et al*, 1997) can also be formed from DNA. Large numbers of these architectures have been used as a starting pool for more complex arrangements, such as DNA machines (Mao *et al*, 1999; Yurke *et al*, 2000; Yan *et al*, 2002; Feng *et al*, 2003; Goodman *et al*, 2005). The various DNA structures provide a foundation of building materials that can be further functionalised for applications. DNA cages have been used for drug

delivery (Linko *et al*, 2015), and DNA templates were used for assembly of silver nanowires (Braun *et al*, 1998).

Although some 2D arrays and cages have been developed, creating nanostructures using RNA is less advanced compared with DNA, mostly because of its labile single stranded nature (Chworos *et al*, 2004, Guo, 2010). Despite this, RNA nanoparticles were recently developed as a therapeutic technology used for *in vivo* drug delivery of RNA (Parlea *et al*, 2016).

1.2.2.3 Carbohydrates

In contrast to nucleic acids, the development of carbohydrates, or saccharides, for use in nanotechnology is still in its infancy, but promises to grow (Han *et al*, 2015). Carbohydrates, such as glycocalyx, play important roles in directing many complex biological processes, such as protein folding, binding between cells, signal transduction and cell motility (Han *et al*, 2015). Their challenging preparation, and heterogeneous structural diversity due to branching occurring on polysaccharide chains (Vilaplana and Gilbert, 2010), and complex binding have made exploring these biomolecules for applications in bionanotechnology difficult. Despite this, glycan microarrays (Houseman and Mrksich, 2002; Oyelaran and Gildersleeve, 2009), synthetic carbohydrate receptors (Ke *et al*, 2012), and carbohydrate-coated nanoparticles (Gross *et al*, 2016) are all promising advances to generate functional technologies from these biomolecules. The creation of 3D-self assembled layers of disaccharide neoglycolipids (Fuss *et al*, 2008) and protein-like tetramerising aminocellulose (Nikolajski *et al*, 2014) are encouraging leaps towards making complex carbohydrate directed hierarchical assemblies.

1.2.2.4 Amino acids

Amino acids are the basic units, which are covalently linked together to form peptide chains and proteins capable of further self-assembly. Due to their diverse chemistries, ease of synthesis and ability to form complex and switchable 2D or 3D architectures, peptides and proteins are promising tectons that constitute a flourishing branch of the current bionanotechnology space (Melis Sardan *et al*, 2016; Gerrard, 2013; Banta, 2007). The 20 possible naturally occurring amino acids provide a richer pool of starting units compared with nucleic acids, and along with the extensive computational tools available, designing and creating novel nanostructures using peptide and protein tectons can be achieved (Tsai *et al*, 2006; Bromley *et al*, 2008; Section 1.3.1).

Peptides are short chains of amino acids. Their tolerance for relatively harsh physico-chemical conditions makes them suitable for nanotechnology (Ryu and Park, 2010; Melis Sardan *et al*, 2016).

Peptides can form numerous structures such as fibres (Takahashi *et al*, 2002; Matsumura *et al*, 2004), rings (Ghadiri *et al*, 1993) and tubes (Saviano *et al*, 1994; Seebach *et al*, 1997; Clark *et al*, 1998; Gao and Matsui, 2005). Peptide tubes or nanowires of < 10 nm cavity diameter are difficult to make (Hartgerink *et al*, 1998; Horne *et al*, 2003). Different peptide-based 2D shapes can also be formed using a modified leucine zipper (Ryadnov and Woolfson, 2003; Ryadnov, 2007). Further functionalisation of these peptide architectures can lead to a wide variety of applications, ranging from metal biomineralisation on the inner and outer surfaces of tubes (Reches and Gazit, 2006) to the generation of peptides as semiconductors (Hauser and Zhang, 2010). Peptide gels can function as a biocompatible extracellular matrix for tissue engineering (Aggeli *et al*, 1997; El-Sherbiny and Yacoub, 2013) or as substrates for tissue growth, such as for neurite and synapse formation (Holmes *et al*, 2000).

Proteins are composed of longer amino acid chains, folding to form sophisticated 3D structures. These folded 3D structures can usually further associate to form higher order complexes with other proteins. Proteins which naturally adopt a huge variety of structures are useful starting architectures for bionanotechnology applications. The role of proteins in bionanotechnology will be further elaborated on in Section 1.3.

1.2.2.5 A combination of materials

In order to utilise the properties and strengths of all available materials, bionanotechnology undoubtedly involves a mixture of components. Not only are these a combination of different biomolecules, but also of biological and non-biological components (Nel *et al*, 2009). Some areas of applications for bionanotechnology will lend themselves towards certain materials. In electronics, organic semiconductors were assembled using self-assembling peptides (Eakins *et al*, 2015), whereas nanotube and nanowire transistor devices can be embedded into lipid bilayers along with biological ion channels to be used as biosensors (Noy *et al*, 2011; Simmel, 2009). For drug delivery, synthetic polymers and protein cages have proved to be a fruitful symbiosis (Rother *et al*, 2016), and carbohydrate-based nanoparticles were shown to pass through various biological barriers (Peptu 2014 Peptu *et al*, 2014). Biological components can act at the interface between inorganic and biological systems to improve biocompatibility for tissue engineering (Li *et al*, 2009; Li *et al*, 2010). These are only a few examples of the countless functional applications of bionanotechnology to highlight the possibilities of what can be created from biomolecules.

1.3 Protein bionanotechnology

1.3.1 Desirable features of protein building blocks/tectons

Proteins are biomolecules responsible for a vast array of functions within living cells (Alberts *et al*, 2002). In order to achieve this, proteins adopt a wide variety of structures, which can be classified into different orders of organisation: primary, secondary, tertiary, and quaternary structure. The amino acid sequence, or primary structure, dictates how a protein tecton folds together and also how these tectons further self-assemble into sophisticated 3D structures. This modular assembly is one of the main advantages of using proteins in bionanotechnology as it allows for precise design and control of the final architecture by introducing changes to the primary sequence from a diverse pool of available amino acid chemistries (O'Donoghue *et al*, 2013; Section 1.3.2.1).

Complex architectures can be assembled from multiple copies of the same (homo-oligomerisation) or different tectons (hetero-oligomerisation) (Pieters *et al*, 2016). Most naturally occurring oligomeric proteins are homo-oligomers and the majority of these structures are symmetrical (Goodsell and Olson, 2000; Section 1.3.3). Homo-oligomeric proteins have enhanced stability (Marsh and Teichmann, 2015) and are also a result of expression from a single gene sequence, making it more convenient to engineer these protein tectons (Section 1.3.2).

The inherent compatibility of proteins with many biologically relevant salt concentrations and pHs lends protein nanotechnology towards biological applications. Often, protein structures can reversibly associate depending on environmental conditions, such as pH, salt concentration, or the presence of co-factors or metal ions, as well as protein concentrations (Nooren and Thornton, 2003). Proteins ideal for bionanotechnology should also be thermally and chemically stable to enable a higher tolerance for different chemical environments. Thermostable proteins are often found in bionanotechnology applications, such as the extensively characterised SP1 proteins (Medalsy *et al*, 2008) to *trp* RNA-binding attenuation protein (TRAP; Heddle *et al*, 2007). Some thermostable proteins originate from thermophilic bacteria and such proteins have been immobilised and can be used as biosensors (De Stefano *et al*, 2008; Staiano *et al*, 2010; Cowan and Fernandez-Lafuente, 2011).

Model protein systems should ideally tolerate modifications of surface residues for functionalisation (van Vught *et al*, 2014), such as the attachment of metal ions (Smith, 2015) to the protein nanostructure. Different regions of protein building blocks have different capacities for

tolerating modifications, depending on their surrounding environments, with flexible regions of proteins generally able to tolerate changes to protein sequence (Guo *et al*, 2004). Additional inherent functions of proteins, such as DNA binding (Heddle *et al*, 2007) or enzymatic activity (Phillips *et al*, 2014), can make these biological materials useful for applications.

1.3.2 Engineering protein tectons

1.3.2.1 Understanding protein synthesis

Proteins are appealing tectons for creating nanostructures due to their inherent ease of synthesis using a variety of commercially available expression systems, including but not limited to certain strains of *Escherichia coli*, mammalian cells as well as *in vitro* protein synthesis (Rosano and Ceccarelli, 2014). Within each expression system, the cellular machinery is harnessed to create recombinant protein tectons based on synthetic DNA sequences. The bacterium, *E. coli*, is one of the most extensively well-studied prokaryotic organisms used for the industrial production of proteins (Baneyx and Mujacic, 2004). With fast growth kinetics (Sezonov *et al*, 2007), the ability to have high cell density cultures (Shiloach and Fass, 2005), and a wide variety of strains developed for specific end uses, whether it be for DNA propagation or protein production (Rosano *et al*, 2014), the *E. coli* expression system is the obvious choice for the creation of protein tectons.

The *in vivo* production of recombinant proteins involves the biomolecules made from nucleic acids (DNA and RNA) as well as proteins. Protein production involves transcription, where DNA is transcribed into RNA by RNA polymerases, and translation, where messenger RNA (mRNA) is translated into amino acid chains by ribonucleoprotein complexes (Laursen *et al*, 2005). These ribonucleoprotein complexes consist of ribosomes that catalyse the formation of peptide bonds between amino acids introduced via charged transfer RNAs (tRNAs), as well as a complex array of initiation factor and elongation factor proteins. The mRNA sequence acts to orchestrate the order in which cognate charged tRNAs bind within the ribosome, and therefore results in the production of encoded amino acid chains (Laursen *et al*, 2005). Correct translation also hinges on another enzyme, called aminoacyl-tRNA synthetase, that catalyses the esterification of specific amino acids and corresponding tRNA pairs, resulting in charged aminoacyl-tRNAs (Ibba and Soll, 2000).

The ease of incorporation of synthetic DNA into *E. coli* (Pope and Kent, 1996), and coaxing the cellular machinery to read this synthetic DNA to overproduce recombinant proteins are key reasons for the widespread industrial use of this expression system (Rosano *et al*, 2014). Various

modifications to wild-type *E. coli* have resulted in multiple strains suited for protein overexpression. In particular, BL21 (DE3) strains contain the λDE3 prophage inserted into the bacterial genome, which encodes the T7 RNA polymerase gene under the *lac*UV5 promoter (Daegelen *et al*, 2009). This means the production of proteins can be switched on with the addition of IPTG, an allolactose mimic, which depresses and allows the transcription of the highly efficient T7 polymerase to transcribe the mRNA of desired recombinant proteins. This system has been modified to incorporate unnatural amino acids into recombinant proteins (Chatterjee *et al*, 2013), and this is further elaborated in Chapter 4.

1.3.2.2 Design strategies

There are two major design strategies for creating self-assembling protein architectures using protein-protein interfaces: 1) Exploiting naturally occurring protein-protein interactions that occur for many self-assembling proteins to create structures that can be embellished with new functions (Pieters *et al*, 2016). Alternatively, protein oligomers can be fused together using linkers to create novel 2D patterns (Usui *et al*, 2009; Sinclair *et al*, 2011). 2) Completely novel protein architectures have been designed *in silico* where new protein-protein interfaces were designed into inherent protein symmetries (King *et al*, 2012). This was achieved by changing certain residues or by remodelling the entire interface (Padilla *et al*, 2001; Grueninger *et al*, 2008; Karanicolas *et al*, 2011). Interfaces can be designed based on many weak protein-protein interactions over large surface areas (King *et al*, 2012). Protein-protein interfaces can be further modified to include other factors which promote association. Such examples include rhodamine, which is used to promote protein layer formation (Brodin *et al*, 2014), as well as metal ions, which are used to drive associations between protein-protein interfaces (Salgado *et al*, 2010; Huard *et al*, 2013).

1.3.3 Protein architectures dictate their applications in bionanotechnology

1.3.3.1 Planar assemblies

Some naturally occurring proteins inherently form planar 2D assemblies as part of their cellular function, such as S-layer lattices, clathrin, and other proteins that cause membranes to bend (Edeling *et al*, 2006; Zimmerberg and Kozlov, 2006). S-layer proteins form the exoskeleton of bacteria and archaea and were found to re-assemble into 2D planar arrays when stripped from the cell membrane (Pum *et al*, 2013). The formation of the S-layer lattices depends on the concentrations of protein as well as divalent cations, such as Ca^{2+} ions, which were found to

stabilise the inter- and intra-domain contacts in the protein crystal structure (Baranova *et al*, 2012; Baneyx and Matthaei, 2014). Proteins that do not naturally form planar assemblies can be coaxed into the act by fusing them to other proteins – this 'protein jigsaw' can generate ordered protein arrays (Sinclair *et al*, 2011; Yeates, 2011). Non-covalent protein-protein interactions have also been engineered to create 2D planar assemblies (Gonen *et al*, 2015). 2D planar arrays enable the high density display of proteins which can have applications in cellular binding (Rothbauer *et al*, 2013), diagnostics and as biosensors (Ilk *et al*, 2011). The periodic arrangements in the nano-scale can provide the precise patterning required for plasmonic, optoelectronic, or magnetic applications (Baneyx *et al*, 2014).

1.3.3.2 Cages

Naturally occurring cage proteins are abundant and come in varying sizes. They are often formed from monomeric proteins that self-assemble into a final symmetric structure, which can vary in shape depending on the monomer (Pieters *et al*, 2016; Rother *et al*, 2016). The most prominent protein cages used in bionanotechnology, thus far, have been spherical and include iron encapsulating protein cages as well as viral capsids.

Classical ferritins and DNA binding proteins (DPS) are related, ubiquitous cage proteins found in all forms of life that bind to iron (**Figure 1.2 A**; Yoshizawa *et al*, 2007; Harrison and Arosio, 1996; B Bozzi *et al*, 1997). Classical ferritins form larger cages composed of 24 subunits resulting in a ~12 nm outside diameter (Lawson *et al*, 1991), whereas DPS cages are formed from 12 subunits with a 9 nm diameter (Stillman *et al*, 2005). They are both highly stable proteins that tolerate heating up to 80 °C in 6 M guanidine, a denaturant, at neutral pH without disassembly (Zhang and Orner, 2011), making these cages ideal for bionanotechnological applications. However, the cages disassemble at higher or lower pHs, allowing for cargoes to be internally trapped; this has been used for loading a variety of drugs (Ji *et al*, 2012; Domínguez-Vera, 2004). Ferritin and DPS proteins are fantastic cage proteins for an array of applications ranging from biomineralisation of metals and semiconductors to the generation of nanodevices, contrasting agents for medical imaging, as well as for drug delivery and nanoparticle vaccines (reviewed in He and Marles-Wright, 2015).

Another abundant class of protein cages are the viral capsids. Spherical and icosahedral viruses range in size from 18 – 500 nm in diameter and have evolved to survive a broad range of chemical environs, making them especially appealing for use in bionanotechnological applications (Young *et al*, 2008). Cowpea chlorotic mottle virus (**Figure 1.2 B**) and cowpea mosaic virus both have N- or C-termini on the outer or inner surface of the capsid to enable attachments and modifications

(Zlotnick *et al*, 2015). Redox-active capsid nanoparticles were created via the modification of exposed carboxylate groups on the cowpea mosaic virus surface with redox-active moieties (Steinmetz *et al*, 2006). The applications of virus capsids are vast and can range from creating nanomaterials, such as encapsulating nanoparticles or forming 2D/3D arrays, to enzyme nanoreactors, as well as biomedical applications such as imaging reagents or drug delivery platforms (reviewed in Young *et al*, 2008).

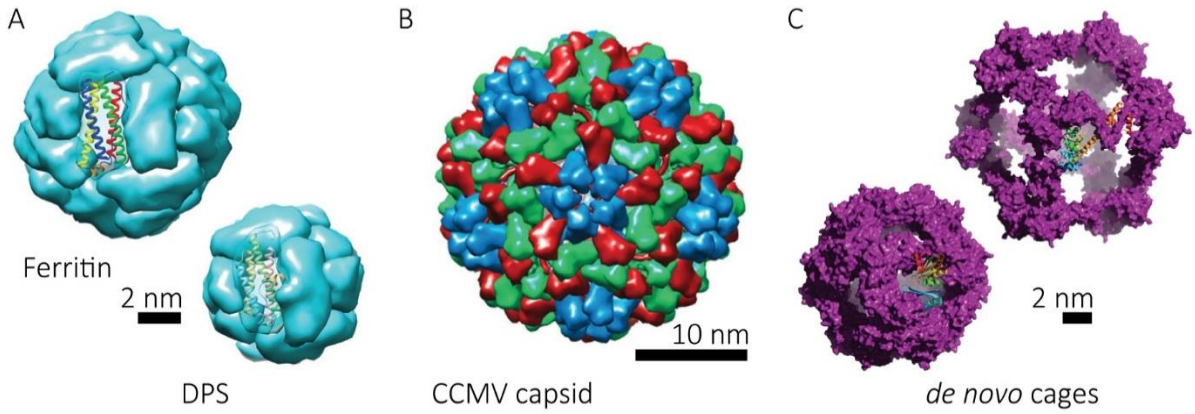

Figure 1.2: Naturally occurring and *de novo* protein cages
(**A**) Ferritin (PDB: 1BFR) and DPS (PDB: 1DPS) protein cages with the self-assembling unit highlighted (rainbow cartoon). Images adapted from Pieters *et al*, 2016 with permission (**B**) The cow chlorotic mottle virus capsids are generated from a pentamer of dimers (blue) which further associate with other dimers to form a large cage structure. (**C**) Some examples of *de novo* cage protein structures (left PDB:3VCD; right PDB: 4QCC) with the self-assembling unit highlighted (rainbow cartoon).

Computational design of protein-protein interactions have resulted in a variety of *de novo* rigid cage structures. Early designed protein nanohedra were created using the symmetrical fusion of two protein halves (Padilla *et al*, 2001). However, the computational analysis of protein-protein interfaces was able to identify key features of interaction and this was used to synthesise completely novel binding surfaces that can generate high-order oligomers, such as trimers or tetramers (Grueninger *et al*, 2008). More complex structures have been generated using data based on rigid interfaces, with resulting self-assembling *de novo* protein architectures such as cages (King *et al*, 2012; **Figure 1.2 C** on left), or porous cube structures (Lai *et al*, 2014; **Figure 1.2 C** on right). When formed, these structures are incredibly stable under a variety of conditions and are most likely the result of the optimised burial of hydrophobic areas designed into the protein-protein interaction surface (Huang *et al*, 2016). The design of *de novo* switchable structures is more challenging as hydrogen bonding patterns and balancing hydrophobic and polar interactions between proteins are difficult to model accurately, and so naturally occurring proteins with switchable assemblies are hard to mimic, for now.

In summary, natural or *de novo* protein cages contain two accessible surfaces: the inside and the

outside (Douglas and Young, 2006). These surfaces can be functionalised, providing points for nucleation of metals (Yoshimura, 2006) or for attachment of other polymers (Rother *et al*, 2016). Cages can inherently carry cargo inside their inner cavity and if the formation of the cage was switchable or porous, it can be used for applications in drug delivery with triggered release of such cargo (Ji *et al*, 2012; Domínguez-Vera, 2004). The inner cavity can also be used to limit the size of nanoparticle growth or for biomineralisation (Yoshimura, 2006). Nanoporous protein shells can encapsulate certain enzymes, increasing their local concentration, thereby enhancing enzymatic activity (Comellas-Aragones *et al*, 2007; Kuchler *et al*, 2016).

1.3.3.3 Rings

Rings or toroidal structures, with different subunit compositions and diameters, are ubiquitous protein architectures that naturally exist within organisms. With lengths less than their diameter and a central hole, rings have four accessible surfaces: the top and bottom of the ring as well as the inside and outside of the ring. Many nucleic acid-binding proteins form ring structures, and these have been harnessed as potential building blocks for bionanotechnology. Some examples include RAD52, Lsm, and TRAP. RAD52 is a DNA binding, ringed protein that promotes single stranded DNA annealing during homologous recombination. It is made from seven monomers (Stasiak *et al*, 2000) that form 12 nm rings. An 11-membered ring is formed when only the N-terminal half of RAD52 is present (Kagawa *et al*, 2002; Singleton *et al*, 2002; Figure 1.3 D). In contrast, TRAP proteins bind single stranded RNA and form stable 11-mer rings, which persist as rings in the gas phase, in the absence of bulk water, using non-denaturing mass spectrometry (Ruotolo *et al*, 2005; Figure 1.3 B). The TRAP protein monomer genes have also been fused in tandem to produce 12-mer protein rings (Heddle *et al*, 2007; Watanabe *et al*, 2008; Figure 1.3 C). Lsm proteins also bind to RNA and form stable heptameric rings (Figure 1.3 A). They have also been explored as potential tectons for nanotechnology (Manea, 2015; Wason, 2014; Malmstrom *et al*, 2015). The ability to bind to nucleic acids is a useful feature of nanotechnology as DNA has proven itself to be an important nano-scaffold (Section 1.2.2.2) with which these protein tectons can bind.

Not only can the inner holes of rings capture biomaterials like DNA, they are also used to capture inorganic molecules using engineered amino acid residues. The HSP60 chaperonin is a barrel-like ring protein that captures gold nanodots at the central core (McMillan *et al*, 2002). Cysteine residues were engineered into the central pore of TRAP proteins enabling them to coordinate gold nanodots (Heddle *et al*, 2007). These protein rings were further modified with titanium-binding peptides (Sano and Shiba, 2003) that facilitate its attachment onto a titanium or silicon oxide surfaces, therefore creating a TRAP-templated prototype of a metal oxide semiconductor capacitor

(Heddle, 2008).

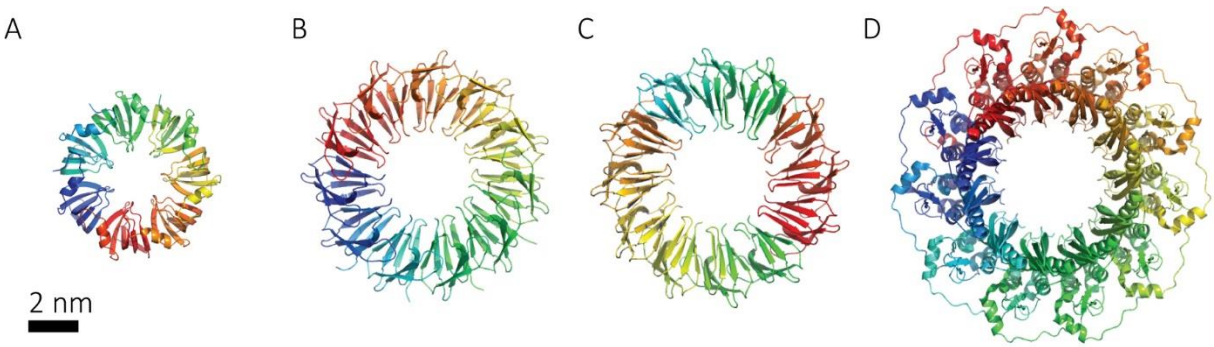

Figure 1.3: Naturally occurring protein ring tectons
Crystal structures of the various ring proteins, with sizes relative to the 2 nm scale bar. (**A**) Lsm is a heptameric ring (PDB: 1i81). (**B**) and (**C**) are both TRAP protein: the wild-type 11-mer protein (PDB: 1QAW) and the engineered 12-mer proteins (PDB: 2ZD0), respectively. (**D**) Engineered RAD51 protein forming an 11-mer ring (PDB: 1KN0).

Controlling ring internal diameter size is a valuable tool for bionanotechnology. The above examples have demonstrated that truncation of protein units (the N-terminal of the RAD52 protein; Kagawa *et al*, 2002) as well as addition of linker regions (linked TRAP proteins; Heddle *et al*, 2007) can result in rings with different subunit compositions compared with their respective original wild-type proteins. Synthetic enzyme nano-rings with sizes from 8 nm to 30 nm, have been engineered by varying linker amino acid length and compositions (Chou *et al*, 2008). These linkers were engineered in between the monomers of homodimeric enzymes, such as dihydrofolate reductase and histidine triad nucleotide binding 1, which then self-assemble into rings with varying catalytic efficiencies depending on the ring size. This demonstrates that the arrangement of supramolecular assemblies may be used to control catalytic parameters (Chou *et al*, 2008). These examples thus far demonstrate that protein rings can be engineered to have altered subunit composition: however, ring pore diameter remains fixed after the protein has been synthesised. An impressive feat has been the creation of protein nano-rings with controllable pore sizes (Bai *et al*, 2013). Glutathione S-transferase proteins, which are normally homodimeric, were embellished with two non-native histidine resides, which coordinated metal ions to promote self-assembly. Buffer ionic strengths were altered to tune the non-covalent interactions between protein subunits to produce a range of protein rings sized from 90 nm – 370 nm.

1.3.3.4 Tubes

Tubes have lengths longer than their diameter and, similar to rings, also have four addressable surfaces, making them useful building blocks within biology as well as bionanotechnology. Examples of such proteins include tubulin and pilin nanotubes (Kumara *et al*, 2006; Audette *et al*, 2004; Malvankar *et al*, 2011), virus-based nanotubes (Miller *et al*, 2007; Balci *et al*, 2006) as well as ring-shaped proteins that self-assemble in tubes (Section 1.3.3.5; Ballister *et al*, 2008; Miranda *et al*, 2009).

Naturally occurring tubes often have limited tolerance towards the modification of amino acids (Malcos and Hancock, 2011) and are usually composed from many different subunits that, occasionally, result in structural features, which make it difficult to utilise all four surfaces – such as small inner cavities (Heddle, 2008). Despite this, the unique inherent properties of naturally occurring nanotubes composed from tubulins and pilins still render them worthy tectons for certain applications. Microtubules are cytoskeletal filaments composed of tubulins that form hollow tubes with diameters of ~ 25 nm. Their inherent 'dynamic instability', where alternating phases of growth and shrinkage occur at the tube ends (Alberts *et al*, 2002), has been exploited for the creation of nifty nanodevices that involve transport of a variety of cargo, in conjunction with partnering motor proteins, kinesins (Malcos *et al*, 2011). The motor protein-microtubule partnership has also created incredible self-organised optical devices (Aoyama *et al*, 2013). Hybrid thermo-responsive gels composed of microtubules and synthetic polymers have also been created (Shigehara *et al*, 2013). Pilin proteins, on the other hand, are prokaryotic appendages used to share information between individual cells. Perhaps due to the inherent shape of self-assembling nanotubes, a major application envisaged for these is the creation of nanowires, despite materials made from amino acids being highly insulating (Hauser *et al*, 2010; Ashkenasy *et al*, 2006). However, a particular conductive pilin from *Geobacter sulferreducens* has natural electronic conductivities of ~ 5 mS cm^{-1}, comparable to carbon nanotubes and other conductive materials (Malvankar *et al*, 2011; Adhikari *et al*, 2016). A recent model for *G. sulferreducens* has proteins self-assembling without a central hole (Xiao *et al*, 2016).

Another classic protein tecton is also derived from a virus. The tobacco mosaic virus (TMV) is made of tubular ribonucleoproteins that assemble in a helical fashion around a RNA core, resulting in a virus of ~ 300 nm in length (Franklin, 1955; Shenton *et al*, 1999; Figure 1.4 A). Longer tubes of variable lengths are obtained when the coat protein is allowed to assemble without RNA. In fact, the size of the RNA template precisely governs the TMV tube lengths (Rego *et al*, 2013).The inner cavity of these viruses can be used to biomineralise nickel, cobalt, cobalt-platinum and iron-platinum nanowires (Knez *et al*, 2003; Tsukamoto *et al*, 2007). The external surface is also able to

be used as a template for biomineralisation of metals (Dujardin *et al*, 2003; Górzny *et al*, 2008). Fluorophores attached to surface cysteine residues on TMV coat protein monomers can self-assemble into a light-harvesting system, collecting light over a wide spectrum with high efficiency (Miller *et al*, 2007). The precisely tuned spatial features on the outer surface of the TMV virus can also be used as a template for the generation of nanowires for making lithium ion battery electrodes (Nam *et al*, 2006).

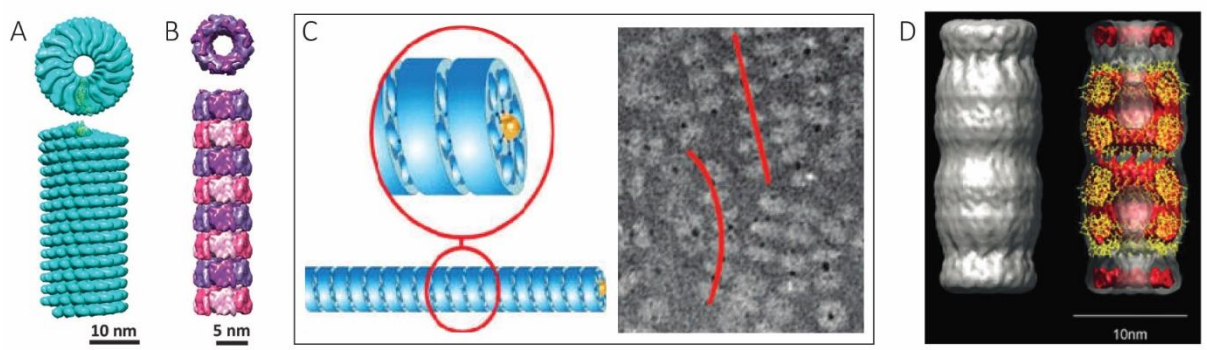

Figure 1.4: Protein nanotubes, naturally occurring as well as engineered tubes
These are examples of various protein nanotube structures in the literature. (**A**) The TMV capsid (PDB: 4UDV) forms nanotubes that are helical in nature. (**B**) Hcp1 from *P. aeruginosa* are ring proteins that can assemble into protein tubes (PDB: 1Y12). Diagrams (A) and (B) are adapted from Pieters *et al*, 2016. (**C**) On the left, a schematic showing the polymerisation of SP1 rings induced by its binding to gold nanodots, and right is a transmission electron micrograph (TEM) of this assembly, where proteins are light grey and nanodots are black dots (Medalsy *et al*, 2008). (**D**) A single particle reconstruction from the TEM of engineered TRAP proteins that assemble upon oxidation of cysteines at the ring-ring interface. This construction is overlaid with the side on view of the TRAP protein crystal. (Miranda *et al*, 2009). All images have been reprinted with permission from their respective journals.

1.3.3.5 Construction of tubes from rings

Protein rings that self-assemble into tubes provides modularity and an extra level of control in the generation of protein nanotubes. Again, some are naturally occurring, whereas there are many examples of modified rings that have been coerced to form tubes. Found in aspen plants, SP1 is a nano-ring made of twelve monomer proteins (Wang *et al*, 2002). The twelve proteins form a double-layered 11 nm six-membered ring with a 2.5 nm central hole where the N-terminus of the proteins are projected (Dgany *et al*, 2004). Six histidines were added to the N-terminus of the proteins which bound to Ni-NTA modified gold nanodots (**Figure 1.4 C**). Part of these dots protruded from each end of the double ring, providing attachment points for further rings to polymerise and to form nanowires (Medalsy *et al*, 2008). Another protein engineered to form nanowires is Hcp1, a homohexameric protein ring found in *Pseudomonas aeruginosa.* The Hcp1 protein ring, with an outer diameter of 9 nm and a 4 nm central hole, forms part of the bacteria's

type VI secretion system (Mougous *et al*, 2006). Hcp1 rings were modified by adding cysteine residues to its top and bottom surfaces so that inter-ring disulfide bonds can promote ring self-assembly into a tube (Ballister *et al*, 2008; Figure 1.4 B). Tubes can be polymerised up to 100 nm in length. Engineered redox sensitivity of these tubes means they can be disassembled when reducing agents are added in a time-dependent manner. In contrast to the engineered 11mer TRAP proteins for which nanotube formation was observed only after the addition of DTT, tube formation was speculated to be a result of a mixture of disulfide bonds and hydrophobic interactions (Miranda *et al*, 2009; Figure 1.4 D).

Having switchable architectures with multiple modes of assembly affords a unique level of control inherent to self-assembling protein tectons, such as peroxiredoxins (Prx). These proteins exhibit an array of structural diversity (Section 1.4.3) from dimers and rings (Wood *et al*, 2003b), to rings that assemble into tubes (Phillips 2014), as well as protein cages (Meissner *et al*, 2007) and catenanes (Cao *et al*, 2005). The use of Prx in bionanotechnology has begun (Section 1.4.4), with reported binding of Prx to nanoparticles (Ardini *et al*, 2014), and localisation onto graphene (Ardini *et al*, 2016), as well as intracellular peroxidase sensors (Morgan *et al*, 2016). The precise biological functions and the various intriguing structures that make Prxs an ideal tecton will be detailed below in Section 1.4. Tailoring protein tectons for applications in bionanotechnology involves investigating their structure and tolerance towards functionalisation, and this inextricably contributes towards fundamental research to understand its quaternary structure and assembly.

1.4 Peroxiredoxins as self-assembling, model tectons

1.4.1 Universal peroxiredoxin motifs and classification

Peroxiredoxins (Prxs) are a superfamily of redox-active enzymes that form a plethora of protein architectures: from monomers and dimers to toroids of different subunit composition. Higher order structures, such as cages and catenanes, have also been detected in certain classes of Prxs using transmission electron microscopy (TEM) and X-ray crystallography respectively (Meissner *et al*, 2007; Cao *et al*, 2005). The dynamic structural state of these Prxs are influenced by pH, salt concentration, phosphorylation and redox state (Wood *et al*, 2003b; Barranco-Medina *et al*, 2009), making Prxs useful model proteins for environmentally influenced self-assembly for bionanotechnology.

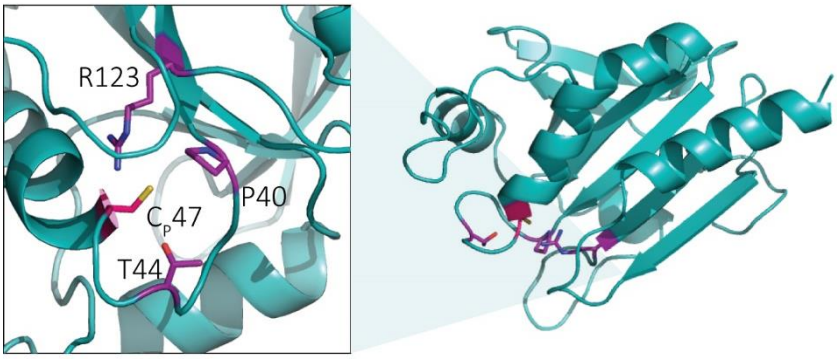

Figure 1.5: The conserved active site of Prxs in the context of a protein monomer
The conserved active site of Prxs (left panel) with key residues highlighted. The peroxidatic cysteine (C_P47 residue in in pink) is housed in a fully folded active site surrounded by conserved proline, threonine and arginine residues that are responsible for high reactivity of the catalytic cysteine, C_P. The details of this will be elaborated in Section 1.4.2.1. This a crystal structure of one bovine Prx3 monomer with a C168S mutation (PDB: 1ZYE).

Found in all forms of life (Rhee *et al*, 2001), Prxs are abundant cysteine-based peroxidases that are as active towards hydroperoxides as other heme-catalysed or selenium-based peroxidases (Perkins *et al*, 2015; Section 1.4.2.1). The key to their success as peroxidases is a universally conserved active site architecture (Figure 1.5). Although the amino acid sequences vary across the Prx superfamily, the active site motif, Proxxx(Thr/Ser)xxCys, is absolutely conserved (Rhee, 2016). This confers precise 3D arrangements of amino acids in the active site to aid substrate positioning and also activate the reactive thiol on the peroxidatic cysteine (Cys_P). The active sites of Prxs are housed in monomers with a conserved thioredoxin-like protein fold (Copley *et al*, 2004). For the majority of Prxs, oxidation occurs in a two-step process, where the activated thiol of the Cys_P initially reacts

with the substrate to form a sulfenic acid, followed by a second reaction with a resolving cysteine (Cys_R) when a disulfide bond is formed between Cys_P and Cys_R (elaborated further in **Section 1.4.2.1**).

In contrast to Cys_P, the location of the resolving cysteine (Cys_R) varies among Prxs, giving rise to different subfamilies grouped according to their catalytic resolution mechanisms (Seo *et al*, 2000; Rhee *et al*, 2005); in typical 2-Cys Prxs, the Cys_R comes from an obligate dimer; in atypical 2-Cys Prxs, the Cys_R is on the same monomer; whereas 1-Cys Prxs require another protein to provide a resolving disulfide bond. Typical 2-Cys Prxs, the largest and most widely distributed subfamily (Hall *et al*, 2009), exhibits changes to its quaternary structure, forming high-order organisations that extend beyond dimers. This makes typical 2-Cys Prxs especially appealing for bionanotechnological applications.

The mechanistic classification of Prxs provides a straightforward means to understand the different modes of catalysis of Prxs (Knoops *et al*, 2007); however, it fails to highlight many important structural distinctions that arise when Prxs are classified according to their phylogenetics and structure (Soito *et al*, 2011; Nelson *et al*, 2011; Poole and Nelson, 2016). Here the conserved active site motif, along with other key structural motifs, derived from 29 distinct Prxs were used to group the Prx superfamily into six evolutionary classes: Prx1, Prx6, AhpE, PrxQ, Tpx and Prx5 (**Table 1.1** on page 19; Soito *et al*, 2011). Some intriguing observations have arisen from this classification, including how certain classes of Prx are excluded from certain phylogenies, such as the PrxQ class, described to be the most ancestral group of Prxs that are no longer observed in metazoans (Perkins *et al*, 2015). The oligomeric state also varies between the six subfamilies: some members of the PrxQ family are monomeric, whereas most Prxs tend to form obligate dimers either via their 'A interface' or 'B interface' (**Figure 1.6**). Typical 2-Cys Prxs, found in both Prx1 and Prx6 classes, form obligate homodimers at the B interface. This interface forms an extended β-sheet structure with mainly hydrophobic interactions. It buttresses the active site of the Prxs and is considered important for its activity (Wood *et al*, 2003a). For typical 2-Cys Prxs, the Cys_R is often on a flexible C-terminal linker that embraces the other monomer to reach the Cys_P at the active site. The obligate dimers further associate at the A interface to form toroidal structures that can vary in subunit composition, and consequently ring diameter. The formation of ringed structures depends on the protein's redox environment, which is consequently determined by the oxidative state of Cys_P (**Section 3.1.4**). The location of Cys_R on the protein varies across the Prx superfamily, suggesting Cys_R arose independently several times during Prx evolution (**Table 1.1**; Perkin 2015). The rates of reaction with substrates also varies between each subfamily (**Table 1.1**). The reasons

for these differences between the evolutionary classes is unknown, and along with the *in vivo* relevance for quaternary structure changes in typical 2-Cys Prxs, there is much to discover about this fascinating superfamily of proteins (some of this will be discussed in **Chapter 4**).

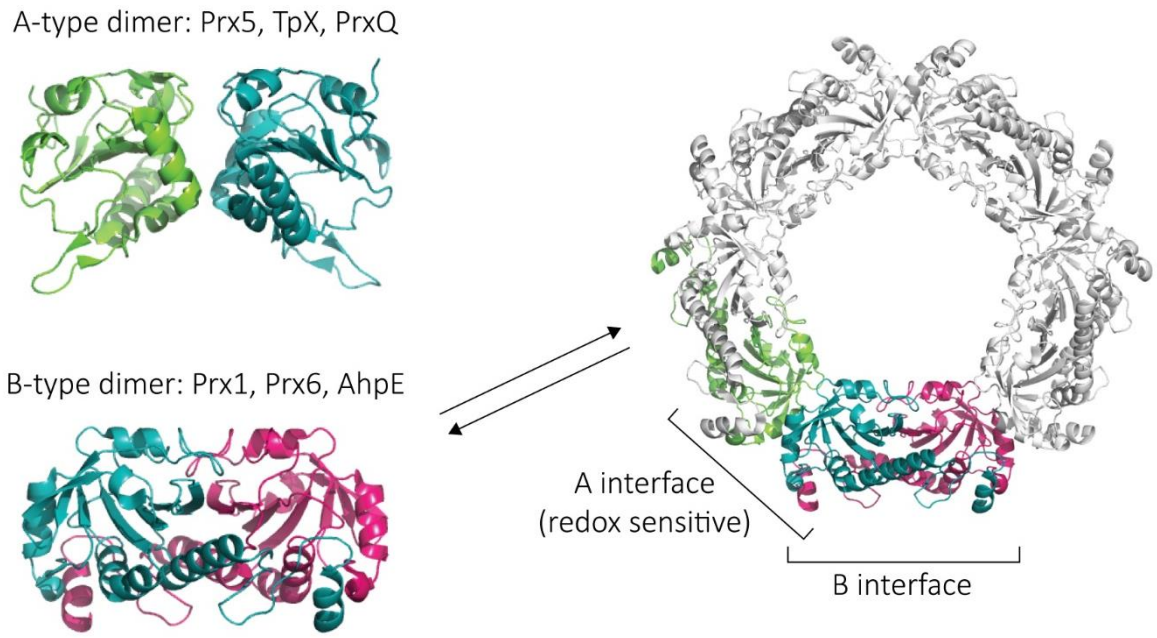

Figure 1.6: The various quaternary structures of Prxs
Dimeric (α_2) complexes are formed at either the A interface, where monomers interact at helix α3, or the B interface, where interactions occur through to extend a β-sheet. Certain typical 2-Cys Prxs are able to assembly further into decameric ring structures. A interface structure was *Aeropyrum pernix* PrxQ (Perkins 2012; PDB 4GQF) and the B interface structure and decamer are HsPrx3 (PDB: 1QMV). This diagram was adapted from Perkins *et al*, 2015 with permission.

Table 1.1: Summary of Prx subfamily distribution, structures and rates of reaction towards H_2O_2 (adapted from Perkins 2015)

Subfamily	Phylogenetic distribution	Structural distinctions relative to Prx core fold	Oligomeric states and interfaces	Typical location and conservation of Cys_R (when present)	Second order rate constants for reactions of Prx towards hydroperoxides ($M^{-1}s^{-1}$)
Prx1	Archaea, bacteria, eukaryotes	Extended C-terminus	B-type dimers, decamers $(\alpha_2)_5$ and rare dodecamer $(\alpha_2)_6$ through A interface	C-terminus of partner subunits (~99%)	$1 \times 10^5 - 7 \times 10^7$ $M^{-1}s^{-1}$ for H_2O_2 at pH 7.0-7.4 and 20-25 °C [a]
Prx6	Archaea, bacteria, eukaryotes	Long, extended C-terminus	B-type dimers, and some decamers $(\alpha_2)_5$ through A interface	No C_R	1×10^7 (for H_2O_2) or 1×10^6 (for peroxynitrite) [b]
AhpE	Bacteria	Extended loop at N-terminus	A-type dimers	Helix α2 (~67%) No C_R (≥ 19%)	10^5 [c]
PrxQ	Archaea, bacteria, plants, fungi (not animals)	Extended helix α4	Monomers and A-type dimers	Helix α2 (~61%) Helix α3 (~6%)	10^4-10^5 [d]
Tpx	Bacteria	N-terminal β hairpin	A-type dimers**	Helix α3 (>95%)	Preferential reactivity with peroxynitrite [e]
Prx5	Bacteria, eukaryotes (not archaea)	Helix insertion in α2, ~20% fused with Grx domain	A-type dimers	Helix α5 (~21%) Between β1 and β2 of N-terminus (~17%)	10^5 [f]

** *Aeropyrum pernix* Tpx, being an important exception, can associate together to form decameric rings and is classified as 2-Cys Prx (Nakamura 2009).

[a] A whole range of Prxs, especially 2-Cys Prxs, have been studied using this (Parsonage 2005; Peskin 2007; Manta 2009; Nelson 2008; Cox 2009; Parsonage 2015)

[b] *Arenicola marina* Prx6 (Loumaye 2011)

[c] AhpE from *Mycobacterium tuberculosis* (Hugo 2009; Reyes 2011)

[d] *Escherichia coli* BCP (Reeves 2011), and most other PrxQs have values this lower range of reactivity. There is notable exception: *Xylella fastidiosa* PrxQ (Horta 2010)

[e] with catalytic efficiencies in the range of 10^6-10^7 $M^{-1}s^{-1}$ towards peroxynitrite (Trujillo 2007)

[f] Human Prx5 (Trujillo 2007; Portillio-Ledesma 2014)

1.4.2 Functions inside of a cell

1.4.2.1 The peroxidase

Peroxides, such as H_2O_2, can arise from the surrounding cellular environment or as a by-product of the mitochondrial electron transport chain. H_2O_2 can have deleterious effects within a cell as it is able to react spontaneously with proteins, lipids and nucleic acids (Boveris and Chance, 1973; Cadenas *et al*, 1977; Turrens, 1997). Sufficient H_2O_2 can induce oxidative stress in cells, which can result in apoptosis (Orrenius, 2007). Within eukaryotes and at lower levels, H_2O_2 has also been implicated as a secondary messenger in cellular signalling. Cellular H_2O_2 concentrations are, therefore, tightly controlled by peroxidases, such as catalase, glutathione peroxidase and Prxs (Poole, 2015).

The relative abundance of each type of peroxidase protein, as well as catalytic turnover rate, are crucial factors that determine the importance of a certain peroxidase in antioxidant defence. These factors vary between cell types and different organisms. Generally, microorganisms lack heme-based and glutathione peroxidases, making Prxs more abundant, crucial antioxidants (Wood *et al*, 2003b). Within the mitochondria of HeLa cells, Prxs are at least 30 fold greater in abundance compared with glutathione peroxidase I (Chang *et al*, 2004). Despite Prxs having a slower catalytic turnover than GPx1, its greater abundance and broader substrate specificity makes Prxs important for front line defence against oxidants (Winterbourn, 2008; Adimora *et al*, 2010).

Prxs reduce peroxides, such as H_2O_2, using sulfur catalysis in a selective manner that achieves high reactivity compared with free cysteines. Although the pK_a of free cysteines is ~ 8.5 (Alberts *et al*, 2002), the positively charged microenvironment within the Prx active site lowers the pK_a of Cys_P, with reported values that range from 5.1–6.3, by stabilising the negatively charged thiolate (Marino and Gladyshev, 2010; Poole, 2015). The lower pK_a means the majority of Cys_P are thiolates at neutral pH, however this lower pK_a also results in a decrease of thiolate nucleophilicity (Whitesides *et al*, 1977). Small molecule thiolates react with peroxides at only 20 $M^{-1}s^{-1}$ (Winterbourn and Metodiewa, 1999), so the enhanced acidity of the critical cysteines are a prerequisite but not the reason for the catalytic efficiencies observed in Prxs. Interactions that stabilise the thiolate within the active site also restrain its activity in the absence of substrate (Ferrer-Sueta *et al*, 2011). The comparison of multiple Prx crystal structures containing peroxide as well as peroxide-mimicking ligands and water molecules, reveals a track of oxygen-binding sites within the active site, which facilitates substrate specificity (Hall *et al*, 2010; Nakamura *et al*, 2010). The polar interactions that stabilise the thiolate in the resting enzyme switch upon substrate binding to the peroxide oxygens,

transiently increasing thiolate nucleophilicity (Ferrer-Sueta *et al*, 2011; Portillo-Ledesma *et al*, 2014). These conserved threonine and arginine residues, along with two back bone amides, form hydrogen bonds with the peroxide substrate, supporting the correct H_2O_2 (or ROOH in **Figure 1.7**) orientation, and polarise it for S_N2 nucleophilic displacement (Ferrer-Sueta *et al*, 2011). These interactions are dynamic and are optimised to stabilise the transition state; this is supported by the Michealis complex of H_2O_2-bound Prx from *Aeropyrum pernix* (Nakamura *et al*, 2010). Over a range of temperatures, a reported large entropic penalty (*TΔS*), was observed in *Mycobacterium tuberculosis* AhpE catalytic rates, which reflects the ordered transition state. This was offset by a large enthalpic change leading to a decrease in free energy of activation (Zeida *et al*, 2013). Large fluorescence changes were observed in *Salmonella typhimurium* AhpC (StAhpC) after the addition of peroxides, which indicate the active site undergoes rearrangements upon substrate binding. This also led to an inferred K_d for H_2O_2 of ~400 nM (Parsonage *et al*, 2015).

The catalytic cycle of Prxs involves two independent half reactions giving rise to double displacement kinetics: the first being the reduction of peroxide by Prx, and the second being the recycling of Prx via a reductant. In a reduced Prx with a fully folded (FF, **Figure 1.7**) active site, an S_N2 reaction between the thiolate of Cys_P and H_2O_2 to form a sulfenic acid derivative, Cys-S_POH. This initial oxidation step of Cys_P with H_2O_2 occurs rapidly (Step 1, **Figure 1.7**) and has a second order reaction rate in the range of 10^7-10^8 $M^{-1}s^{-1}$ (Perkins *et al*, 2015). The Prx active site is in equilibrium between the fully folded state and locally unfolded state (LU, **Figure 1.7**), and this is especially important for hyperoxidation (elaborated in **Section 1.4.2.2**). In typical 2-Cys Prxs, when the active site adopts a locally unfolded conformation, the Cys-S_POH can then react with Cys_R, generating a disulfide bond (**Steps 1 and 2** in **Figure 1.7**). The resulting disulfide bond can be reduced by reducing agents, such as DTT, TCEP or β-mercaptoethanol, or in a physiological context specifically by thioredoxin (Trx) to complete the catalytic cycle (**Step 3**, Wood *et al*, 2003a). Within the cell, the rate of this final recycling step is restricted by the catalytic turnover as well as the low cellular abundance of Trx. At around 10^5 $M^{-1}s^{-1}$, this rate limiting step is generally observed to be 2 orders of magnitude lower than Prx reduction of peroxide (Watabe *et al*, 1997; Hampton and O'Connor, 2016; Winterbourn and Hampton, 2015). For this reason, the misassumption arose of Prxs being poor peroxidases in comparison to gluthione peroxidases and catalases, as early kinetic experiments studied the full catalytic Prx cycle. The high abundance of Prx, and its initial high reactivity towards H_2O_2, still makes it a key peroxidase for the maintenance of the redox landscape, and this double displacement kinetics could even be useful for its cellular function (Winterbourn *et al*, 2015).

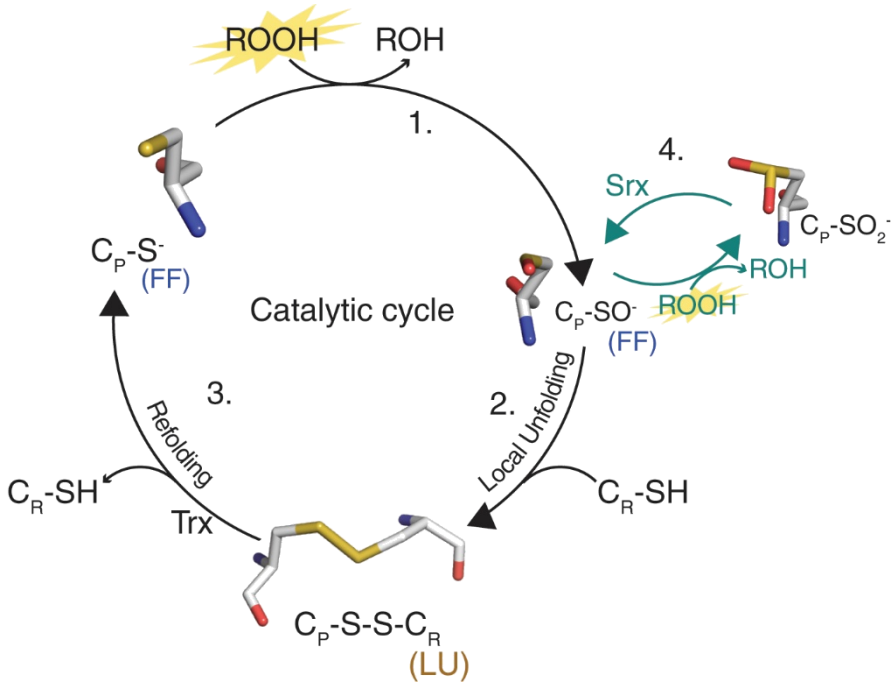

Figure 1.7 The catalytic cycle of Prxs
The fully folded (FF) active site of Prxs houses an activated, deprotonated peroxidatic cysteine (C_P), ready for the nucleophilic attack of hydroperoxides (ROOH, which includes H_2O_2) (**Step 1**). The sufenic acid can go on to further react with another H_2O_2 to form hyperoxidised proteins (**Step 4**), or local unfolding of the α2 helix occurs to facilitate disulfid bond formation (**Step 2**). The recycling step of Cys_P (**Step 3**) is completed upon reacting with enzymes, such as thioredoxin proteins, *in vivo*.

Prxs also have the ability to reduce a wide range of other peroxide derivatives (Wood *et al*, 2003b, Hofmann *et al*, 2002). In fact, eukaryotic Prxs are able to reduce peroxynitrite, alkylhyperoxidases and peroxides (Peskin *et al*, 2010), with human Prx2 able react with t-butyl and cumene hydroperoxides, albeit with less efficiency compared with H_2O_2 (Peskin *et al*, 2007). Prxs are the only known enzymes to catalyse the reduction of peroxynitrite to nitrite, an important signalling molecule (Perkins *et al*, 2015). The lower catalytic efficiencies observed for other larger substrates has been attributed to the slower rate of binding of this substrate (Parsonage *et al*, 2005).

1.4.2.2 Hyperoxidation and the floodgate model

Aside from its peroxidase activity, Prxs have been associated with many other physiological roles, such as redox sensors, mediators of cellular signalling and circadian rhythms (**Section 1.4.2.3**) as well as molecular chaperones (**Section 1.4.2.4**). These roles are closely linked to the oxidation state of the Cys_P. Prxs that are more susceptible to hyperoxidation have evolved sequence motifs GGLG and YF. The YF motif, which is part of an extra C-terminal region that forms a α7-helix, interacts

with the GGLG motif that lies in a loop region neighbouring the Cys_P, restricting the movements within the active site (Wood *et al*, 2003a). The reduced flexibility of the active site shifts the equilibrium of the active site towards a fully folded state, where resolution by Cys_R (**Step 2** in **Figure 2.17**) is delayed, creating a 'kinetic pause'. Interestingly, the rates of disulfide bond formation inversely correlates to the Prx sensitivity towards hyperoxidation, where the highly sensitive human Prx2, less sensitive Prx3, and robust StAhpC form disulfide bonds at rates of 1.7 s^{-1}, 22 s^{-1}, and 75-88 s^{-1} respectively (Pace *et al*, 2013; Perkins *et al*, 2015; Parsonage *et al*, 2015). This 'kinetic pause' provides an opportunity for the sulfenic Cys_P-SOH to react further to form sulfinic acid, Cys_P-SO_2H and/or sulfonic acid, Cys_P-SO_3H (Wood *et al*, 2003a). PrxQ protein crystals were soaked with H_2O_2 to obtain 15 high resolution crystal structures, which depicted each stage of hyperoxidation from the Cys_P-SOH form to the Cys_P-SO_2H form (Perkins *et al*, 2015). The universally conserved arginine residue adopts an inverted position to make space in the binding site for the second H_2O_2. Hyperoxidised Prxs are removed from the catalytic cycle as they no longer react with H_2O_2, allowing H_2O_2 to act as a secondary messenger. This can be a transient feature as, in some cases, hyperoxidised Prxs with Cys_P-SO_2H can be reduced by sulfiredoxin (Srx) (**Step 4** in **Figure 2.17**), which restores peroxidase activity (Lowther and Haynes, 2011). This is a slow and energy consuming process, with the mammalian Srx requiring one ATP and two glutathione or thioredoxin molecules to reduce a single hyperoxidised cysteine (Jeong *et al*, 2006). This heightened sensitivity towards hyperoxidation has been proposed as a unique mechanism by which Prxs are redox sensors that can transmit signals during a H_2O_2 flux, acting as a 'floodgate' as part of part of H_2O_2-mediated signalling (Finkel, 2011). Thus far, Srx genes have only been detected in eukaryotes and cyanobacteria (Boileau *et al*, 2011), so this 'floodgate' hypothesis may only apply for certain types of Prxs.

1.4.2.3 Diverse roles: cell signalling processes to circadian rhythms

Prxs have diverse roles that can range from protecting telomeric DNA from oxidative damage (Aeby *et al*, 2016), to being crucial biomarkers for apoptosis (Hampton *et al*, 2016), as well as having cytoprotective roles in inflammation (Knoops *et al*, 2016). However, highlighted will be examples of Prxs that mediate the cellular redox landscape in processes that involve H_2O_2 in a non-stress related function.

At low physiological levels, H_2O_2 acts as a crucial secondary messenger in many signalling processes such as growth factor signalling resulting in proliferation, cellular migration, Toll-like receptors and autophagy (Gough and Cotter, 2011; Finkel, 2011). H_2O_2 oxidises thiol residues on cell surface receptors, such as the tumour suppressor PTEN (Kwon *et al*, 2004), the apoptotic kinase ASK1

(Nadeau *et al*, 2007), and the protein tyrosine phosphatases (Lee *et al*, 1998). The oxidation of phosphatases inactivates the protein, but this also is reversible, allowing for restoration of reduced thiols that can act to 'brake' kinase-mediated phosphorylation cascades (Rhee *et al*, 2005). This reaction between the target thiols and H_2O_2 is several orders of magnitude slower compared with that of Cys_P towards its substrate (Winterbourn, 2013), suggesting that Prx proteins close by must be inactivated to allow for other proteins to react with H_2O_2 (Woo *et al*, 2010, Lim *et al*, 2015). Alternatively, redox-regulated proteins are not directly oxidised by H_2O_2, but rather their oxidation is mediated by Prx proteins that act as redox relays (Randall *et al*, 2013). In the presence of H_2O_2, the Cys_P reacts to form sulfenic Cys_P or a disulfide bond with Cys_R. The oxidised Prx can then be reduced by effector proteins that cause a change in effector functions, such as ASK1 (Nadeau *et al*, 2007) as well as transcription factors: PAP from yeast as well as mammalian STAT3 (Vivancos *et al*, 2005, Sobotta *et al*, 2015).

Hyperoxidised 2-Cys Prxs were found to be a transcription-independent circadian biomarker across a variety of organisms (Edgar *et al*, 2012; Olmedo *et al*, 2012; Hoyle and O'Neill, 2015). In fact, oscillation in 2-Cys Prx-SO_2H abundance is the effect of an underlying rhythm in oxidative metabolism (Causton *et al*, 2015). Within mouse adrenal gland cortex mitochondria, P450 enzymes oxidise cholesterol to corticosterone and H_2O_2 is generated as a by-product, hyperoxidising and inactivating human Prx3 (Kil *et al*, 2012). The inactivated HsPrx3 results in the accumulation of H_2O_2, which activates p38 kinase and leads to the suppression of steroidogenesis. The levels of hyperoxidised HsPrx3 and its recycling enzyme, Srx, show circadian oscillations. This suggests that the 'floodgate' hypothesis with reversibly hyperoxidised HsPrx3 is intertwined with the circadian production of corticosterones and the feedback inhibition of steroidogenesis (Kil *et al*, 2015). In fact, cytosolic Srx is imported into the mitochondria via the formation of a disulfide bond with Hsp90 proteins, and this is likely to be promoted by the release of H_2O_2 from the mitochondria, and again, this shows circadian oscillations (Rhee and Kil, 2016).

1.4.2.4 Molecular chaperones under stress conditions

2-Cys Prxs have been shown to behave as molecular chaperones *in vitro* under stress conditions. This was first highlighted in yeast 2-Cys Prxs, which under normal conditions formed decameric rings, but when the protein is hyperoxidised or undergoes heat shock, they assemble into protein balls with chaperone activity (Jang *et al*, 2004). This assembly from a low molecular weight (LMW) ring form of a 2-Cys Prx into a high molecular weight (HMW) form after exposure to stress conditions is associated with loss of peroxidase activity and onset of chaperone activity (An *et al*, 2015; Barranco-Medina *et al*, 2009). This was also observed for hyperoxidised human Prx2, which

formed a range of HMW structures (Moon *et al*, 2005). Hyperoxidation of yeast Prx1 was found to be reversible, with Srx dissociating the HMW form and restoring peroxidase activity (Moon *et al*, 2013).

However, neither hyperoxidation nor higher order oligomerisation is necessary for chaperone function of certain species. At elevated temperatures, reduced decameric rings of *Leishmania infantum* mitochondrial 2-Cys Prx, mTXNPx, undergoes structural rearrangements to expose hydrophobic areas at the centre of the ring where substrates can bind (Castro *et al*, 2011; Teixeira *et al*, 2015). Whereas, hyperoxidised 2-Cys PrxA from *Arabidopsis thaliana* chloroplasts exhibited holdase activity for decameric rings, as opposed to HMW structures (König *et al*, 2013). Further analysis reveals 2-Cys PrxA can form spherical-shaped HMW complexes with high chaperone activity compared with its dimeric forms, which had peroxidase activity (Lee *et al*, 2015) – note that having dimeric peroxidases is the opposite of typical 2-Cys Prxs. The S150C mutein of 2-Cys PrxA was also demonstrated to increase in both chaperone and peroxidase activity due to the stabilisation of the dimer-dimer interface that forms the Prx ring, as S150 occurs at this interface (Lee *et al*, 2015).

Further expanded in **Chapter 2**, certain Prx rings can also assemble in stacks of rings at lowered pH, which was suggested to be another HMW form of Prx molecular chaperones (Saccoccia *et al*, 2012). Prx chaperone activity was shown to be vital for the *in vivo* protein homeostasis of zinc-deficient yeast (MacDiarmid *et al*, 2013). Whereas, *in vivo* relevance of chaperone function or HMW formation of many Prxs has yet to be established (Toledano and Bo, 2016).

1.4.3 Diversity of peroxiredoxin structures that make them appealing tectons

Typical 2-Cys Prxs can form a wide variety of protein structures (**Figure 1.8**). Many typical 2-Cys Prxs oligomerise as toroids, composed of eight to twelve subunits, when Cys_P is reduced, whereas disulfide bond formation shifts the equilibrium towards dimers (Barranco-Medina *et al*, 2009; **Section 1.4.2.1**; **Chapter 3**). Protein rings can further self-assemble into HMW forms such as protein tubes (**Chapter 2**) as well as proteinaceous spheres with molecular chaperone function (Jang *et al*, 2004; Teixeira *et al*, 2015; **Section 1.4.2.4**). Other HMW structures include the formation of cages and catenanes observed under the unnatural preparatory conditions used for structural analysis (Cao *et al*, 2005; Meissner *et al*, 2007). Human Prx2 are usually reduced, decameric ringed proteins. However, under certain preparatory conditions (ammonium molybdate at pH 6.5 and 0.2% (w/v)

PEG1000) for TEM, this protein can form dodecahedral cages that are most likely artefacts of the staining technique used (Meissner *et al*, 2007; Figure 1.8 D). Catenanes, or interlocked rings, were observed in the crystallisation of bovine mitochondrial Prx3 (BtPrx3) (Cao *et al*, 2005; Figure 1.8 C). These catenanes were rotated at 55° with respect each other, with hydrophilic interactions in 12 areas on the ring surface driving the initial contacts required to generate the catenane. The dynamic nature of ring formation was demonstrated when the crystal containing the catenane was dissolved and recrystallised to form a non-catenane ring, as well as under the TEM, where a mixed population of catenanes and single rings were observed (Cao *et al*, 2007). Whether these cages and catenanes are biologically relevant is still unclear, but these environmentally sensitive, diverse architectures make Prxs an attractive model for protein bionanotechnology.

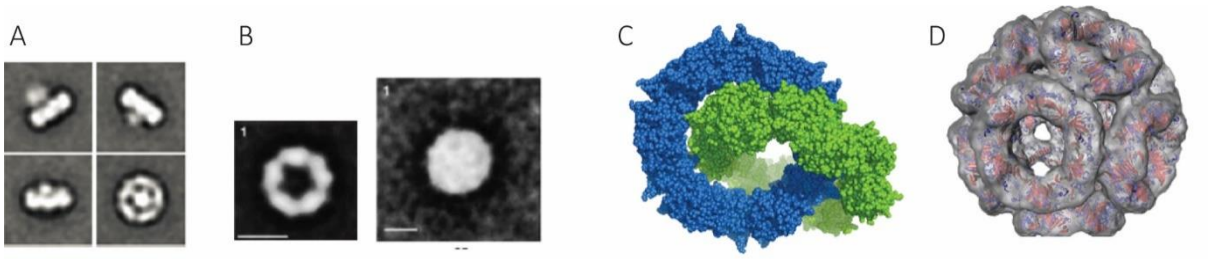

Figure 1.8: Various Prx HMW structures
Prxs are known to form HMW structures that can have chaperone function: (A) *Leishmania infantum* mitochondrial Prx is seem to bind to a substrate at the ring centre (Teixeira *et al*, 2015), whereas (B) are proteinaceous balls observed to formed in yeast (Jang *et al*, 2004). (C) Crystal structure of bovine Prx3 interlocked as catenanes (PDB: 1ZYE, Cao *et al*, 2007). (D) Single particle averaging of TEM images to give a 3D reconstruction for human Prx2 (Meissner *et al*, 2007). All images have been reprinted with permission from their respective journals.

The variety of protein architectures make typical 2-Cys Prxs great candidates for tectons in protein nanotechnology (Phillips *et al*, 2014; Phillips *et al*, 2014). The inherent ability for typical 2-Cys Prxs to switch quaternary structure according to oligomeric state has proved to be a useful feature in the design of artificial real-time intracellular H_2O_2-sensors, where Prxs were fused with redox-dependent GFP proteins (Morgan *et al*, 2016). Prx rings can self-assemble into tubes, and similar to the SP1 protein example mentioned in Section 1.3.3.5 (Medalsy *et al*, 2008), this has been used to generate prototype 'nano-peapods' where histidine tags at the ring centre of Prx1 from *Schistosoma masoni* (SmPrx1) can bind to metal ions as well as nanoparticles (Ardini *et al*, 2014). SmPrx1 patterned graphene-oxide layers were generated to capture nanoparticles (Ardini *et al*, 2016). The use of Prxs in nanotechnology has just begun. Many functions of the protein superfamily can be exploited for use in bionanotechnology, such as the weak DNA binding properties of human Prx1 (Aeby *et al*, 2016) or the phospholipid-binding Prx6 (Manevich *et al*, 2007).

1.5 Human peroxiredoxin 3: tuning natural function towards new functionalisable tectons

1.5.1 Why human peroxiredoxin 3?

The mitochondrial typical 2-Cys Prx, human peroxiredoxin 3 (HsPrx3), is an ideal tecton for protein bionanotechnology because of the various structures it exhibits: dimers, dodecameric rings, as well as rings that self-assemble into tubes, and also the closely related bovine Prx3 forms catenanes (**Chapters 2 and 3**). Exploring the self-assembly of HsPrx3 will not only be beneficial for its application in bionanotechnology, but also will provide insights into its natural function. Now that the context has been set for a plethora of cellular functions of the Prx superfamily, the intracellular roles and importance for specifically HsPrx3 will be explored, with links back to its structure as well as how this protein can make a promising tecton.

1.5.2 Peroxiredoxin populations within the human cell

Among eukaryotes, different Prx isoforms exist due to gene duplication and cellular compartmentalisation (Hofmann *et al*, 2002; Wood *et al*, 2003b); these isoforms can have varying physiological roles. Mammalian Prxs include six different isoforms (**Table 1.2**), and are highly abundant: comprising 1% of soluble cellular proteins (Chae *et al*, 1999). The abundance of each isoform varies between cell types as well as within the different cellular compartments.

Table 1.2: Comparing and summarizing the different isoforms of Prx present inside mammalians

Prx isoforms	Prx1	Prx2	Prx3	Prx4	Prx5	Prx6
Mechanistic type	Typical 2-Cys				Atypical 2-Cys	1-Cys
Phylogenetic subfamily	Prx1				Prx5	Prx6
Cellular location	Cytosol, nucleus	Cytosol, membrane	Mitochondria	Cytosol, golgi, secreted, membrane	Cytosol, peroxisome, mitochondria	Cytosol
Oligomeric state	Decamer	Decamer	Dodecamer	Decamer	Decamer	Monomer
Structure code on PDB?	4XCS	1QMV	Just bovine 1ZYE	3TJB	4MMM	5BEM

To provide insights on the structure and function of HsPrx3, previous research on related proteins, collectively called peroxiredoxin 3 (Prx3), is discussed. Throughout history, the discovery of Prxs in

different organisms and cellular contexts have resulted in various names for the same protein. Prx3 can be found in mitochondria of various eukaryotic organisms and previous nomenclature used include: AOP-1 (this is often also the gene name for Prx3); MER5, the mouse equivalent; and SP-22, the bovine equivalent of HsPrx3 that is also called BtPrx3.

Functionally characterising HsPrx3 is an ongoing collaboration with Mark Hampton from the Otago School of Medicine, who is interested in this important human protein in a physiological context. Previous work from within the lab by Amy Phillips and Helen Ashmead paves the way for using HsPrx3 as a tecton for applications in bionanotechnology.

1.5.3 Human peroxiredoxin 3: Functions inside of the cell

1.5.3.1 The minder of the mammalian mitochondrial oxidant landscape

The mitochondrion is the major intracellular compartment for oxygen consumption. It also contains the electron transport chain which tend to leak electrons, especially from complexes I and III (Boveris *et al*, 1973; Cadenas *et al*, 1977; Turrens, 1997). These electron escapees can univalently reduce oxygen to $O_2^{\bullet-}$, a reactive oxygen species. Reactive oxygen species can wreak havoc within a cell by causing mutations to DNA bases and disrupting the structure and function of proteins and lipids (Murphy, 2009). $O_2^{\bullet-}$ does not readily cross membranes as it is charged and remains trapped in the mitochondria, disrupting the Fe-S centres in the electron transport chain (Wallace, 1999). Mn^{2+}-dependent superoxide dismutase, localised in the mitochondria, acts in the front lines of antioxidant defence by converting $O_2^{\bullet-}$ into H_2O_2 (Chance *et al*, 1979). Although a less reactive oxidant, H_2O_2 can be readily converted to another reactive oxygen species, such as $OH^{\bullet}$, with deleterious cellular effects, and so its levels must be carefully controlled. H_2O_2 is also known as the 'Jekyll and Hyde' signalling molecule, because at low physiological levels, it is an important secondary messenger for cellular signalling processes (Gough *et al*, 2011).

H_2O_2 levels are regulated by a team of peroxidases within the cell; the exact composition of which vary between cellular compartments and between cell types. Intracellular H_2O_2 can be reduced by catalases, glutathione peroxidase 1 (GPx1) with glutathione as an electron donor, and Prxs. Despite a high reaction rate of 10^7 $M^{-1}s^{-1}$ with H_2O_2, only ~2 µM GPx1 is localised to mitochondria which then accounts for ~9% of the H_2O_2 degrading capacity of the mitochondrial matrix (Cox *et al*, 2010). Glutathione must also be imported because there are no mitochondrial enzymes for its synthesis (Esworthy *et al*, 1997; Panfili *et al*, 1991; Legault *et al*, 2000; Ho *et al*, 1997). Conversely, Prx3 and

an atypical 2-Cys peroxiredoxin V (Prx5) both localise to the mitochondria. These Prxs are by far the most abundant peroxidases, at ~60 μM and ~20 μM respectively, making them especially relevant for maintaining the mitochondrial oxidant landscape (Chang *et al*, 2004; Cox *et al*, 2010). Prx3 favours H_2O_2 as a substrate, with reaction rates in the order of 10^7 $M^{-1}s^{-1}$ (Cox *et al*, 2009b). Assays have shown that Prx5 favours peroxynitrite as its substrate, reacting with rates 10^7 $M^{-1}s^{-1}$ and with H_2O_2 at 10^5 $M^{-1}s^{-1}$ (Trujillo *et al*, 2007). Therefore conferring a niche for each Prx, where Prx3 acts as the main peroxidase targeting H_2O_2 within the mammalian mitochondria, accounting for ~90% of the potential H_2O_2 degradation capacity (Cox *et al*, 2010).

HsPrx3 contains the conserved motifs, YF and GGLG, which confer susceptibility towards hyperoxidation (Cox *et al*, 2009b). However, HsPrx3 is more resistant to hyperoxidation compared with the other 2-Cys Prxs, HsPrx2 and HsPrx1, due to the faster formation of disulfide bonds between adjacent HsPrx3 monomers (Section 1.4.2.2; Cox *et al*, 2009b; Pace *et al*, 2013; Haynes *et al*, 2013). Oxidised HsPrx3 is recycled by Trx2 (Cunniff *et al*, 2015), whereas hyperoxidised HsPrx3 can be recovered by Srx (Noh *et al*, 2009), and both enzymes, like Prx, are nuclear-encoded and are imported from the cytosol. Hyperoxidation of HsPrx3 has been implicated in a negative feedback loop of steroidogenesis with protein levels exhibition circadian oscillations (Kil *et al*, 2012).

1.5.3.2 Prx3 is not required for short-term organismal survival

In order to probe the physiological significance of Prxs, knock out mice were used to examine the phenotypes of null mutants for each of the six isoforms. Despite Prxs being important peroxidases for a variety of cellular processes - such as growth, differentiation, apoptosis and even malignant transformation – mice deficient in a particular Prx occasionally appear outwardly healthy and are fertile (Neumann *et al*, 2003; Szabó *et al*, 2009). Despite this, each type of Prx null mice have specific pathophysiological phenotypes that demonstrate the unique roles played by each isoform of Prx (Table 1.2; Li, 2016). Female mice with knocked out Prx3 have deficient placental defence, resulting in an increase in still births (Li *et al*, 2008). Prx3 null mice also exhibit oxidative stress in their adipose cells (Huh *et al*, 2012) and are more susceptible to lipopolysaccharide-induced oxidative stresses (Li *et al*, 2007). Prx3 deficiency induced accelerated oxidative stress and mitochondrial impairment that is important for muscle function within mice – these effects becoming more pronounced over time when comparing Prx3 null and normal mice (Zhang *et al*, 2016). Although important for long-term normal cellular function, Prx3 is not necessarily required for short-term organismal survival, which may prove to be useful as a synergistic target against disease.

1.5.3.3 Human diseases linked to cellular redox homeostasis: roles of peroxiredoxin 3

Redox homeostasis within cells must be finely tuned in order to prevent abnormal functions that cause disease phenotypes. Lowered levels of active Prx3 has been identified as a marker in a variety of neurodegenerative diseases, such as Alzheimer's disease, Down syndrome as well as Parkinson's disease (Kim *et al*, 2001; Angeles *et al*, 2011). 30-40% of Parkinson's disease patients have mutant LRRK2 kinases that aberrantly phosphorylate Prx3, diminishing its peroxidase activity, and leads to an increase in neuronal cell death (Angeles *et al*, 2011). Another example where Prx3 levels can aid disease prevention is when Prx3 is overexpressed in mice hearts (Matsushima *et al*, 2006). Overexpressed Prx3 attenuates the deleterious effects of oxidative stress that results after myocardial infarction, which can then lead to left ventricular remodelling.

In contrast, the overexpression of Prx3 has been found to be a marker for a variety of cancer tissues and cell lines (reviewed in Li and Yu, 2015). Prx3s can also function as tumour suppressors and is associated with resistance towards chemo- and radiotherapies (Wang *et al*, 2013; Nonn *et al*, 2003). In fact, colon cancer stem cells were found to have higher reactive oxygen species and oxygen consumption, so by knocking down levels of Prx3 protein, the viability of these cancer stem cells was diminished due to mitochondria dysfunction (Song *et al*, 2011), whereas normal cells remain unaffected. Elevated Prx3 levels established a redox set point for malignant mesothelioma cells to thrive at increased levels of reactive oxygen species (Cunniff *et al*, 2014), and so disabling Prx3 was an effective therapeutic against these cancer cells (Cunniff *et al*, 2015).

1.6 Aims and objectives of this thesis

As a typical 2-Cys Prx, HsPrx3 exhibits a wide variety of structures that can range from dimers to dodecameric rings as well as stacked rings, and closely related bovine Prx3 can form catenanes (Phillips, 2014). Not only does this protein carry many hallmarks of a great tecton, such as protein stability and ease of production, this diversity in switchable structures makes HsPrx3 highly appealing tectons for the creation of new smart materials and functions in bionanotechnology.

Chapter 2 characterises the first crystal structure of wild-type HsPrx3, revealing an intriguing HMW assembly of three stacked rings. This structure not only enables the formulation of a novel hypothesis for protein chaperone function, but also provides the blueprint for which further modifications can be made to tailor new functions to these protein building blocks.

Chapter 3 investigates the mechanism by which HsPrx3 proteins assemble into HMW protein tubes using native mass spectrometry. This sensitive technique enables the detection of populations of large protein oligomers in the gas phase, providing conclusive evidence for non-commutative HsPrx3 ring stacking behaviour. This precise assessment of HsPrx3 self-assembly provides a foundation for the use of these tectons in bionanotechnology.

Chapter 4 involves disentangling the redox switch of HsPrx3 to understand the role of protein quaternary structure for its peroxidase activity. Muteins S75E and S78C were designed at the dimer-dimer interface, and the resulting quaternary structure changes were characterised using biophysical techniques as well as crystallography. S75E forming an obligate dimer and S78C forming stabilised toroids. The effect of these quaternary structure changes on peroxidase activity was assessed using competitive assays with horse radish peroxidase, as well as catalase. The creation of new building blocks, especially the stabilised toroids, provides improved stability of HsPrx3 tectons which can be useful for future applications.

Chapter 5 explores ways to functionalise HsPrx3 protein tectons with new chemistries via the incorporation of unnatural amino acids. Click chemistry, in the form of p-azidphenylalanine, was chosen as a versatile means to embellish the HsPrx3 tecton surface. An already developed *E. coli* protein expression system with orthogonal tRNA and aminoacyl-tRNA synthetases was used to incorporate p-azidophenylalanine into amber stop codons (Chatterjee *et al*, 2013). Despite the current marginal success with this system, it is a first step towards the generation of functionalisable HsPrx3 tectons.

Chapter 2: High molecular weight assemblies of human peroxiredoxin 3

The work presented in this chapter has been published in the following:

Yewdall NA, Venugopal H, Desfosses A, Abrishami V, Yosaatmadja Y, Hampton MB, Gerrard JA, Goldstone DC, Mitra AK, Radjainia M (2016) Structures of Human Peroxiredoxin 3 Suggest Self-Chaperoning Assembly that Maintains Catalytic State. *Structure* 24: 1120-9.

2.1 Introduction

2.1.1 HsPrx3: the dodecameric typical 2-Cys Prx as a tecton

Human peroxiredoxin 3 (HsPrx3) are not only crucial peroxidases that exclusively localise to the mitochondria, but are also promising tectons for the development of protein-based nanotechnologies (Section 1.5). There is a need to have a molecular understanding of how these proteins self-assemble, yet, there are currently no high resolution structures of HsPrx3. Crystallographic information for all Prx3 proteins has been based on bovine Prx3 (BtPrx3) (Cao *et al*, 2005). BtPrx3 shares 93% sequence homology with HsPrx3, and was initially characterised using TEM, with external and internal diameters of 150 and 70 Å respectively (Gourlay *et al*, 2003). Subsequent crystal structures of BtPrx3, containing point mutations, reveal two dodecameric rings interlocked as catenanes (Cao *et al*, 2005, Cao *et al*, 2015). These BtPrx3 structures informed the previous studies of HsPrx3 in our lab (Phillips, 2014; Ashmead, 2016). TEM was used to generate a low resolution single particle model of the dodecameric HsPrx3 ring (Phillips *et al*, 2014) and higher resolution structures of the protein were also obtained using cryo-electron microscopy (cryo-EM; Radjainia *et al*, 2015).

2.1.2 Previously observed high molecular weight assemblies of Prx

2-Cys Prx proteins can extend their quaternary structure repertoire by self-associating to form high molecular weight (HMW) structures that extend beyond dimers and rings, to include spherical

clusters, stacks of rings, cages, and catenanes (Section 1.4.3; Jang *et al*, 2004; Harris *et al*, 2001; Meissner *et al*, 2007; Cao *et al*, 2005).

Prx stacks have been observed for HsPrx2, HsPrx3, and bovine and rat Prx3s using TEM (Kato, 1985; Harris *et al*, 2001; Gourlay *et al*, 2003). At the outset of this work, the only crystal structure where Prx rings display a stacked configuration was of Prx1 from the parasite, *Schistosoma masoni* (SmPrx1) formed at pH 4.2 (PDB: 3ZVJ, Saccoccia *et al*, 2012). Lowering solution pH causes HsPrx3 rings to assemble into long, straight filaments (Phillips *et al*, 2014), allowing for 7 Å resolution cryo-EM reconstruction of the HMW form (Radjainia *et al*, 2015).

2.1.3 Factors influencing Prx tube formation

The formation of HMW Prx tubes can be influenced by a variety of factors, including pH, hyperoxidation, salt concentrations, and tags. A molecular understanding of HMW structures, especially at the ring interface (R interface), provides invaluable insight to rationalise how these factors affect protein association. Based on the small number of detailed HMW structures currently available, a locally unfolded active site was a recurring structural change caused by these factors, which was hypothesised to contribute towards formation of HMW tubes (Saccoccia *et al*, 2012, Radjainia *et al*, 2015). Examining the HsPrx3 model system within the context of these factors would also be a crucial first step towards creating protein tubes with a controllable length.

2.1.3.1 Lowering solution pH can reproducibly form HMW stacks

Protein oligomerisation that is pH-dependent is not unique to Prxs (Kristensen *et al*, 1999; Kilic *et al*, 2006; Zhang *et al*, 2012) and is known to occur for at least two types of Prx: SmPrx1 and HsPrx3 (Saccoccia *et al*, 2012, Radjainia *et al*, 2015). SmPrx1 crystallised under reducing conditions at pH 4.0 and diffracted to 3 Å to reveal two stacked rings and the atomic clues as to their association (PDB: 3SVJ). The R interface formed between SmPrx1 rings is comprised of two interacting regions, where one monomer interacts with two apposing monomers from the other ring, resulting in a cog-wheel-like R interface (Saccoccia *et al*, 2012). The first region of interaction occurs at the ends of the α2 and α6 helices, whereas the second occurs between β2 strands (Figure 2.1 A).

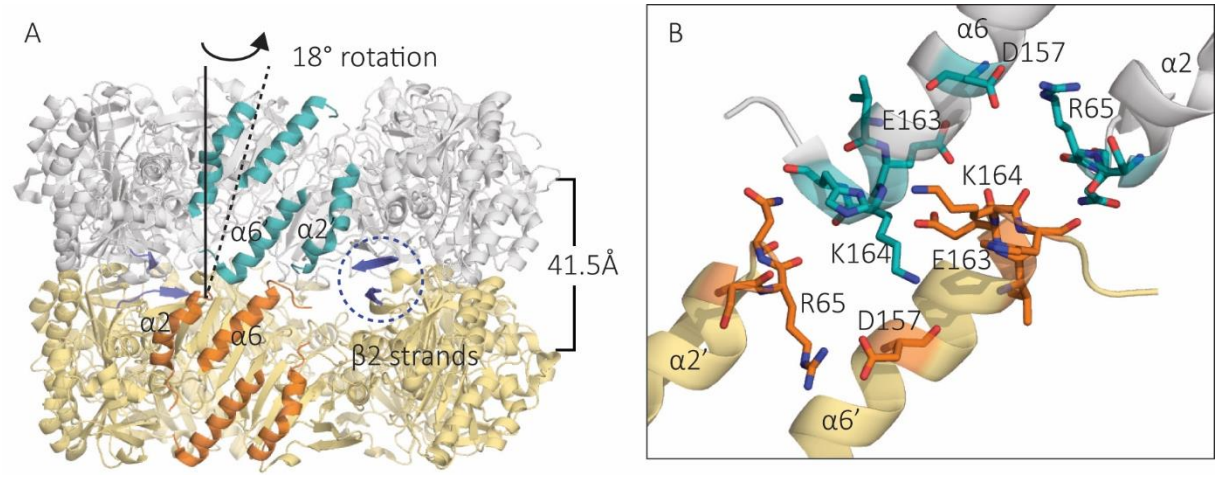

Figure 2.1: SmPrx1 crystal structure showing two stacked rings (PDB: 3ZVJ)
SmPrx1 protein rings interact with a helical rise of 41.5 Å and an azimuthal rotation of 18 ° between respective rings (**A**). The R interface of SmPrx1 is comprised of two main regions that are associated by hydrogen bonds and polar contacts (Saccoccia *et al*, 2012): the α2 and α6 helix of one ring was in contact with the adjacent, equivalent helices of the other ring (important residues highlighted as sticks in **B**); and the β2 strand of one subunit interacts with the equivalent strand in the opposing subunit (dashed circle in **A**).

Comparison of low resolution 7 Å cryo-EM structure of HsPrx3 with SmPrx1 stacks formed at pH 4.2, revealed important differences (Radjainia *et al*, 2015). In the cryo-EM map, the HsPrx3 C-termini were partially folded, suggesting that the stated requirement for an unfolded C-terminus to facilitate stacked assemblies (Saccoccia *et al*, 2012) may only be applicable for SmPrx1 proteins. As in the case of SmPrx1 stacks, the active site of the HsPrx3 cryo-EM reconstruction was seen to be in a locally unfolded state, a conformational change that has been attributed to a protonated Cys_P at pH 4 (*pKa* of the Cys_P ~ 5; Nagy *et al*, 2011). A locally unfolded active site is thought to be a requirement for, and facilitator of, stacking of the Prx rings (Saccoccia *et al*, 2012). Although the SmPrx1 crystal structure and the low resolution cryo-EM map of HsPrx3 both provide a solid basis for analysing interactions that occur at the interface between the two rings, the R interface, these interactions may be limited to pH-influenced protein oligomerisation.

2.1.3.2 Hyperoxidation causing HMW tube formation and the holdase hypothesis

Prx hyperoxidation (**Section 1.4.2.2**) has been linked to the formation of HMW structures, such as spherical protein clusters, that have a molecular chaperone function defined by their holdase activity (**Section 1.4.2.4**, Jang *et al*, 2004, Rhee, 2011). *In vivo* fluorescent-labelling of Prx2 proteins suggest that, during oxidative stress situations, these proteins form filamentous structures. (Phalen *et al*, 2006). Whether these filamentous structures occur through ring stacking or association to some other long scaffold protein has yet to be conclusively determined. The Cys_P of SmPrx1 was

mutated to aspartic acid to mimic the negatively charged nature of a sulfenic acid (**Table 2.1**, Angelucci *et al*, 2013), resulting in the formation of HMW tube structures. The structure of hyperoxidised HsPrx3 has yet to be determined. Interestingly, hyperoxidation of HsPrx3 destabilises its toroid form, resulting in dimer formation; this is in contrast to other Prxs, such as Prx2, which forms stabilised rings (Poynton *et al*, 2016).

Linking hyperoxidation of Cys_P with resulting structural changes that cause the stacking behaviour of Prx proteins remains weakly supported in the current literature. There have been suggestions that sulfenic acid disrupts normal hydrogen bonding interactions that occur, with Cys_P causing the active site to unfurl into a locally unfolded conformation, much like in acidic conditions, enabling protein rings to stack (Angelucci *et al*, 2013). However, this has yet to be directly verified – and is at odds with crystal structures with hyperoxidised Cys_P displaying fully folded active sites (Hall *et al*, 2011, Wang *et al*, 2012).

Table 2.1: Summary of the structural and functional characteristics of SmPrx1 wild-type and mutants (Angelucci *et al*, 2013) n/d - not determined, LMW - low molecular weight (rings and dimers), HMW - high molecular weight (protein tubes); TEM - transmission electron microscopy; SEC – size exclusion chromatography

Enzyme (SmPrx1)	Rationale	Quaternary structure assembly by X-ray crystallography	Quaternary assembly by TEM or SEC
Wild-type	-	Single decamer pH 7.4	Single decamer at pH 7.4 by TEM, mostly LMW from SEC
		Double decamer pH 4.2	Mostly HMW by SEC
C48S	Mimics protonated Cys_P	Single decamer (with 0.2 M SO_4^{2-}) pH 7.4	Nanotubes at pH 7.4 (without SO_4^{2-}) by TEM, HMW by SEC
C48D	Mimics hyperoxidised Cys_P	n/d	LMW & HMW forms by SEC & TEM
C48P	Mimics unwinding of α2 helix	Single decamer pH 7.4	LMW & HMW forms by SEC & TEM
C-terminus deletion	Mimics unfolded C-terminus	n/d	LMW & HMW forms by SEC & TEM

The holdase activity, characterised by the recognition and binding of unfolded substrates, is used to confer molecular chaperone functions to a protein (Jang *et al*, 2004). There has been one instance where holdase activity was characterised for HMW protein tubes (Angelucci *et al*, 2013).

Active site mutations of SmPrx1 that mimic different oxidative states of the peroxidatic cysteine were used to study the connection between stacked ring lengths and holdase behaviour (Table 2.1; Angelucci *et al*, 2013). The holdase activity was inversely correlated to stack lengths, and this was attributed to the decrease in available R interfaces where hydrophobic patches, which were proposed to bind other proteins, are located. Holdase activity has yet to be determined for HsPrx3.

2.1.3.3 Salts influencing Prx oligomerisation

Changes in ionic strength of solutions and the presence of particular salts have been reported to affect the oligomeric state of Prxs (König *et al*, 2013; Barranco-Medina *et al*, 2009), and could be a potential means to control protein nanotube lengths. Salts, such as the magnesium cation (Mg^{2+}) have been shown to promote formation of rat Prx3 tubes (Kato, 1985) and also HMW oligomers in chloroplast 2-Cys Prx (Aran *et al*, 2011), but the mechanism has yet to be explored.

Another study attributes the non-physiological effect of sulfate ions (SO_4^{2-}) bound in the active site to tube dissociation. C48S SmPrx1 proteins often form protein stacks at pH 7.4, but this was not observed in its crystal structure or SEC experiments containing sulfate ions in the running buffer (Table 2.1, Angelucci *et al*, 2013). The non-physiological effect of SO_4^{2-} was postulated to introduce constraints within the active site, when bound in 9 out of 10 protein crystal monomers. The SO_4^{2-} made polar contacts to a close serine residue and an arginine residue within the active site, resulting in a fully folded α2 helix that co-exists with an unfolded C-terminus (as seen in the crystal structure PDB: 3ZL5). This switch between a stacked ring and a single ring is reversible on the addition or removal of SO_4^{2-}. This indicates that C-terminal unfolding, alone, is insufficient for SmPrx1 protein stack formation. Both α2 unwinding and C-terminus unfolding is required (Saccoccia *et al*, 2012). A decrease in HMW species on the addition of SO_4^{2-} at pH 4 was also observed for wild-type HsPrx3 (Phillips, 2014). Protein tubes were still observed, presumably because of the lowered pH (Phillips, 2014). This suggests that lower pH has an effect on other amino acids that facilitate protein tube stacking, other than Cys_P. Preliminary studies also suggests that phosphate ions (PO_4^{3-}) behave similarly to SO_4^{2-} by stabilising the active site in a fully folded conformation, encouraging HsPrx3 into a dodecameric state (Littlejohn, 2012; Phillips, 2014). Stabilising the active site may prevent the transition of fully folded to locally unfolded, and thus, toroid dissociation on oxidation.

The effect of salts in solution may affect the active site of Prxs, but also changes the effective protein concentration within a solution. This “crowding out” is a technique often used to purify

protein (Burgess, 2009), and increased molecular crowding effects could also drive protein-protein associations required for tube formation

2.1.3.4 Histidine purification tags can affect Prx oligomerisation

An important, but often overlooked, feature of recombinant proteins is whether their purification tags, such as a six histidine tag (His_6-tag), are cleaved off or remain part of the protein (Kimple *et al*, 2001). There are numerous examples of proteins whose function and oligomerisation are affected by the presence of their His_6-tags (Majorek *et al*, 2014; Thielges *et al*, 2011), and this also the case for Prxs. His_6-tags stabilised the ring form of BtPrx3, lowering its peroxidase activity towards hydrogen peroxide (H_2O_2) (Cao *et al*, 2007). Similar observations were concluded for HsPrx3 (Phillips, 2014). This inspired part of Helen Ashmead's PhD work studying the effect of His_6-tags on HMW structures of HsPrx3, with different histidine tag lengths as means to control the formation of different stacked tubes (Ashmead, 2016). It is important to also note that SmPrx1 protein also contains a His_6-tag (Saccoccia *et al*, 2012), and this could influence how the proteins associate.

2.1.4 Chapter overview

This chapter describes the first crystal structure of wild-type HsPrx3 in a novel HMW assembly with a fully folded active site. This not only challenges a previous hypothesis of how Prx proteins associate together to form protein tubes, but also provides a needed blueprint with which the tecton can be can altered to enable future functionalisation. The crystal structure, at 2.8 Å, also enables molecular insights to rationalise how various factors, such as salt, pH or His_6-tag, influence HMW structure formation.

2.2 Wild-type HsPrx3 expression and purification

Pure wild-type HsPrx3 protein, both His_6-tagged and cleaved, were required for crystallography (**Section 2.3**) as well as native mass spectrometry analysis (**Chapter 3**). Recombinant His_6-tagged HsPrx3 was successfully expressed and purified (**Sections 7.3 and 7.4**), with yields of ~100 mg per litre of growth media. His_6-tagged HsPrx3 proteins were purified using immobilised metal affinity chromatography (IMAC) and size exclusion chromatography (SEC) (**Figure 2.3 A and B**). rTEV protease was used to cleave His_6-tagged HsPrx3 to generate cleaved HsPrx3 (**Section 7.5.3.2**). The masses of the pure cleaved and His_6-tagged wild-type HsPrx3 proteins were verified using liquid chromatography coupled mass spectrometry (LC-MS).

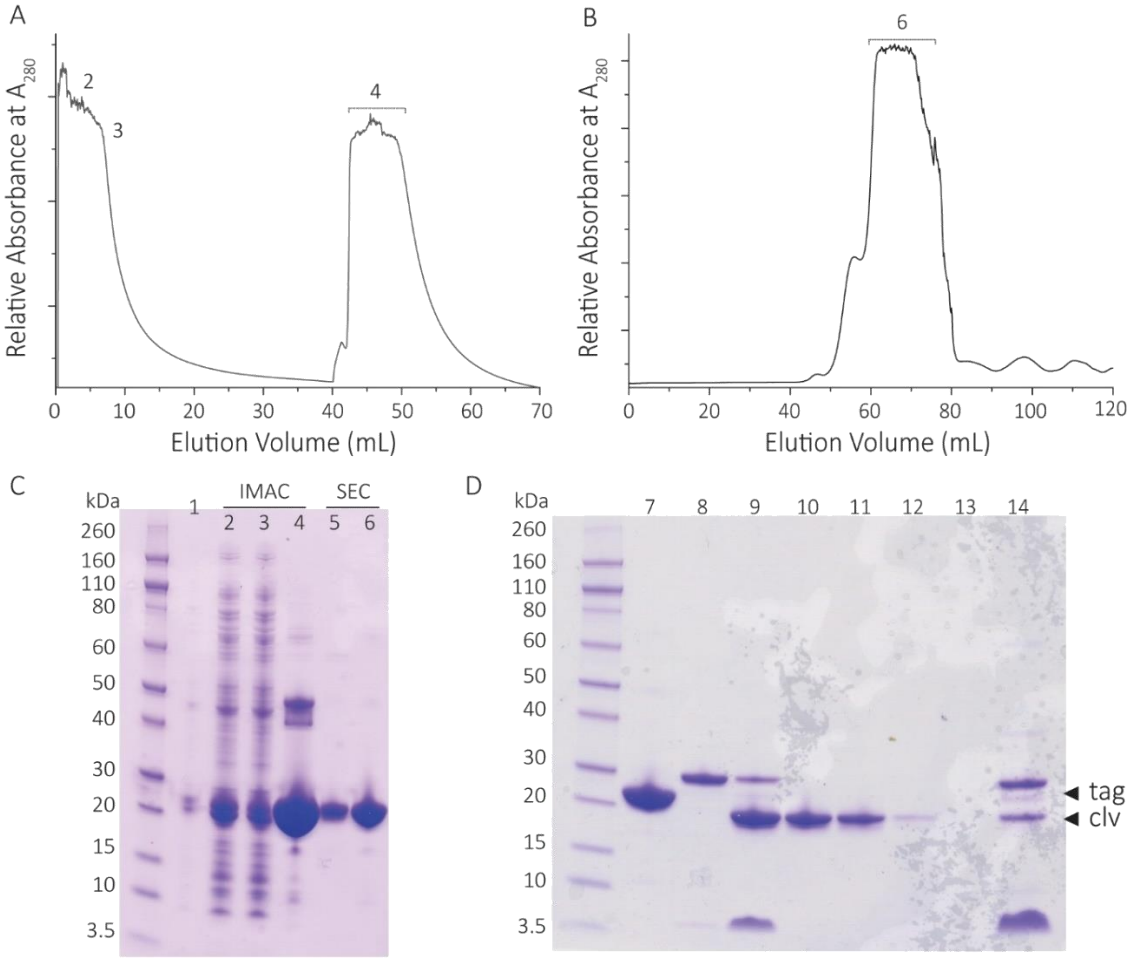

Figure 2.3: Purification of wild-type HsPrx3 and cleavage of His_6-tag
Absorbance at 280 nm, indicating presence of protein, was plotted against the elution volume from purification steps using IMAC (**A**) and SEC (**B**). A SDS-PAGE gel (**C**) of the protein purification: 1 – total protein lysate diluted 1 in 100; 2 to 4 – correspond to IMAC trace; 5 – sample loaded onto SEC; 6 – corresponds to pooled main elution peak from the SEC. A SDS-PAGE gel of the TEV cleavage His_6-tagged HsPrx3 and the subsequent purification of cleaved protein (**D**), where 7 - His_6-tagged wild-type HsPrx3; 8 – rTEV protease; 9 – mix of HsPrx3 and rTEV protease; 10 and 11 – flow through and wash containing cleaved HsPrx3, 12 and 13 – additional wash steps; 14 – proteins remaining attached to cobalt beads (**Section 7.5.3.2**).

2.3 Crystal structure of cleaved wild-type HsPrx3

2.3.1 Crystallisation of wild-type HsPrx3

Crystallisation trials were performed with cleaved HsPrx3 under reducing conditions that favour the formation of rings. As described in Section 7.8, protein concentrations of 20, 30, 35 mg/mL were used in an array of initial screening conditions. Needle-like protein crystals were observed within 3 weeks of initial tray setting for many conditions in the MORPHEUS screen using 35 mg/mL of HsPrx3 protein. Condition D12 of the MORPHEUS screen, which is comprised of 12.5% PEG1000, 12.5% PEG3350, 12.5% MPD, 0.02 M alcohol additives at pH 8.5 (Gorrec, 2009), yielded needles as well as rod-shaped crystals. The rod-shaped crystals were harvested directly from the MORPHEUS screen and cryo-protected using 20% glycerol, before being flash frozen at 110 K in liquid nitrogen. X-ray diffraction data were collected from native crystals at the Australian Synchrotron on beamline MX2 at a wavelength of 0.979 Å.

2.3.2 Data processing and refinement of wild-type HsPrx3 crystal structure

Crystals diffracted to a maximum resolution of 2.8 Å (full data collection statistics in Table 2.2). The structure of HsPrx3 was determined by molecular replacement using Phaser (McCoy *et al*, 2007) with the structure of bovine Prx3 (PDB: 1ZYE; Cao *et al*, 2005) as a search model. The Matthews coefficient of 2.25-3.01 Da/Å^3 (cell content analysis) corresponds to between 9-12 molecules in the asymmetric unit. Phaser located nine monomers with a final translational function Z score of 14.2. The structure was built and refined with iterative cycles of model building in COOT (Emsley and Cowtan, 2004) and refinement in Refmac5 (Murshudov *et al*, 1997).

Table 2.2: Data collection and refinement statistics wild-type HsPrx3, PDB: 5JCG.
There are nine monomers within the I222 asymmetric unit.

Data collection		Refinement	
Space group	I222	Resolution (Å)	2.80
Cell dimensions		No. unique reflections	61455
a, *b*, *c* (Å)	133.2, 168.7, 221.6	R_{work}/ R_{free}	0.183/0.229
α, β, γ(°)	90.0 , 90.0 , 90.0	No. atoms	
Resolution (Å)	52.3 - 2.8 (2.87 - 2.8)	Protein	13658
R_{pim}	0.176 (0.713)	Water	159
$I/\sigma I$	6.6 (1.9)	B-factors (Å^2)	
$CC_{1/2}$	0.954 (0.414)	Protein	23.2
Completeness (%)	99.8 (99.7)	Water	15.1
Redundancy	12.7 (12.3)	R.m.s deviations	
		Bond lengths (Å)	0.009
		Bond angles (°)	1.378

The crystallographic asymmetric unit is comprised of nine copies of the HsPrx3 monomer, which, together with three other symmetry-related copies in the crystal lattice, complete a dodecameric ring. Interestingly, when all the symmetry equivalent molecules in the crystal lattice were generated, it reveals an organisation comprised of three, stacked dodecameric rings. These short stacked rings align in the crystal to form long channels, with limited contacts between each segment (**Figure 2.4**).

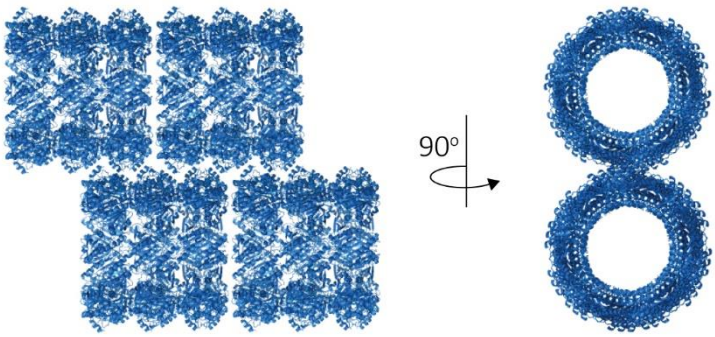

Figure 2.4 Crystal packing of wild-type HsPrx3
Here symmetry equivalent molecules in the crystal lattice were generated to reveal four short stacks of HsPrx3 rings packed together. These short stacks are composed of three dodecameric rings that align to form channels.

2.3.3 HsPrx3 crystal structure: comparison of the low molecular weight forms

The HsPrx3 monomer displays, as for other Prx3s, the conserved thioredoxin-like fold with a central 7-stranded β-sheet and 7 α-helices (**Figure 2.5**; Copley *et al*, 2004). Comparison of the HsPrx3 monomer with the BtPrx3 monomer (PDB: 4MH2, Cao *et al*, 2015) yields an RMSD of 0.365 Å across equivalent Cα-atoms. However, unlike in BtPrx3 (Cao *et al*, 2005; Cao *et al*, 2015), the C-terminus of HsPrx3 comprised of a 14 amino acid residue loop between G165 and I179 followed by the C-terminal helix α7 is fully ordered (**Figure 2.5 B**). The active site of HsPrx3 in the crystal, generated under reducing conditions, is fully folded with helix α2 starting at residue V46. The active site pocket is located in an area of strong positive charge consistent with a binding site for H_2O_2, while the surface surrounding the active site is hydrophobic in nature. The sulfhydryl of the peroxidatic cysteine (Cys_P) within the active site is linked by hydrogen bonds to the side chains of the conserved R123 and T44 (**Figure 2.5 A**). The amino acids that differ between HsPrx3 and BtPrx3 sequences populate the solvent exposed surface of the two proteins, with a large proportion of the amino acid changes (5 amino acids out of 13 differences) being located on the C-terminal region after residue 163, the last resolvable residue in the bovine structure. Comparison with HsPrx2, which displays a similarly ordered C-terminal tail, yields a RMSD of 0.593 Å across 179 equivalent Cα positions. The structural similarity of the HsPrx3 monomer with those for other Prxs is evident and also translates into the higher order associations of this protein, yielding similar interaction at the protein-protein interface as previously described for other 2-Cys Prxs (**Figure 2.5 C and D**; Barranco-Medina *et al*, 2009).

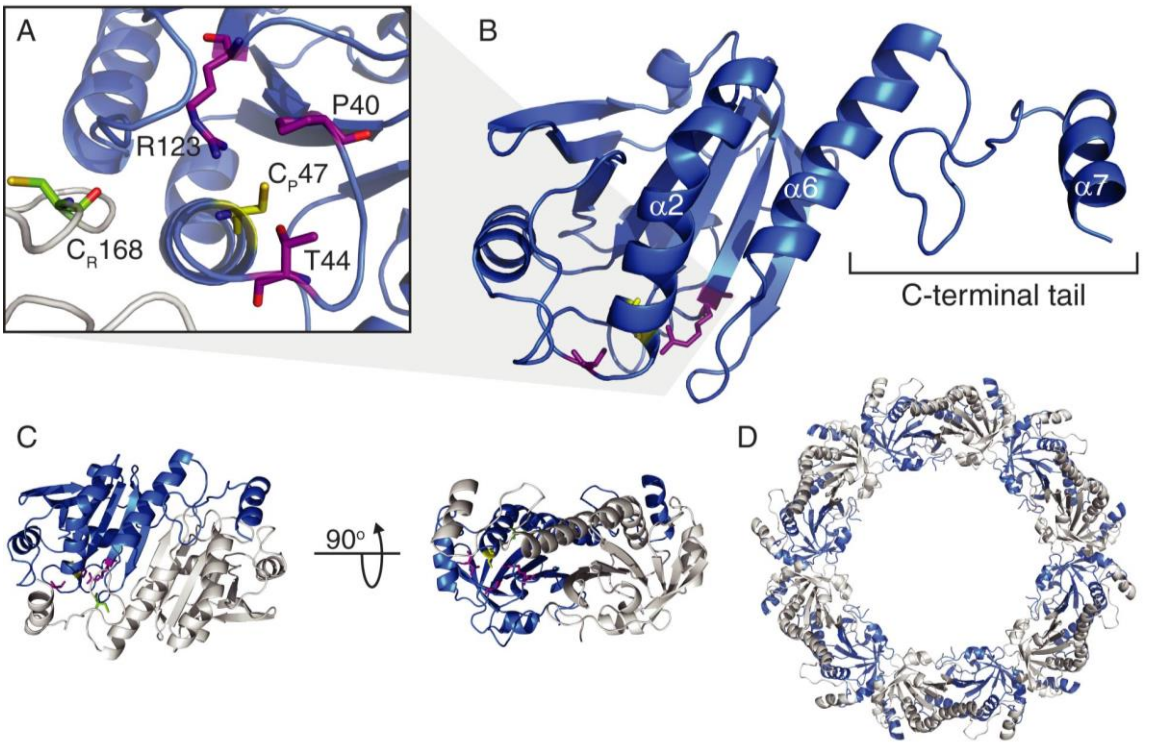

Figure 2.5: HsPrx3 crystal structure with resolved C-terminus and fully folded active site
The active site (**A**) showing the peroxidatic cysteine (C_P47 in yellow) in a fully folded conformation surrounded by the conserved active site residues (T44, P40, R123 in purple). The folded C-terminus also reveals the resolving cysteine (C_R168 in green), from the adjacent monomer (grey). The HsPrx3 monomer (**B**) indicating the locations of helices α2 and α6 involved in protein stacking, and the α7 helix, which is part of the C-terminal tail. HsPrx3 homodimers (monomers coloured blue and grey) in two orthogonal views (**C**). Six copies of the HsPrx3 homodimer showed in (**C**) organise as a dodecameric ring (**D**), under reducing conditions.

2.3.4 Interactions at the R interface of HMW Prx structures

Prx stacks have been observed for HsPrx2, HsPrx3, and bovine and rat Prx3s using TEM (Kato, 1985; Harris *et al*, 2001; Gourlay *et al*, 2003). As mentioned in **Section 2.1.2**, the only crystal structure of a Prx in a HMW stack conformation is that of SmPrx1, which forms decameric rings arranged as a stack of two rings (Saccoccia *et al*, 2012; **Figure 2.1**). This is reminiscent of the arrangement of HsPrx3 stacks, but with differences in the interactions that mediate stacking at the R interface. Specifically, the SmPrx1 stacks report interactions between the β2 strands of adjacent monomers; this interaction is not observed in the HsPrx3 stacks (**Figure 2.6 A**). This additional region of interaction at the SmPrx1 R interface is attributed to its quaternary structure being a decamer. Notwithstanding the different decameric and dodecameric organisations, in both cases, salient components of the R interface include the complementary fit of helices α2 and α6 contributed by the two apposing monomers, as well as additional contacts between the linker region connecting β6 and β7 (**Figure 2.6 B** compared with **Figure 2.1 B**).

In contrast, the R interface interactions of HsPrx3 occur only between the α2 and α6 helix pair of two apposing monomers, and is held together by a network of hydrogen bonds (**Figure 2.6**). The α2-α6 helix pair are arranged side-by-side on the face of one monomer and are staggered with an overhang of approximately two turns of helix α6. Their respective C-termini, aligned with each other, give the impression of one long, continuous helix (**Figure 2.6 A**). The helices are also slightly offset so that the side chain amino group of N65 in helix α2, located between these two helices, participates in a hydrogen bond with the backbone carboxylate of E162 from the α6' helix on the apposing monomer (**Figure 2.6 B**). This caps and presumably neutralises the dipole of helix α6'. Also, the same side chain amino group of N56 is held in place by a hydrogen bond with the backbone carboxylate of G31 from the same monomer. To avoid steric clashes, the backbone carboxylate groups of helices α2 and α6 are splayed out at the ends of the helix. In addition, the side chain of Q159 forms a hydrogen bond with the backbone carboxylate of V64 from the same monomer.

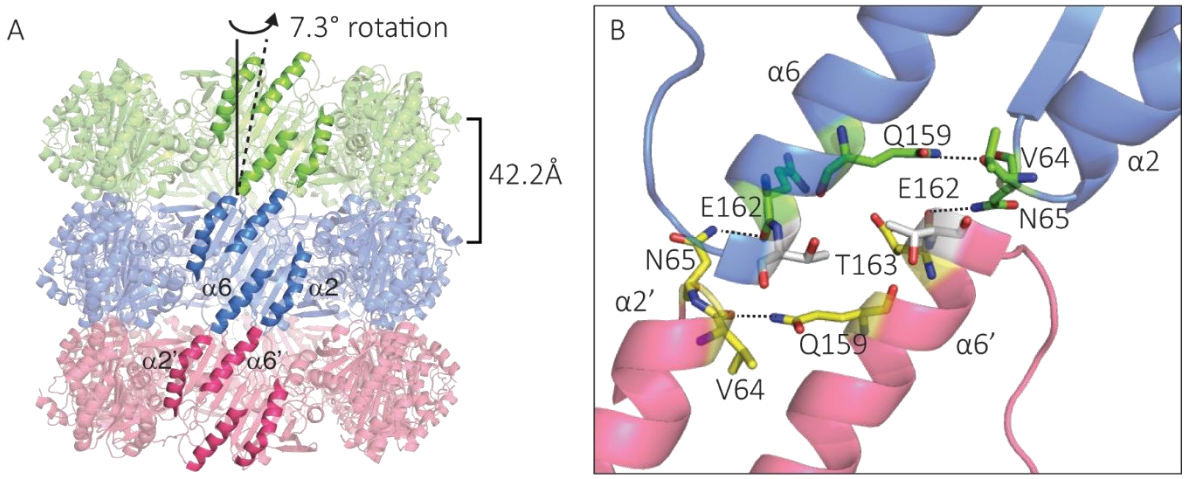

Figure 2.6: Crystal structure at 2.8 Å of HsPrx3 HMW structures at pH 8.0 (PDB: 5JCG)
The HsPrx3 crystal structure at pH 8.0 has an azimuthal rotation of 7.3 ° and the vertical separation of 42.2 Å between successive rings. Helices α2 and α6 are highlighted as main components of the stacking interaction. The R interface in HsPrx3 crystal structure (**B**) is formed from two adjacent monomers (blue and pink) with important residues highlighted (green, yellow and grey). Hydrogen bonds (black dotted lines) link residues V64 and Q159 on the same monomer as well as residues N65 and E162 on apposing monomers. T163 residues (grey) from apposing monomers are angled towards one another creating a hydrophobic pocket that encourages stacking of the rings.

Interestingly, the region between the staggered α2 and α6 helices of two apposing HsPrx3 monomers also house a hydrophobic pocket that is formed by the T163 residue at the R interface (**Figure 2.6 B**). In three of the monomers, where chains C, F and I in the crystal lattice do not participate in the interstack interaction, T163 adopts an alternate rotamer with the side chain rotated ~180° so that the hydroxyl group is exposed to the solvent. The T163 residue is not

conserved in SmPrx1, however the methyl groups of the K164 and E163 residues are sandwiched between the helices to form a similar hydrophobic interaction (**Figure 2.1 B**).

Comparison of the R interface residues for all of the Prxs that were reported to form HMW stacks, reveals H164 as the only conserved residue (**Figure 2.7**). The R interface for HsPrx2 is composed of amino acid residues that are distinct from the R interfaces of SmPrx1 and the Prx3s, indicating possibly a different set of interactions in this case of decamer stacks as observed by TEM (Harris *et al*, 2001).

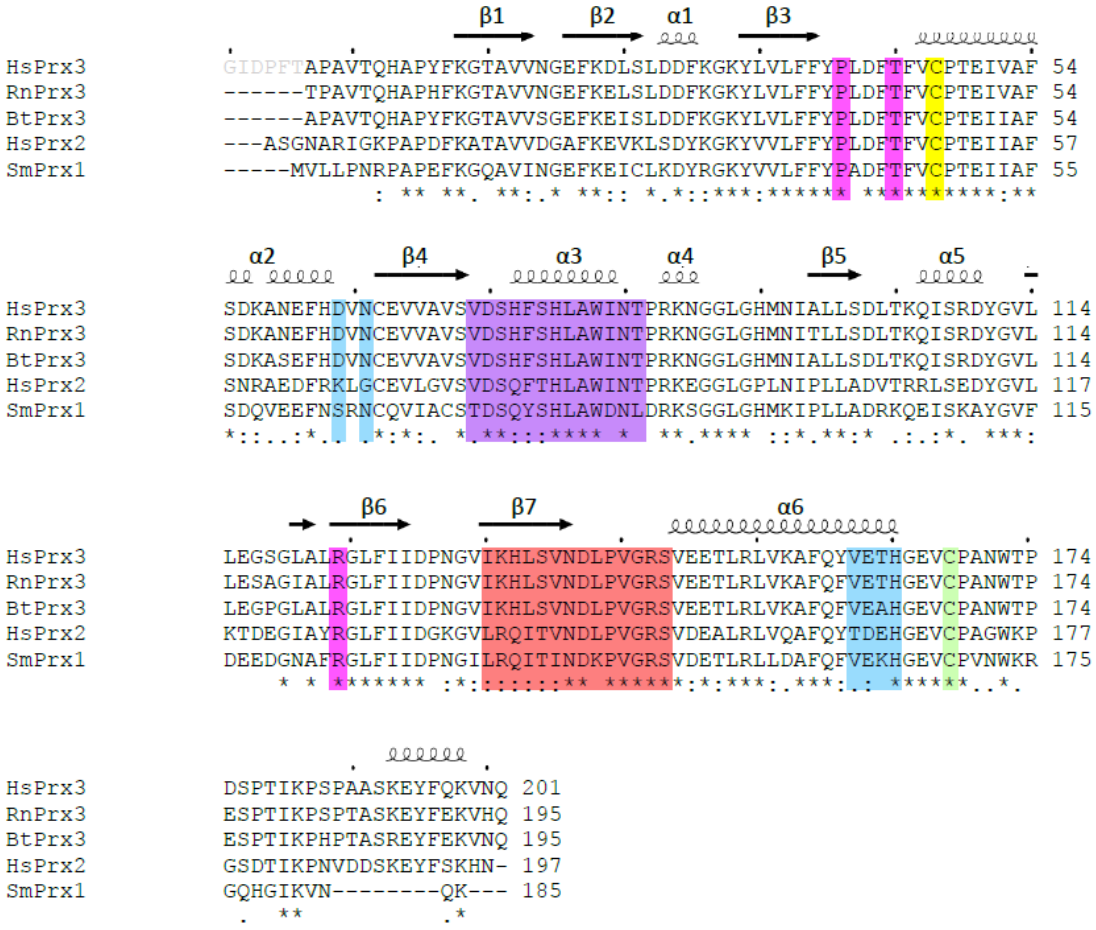

Figure 2.7: Sequence alignment of Prxs that have been observed to stack.
Amino acid sequence alignments for human Prx2 [P32119] and Prx3 [P30048], *Rattus norvegicus* Prx3 [G3V7I0], and *Bos Taurus* Prx3 [P35705], and *Schistosoma masoni* Prx1 [O97161]. The UniProt accession numbers are indicated in square brackets. The individual coloured residues correspond to those shown in **Figure 2.5**, with peroxidatic cysteine (yellow), conserved active site residues (purple), and the resolving cysteine (green). The main A and B interface residues are highlighted in purple and red, respectively. Further B interface interactions (not shown) can occur if the C-terminal α7 is fully folded, making contacts with the apposing monomer. The R interface residues between the α2 and α6 helices are highlighted in the blue. CLUSTAL v2.1 was used for this multiple sequence alignment (Larkin *et al*, 2007).

2.3.5 Comparison of HsPrx3 R interface interactions at pH 4.0 and 8.0

As part of our published study, we collaborated with Alok Mitra's group in order to create a 4.1 Å resolution cryo-EM reconstruction of the HsPrx3 filaments at pH 4.0. This structure enables the comparison between HsPrx3 and SmPrx1 (**Figure 2.8**). Whereas the HsPrx3 crystal structure reveals R interface interactions that allow stacking at high pH (pH 8.5), the 4.1 Å cryo-EM density map for the filaments, reveals details of this interface under acidic conditions (pH 4.0). Examining the cryo-EM map, it is clear that, even at high threshold (2.45 σ), densities could be populated by many of the bulky side chains in the pseudo-atomic model (**Figure 2.8 B**). At this threshold, clear density, which appears to link the α2 helix of one toroidal ring with the α6 helix of the adjacent toroid is visible, which is in line with the positioning of N65 seen in the crystal structure. Overall, at the level of 4.1 Å resolution of the cryo-EM map, no distinct difference of R interface interactions could be discerned when compared to those present in the crystal structure (compare **Figure 2.6 and 2.8**). This suggests that there are no drastic alterations at the R interface and that the stacking interactions of HsPrx3 are similar for both pH states.

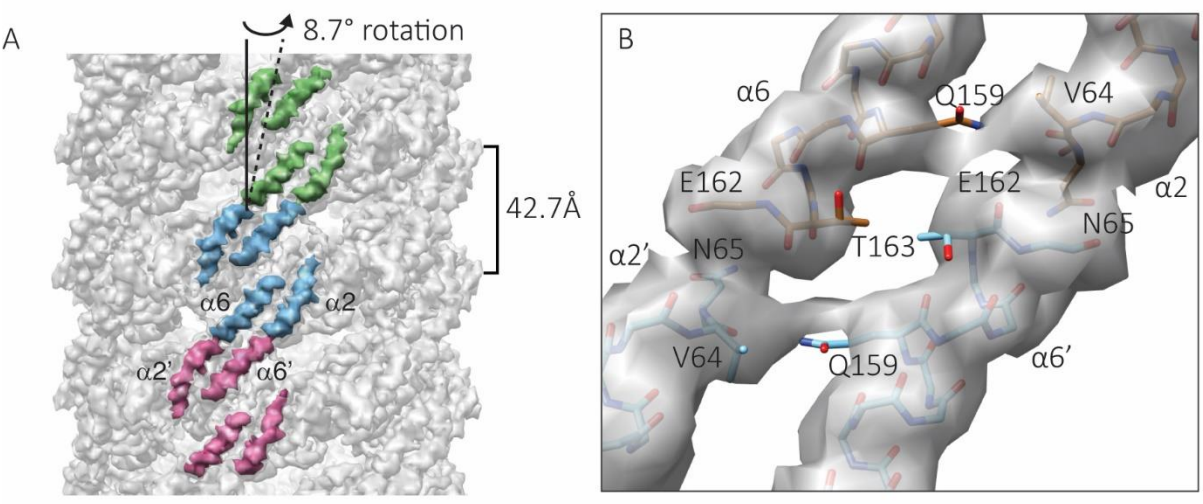

Figure 2.8: Cryo-EM model at 4.0 Å of HsPrx3 HMW structures at pH 4.0 (EMD: 3414)
The HsPrx3 cryo-EM model at pH 4.0 showing stacked ring filaments with the azimuthal rotation of 8.7 ° and the vertical separation of 42.7 Å between successive rings (**A**). Helices α2 and α6 are highlighted as main components of the stacking interaction. A PHENIX-refined (Afonine *et al*, 2012) pseudo-atomic model, shown as sticks, was made by David Goldstone and fitted to the cryo-EM map (2.0 σ) of HsPrx3 helical filaments at pH 4.0 (**B**). This suggests a similar hydrogen bonding pattern between the HsPrx3 cryo-EM model and crystal structure. Images were adapted from those supplied by Hari Venugopal.

It is important to note that at pH 8.0, cleaved wild-type HsPrx3 proteins predominantly form dodecameric rings; however, lowering of solution pH to 4.0 causes HsPrx3 proteins to assemble into long helical stacks (Phillips *et al*, 2014; Radjainia *et al*, 2015). The reason for this dramatic

change in assembly has been proposed to occur due to altered charged states of the amino acid residues at the R interface, in particular the conserved H164 residue has been hypothesised to play an important role in facilitating stacking at lower pH (Radjainia *et al*, 2015; Saccoccia *et al*, 2012).

2.3.6 Accessible conformations of the active site for HMW assembly

The Prx active site undergoes concerted conformational transitions during its catalytic cycle. This shift from a fully folded (FF, **Figure 2.9**) to a locally unfolded (LU, **Figure 2.9**) active site enables disulfide bond formation between Cys_P and Cys_R. Previous studies have drawn correlations between the redox state of the active site and the conformation of the C-terminal region, and their impact on the ability of Prxs to form HMW structures or stacks (Radjainia *et al*, 2015; Saccoccia *et al*, 2012).

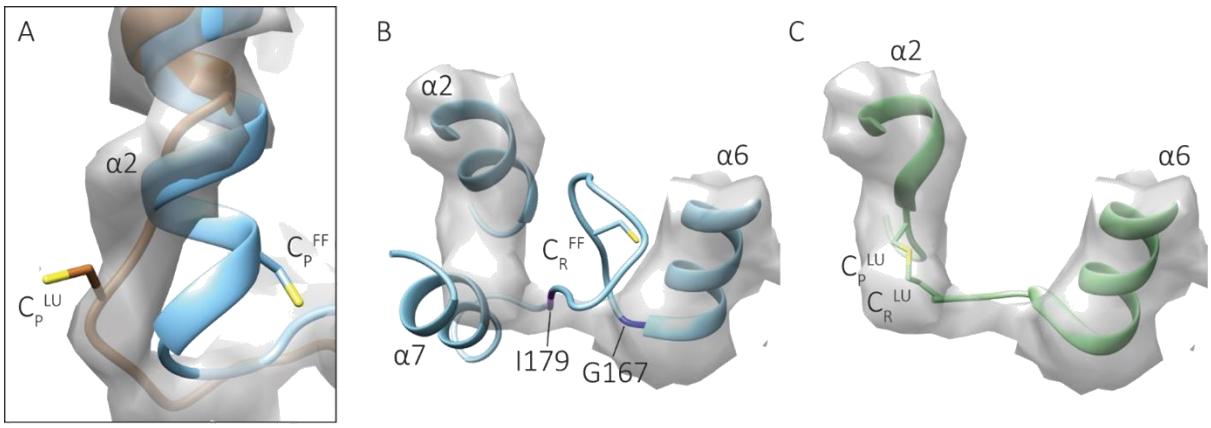

Figure 2.9: Close up details of the cysteines, C_P and C_R, and the C-terminus
The active site (**A**) of the HsPrx3 crystal structure (blue) is seen in the fully folded (FF) conformation whereas the same region with the fitted pseudo-atomic model of cryo-EM structure (brown) shows it to be locally unfolded (LU). The density map was rendered at 2.45 σ. The C-terminus of a monomer in the unsharpened cryo-EM density (**B**) is seen as partially disordered. The folded C-terminus seen in the HsPrx3 crystal structure (blue) does not fit into this density map, rendered at 1.8 σ. However, the fit of F190L BtPrx3 (PDB: 4MH3; green, **C**) dimer suggests the possibility of a disulfide bond between the C-terminal resolving cysteine (C_R) and the peroxidatic cysteine (C_P), in the cryo-EM density for the filament, rendered at 1.8 σ. Images were adapted from those supplied by Hari Venugopal.

To critically assess the conformation of active site between the HsPrx3 crystal structure and the cryo-EM reconstruction at lower pH, the model of the dimer from the X-ray structure was morphed into the cryo-EM map by rebuilding the residues surrounding the active site using real-space refinement in PHENIX (done by David Goldstone; Afonine *et al*, 2012). Inspection of the active site in the current 4.1 Å model derived from the cryo-EM map of the HsPrx3 HMW form, confirms earlier results that this region is locally unfolded (**Figure 2.9 A**), as also observed in the double stack

present in the SmPrx1 crystal structure (Radjainia *et al*, 2015; Saccoccia *et al*, 2012). The active site in the HMW form in the HsPrx3 crystal structure, produced at pH 8.5, clearly shows a fully folded conformation for this region (**Figure 2.9 A**). Comparison of the fully folded and locally unfolded active sites show a 7.2 Å shift in the Cα position of the Cys_P accompanied by the unwinding of the final turn of helix α2. This observation is at odds with the generally held notion that local unfolding of the active site accompanies HMW formation (Saccoccia *et al*, 2012).

The active site conformation has ramifications for the arrangement of the C-terminal region. In other Prx structures, a locally unfolded active site is always accompanied by an unfolding of the C-terminus, whereas C-terminal unfolding only acts to destabilise the fully folded state of an active site (Perkins *et al*, 2013). The HsPrx3 crystal structure clearly has a fully folded active site and a structured C-terminus. In the cryo-EM structure, the density at the C-terminus can only be partially attributed to the folded state. Thus, most of the density corresponding to the loop (residues G165 to I179) seen in the pH 8.5 crystal structure is not visible (**Figure 2.9 B**). Density is observed corresponding to the loop extending from the end of helix α6 towards Cys_P, placing Cys_R in a position to form a disulfide bond analogous to that seen in the structure of F190L BtPrx3 in the oxidised state (PDB: 4MH3) (**Figure 2.9 C**). Beyond this volume of density, which is not as pronounced as those for the surrounding structural elements, there is additional weak density towards the C-terminal end, as also observed in a recent 4.4 Å cryo-EM structure of HsPrx3 obtained by phase-plate imaging (Khoshouei *et al*, 2016). This density volume possibly indicates averaging of several alternative conformations. The cryo-EM samples were prepared at pH 4.0, without the addition of reducing agent, which could result in the active site being primarily locally unfolded. It is therefore likely that the C-terminal region in the cryo-EM density map elaborates an averaged picture of multiple conformational states including the disulfide bonded state.

2.4 Discussion

2.4.1 A locally unfolded active site is not a requirement for Prx stacking

The 2.8 Å crystal structure of reduced HsPrx3 are arranged in a novel stack of three dodecameric rings, with fully folded active sites. This structure challenges the pre-existing hypothesis that a loosely unfolded active site is a necessary structural change for the association of Prx rings into HMW tubes. In fact, in the case of HsPrx3, very little structural changes occur to facilitate stacking of the rings, with associations in the form of hydrogen bonds between the α2 and α6 helices of

apposing monomers in the R interface. The geometry of HsPrx3 being dodecameric rings lends itself towards this kind of association. However, it the case of the decameric SmPrx1, additional structural changes may have to occur to encourage protein ring association at both the α2-α6 region as well as between the β2 strands. The unfolding of active site and C-termini were hypothesised to expose hydrophobic patches at the R interface that enables SmPrx1 to associate together with holdase activity (Angelucci *et al*, 2013).

The following attempts to analyse the pre-existing hypothesis and explore how the active site state of Prxs can influence their stacking into tubes. In particular, the two distinct, but related factors that influence the active site conformation will be highlighted: the pH of the surrounding solution and the oxidation state of Cys_P.

Previous reports of protonated states of Cys_P in crystallography and EM (Radjainia *et al*, 2015; Saccoccia *et al*, 2012), have established a strong correlation between protonated Cys_P thiols and a locally unfolded active site. When the solution pH is below the pKa of Cys_P (pH < pKa ~ 5), Cys_P is protonated and the hydrogen bonding network within the active site is disrupted, facilitating a locally unfolded active site (Hall *et al*, 2011; Saccoccia *et al*, 2012). At pH 8.5, the majority of Cys_P residues are deprotonated, allowing the reactive cysteine to be held in place by surrounding active site residues (R123 and T44) and the active site is fully folded.

To highlight the complex interplay between pH and redox state of Cys_P, 12 available crystal structures of 2-Cys Prxs, with folded C-termini and fully folded active sites, were examined (**Table 2.3**). The pH at which these structures were studied range from 7.5 – 8.5, with the exception of two structures featuring Cys_P to serine (C_PS) mutations where the protein was crystallised at pH 5 and pH 4.2 (Matsumura *et al*, 2008; Tairum Jr *et al*, 2012). Traditionally, the C_PS mutations were chosen as a mimic for protonated Cys_P (Angelucci *et al*, 2013, König *et al*, 2013). However, it has been observed that C_PS mutations stabilise the active site in a fully folded state, even more than reduced thiols do (Perkins *et al*, 2013), making C_PS a bad mimic of low pH situations. This stabilisation could encourage the formation of fully folded active sites even at low pH, as seen in the crystal structures (**Table 2.3**), allowing the C-terminus to also fold. Instead, C_PS mutations stabilising a folded active site resembles the situation of Cys_P becoming increasingly oxidised (Wang *et al*, 2012). An alternative hypothesis suggests that mutation of Cys_P to amino acid residues, such as aspartate, serve to mimic the charged hyperoxidised state of Cys_P known to be associated with the HMW form (König *et al*, 2013).

Table 2.3: Prx structures with fully folded active sites and folded C-termini deposited on the PDB

PDBid	Organism	Prx Name	Mutation	pH	References
1qmv	*Homo sapiens*	HsPrx2		7.5	Schroder *et al*, 2000
2i81	*Plasmodium vivax*	2-Cys Prx		8.4	Artz (unpublished)
2pn8	*Homo sapiens*	HsPrx4		7.5	Pilka (unpublished)
2z9s	*Rattus norvegicus*	Prx1	C52S	5	Matsumura *et al*, 2008
3qpm	*Pseudosciaena crocea*	2-Cys Prx		8	Mu *et al*, 2013
3sbc	*Saccharomyces cerevisiae*	Tsa1	C47S	4.2	Tairum Jr *et al*, 2012
3tjf	*Homo sapiens*	HsPrx4	C51A	8.5	Cao *et al*, 2011
3tkp	*Homo sapiens*	HsPrx4		8.2	Wang *et al*, 2012
3tkq	*Homo sapiens*	HsPrx4		8.2	Wang *et al*, 2012
3tkr	*Homo sapiens*	HsPrx4	T118E	8.2	Wang *et al*, 2012
3tks	*Homo sapiens*	HsPrx4		8.2	Wang *et al*, 2012
4llr	*Trypanosoma cruzi*	TXPNx		7.5	Piñeyro *et al*, 2005
3zl5	*Schistosoma masoni*	SmPrx1	C48S	7.0	Angelucci *et al*, 2013

Crystallised Prxs with hyperoxidised Cys_P almost always harbour a fully folded active site (Hall *et al*, 2011), with the exception being crystals of Prxs bound to sulfiredoxin, the recycling enzyme (Jonsson *et al*, 2009). Wang *et al*, 2012 observed that hyperoxidised Cys_P stabilises the fully folded active site, more so when compared to other oxidation states of Cys_P. For instance, as reflected by the crystallographic B-factors, the increased oxidation of the Cys_P in the HsPrx4 structure translates to increased conformational rigidity of both the α2 and the C-terminal YF helix (α7) as well as to increased rigidity for the C-terminal end of α6. Hyperoxidised Cys_P stabilises the fully folded active site reducing the flexibility of both α2 and α6 helices; this would increase the chances of favourable hydrogen bonds at the R interface that promote stacking for hyperoxidised Prx proteins. Hence, C_PS mutants in Prxs, that mimic hyperoxidised Prxs, tend to also form stacked rings at physiological pH or be stabilised by them, whereas reduced HsPrx3 proteins remain as single toroidal rings in solution (Gourlay *et al*, 2003; Angelucci *et al*, 2013).

2.4.2 How protein environment can affect interactions at the R interface

The mechanism of Prx stacked ring formation under acidic conditions and oxidative conditions are distinct but related. Stacking of HsPrx3 rings require the formation of favourable hydrogen bonds between the α2 and α6 helices, but factors which encourage such interactions vary. At physiological pH, hyperoxidised Cys_P or the C_PS mutation is required for stabilisation of a fully folded

active site that enables Prxs to stack in solution. Whereas, appropriate hydrogen bonding may also be fostered at pH 8.5 under reducing conditions by increasing the local concentration of protein, such as that during crystal formation, resulting in the structure of the stacked HsPrx3 rings (PDB 5JCG). HsPrx3 toroids organised as long stacked filaments of rings at pH 4.0, become disassociated when pH was raised to 8 (Section 2.4.5). In addition to other stabilising interactions that are largely unaltered at the R interface for both high and low pH, low pH leads to favour electrostatic interactions that further stabilise the stack, and could explain the increased propensity of HsPrx3 toroids to form long ordered filaments at pH 4.0 rather than at pH 8.5. In this context, conserved H164 at the R interface is of particular interest since, due to its pKa being 6, it will be neutral at pH 8.5 but protonated and positively charge at pH 4.0, making it an important player in the aforementioned switch in the nature of the R interface surface-charge.

2.4.3 HMW form as a self-chaperoning assembly of HsPrx3 in a catalytically active conformation

These HMW Prx stacks can form under a variety of conditions and are distinct from those observed in Jang *et al*, 2004 and Moon *et al*, 2005, which appear to form spherical aggregates. Despite some differences in structure that may be attributed to both the redox state and pH, in terms of the spontaneous assembly into HMW forms, the close structural similarity of the HsPrx3 crystal and cryo-EM structures suggests that the observed crystal packing may faithfully represent a putative chaperone. The pH of the mitochondrial matrix is alkaline due to proton transport into the intermembrane space during respiration (Santo-Domingo and Demaurex, 2012). Furthermore, a high proton motive force promotes superoxide generation by respiratory complexes (Murphy, 2009). Therefore, the stacking of Prx rings observed at pH 8.5 could be of physiological significance. The fully folded active site means this protein would retain its peroxidase activity, even after assembly to HMW forms. In fact, this observation of HsPrx3 with elements of fully folded and loosely unfolded active sites, supports that the full reaction cycle is accessible to the HMW species.

Functional implications of these observations are intriguing and the question arises as to why such a dramatic structural response occurs for these proteins under acidic conditions or oxidative stress. Prx proteins are highly abundant within cells and HsPrx3 is estimated to be present at a concentration of >100 µM within the human mitochondria (Cox *et al*, 2009a). All of the environmental and chemical conditions that favour Prx3 proteins stacks (Figure 2.10) have unfavourable influences on protein stability: acidic conditions in protein environments often cause proteins to aggregate (Mazzini *et al*, 2007; Fink *et al*, 1994); crystallisation conditions forces

proteins to precipitate out of solution to form crystals; and the C_PS mutations for Prx3 have been observed to be very unstable (Phillips, 2014; Gourlay *et al*, 2003) and hyperoxidised HsPrx3 proteins also tend to be insoluble (Poynton *et al*, 2016).

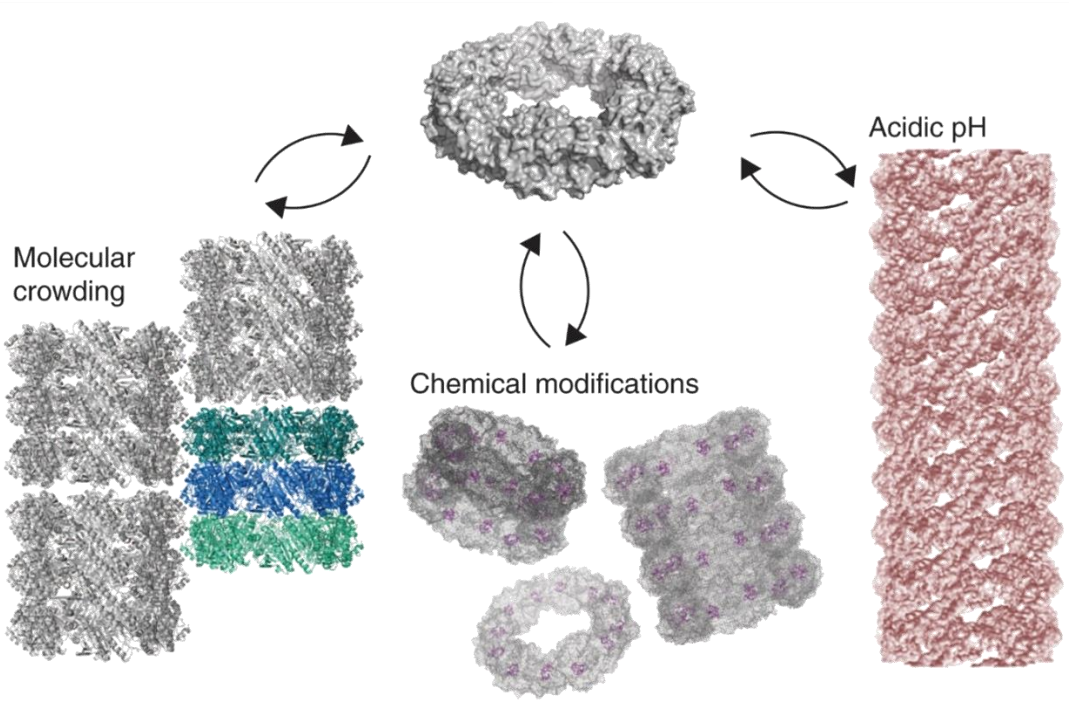

Figure 2.10: A postulated model depicting that cellular stress induces Prxs to function as self-assembling chaperones

Stacking interactions of Prx proteins can be facilitated by molecular crowding, chemical modifications of the active site (such as C_PS mutations or hyperoxidation), or by acidification. Prx rings can associate together to form HMW stacks as a means to prevent universal aggregation of protein under these unfavourable conditions.

This controlled clustering of HsPrx3 is hypothesised to be favoured in the crowded environment inside the mitochondria as a protective mechanism against catastrophic aggregation in which HsPrx3 is a self-associating chaperone. Prevention of aggregation while maintaining proper function of an essential protein may be critical to cell survival. This is an alternate hypothesis to the previous suggestion that stacked Prxs act as chaperones to aid in folding of other proteins. This hypothesis is consistent with recent observations in yeast cells where proteins tend to be reversibly sequestered during times of cellular stress in order to prevent aberrant aggregation (Wallace *et al*, 2015) as well as for storage (Petrovska *et al*, 2014). Intriguingly, in the case of Petrovska *et al*, 2014, the metabolic enzyme glutamine synthetase (Gln1), which forms a decameric ring, was observed to assemble into filaments *in vivo* at low pH triggered by cellular starvation, leading to enzymatic inactivation. This inactive enzyme becomes active again after disassembly. Latest advances in cryo-tomography, which allows for detailed structure determination *in situ*, such as for the crystalline

structures of aldehyde dehydrogenase Ald4p in yeast mitochondrial matrix (Fukuda *et al*, 2015, Misonou *et al*, 2014), may address the important issue of whether Prx3 is a constituent of similar arrays in mitochondria and the *in vivo* role of HMW Prxs.

2.5 Summary

The 2.8 Å crystal structure of HsPrx3 is the first crystal structure of a reduced peroxiredoxin (Prx) known to form HMW stacks at pH 8.5. Although the HsPrx3 monomer and ring assembly are similar to other typical 2-Cys Prxs, it is how these proteins further associate into stacks of three rings that makes this crystal structure especially interesting for understanding the molecular interactions involved in the formation of Prx HMW assemblies. In particular, the interactions at the ring interface (R interface) predominantly occur *via* hydrogen bonding, as well as a hydrophobic patch formed by T163 residues. Comparing both the cryo-EM structure at pH 4.0 and the crystal structure at pH 8.5 of HsPrx3 proteins reveals very similar R interface interactions, with no large conformational changes occurring to facilitate protein association. Notably, the H164 residue is conserved between Prxs that are known to form HMW stacks and this residue could influence the electrostatic interactions between protein rings at different pHs. However, the specific amino acid interactions at the R interface may not be universally conserved between different Prxs as seen in the sequence alignment, but provide an ideal standing point from which HsPrx3 protein associations can be critically assessed as a tecton.

The fully folded active site of HsPrx3 in the crystal structure demonstrates that this conformation is accessible to the HMW structures, and is at odds with the previously hypothesised requirement for the active site to be unfolded to enable ring stacking (Section 2.6.1). This active site conformation, along with other parallel observations of HsPrx3 tube formation under conditions of stress, instigated a new hypothesis that ring stacking was the result of a self-chaperoning biological function for these protein tubes.

Chapter 3: Self-assembly mechanism of human peroxiredoxin 3 protein tubes

3.1 Introduction

3.1.1 Proposed mechanisms for Prx tube formation

Although protein structures derived from EM and crystallography are valuable for exploring the crucial interactions required for HMW structure formation, they are simply static snap-shots whereby the mechanisms by which Prx tubes form are hinted at, but not directly observed. Assembly of protein architectures can occur *via* two different mechanisms (**Figure 3.1**): commutative (such as how actin filaments and microtubules assemble; Yamada *et al*, 2005) or non-commutative (such as how Sp1 proteins assemble where rings associate with one another) (Lehn, 2002).

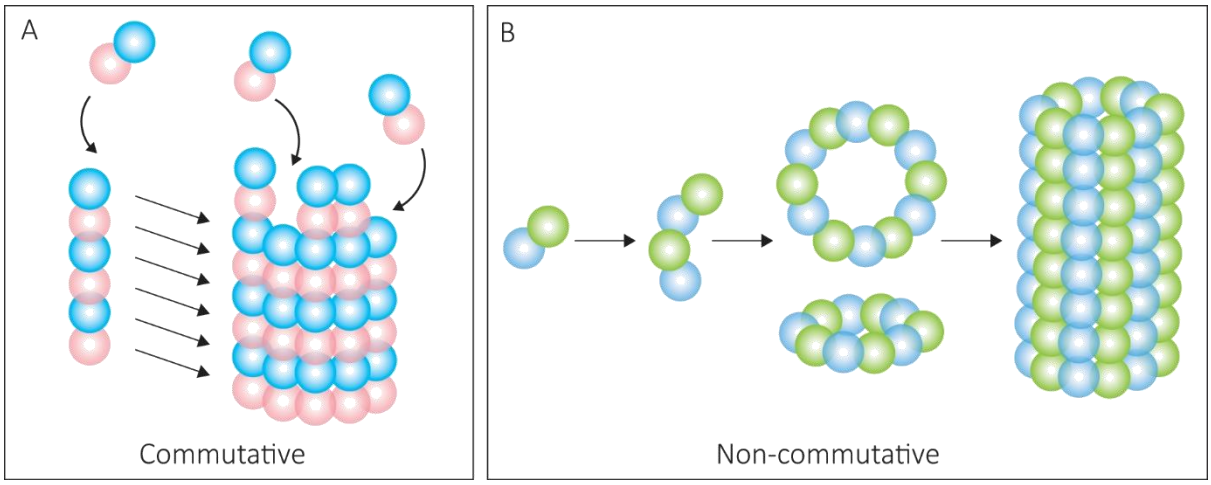

Figure 3.1: Commutative versus non-commutative assembly
Commutative assembly (**A**) occurs when steps can be interchanged along an overall pathway that leads to a final "open" structure. Microtubules are a good example of this, where tubulin dimers can self-assemble directly or *via* the formation of a protofilament into a final super structure (Alberts *et al*, 2002). Non-commutative assembly (**B**) involves the progressive formation of a final structure through building up from a defined set of intermediates. Protein rings, such as Hcp1 (Ballister *et al*, 2008) or TRAP (Miranda *et al*, 2009), form rings prior to assembly into protein tubes (as elaborated in **Section 1.3.3.5**).

HsPrx3 proteins have two basic tecton units that can assemble into the HMW tubes: homodimers consistent with a commutative mechanism, or dodecameric rings consistent with a non-

commutative mechanism. Protein self-assembly for Prxs has been postulated occur *via* a non-commutative mechanism (Angelucci *et al*, 2015), but not yet directly shown. The time scale at which these tubes form is also unknown.

3.1.2 Chapter overview

The mechanism of high-order oligomerisation was also probed using native mass spectrometry (nMS) in collaboration with the lab of Carol Robinson. nMS is a powerful technique that has been used extensively to observe protein oligomers in the gas phase, and enables the direct detection of species involved in protein assembly (Sakata *et al*, 2011; Pukala *et al*, 2009; Zhou and Robinson, 2010b). The nMS results reveal non-commutative assembly of HsPrx3 rings occurring at a sub-60 second time scale. Comparison between tagged and cleaved HsPrx3 also reveals a difference in assembly of HMW tubes, and gives insights into how HsPrx3 tube lengths could be controlled.

3.2 Mechanism of HsPrx3 assembly into HMW tubes

3.2.1 Probing the stacking mechanism using native mass spectrometry

The previously described HsPrx3 HMW structures provide insights into the molecular details that frames the rationale behind protein self-assembly. However, these static interpretations of HMW structure do not reveal the mechanisms by which HsPrx3 HMW structures form. As discussed in Section 3.1.4, HsPrx3 can assemble in a commutative manner, where dimers can associate interchangeably to form the final HMW tube structure, or in a non-commutative manner, where dimers must sequentially assemble into rings, followed by rings stacking to form HMW tubes. nMS is a highly sensitive tool that can be used to probe protein oligomeric states and can even be used to monitor their self-assembly in real-time (Sharon and Robinson, 2007; Painter *et al*, 2008; Bernstein *et al*, 2009; Benesch *et al*, 2010). This is the technique that will be used to explore the self-assembly mechanism of both cleaved HsPrx3 and His_6-tagged proteins. Prepared as described in Section 2.2, frozen stock aliquots of purified cleaved HsPrx3 and His_6-tagged HsPrx3 proteins were used for all of the experiments in this chapter.

3.2.2 Stability of HsPrx3 protein in ammonium acetate

The easiest and most reproducible means to promote stacking of HsPrx3 proteins in solution is to lower the solution pH from 8.0 to 4.0 (Phillips *et al*, 2014, Radjainia *et al*, 2015). nMS was used to probe the stacking mechanism of HsPrx3 for both cleaved and His_6-tagged forms, separately. However, this technique requires the use of volatile buffers, such as ammonium acetate, that will desolvate readily during the electrospray ionisation process. 100 mM ammonium acetate was an optimal concentration where HsPrx3, both cleaved and tagged, remained stable (**Figure 3.2 A**) and the native mass spectra gave the narrowest peaks due to optimal desolvation. HsPrx3 proteins also retain their ability to form dodecameric rings in 100 mM ammonium acetate, pH 8.0 (**Figure 3.2 B**) as observed by analytical ultracentrifugation (AUC) (**Section 7.7.4**).

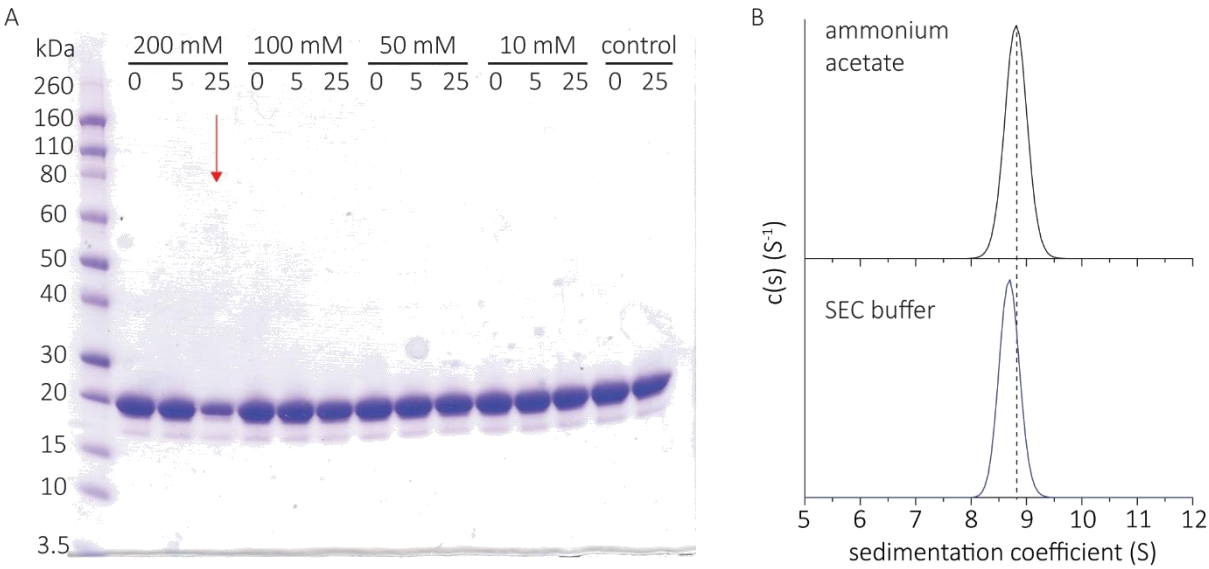

Figure 3.2: **HsPrx3 protein stability in ammonium acetate**.
A SDS-PAGE gel (**A**) of soluble cleaved HsPrx3 protein over time (taken at 0, 5, and 25 hours) in pH 8.0 ammonium acetate solution (200 mM, 100 mM 50 mM, 10 mM). The control condition was HsPrx3 kept in 20 mM HEPES pH 8.0, 150 mM NaCl. A decreased protein band intensity (red arrow) was observed for 200 mM ammonium acetate after 25 h, indicating that HsPrx3 formed precipitates in this buffer (**Section 7.5.3** for this method). The AUC experiments were (**B**) conducted, as per **Section 7.7.4**, using purified cleaved HsPrx3 (20 µM) in either ammonium acetate (black trace) or 20 mM HEPES, 150 mM NaCl, pH 8.0 (blue trace); HsPrx3 retains its dodecameric oligomeric state with sedimentation coefficients of 8.8 S and 8.7 S, respectively. The frictional ratio (f/f_0) was 1.63 for HsPrx3 in both buffer conditions. The same results were obtained for His_6-tagged HsPrx3 (data not shown).

3.2.3 HsPrx3, both cleaved and His_6-tagged, are dodecamers at pH 8.0 in the gas phase

In order to probe HsPrx3 oligomeric state by nMS, both cleaved and His_6-tagged proteins were separately buffer exchanged into fresh 100 mM ammonium acetate, pH 8.0, solution and analysed on a Synapt nESI-MS instrument (according to **Section 7.9.3**). The experimental molecular weights (MWs) for cleaved and His_6-tagged HsPrx3 were at 266560 ± 68 Da and 305045 ± 89 Da respectively, consistent with the predicted MWs of 266042 Da and 303872 Da (**Figure 3.3**; Marty *et al*, 2015). Notably, in both cases, the protein is homogenous in that the only observed species is the dodecamer, and no other stoichiometry was observed. The insufficient removal of adducts, such as salt, can cause the experimental MW to appear greater than the theoretical MW (Benesch, 2009). The dodecameric HsPrx3, both cleaved and tagged, can be stably sprayed for up to an hour without any noticeable changes to the spectra or to the corresponding MW.

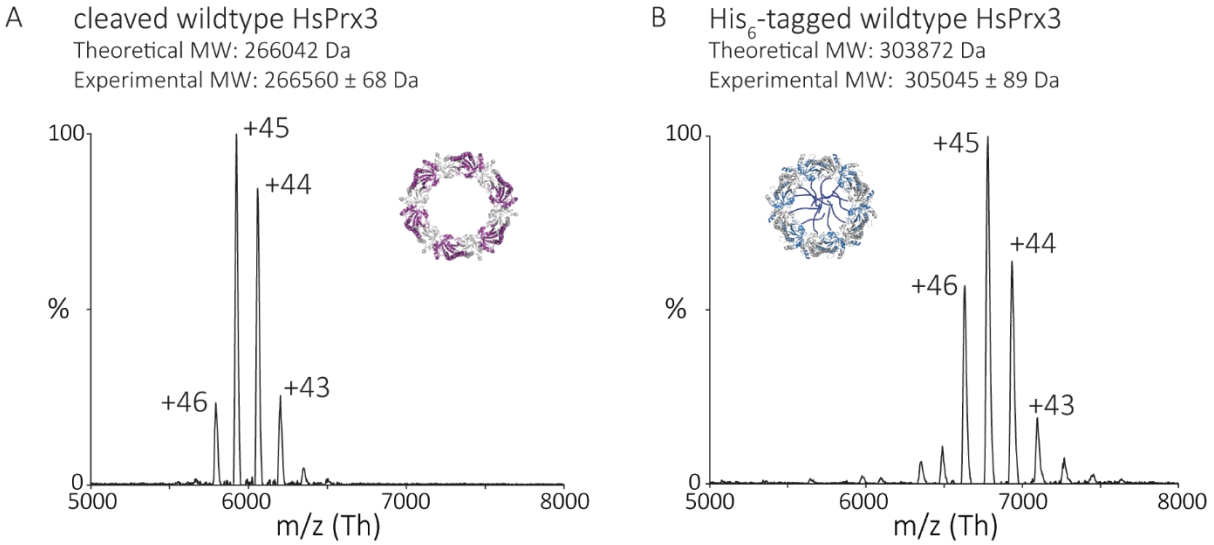

Figure 3.3: HsPrx3 remains a dodecameric ring in ammonium acetate and in the gas phase
These mass spectra were analysed with *UniDec* software (Marty *et al*, 2015). 20 µM of cleaved HsPrx3 (**A**) and 20 µM His_6-tagged HsPrx3 (**B**) in 100 mM ammonium acetate, pH 8.0, were ionised in positive ion mode (**Section 7.9.3**), and peaks were assigned charged states that range from +43 to +46. In both cases, the spectra corresponds to the proteins being in a dodecameric oligomeric state. The trap collision energy used for both spectra was 20 V.

These results were consistent with previous reports of the dodecameric structure of HsPrx3 in pH 8.0 solutions, and the existence of ring-like quaternary structure (Phillips, 2014). SEC coupled with static light scattering (SEC-SLS) was used to corroborate the MS data and confirm that the results are representative of the aqueous state, where both cleaved and His_6-tagged HsPrx3 remain as intact dodecameric rings, with comparable experimental MWs of 266 kDa and 300 kDa respectively (**Figure 3.4**).

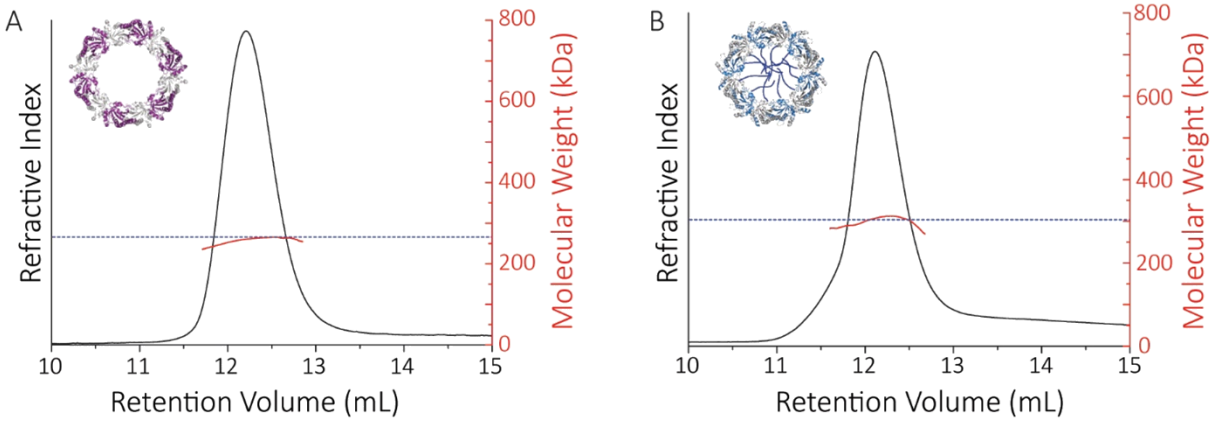

Figure 3.4: SEC-SLS solution MWs of HsPrx3 proteins in 100 mM ammonium acetate, pH 8.0
SEC-SLS of 20 µM cleaved HsPrx3 (**A**) and 20 µM His_6-tagged HsPrx3 (**B**), both in 100 mM ammonium acetate, pH 8.0. The refractive index (black line) and right-angle light scattering were used to calculate MWs (plot and right axis in red) of particles in solution. The main protein peak is a dodecamer (~266 kDa for cleaved HsPrx3 and ~300 kDa for tagged HsPrx3), which these agree with the theoretical MW for each species dotted blue line).

Collision induced dissociation inside the mass spectrometer disrupts the dodecameric protein structure *via* symmetric dissociation. Tandem mass spectrometry (MS/MS) was performed where the species at m/z 6080 was quadrupole isolated. For cleaved HsPrx3 MS/MS analysis, the collision energy was increased to 90 V and the resulting MW for the monomers and dimers were 22219 ± 11 Da and 44344 ± 32 Da respectively (**Figure 3.5 A**). The single peak at m/z 6770 was isolated for His_6-tagged HsPrx3 MS/MS analysis and the resulting MW for the monomers and dimers were 25391 ± 10 Da and 50731 ± 10 Da respectively (**Figure 3.5 B**). Thus, the nMS spectra observed are of oligomers composed of monomer and dimers which correspond well to theoretical MWs.

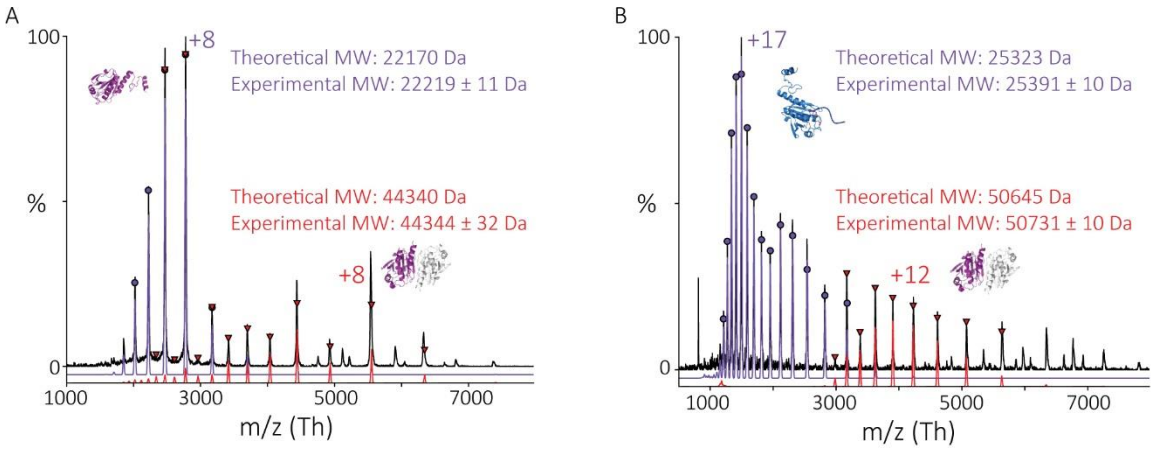

Figure 3.5: Collision induced dissociation of HsPrx3 m/z peaks show constituent protein oligomers
MSMS spectra of 6080 m/z peak of cleaved HsPrx3 (**A**). The collision energy was 90 V. The spectrum observed consists of monomers (purple) and dimers (red) with the *UniDec* peak assignments coloured. His_6-tagged HsPrx3 (**B**) MSMS spectra of 6770 m/z peak. The collision energy was 90 V. The spectrum observed consists of monomers (purple) and dimers (red) with the UniDec peak assignments coloured.

3.2.4 HsPrx3 assembles as discrete stacks of rings at pH 4.0

To monitor the pH-controlled oligomerisation, HsPrx3 proteins were buffer exchanged from 100 mM ammonium acetate at pH 8.0, into 100 mM ammonium acetate at pH 4.0. The time from initiation of exchange to recording the mass spectra was approximately 60 s. In both cases for cleaved and His_6-tagged HsPrx3, HMW species were immediately observed upon spraying with a distinct charge state series for each species (Figure 3.6 and 3.7). The HMW species for cleaved HsPrx3 corresponds to between one and six rings. From previous studies of HsPrx3 using TEM and cryo-EM (Phillips *et al*, 2014; Radjainia *et al*, 2015), these species are likely to correspond to stacked protein rings. As the formation of the HMW stacks is rapid, kinetic parameters were challenging to determine. During certain experiments, the population of rings change over time as the mass spectra were being recorded (Appendix A). Intermediate species composed of partial HsPrx3 rings were not detected as the stacked ring stoichiometry evolves, indicating that the mechanism of HsPrx3 HMW protein tube formation occurs non-commutatively, and exclusively through the association of rings.

Due to the large nature of these HMW HsPrx3 structures, AUC was used to corroborate the stacking behaviour in solution with those observed using nMS. The stacking behaviour of cleaved HsPrx3 observed by AUC was different from that recorded by nMS. Changing the pH of the ammonium acetate solution from 8.0 to 4.0 resulted in the formation of larger structures with c(s) values of over 100 S, with no smaller stacked ring species observed using the AUC (Figure 3.6 C). A main peak at c(s) of 120 S was observed, corresponding to a species with a mass of approximately 9 MDa, equating to a stacked species comprised of at least 34 rings. This discrepancy between the two techniques could arise due to very large stacks, if ionised at all, would unlikely transmit through the mass spectrometer. These large stacks could also be falling apart during electrospray ionisation, and before the final ionisation of the molecules. Each AUC experiment typically takes a few hours to complete a run, and over the course of the experiment, local concentrations of proteins increase – these variables of time and protein concentration could also account for the observed difference between nMS and AUC.

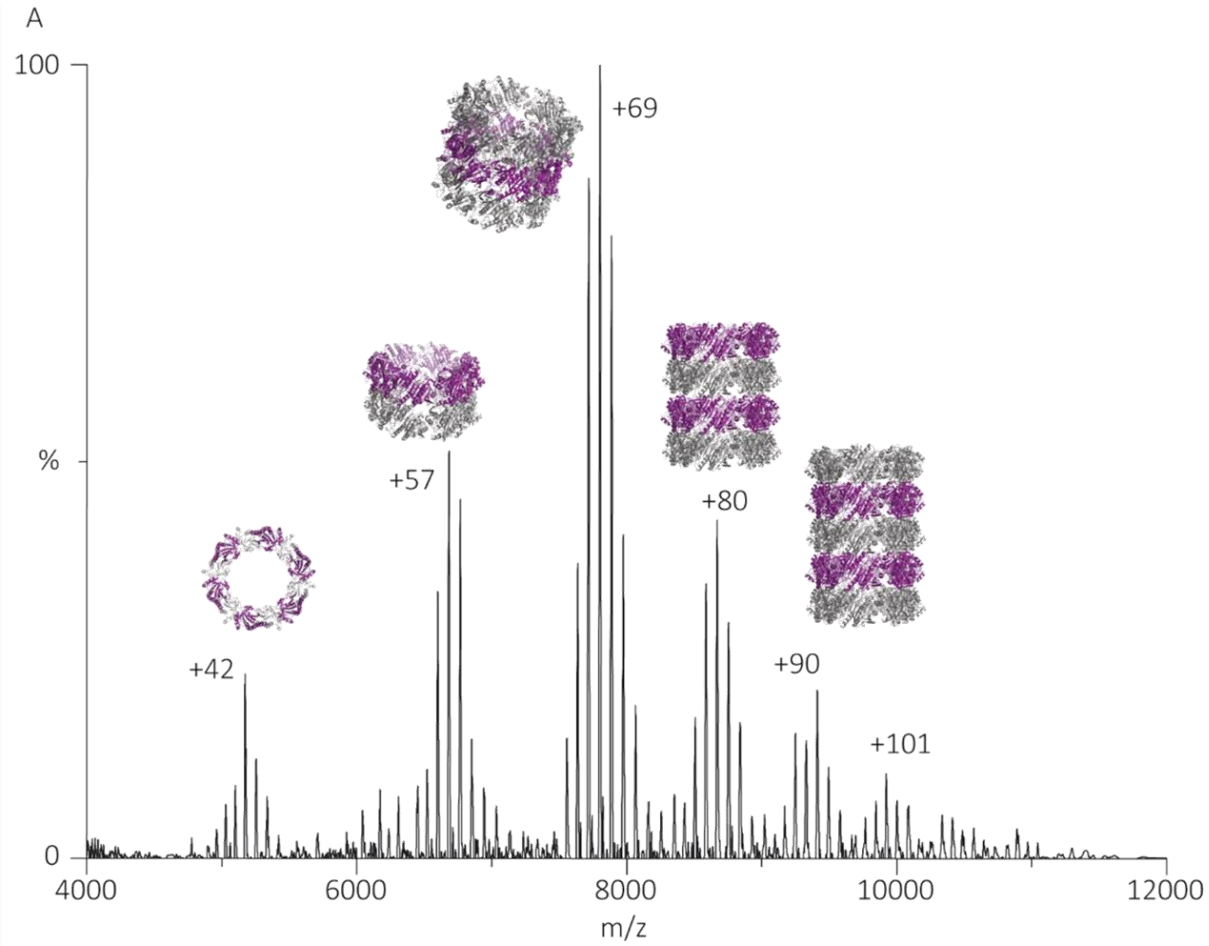

B

Theoretical MW (Da)	Experimental MW (Da)
266042	266718 ± 32
532085	533746 ± 113
798127	800319 ± 86
1064170	1066971 ± 80
1330212	1333927 ± 109
1596254	1600556 ± 148

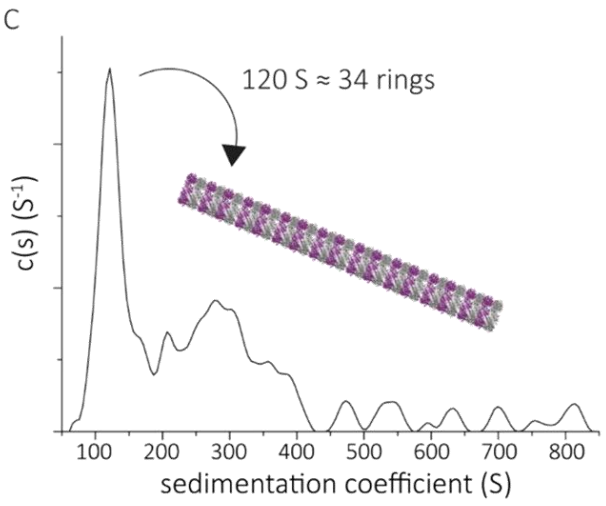

Figure 3.6: Cleaved HsPrx3 associates into large HMW stacks at pH 4.0

The mass spectrum (**A**) showing distinct charge state series for each discrete HMW HsPrx3 stacked species, with the MWs (**B**) corresponding to stacks of one to six rings in solution at pH 4.0. There were no observable peaks in the spectrum for monomers or dimers. The AUC experiment (**C**) shows a population of large species, with a predominant population at 120 S which corresponds to 34 stacked rings of 9 MDa. The frictional ratio (f/f_0) is 1.3.

In contrast, decreasing solution pH from 8.0 to 4.0 of 100 mM ammonium acetate causes His_6-tagged HsPrx3 to form short tubes composed of 2-3 rings. This ring stacking phenomenon seems to occur slowly, with AUC experiments taking a few hours to collect data supporting the nMS spectra collected 3 h after buffer exchange into the pH 4.0 solution (**Figure 3.7**).

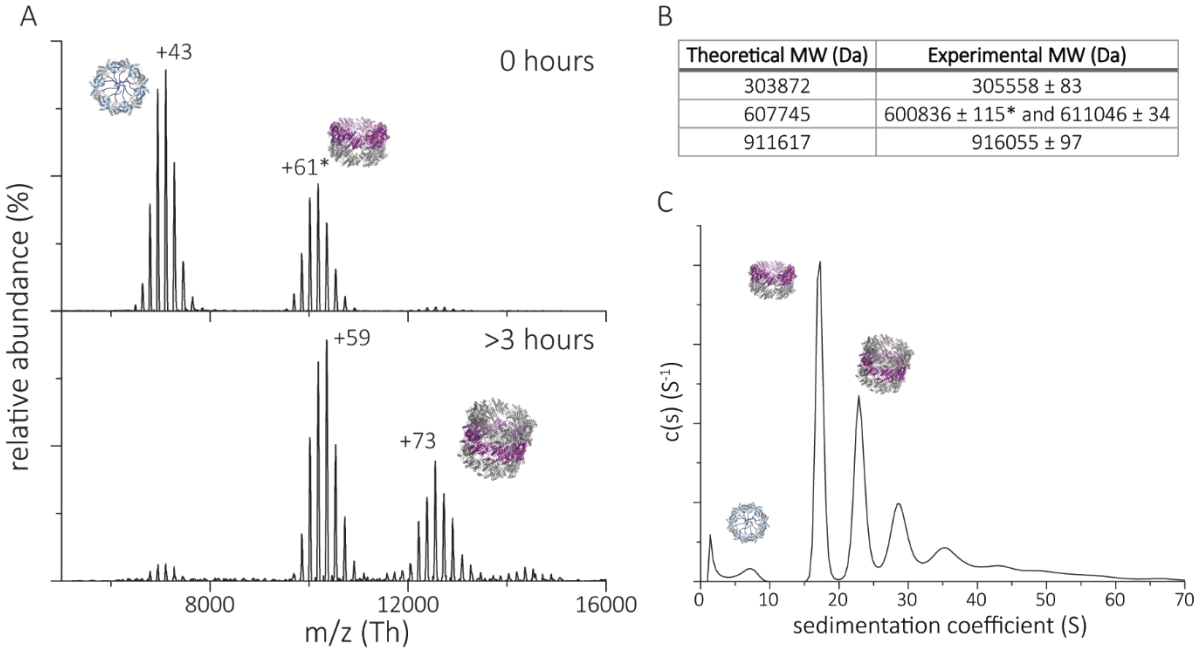

Theoretical MW (Da)	Experimental MW (Da)
303872	305558 ± 83
607745	600836 ± 115* and 611046 ± 34
911617	916055 ± 97

Figure 3.7: His_6-tagged HsPrx3 forms short stacks of rings at pH 4.0
Mass spectra (**A**) comparing the assembly of HsPrx3 rings between initial injection (0 h after the time of buffer exchange) to the same sample after 3 h at pH 4.0. The population of stacked rings shifts to that of higher MW. Charged states are that for the most intense peak for each spectra series. A table (**B**) comparing the theoretical MW with experimental MW derived from the mass spectra in **A**. Asterisks indicates experimental MW for species being lower than expected. The AUC analysis showed similar stacking behaviour for His_6-tagged HsPrx3, with sedimentation coefficients for the three highest peaks are 17 S, 23 S, 29 S. These correspond to the formation of HMW species composed of two to four rings. The frictional ratio (f/f_0) is 1.11.

3.2.5 Reversibility of stacking

Increasing the solution pH of ammonium acetate from 4.0 to 8.0 reverts the stacked population of rings back into single rings, with no chemical changes to the protein sequence. This phenomena occurs for both cleaved HsPrx3 (**Figure 3.8**) and His_6-tagged HsPrx3. Although previously assumed (Phillips, 2014), this is the first time this switch has been directly observed. This process, much like low pH induced stacking, occurs in under 60 s. Detecting this disassembly of stacks using the AUC was not possible, as during the course of the experiment, proteins are spun to the bottom of the cells thereby increasing local concentrations and, in this case, HsPrx3 in 100 mM ammonium acetate, pH 4.0, formed visible protein precipitates.

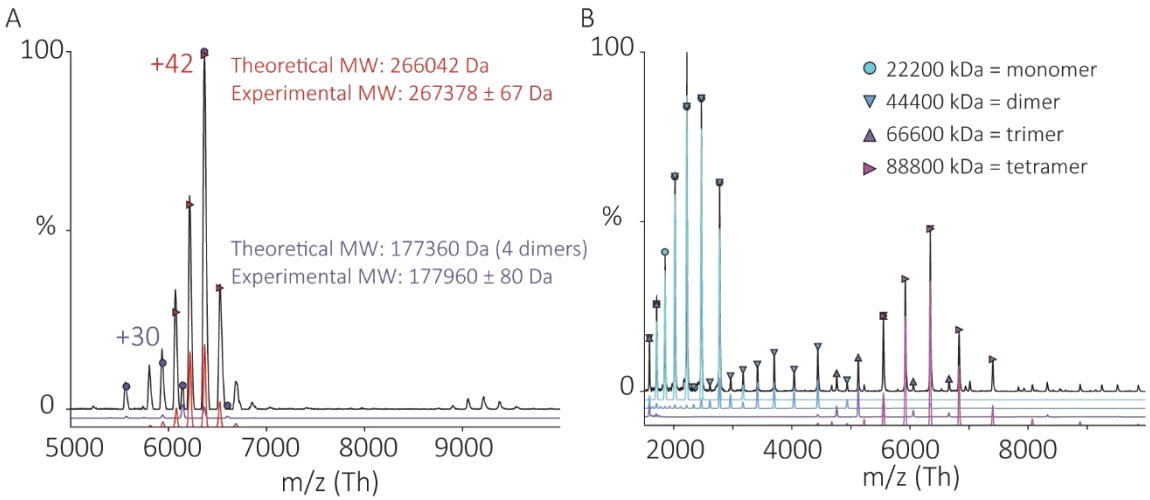

Figure 3.8: pH switch of cleaved HsPrx3 from pH 4.0 stacks back to pH 8.0
HsPrx3 protein was buffer exchanged from 100 mM ammonium acetate, pH 4.0, back into 100 mM ammonium acetate, pH 8.0, and sprayed into the native mass spectrometer to give spectra (**A**). The majority of the species returned to single rings (red triangle), with a small detectable population of two stacked rings (the small peaks around 9000 m/z). There is another charged series attributed to a dissociated ring (purple circle) with molecular weights (MWs) corresponding to four dimers. The collision induced dissociation of an isolated peak at 6365 m/z at 60 V gives the spectra (**B**) that also shows the *UniDec* deconvolutions of component spectra that could compose the experimental spectra. Dissociated species range from monomers to tetramers. The resulting monomer masses are the same as before lowering the pH (**Figure 3.5 A**), with no changes to the sequence or chemical modifications of the protein after stacking occurs.

3.3 Mixing tagged and cleaved tectons to modulate HMW tube formation

3.3.1 Cleaved and tagged HsPrx3 rings do not interchange dimer subunits at pH 8.0

Proteins that self-associate to form HMW oligomers often interchange subunits with one another in a state of equilibrium (Sobott *et al*, 2002), and this could be a useful feature for a protein tecton. This subunit switching behaviour was probed for the HsPrx3 model tectons using His_6-tagged HsPrx3 and cleaved HsPrx3, because both proteins have the same A interface where dimers interact to form rings. However, the equimolar mix of cleaved and His_6-tagged HsPrx3 resulted in two distinct spectra, indicating that it is unlikely that subunit exchange is occurring in solution (**Figure 3.9**). The *UniDec* deconvolution software assigns MWs to the spectra that suggests subunit exchange between the rings can occur; however, this assignment could also be a result of having broad mass-to-charge (m/z) peaks. Similar spectra, composed of two distinct charge state series for cleaved and tagged HsPrx3, can be generated again even after 24 h of mixing, and also when different ratios of cleaved and His_6-tagged are mixed together. This suggests that dimer subunit swapping does not occur between the HsPrx3 protein rings.

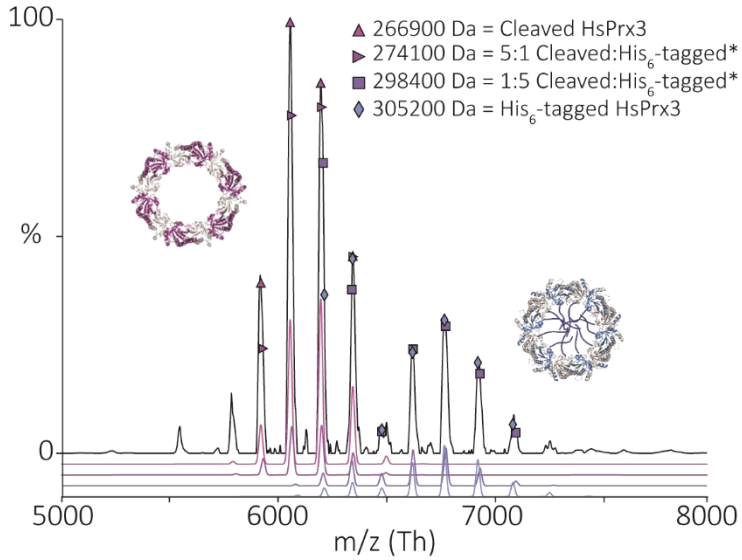

Figure 3.9: An equimolar mix of cleaved and His_6-tagged HsPrx3 at pH 8.0
Mass spectrum of a 1:1 mix of cleaved and His_6-tag HsPrx3 at a total protein concentration of 20 µM in 100 mM ammonium acetate, pH 8.0. *Unidec* peak assignment shows that this spectrum is composed of two distinct species of HsPrx3, but the peaks were too low in resolution to distinguish between possible single subunit exchanges.

The above spectra is that of an equimolar mix of proteins. The resulting mismatch in peak intensities, where cleaved HsPrx3 appeared to be more abundant, was an intriguing result. To rule out disproportionate protein aggregation of His_6-tagged HsPrx3, the sprayed samples were run on an SDS-PAGE gel to reveal protein bands of similar intensities (**Figure 3.10**). Where the loss of protein occurred, the degree to which it did was not influenced by the presence of the His_6-tag. Variations in intensity observed on the nMS can occur through differences in ionisation, due to the proteins themselves, or needle-to-needle variation.

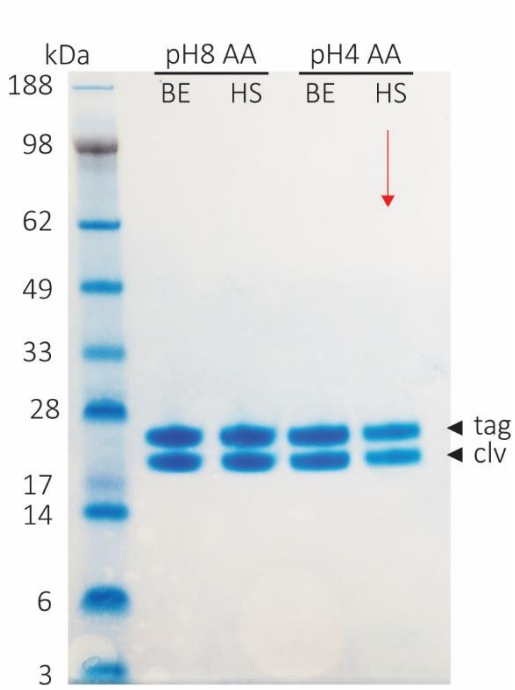

Figure 3.10: HsPrx3 proteins after buffer exchange into ammonium acetate
SDS-PAGE gel shows 1:1 protein bands for His_6-tagged (tag) and cleaved (clv) wild-type HsPrx3 throughout the buffer exchange process (**Section 6.9.3**) from 100 mM ammonium acetate at pH 8.0 (pH8 AA) to pH 4.0 (pH4 AA). There is notable protein loss at the last step (red arrow), after buffer exchanging into pH 4.0 ammonium acetate and then centrifugation of the sample. **BE** – buffer exchange (sample recovery after running sample through Bio-Spin6 columns, **Section 7.5.2**). **HS** – sample after centrifugation at 20000 xg, 10 min to remove precipitated proteins. Samples after centrifugations (or after 0.22 µm filtration) were analysed by the nMS.

3.3.2 Modulation of stack lengths: cleaved and His_6-tagged HsPrx3 combine when stacking at pH 4.0

Lowering the pH to 4.0 of an equimolar solution containing cleaved and His_6-tagged HsPrx3 causes these proteins to assemble together as rings. Intriguingly, the nMS spectrum now shows a higher relative abundance of His_6-tagged HsPrx3 species detected compared to cleaved HsPrx3, despite being present in equimolar concentration. *Unidec* deconvolutes the somewhat complex spectra, assigning peaks for stacks of up to three rings (**Figure 3.12**). Curiously, pH 4.0 solutions favour the ionisation of His_6-tagged HsPrx3 species, as the single ring spectra appears at a higher intensity for His_6-tagged HsPrx3 compared to cleaved HsPrx3. In the centre of this this spectrum, masses can be assigned to three different populations of two stacked rings composed of two cleaved proteins associating (◊ on **Figure 3.12**), or two His_6-tagged proteins assembling (□ on **Figure 3.12**), or one cleaved and one His_6-tagged HsPrx3 associating together (☆ on **Figure 3.12**). This experiment was also performed using the AUC (**Figure 3.11**), which supported these results, in that the species detected were sized between the observed stacked ring populations for the cleaved and tagged species on their own (Compare to **Figures 3.6 C and 3.7 C**). In fact, the His_6-tagged species dampened the formation of large cleaved HsPrx3 stacks of >34 rings, consistent with this species only forming up to three stacked rings. This demonstrates that His_6-tagged HsPrx3 protein can modulate the formation of HMW stacked species. Again, the AUC indicated that larger stacked species were observed in solution, than those observed by nMS.

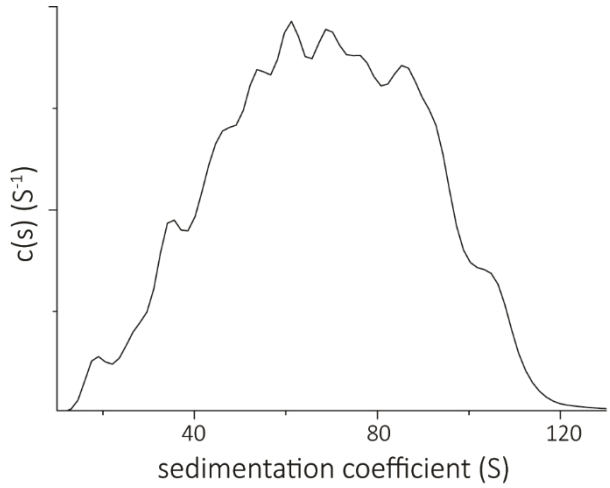

Figure 3.11: AUC of 1:1 mix of cleaved and His_6-tagged HsPrx3 at pH 4.0
This trace shows HMW species with S values that range between that of cleaved HsPrx3 at pH 4.0 (Figure 3.6) and tagged HsPrx3 at pH 4.0 (Figure 3.7) separately. The frictional ratio (f/f_0) is 1.02 and P at 0.66. This result indicates that His_6-tag HsPrx3 can influence cleaved HsPrx3 protein stacking, limiting protein tube size.

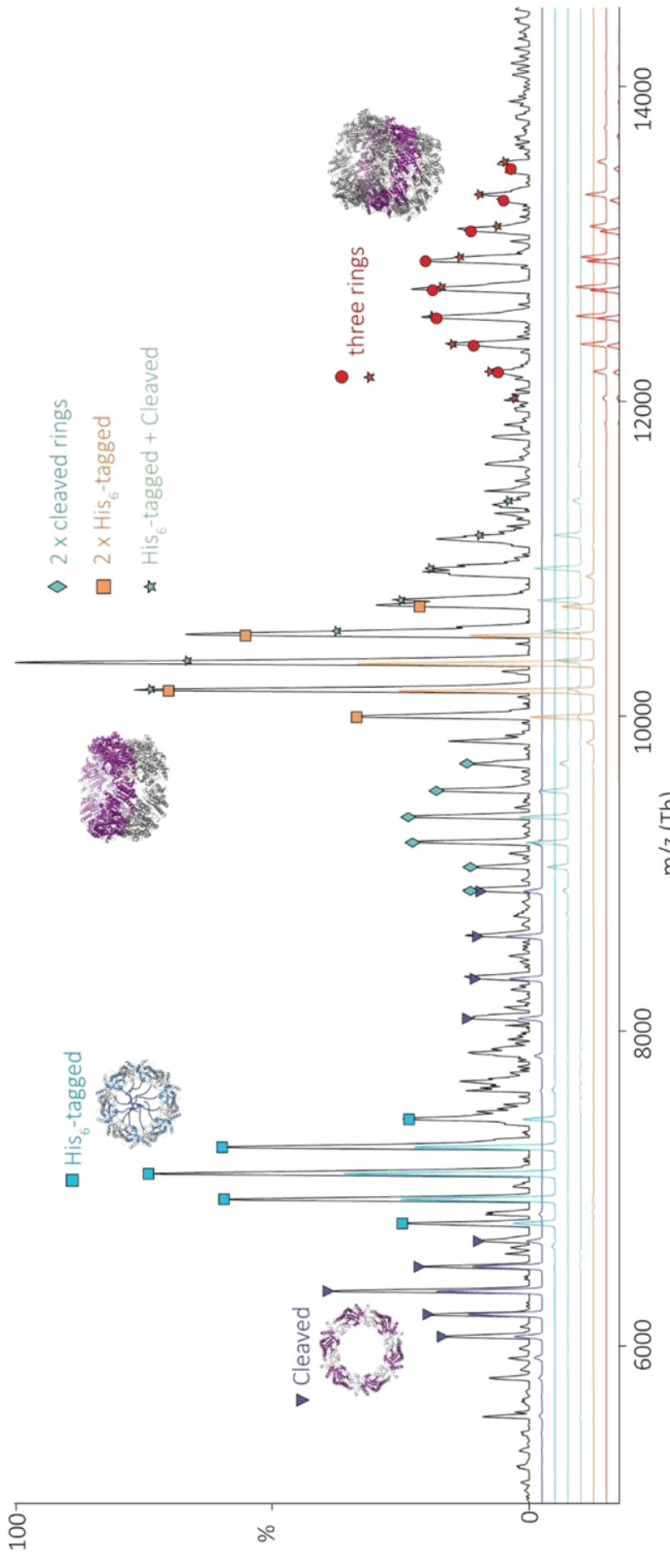

Figure 3.12: An equimolar mix of cleaved and His$_6$-tagged HsPrx3 proteins in 100 mM ammonium acetate, pH 4.0
The mass spectra (black line) with *Unidec* deconvolutions (coloured lines) showing different of species of rings and stacked rings, which contribute intensities towards nMS spectra. The cleaved (▼) and His$_6$-tagged (■) populations of HsPrx3 remain as distinct rings as seen in pH 8.0 ammonium acetate (**Figure 2.17**). These rings associate with themselves and each other to form 3 distinct species of double stacked rings (◆, ■, and ★). Triple stacked rings are also observed, but the wide m/z peaks means multiple assignments can be made to that one range of peaks (●, and ★). No larger stacked species were observed.

3.4 Discussion

3.4.1 Mechanism of formation of HMW Prx stacked species

The self-assembly of protein tectons can generate diverse quaternary structures with different functions (Section 1.3). nMS is a powerful tool to probe protein self-assembly into different oligomeric states. This is the first time a 2-Cys Prx oligomer has been observed in the gas phase, shedding light on the mechanism by which HsPrx3 proteins form HMW assemblies: with whole rings associating to form discrete stacked ring intermediates. HsPrx3 formation of HMW protein tubes occur *via* a non-commutative mechanism (see Figure 3.1). Having the non-commutative associations of rings, as opposed to the commutative associations of individual dimers, would also increase the protein-protein interaction surface area at the R interface, where favourable electrostatic and hydrogen bonds can occur, to promote protein tube formation.

Previous observations of HsPrx3 HMW structures have described this phenomenon occurring on the hour time scale (Phillips *et al*, 2014, Radjainia *et al*, 2015). However, this study shows ring stacking occurring rapidly in less than 60 s, thus allowing HMW stack formation as a self-preserving response to stress conditions, such as acidification. This is also the first time it has been directly shown that HsPrx3 stack formation is a reversible process that also occurs quickly (< 60 s) when solution pH is increased from 4.0 to 8.0. This drastic change in quaternary structure, which occurs rapidly, has yet to be observed *in vivo*, but this has not prevented other researchers from postulating its relevance in cell signalling during transient stress conditions (Saccoccia *et al*, 2012, Angelucci *et al*, 2013). Nonetheless, it is this switching behaviour of HsPrx3 that makes it an ideal tecton for applications in the realms of nanotechnology.

3.4.2 Towards controlling HMW tube formation and lengths

The HsPrx3 quaternary structure has proven to be highly sensitive to fluctuations to its solution environment. In this study, various conditions have been explored – including the effect of different salts and the presence of His_6-tag - with the aim of uncovering the features responsible for HsPrx3 HMW tube formation.

An important caveat to this work includes the lack of control for metal binding to the His_6-tag. Measures to chelate any residual metal ions that could have been introduced during the purification of HsPrx3, such as by using EDTA, were not performed (as this was not the focus of

these experiments at the time), so stacking behaviour that could have been encouraged by this (Ardini *et al*, 2014) was not accounted for. His_6-tagged Prx3 rings were shown to be stabilised in comparison their cleaved counterparts, with lowered activity towards H_2O_2 (Cao *et al*, 2007; Ashmead, 2016). This ring structure stabilisation has also been observed for HsPrx3 (Ashmead, 2016) and is perhaps the reason why dimer subunits do not readily interchange between cleaved and His_6-tagged HsPrx3, as observed in the nMS spectra. The histidine tag also shifts the equilibrium of His_6-tagged HsPrx3 towards smaller stacked species in 100 mM ammonium acetate, pH 4.0, compared with cleaved HsPrx3 proteins. His_6-tagged HsPrx3, when mixed with cleaved HsPrx3, can be used to modulate the overall size range of the species observed using the AUC. His_6-tagged HsPrx3 rings are composed of 12 monomers that have an extra 27 amino acid peptide chain protruding from the N-terminus of the protein. These flexible peptide chains are situated at the centre of the ring, and could conceivably cause sufficient steric hindrance towards the formation of favourable hydrogen bonds at the R interface. This, in turn, could slightly shift the equilibrium of ring associations towards that of single rings. An interesting observation is that SmPrx1, the only other crystal structure of stacked Prx, retains its histidine tag and this is probably why the protein purifies a discrete species of two stacked rings at pH 4.2 (Saccoccia *et al*, 2012). It would interesting to see how this protein behaves without a tag. The ability of HsPrx3 to form stacks of >2 rings, even with the histidine tag still attached, is a testament to the versatile R interface and the facilitating ring symmetry of this dodecameric tecton.

The nMS experiments were performed in ammonium acetate, and this does not represent the crowded environs within a mitochondria. In fact, repeating these experiments with SEC buffer (20 mM HEPES, 150 mM NaCl) with rapid buffer exchange from pH 8.0 to 4.0 resulted in precipitated proteins. However, with slow decrease in pH *via* overnight dialysis, HsPrx3 can stack to form long tubes (Phillips *et al*, 2014, Radjainia *et al*, 2015), such as those observed in the AUC experiments. These interesting inconsistencies could be due to a combination of factors including influences of different salts on protein assembly, as well as effects of the bulk environment versus the microenvironment on assembly. These salt-dependent, time-sensitive associations of HsPrx3 is a complex process with biological relevance yet to be verified. Nevertheless, the R interface of HsPrx3 is a versatile surface for protein-protein association, which can be tuned towards different stacking behaviours *via* the use of different solution components whether it be salts, crowding agents or pH.

3.5 Summary

In this chapter, native mass spectrometry was used to investigate the differing stacking mechanisms of cleaved HsPrx3 proteins as well as His_6-tagged HsPrx3 proteins. Both proteins are shown to assemble into HMW tube structures *via* a non-commutative mechanism, with dimers associating first to form rings, and then these ring coming together to form stacks of proteins. AUC analysis of HsPrx3 in pH 4.0 was used to compare the behaviour of proteins in solution with that using nMS. AUC and nMS results for the His_6-tagged HsPrx3 agree well, showing the formation of shorter stacks of HsPrx3 rings. Whereas, the nMS of the cleaved HsPrx3 showed a mixed population of HMW stacks composed of one to six rings. The AUC data, on the other hand, did not reflect this result, with large HMW species that would correspond to >34 rings observed. The reversibility of ring stacking was also demonstrated using nMS, showing the versatility of HsPrx3 as a tecton with reversible self-assembly as a key feature.

On mixing equimolar concentrations of the cleaved HsPrx3 and His_6-tagged HsPrx3, it was observed using nMS that the dimer subunits do not readily interchange between two populations of dodecameric rings. This surprising result could be attributed to the His_6-tag causing ring stabilisation. In addition, when the solution pH was lowered from 8.0 to 4.0, the rings associated together at the R interface, resulting in a population of mixed stacks of rings. The use of His_6-tagged HsPrx3 skewed the equilibrium of tube formation, as observed using the AUC, so that the whole population of protein tubes did not extend beyond 120 S, which is equivalent to ~34 rings. Using a mixed population of cleaved HsPrx3 and His_6-tagged HsPrx3 could be a means with which to control HsPrx3 protein tube lengths.

Chapter 4: Removing the redox switch in peroxiredoxin quaternary structure

4.1 Introduction

4.1.1 Is Prx quaternary structure linked to its activity and how can this be used in nanotechnology

Protein oligomerisation confers evolutionary advantages to cells, where greater functionality can result from a smaller DNA blueprint (Marsh *et al*, 2015; Ahnert *et al*, 2015; Levy *et al*, 2008). The oligomeric state of proteins is often linked to its catalytic activity: parts of active sites can form at the interface between two proteins, or allosteric interactions between proteins can govern its activity (Griffin and Gerrard, 2012). The quaternary structures of proteins can sometimes confer a function (such as scaffold proteins), and often form precise architectures to house catalytic reactions that hinge on the precise spatial arrangement of reactive amino acids (Grishin and Phillips, 1994; Griffin *et al*, 2012). Hence, disruption of protein oligomeric state often adversely affects protein activity, and this has been used as a strategy to target proteins associated with pathologies and remove their activity all together (Fischer *et al*, 2015).

Redox systems, with their biological electron transfer capabilities, have been used for bionanotechnology, such as for biosensor applications (Gilardi *et al*, 2002). Redox sensitivity is usually engineered into recombinant proteins by inserting cysteine residues to create protein surfaces linked by disulfide bonds (Ballister *et al*, 2008). Peroxiredoxins (Prxs) are naturally occurring redox-sensitive proteins that are able to alter their quaternary structure based on the redox status of their catalytic cysteine. The intricacies of this redox switch, and the subsequent quaternary structural changes, need to be unravelled to facilitate the full utilisation of this tecton.

4.1.2 Redox-dependent mechanism of 2-Cys Prx oligomerisation

Prx proteins are considered guardians of the redox landscape within cells (Perkins *et al*, 2015). As detailed in Sections 1.4.1 and 1.4.2.1, the solvent exposed active sites of Prxs are highly conserved across all domains of life (Rhee *et al*, 2005). The conserved spatial positions of residues act to lower

the pK_a of the peroxidatic cysteine (Cys_P) and also activate the sulfur atom for nucleophilic attack of H_2O_2. In contrast, the location of the resolving cysteine (Cys_R) varies between different types of Prx; for typical 2-Cys, like HsPrx3, the Cys_R comes from an obligate homodimer. This initial oxidation step of deprotonated Cys_P with H_2O_2 occurs rapidly to form Cys-S_POH (**Step1** in **Figure 4.1**) and has a second order reaction rate of ~10^7 $M^{-1}s^{-1}$ that is on par with other peroxidases (Perkins *et al*, 2015). In typical 2-Cys Prxs, the Cys-S_POH on one monomer reacts with the Cys_R on a pairing monomer to generate a disulfide bond between the two monomers (**Step 2**). Therefore one or two disulfide bonds can be held per Prx dimer. The disulfide bonds are reduced to complete the catalytic cycle either by chemical agents, such as DTT, TCEP or β-mercaptoethanol, or in a physiological context, by antioxidant proteins such as thioredoxins (Wood *et al*, 2003a, Rhee *et al*, 2005; Karplus, 2015). Within the cell, the rate of this final recycling step (**Step 3**) is restricted by the slow catalytic turnover, with a rate of ~10^5 $M^{-1}s^{-1}$, as well as the low cellular abundance of thioredoxin (Winterbourn and Peskin, 2016). This rate limiting step is 2 orders of magnitude lower than other cycling rates of other peroxidases (Watabe *et al*, 1997), which confers unusual properties to Prxs that allow them to perform diverse functions within a cell (highlighted in **Section 1.4.2**).

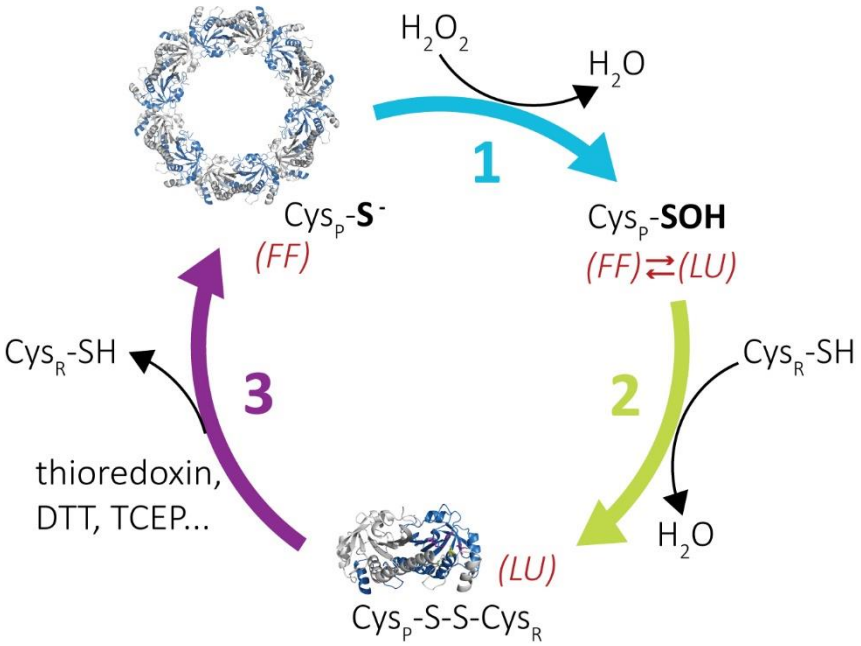

Figure 4.1: Catalytic cycle of 2-Cys Prxs, such as human Prx3 (HsPrx3)
The catalytic cycle of Prxs can be segmented into three main steps 1) peroxidation, 2) resolution, and 3) recycling. Reduced Prxs have unhindered catalytic cysteines that enable protein assembly into rings. The thiol of Cys_P, in a fully folded active site (FF), is deprotonated and primed for S_N2 nucleophilic attack of H_2O_2 (Step 1). When the active site unfurls into a locally unfolded (LU) state, the sulfenic form of Cys_P forms a disulfide bond with the resolving cysteine, Cys_R, resulting in the formation of oxidised dimers. This disulfide bond can then be reduced either by the thioredoxin enzyme *in vivo*, or reducing agents (such as TCEP or DTT) *in vitro*.

The redox state of Cys_P, dictates changes to the quaternary structure in certain Prxs, where reduced Prxs form rings, and oxidised Prxs form dimers (Barranco-Medina *et al*, 2009). In a reduced state, the deprotonated Cys_P is poised for reaction in a fully folded active site which encompasses the α2 helix end. Oxidation of Cys_P causes the α2 helix to enter a locally unfolded conformation, which enables a disulfide bond to form between Cys_P and Cys_R from the adjacent monomer. This partial uncoiling during disulfide bond formation destabilises the dimer-dimer interface (or A interface) disrupting the toroidal structure to generate obligate dimers (Wood *et al*, 2003a). It is this sensitive control of the quaternary structure for certain Prxs, such as that of human Prx3 (HsPrx3), which makes these proteins such appealing tectons for creating switchable protein architectures.

4.1.3 Other Prx muteins provide insight to the relationship between oligomerisation and activity

The redox mechanism for certain Prxs, such as HsPrx3, connects the active site state with conformational changes that can alter the overall quaternary structure. To investigate this close relationship between the quaternary structure of Prxs and their activity, a handful of mutagenesis studies have been performed on the toroid-building 'A interface' as well as within the active site of 2-Cys Prxs. The effects of these mutations on the redox switch, that is, the peroxidase activity of Prxs, were monitored thus far for the eukaryotic Prxs: StAhpC, *Schistosome masoni* Prx1 (SmPrx1) and HsPrx3 (Parsonage *et al*, 2005; Angelucci *et al*, 2013; Phillips, 2014). These studies reveal that oligomerisation confers greater peroxidase activity to particular 2-Cys Prxs, enabling more efficient H_2O_2 scavenging. Active site mutations that abolish peroxidase activity often yielded ringed Prxs, suggesting that disulfide bond formation is key for destabilising the A interface.

Table 4.1: Activity of various muteins and wild-type of StAhpC (Parsonage *et al*, 2005)

Enzyme (StAhpc)	Effect of mutation	k_{cat} (s^{-1})	K_M (H_2O_2) (μM)	k_{cat}/K_M (H_2O_2) ($M^{-1}s^{-1}$)	Rates compared with wild-type
Wild-type	-	55.1 ± 0.8	1.4 ± 0.2	(3.9 ± 0.5) x 10^7	-
T77V	Stabilised decamer	75.8 ± 1.6	1.6 ± 0.2	(4.7 ± 0.4) x 10^7	Slightly faster
T77I	Dimer	25.0 ± 1.0	93.4 ± 8.8	(2.7 ± 0.2) x 10^5	100-fold slower
T77D	Dimer	31.5 ± 1.9	62.0 ± 9.5	(5.1 ± 0.6) x 10^5	100-fold slower

Mutagenesis of StAhpC, was performed at the A interface, to generate dimeric muteins as well as stabilised decameric muteins (Parsonage *et al*, 2005). The activity of each mutein to reduce H_2O_2 was assessed using an intrinsic fluorescence-based assay (**Table 4.1**). Mutation of residues at the decamer building interface, T77I and T77D, disrupted the toroid formation and lowered the StAhpC

mutein activity by 100 fold; whereas the toroid stabilisation mutation, T77V, showed a slight increase in activity when compared to the wild-type protein. This work demonstrates that the toroid ring is not necessarily required for activity, as the dimeric mutant was still active, but is required for optimal activity.

Mutations of HsPrx3 at both the A interface and active site were created by Amy Phillips (Phillips, 2014) and the activity of these proteins (Table 4.2) was tested using the optimised competitive assay with horse radish peroxidase (Section 7.10.1). Errors were not reported for these results. Nonetheless, the A interface T104W mutein, with destabilised dodecameric ring formation under reducing conditions, demonstrated slightly lowered activity towards H_2O_2 compared to wild-type HsPrx3. These results suggest, like in the case of StAhpC, that ringed quaternary structures of HsPrx3 are required for optimal activity. Mutations to residues within the active site that disrupted the peroxidase function of Cys_P not only stabilised ring formation, but also encouraged the formation of HMW structures. These active site mutein results have also been demonstrated in SmPrx1 proteins, where the increased formation of HMW stacked rings were observed (Angelucci *et al*, 2013). This suggests that peroxidase activity, or specifically disulfide bond formation, is important for the redox switch from rings to dimers.

Peptide tags containing six histidines (His_6-tag) are routinely used in recombinant protein purification, were found to stabilise the ring structure of Prxs, and this has been studied with respect to their peroxidase activity. In BtPrx3, these stabilised His_6-tagged toroids exhibited decreased activity compared with untagged BtPrx3 (Cao *et al*, 2007). Similar results were shown for the HsPrx3 system (Ashmead, 2016), where activity for His_6-tagged wild-type HsPrx3 was reported to be (3.4 ± 0.2) x 10^7 $M^{-1}s^{-1}$. Note that this is the opposite of what is observed for the stabilised decamer StAhpC mutein (Parsonage *et al*, 2005), suggesting that the ring stabilisation caused by the His_6-tag occurs via a different mechanism than that of A interface residue mutations.

It is important to note that these observations are specific to certain Prxs. For instance, oligomerisation into rings is not necessary for optimal activity in 2-Cys Prxs from *Arabadopsis thaliana* (*At*-CysPrx) (König *et al*, 2013). The His_6-tagged variant and the dimeric mutein both have *higher* activity than the wild-type protein. This is the opposite of what is observed in StAhpC, HsPrx3 and SmPrx1. Also, the formation of disulfide bonds do not necessarily cause ring destabilisation in all 2-Cys Prxs. The human Prx4 (HsPrx4) is a permanent decameric ring with an activity of 2 x 10^7 $M^{-1}s^{-1}$ towards H_2O_2 and on disulfide bond formation, it remains as a ring (Wang *et al*, 2012). The ring stability has been attributed to an A interface held together by hydrophobic and van der Waals interactions.

Table 4.2: Summary of the rationale behind mutational design of HsPrx3 muteins (Phillips, 2014). SEC-SLS non-running buffer was 20 mM HEPES, 150 mM NaCl, pH 8.0; reducing buffer was the same as non-reducing buffer but contained 2 mM TCEP. n/d = not determined. HMW = high molecular weight; ** no errors were reported.

Enzyme (HsPrx3)	Rationale	Quaternary assembly by SEC coupled with static light scattering (SEC-SLS)		Electron microscopy (reducing)	Relative activity H_2O_2 ($M^{-1}s^{-1}$) **
		Non-reducing	Reducing		
Wild-type		Dimer	Dodecamer, dimer	Dodecamer	1.1×10^7
Interface A mutations					
S78A	Stabilise A interface. Altered packing could lead to increased stability as seen in Parsonage *et al.* 2005	HMW, dodecamer, dimer	Dodecamer	Potential cages (like Meissner *et al.* 2005)	2.7×10^7
T104W	Stabilise A interface. Introduced the potential for a novel H-bond, mimicking the A interface of *Mycobacterium tuberculosis* AhpE	Tetramer, dimer	Dodecamer, tetramer	Potentially smaller diameter rings	4.5×10^6
Active site mutations					
C47S	Prevents disulfide bond formation and A interface destabilisation by mimicking the protonated Cys_P	HMW, dodecamer	Dodecamer	n/d	Inactive
P48A	Decreasing the propensity of Cys_P loop to unfold	Dodecamer	Dodecamer	n/d	0.4×10^7
R123G	Removing the Cys_P thiolate-R123 ionic bond, encouraging loop unfolding	HMW, dodecamer	Dodecamer	No ring or HMW structures	Inactive
C47S S78A	Combining both toroid stabilising mutations	HMW, dodecamer	Dodecamer	Catenanes are more frequent	n/d

4.1.4 Chapter overview

The redox switch of certain typical 2-Cys Prxs, like HsPrx3, are intertwined with its oligomeric state. The active site influences tertiary structural movements that can disrupt interactions at the A interface, resulting in destabilised ringed assemblies. By engineering in or disrupting associative bonds, via amino acid mutations, at the A interface, the importance of the redox-induced oligomeric switch to peroxidase activity for HsPrx3 can be studied and can shed light on the connection between oligomerisation and peroxidase activity across this particular group of Prxs. StAhpC and AtPrx1 proteins share low sequence similarity with HsPrx3: 37% and 55% respectively. The characterisation of oligomeric state and peroxidase activity has not yet been examined for any mammalian Prxs. This study presents the first active human 2-Cys dimer and stabilised toroid that has been biophysically characterised in association with activity.

A interface muteins, S75E HsPrx3 and S78C HsPrx3, were generated that favour the dimer or ring quaternary structures, respectively. X-ray crystallography alongside other biophysical techniques, including analytical ultracentrifugation (AUC), small angle X-ray scattering (SAXS), and size exclusion chromatography coupled with multi-angle light scattering (SEC-SLS), were performed to ascertain the structure of these muteins under various redox conditions. Activity assays of these muteins reveals the link between structure and peroxidase function.

Disentangling the oligomeric state of HsPrx3 from the redox state of Cys_P would not only give insights into the catalytic mechanism of this crucial enzyme, but will also generate a complete set of protein building blocks as tectons for nanotechnological applications.

4.2 Design rationale for A interface mutants

In order to study the relationship between the quaternary structure switch of HsPrx3 and its redox activity, dimer and ring tectons were separately generated by designing disruptive or stabilising mutations at the A interface. The A interface of the wild-type HsPrx3 crystal structure (PDB: 5JCG, Yewdall 2016; Chapter 2) was analysed using PDBePISA which identifies important residues that interact to form a macromolecular interface (Krissinel and Henrick, 2007). With a buried surface area of 655 $Å^2$, the A interface involves an extensive network of hydrogen bonds that occur along the α3 helix as well as between a couple of loop regions composed of residues L103-K105 and E116-L120.

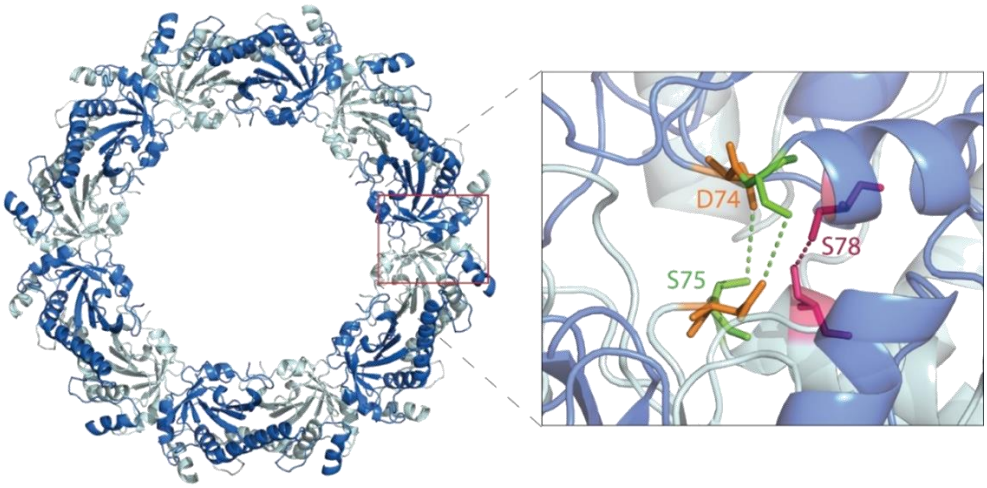

Figure 4.2: A interface amino acid mutations
Within the A interface, the mentioned residues are: D74 (orange), S75 (green) and S78 (red). Hydrogen bonds are indicated with dotted lines. (PDB: 5JCG)

A particular region of interest was from residues serine 75 (S75) and serine 78 (S78). The residues interact with the equivalent residue on the adjacent monomer (**Figure 4.2**). In particular, the S78 residue hydrogen bonds with the equivalent residue on the apposing dimer, and this has been demonstrated to be a key interaction to form this interface (Phillips, 2014). The S75 residue forms a hydrogen bond with D74 on the adjacent molecule.

A single point mutation to amino acid residues were proposed at the S78 and S75 sites. Replacing S75 with a negatively charged glutamic acid (S75E mutein) was predicted to disrupt its interaction with D74, due to charge-charge repulsions of two negatively charged amino acids in close proximity, resulting in the formation of only dimers. Whereas, S78 interacts directly with the adjacent homodimer S78. Mutating S78 to a cysteine residue (S78C mutein) was chosen as a strategy to generate stabilised toroids. Cysteine residues, in close proximity and under oxidising conditions, can form disulfide bonds, however, the A interface is closely packed and not solvent exposed, so it is unlikely disulfide bonds will form between S78C dimers under oxidising conditions. Alternatively, cysteine residues have been shown to behave similarly to non-bulky hydrophobic amino acids when localised at interfaces (Poole, 2015). This cysteine-induced ring stabilisation is perhaps a similar phenomenon to what is observed for HsPrx1, which possesses a naturally contain cysteine (C83) at a homologous position to S78 in HsPrx3 (Lee *et al*, 2007).

Molecular biology and site directed mutagenesis was performed on the N-terminal His_6-tagged wild-type HsPrx3 gene, to create both the S75E HsPrx3 mutein and S78C HsPrx3 mutein (Epoch Lifesciences). The resulting expected masses and pIs for tagged and cleaved proteins are detailed in the table below.

Table 4.3: Theoretical molecular weights and pI of A interface muteins.

HsPrx3	MW (Da)	pI
S75E		
His_6-tagged	25364.81	5.86
Cleaved	22212.26	5.43
S78C		
His_6-tagged	25338.83	5.97
Cleaved	22186.29	5.59

4.3 The obligate dimer: S75E HsPrx3

4.3.1 Expression, purification and identification

Recombinant N-terminal His_6-tagged S75E HsPrx3 was expressed and purified (**Section 7.4 and 7.5**). Briefly, His_6-tagged S75E HsPrx3 proteins were purified using IMAC, the elution peak from which was pooled and run through the SEC column for further purification (**Figure 4.3**). S75E muteins were overexpressed with purified yields of ~70 mg/L of growth media used.

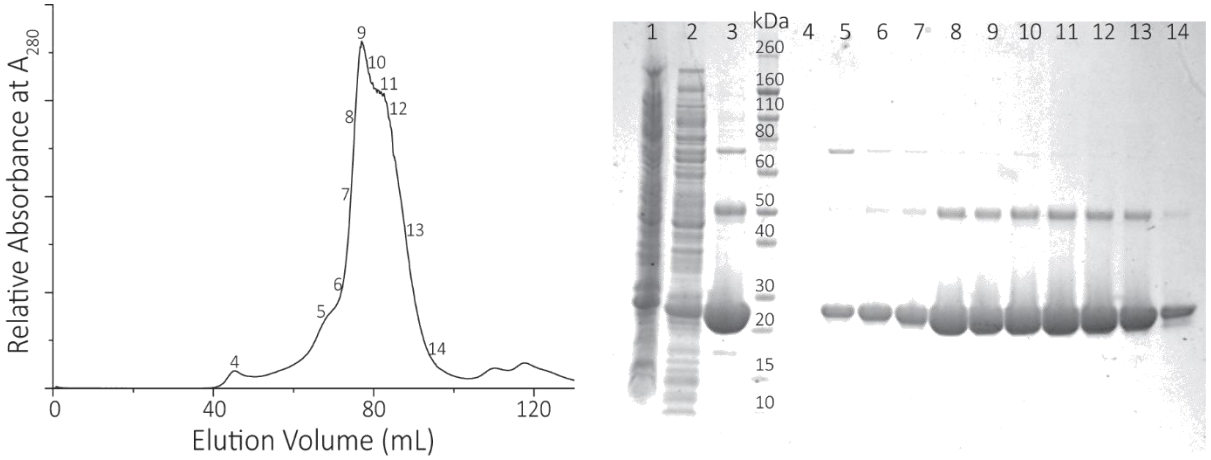

Figure 4.3: S75E HsPrx3 purification using size exclusion chromatography
The SEC trace (**A**) showing proteins eluted into 20 mM HEPES pH 8.0, 150 mM NaCl, 2 mM TCEP. The major protein peak elutes in the size range expected for dimeric proteins. The reducing SDS-PAGE gel (**B**) confirms successful overexpression of S75E HsPrx3. There is a notable higher band co-eluting at ~50 kDa which corresponds to oxidised dimeric protein, discussed in **Section 4.6.2**. The gel numberings are as follows: 1 – total proteins in lysate; 2 – total soluble proteins; 3 – pooled IMAC elution; 4 to 14 – fractions eluted off the SEC column.

The SEC chromatograms from these initial purifications, shows the major protein peak eluting at volumes that correspond to dimeric proteins. The reducing SDS-PAGE gel reveals two protein bands corresponding to reduced S75E HsPrx3 and oxidised S75E HsPrx3. In fact, S75E HsPrx3 were later shown to be notoriously difficult to completely oxidise (**Section 4.5.2** and discussed in **Section**

4.6.2). The His_6-tag was cleaved using rTEV protease (Figure 4.4, Section 7.5.3). The mass of the pure protein, both tagged and cleaved, was assessed using LC-MS to verify it was the correct mass for S75E HsPrx3.

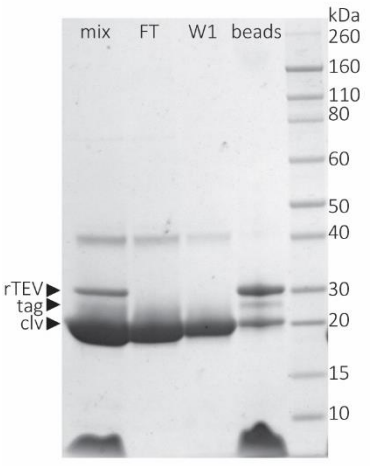

Figure 4.4: His_6-tag cleavage of S75E HsPrx3 proteins using rTEV protease
His_6-tagged rTEV protease (~28 kDa band) and His_6-tagged S75E muteins were pre-mixed and incubated to allow to cleavage to occur. The mix after 24 h (mix) was loaded onto Co^{2+}-beads. Cleaved S75E HsPrx3 eluted off the beads in the flow through (FT) and also after washing with SEC buffer (W1). The beads (beads) were also run on a gel to check for cleavage efficiency of the rTEV protease (good efficiency is when there are no more 'tag' bands visible) as well as to check which proteins remained attached to the beads.

4.3.2 Crystallisation trials

Multiple crystallisation screens and fine screens were used in an attempt to grow S75E HsPrx3 crystals, but to no avail (Section 7.8). However, after 12 months, small cubic crystals were observed in the RS3 screen, condition F9 (0.75 M tri-sodium citrate, 10 mM sodium borate, pH 8.5; Stura *et al*, 1992) for 20 mg/ml His_6-tagged S75E HsPrx3 (Figure 4.5).

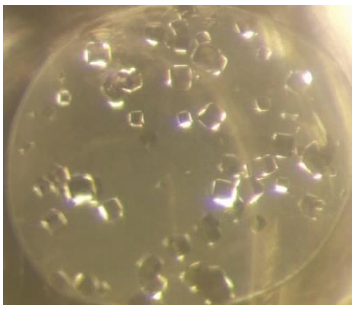

Figure 4.5: His_6-tagged S75E HsPrx3 protein crystals
A droplet from the crystal screens made in-house shows cubic crystals of S75E HsPrx3 formed after 12 months. 20 mg/mL protein and mother liquor were mixed at a 1:1 ratio (Section 7.8.1). The screen condition contains 0.75 M tri-sodium citrate, 10 mM sodium borate, pH 8.5 (Stura *et al*, 1992).

Izit Crystal Dye (Hampton Research; Section 7.8.1.3), a blue molecular dye that binds to solvent channels in macromolecular crystals, was used to check whether these crystals were proteinaceous. After 20 minutes, a single crystal incubated in Izit was coloured blue, indicating that it was protein. However, these crystals did not diffract and attempts to replicate crystal growth in these conditions were not fruitful in the short-term time scale during the last 6 months of this thesis. Suggestions for future work to explore these and other conditions to resolve the structure are detailed in Section 4.6.2.

4.3.3 Quaternary structure characterisation

Previous work on wild-type HsPrx3 has shown that His_6-tags stabilised the ring quaternary structure of these proteins (Ashmead, 2016), so both His_6-tagged and cleaved S75E HsPrx3 were studied in the following experiments with the hypothesis that the His_6-tag may encourage toroid formation despite the point mutation.

4.3.3.1 Circular dichroism of S75E HsPrx3 to check for secondary structure

To ensure that S75E HsPrx3 protein is fully folded, its secondary structure was examined using circular dichroism spectroscopy. The spectrum recorded showed that the cleaved S75E HsPrx3 protein is folded (**Figure 4.6**). A minimum is recorded at 208 nm and 222 nm, which is characteristic of folded globular proteins (Greenfield, 2007).

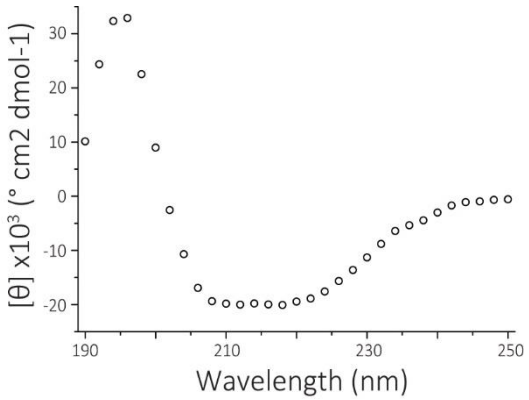

Figure 4.6: Circular dichroism spectra of cleaved S75E HsPrx3
Circular dichroism spectroscopy was conducted with 0.1 mg/mL protein diluted in MilliQ. The mean residue ellipticity, [θ], is plotted as a function of the wavelength (data represented as ◦).

4.3.3.2 S75E muteins do not form a ring in solution

Biophysical analyses of S75E HsPrx3 was performed, using SEC-SLS and AUC, to investigate the protein quaternary structure. As determined by SEC-SLS, the experimental molecular weight (MW) of cleaved S75E HsPrx3 proteins is 44 kDa in non-reducing buffer conditions (20 mM HEPES pH 8.0, 150 mM NaCl) (**Figure 4.7 A**). This is consistent with S75E HsPrx3 being a dimeric species in solution. In fact, S75E muteins, both cleaved and His_6-tagged, were dimeric under both reducing and non-reducing conditions, as seen on the AUC (**Figure 4.7 B**). In this AUC experiment, a variety of protein concentrations for His_6-tagged S75E HsPrx3 were sampled simultaneously in reducing buffer conditions (20 mM HEPES pH 8.0, 150 mM NaCl, 2 mM TCEP). There is a notable appearance of some tetrameric species at higher concentrations of 45 µM, which is consistent with what is

observed in the SEC-SLS. This is intriguing as assembly via the A interface is unlikely due to the introduced charge-charge repulsions; however, the interface that forms catenanes, such as that seen in BtPrx3 (Cao 2005), remains unperturbed and could facilitate further dimer-dimer associations. Nonetheless, an obligate dimeric HsPrx3, with or without a His_6-tag, has been successful created that cannot form rings under reducing conditions.

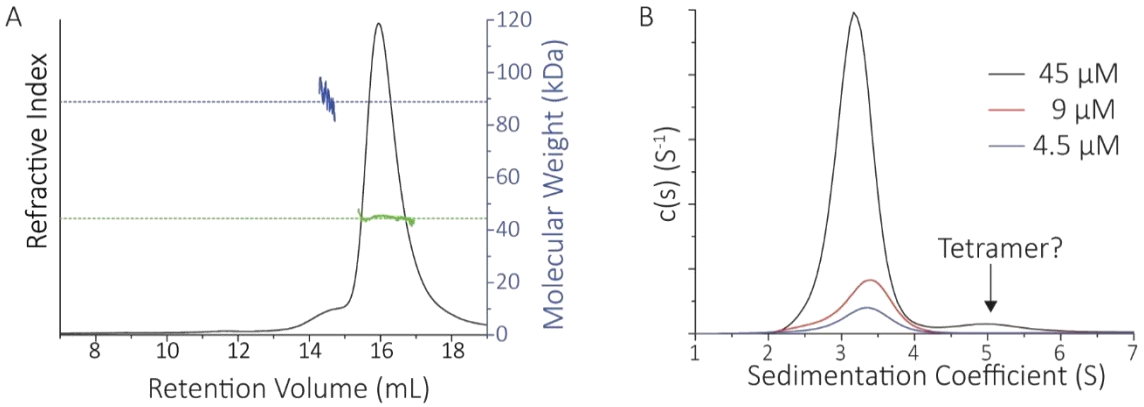

Figure 4.7: Biophysical characterisation of S75E HsPrx3 shows it forms mostly a dimeric species
(**A**) SEC-SLS of 45 µM cleaved S75E HsPrx3 run at 0.4 ml/min in non-reducing buffer (20 mM HEPES, pH 8.0, 150 mM NaCl). The refractive index (black line) and right-angle light scattering were used to calculate experimental MWs (right axis in blue) of particles in solution. The main protein peak is a dimer (~44 kDa, green) and also some tetramers (~88 kDa, blue) were also detected. The dotted lines indicate the theoretical MWs. (**B**) Sedimentation velocity experiments of His_6-tagged S75E HsPrx3 in reducing buffer (20 mM HEPES, pH 8.0, 150 mM NaCl, 2mM TCEP). The protein was run at a range of concentrations: 45 µM (black), 9 µM (red); 4.5 µM (blue). The sedimentation coefficients for the major peaks are between 4.2-3.4 S, which correspond to that expected for dimeric HsPrx3. The smaller peak in the 45 µM sample is that of the tetramer protein at 5 S. The frictional ratio for all samples was 1.3. For more experimental details, see **Section 7.7.4.**

4.3.3.3 Small angle X-ray scattering analysis of the solution structure

SAXS of S75E mutein verifies the results determined by AUC and SEC-SLS, and gives insights on the shape of this protein in solution. Sample and data quality were assessed using Guinier analysis of the SAXS scattering curve at low angles. The linearity of the plot (**Figure 4.8 A**) shows that the scattering of the S75E HsPrx3 is reliable and no sample aggregation and/or interparticle interference is present (Putnam *et al*, 2007). Scattering data intensity were plotted along with the real-space pair-wise distance distribution function *P(r)* (**Figure 4.8 B**). The maximum dimension of the scattering particle (D_{max}) was 74 Å as calculated by *AUTOPOROD* (Petoukhov *et al*, 2012). The radius of gyration (R_g) was calculated to be 26 Å, which is in agreement with the Guinier determined R_g at 25 Å. The experimental Porod volume was determined to be 77753.9 nm^3, and the molecular weight extracted from this was 48.6 kDa (Svergun *et al*, 1995), which is slightly higher than the theoretical MW at 44.4 kDa, but within the ~20 % accuracy from using volume to determine mass

as hydration sphere of proteins vary with shapes, such as elongated proteins due to greater surface area to volume ratio. The *P(r)* plot shows a single peak with an asymmetrical shape, with a positively skewed tail at the long distances, indicating that S75E HsPrx3 is a prolate ellipsoid in solution. This is consistent with S75E HsPrx3 being dimeric in both reduced and non-reducing conditions.

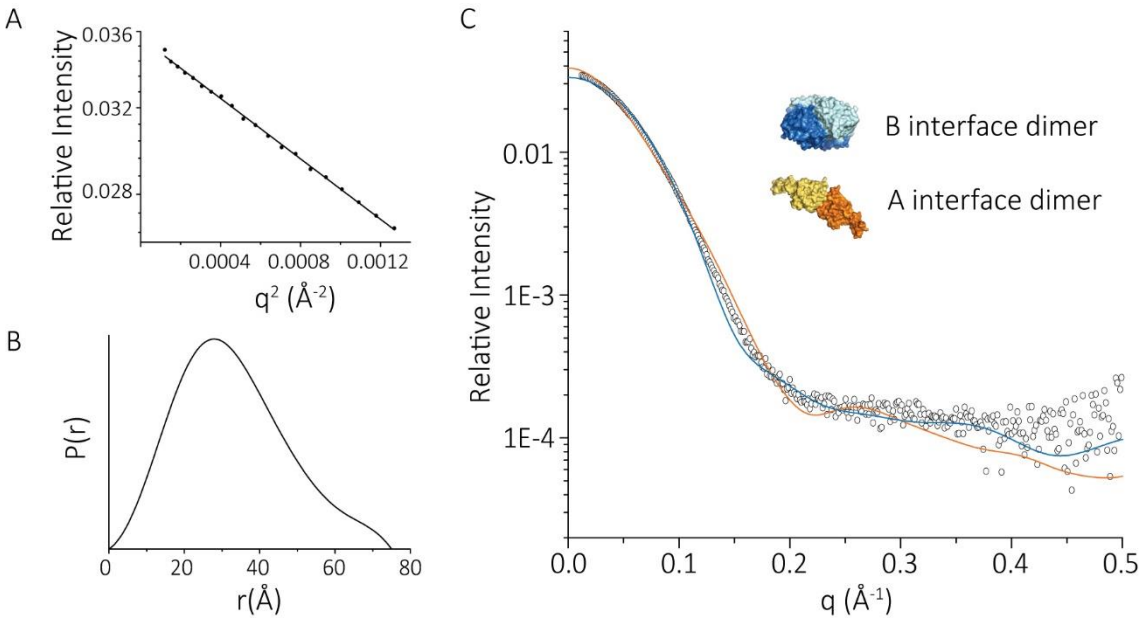

Figure 4.8: S75E HsPrx3 is be dimeric as seen by SAXS
(**A**) The linear Guinier plot as determined using *PRIMUS QT*. (**B**) *P(r)* plot determined using *PRIMUS QT*. (**C**) The experimental scattering profile of S75E HsPrx3 (presented as open circles, o) overlaid with theoretical scattering profiles of the wild-type HsPrx3 dimer structures (PDB: 5JCG) generated with a B interface (blue) or an A interface (orange).

This experimental scatter was compared, using *CRYSOL*, with theoretical scattering from atomic coordinates generated from the wild-type HsPrx3 crystal structure (PDB: 5JCG, Svergun *et al*, 1995; **Figure 4.8 C**). The overall shape information from the SAXS model matches better with the crystal coordinates for the B interface dimer (chi = 1.9) rather than the A interface dimer (chi = 2.5). Despite almost sharing the same sequence identity (99.5 %); however, the fits between the experimental and both theoretical scattering are relatively poor. This is indicative of a difference between the shape of S75E HsPx3 in solution and the crystallised state of the wild-type in which the dimers are part of stacked rings (Putnam *et al*, 2007). The difference in theoretical and experimental shapes can be observed on comparison of the calculated Porod volume of the A interface dimers (64800 nm^3) and B interface dimers (59310 nm^3), with the larger experimental Porod volume of S75E HsPrx3 at 77753.9 nm^3. These suggests that S75E HsPrx3 may be adopting a more elongated conformation.

4.4 The stabilised toroid: S78C HsPrx3

4.4.1 Expression, purification and identification

In a similar manner to the above S75E mutein, recombinant N-terminal His_6-tagged S78C HsPrx3 was expressed and purified using a combination of IMAC and SEC (Section 7.4 and 7.5; Figure 4.9). S78C muteins overexpressed and purified with yields of ~100 mg per litre of growth media used, similar to wild-type proteins.

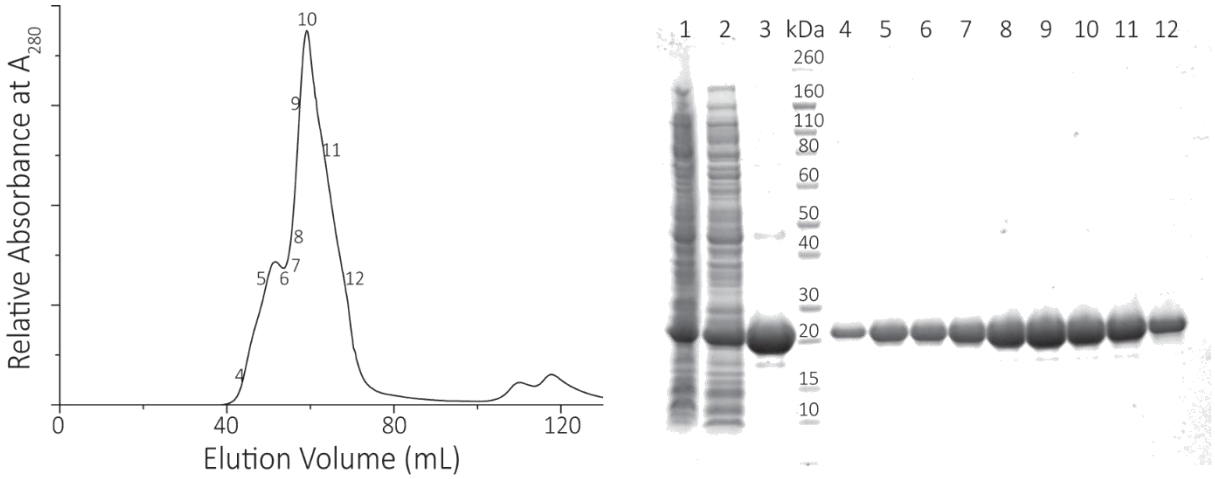

Figure 4.9: S78C HsPrx3 purification showing the SEC trace with accompanying SDS-PAGE gel
The SEC trace (**A**) shows a protein peak eluting into 20 mM HEPES pH 8.0, 150 mM NaCl, 2 mM TCEP. The major protein peak elutes in the size range expected for dodecameric proteins, with the small peak between 5 and 6 suggesting potential ring stacking. The SDS-PAGE gel (**B**) shows the successful overexpression of S75E HsPrx3. The gel numberings are as follows: 1 – total proteins in lysate; 2 – total soluble proteins; 3 – pooled IMAC elution; 4 to 12 – fractions eluted off the SEC column.

The SEC chromatograms from these initial purifications, shows the major protein peak eluting at volumes that correspond to dodecameric proteins. The His_6-tag was cleaved using rTEV protease (Figure 4.10, Section 7.5.3). The mass of the pure protein, both tagged and cleaved, was assessed using LC-MS to verify it was the correct mass for S78C HsPrx3.

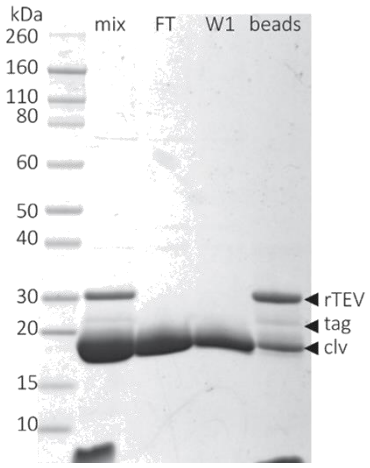

Figure 4.10: His_6-tag cleavage of S78C HsPrx3 proteins using rTEV protease
His_6-tagged rTEV protease (~28 kDa band) and His_6-tagged S78C muteins were pre-mixed and incubated to allow to cleavage to occur. The mix after 24 h (mix) was loaded onto Co^{2+}-beads. Cleaved S78C HsPrx3 elutes off the beads in the flow through (FT) and also after washing with SEC buffer (W1). The beads (beads) were also run on a gel to check for cleavage efficiency of the rTEV protease (good efficiency is when there are no more 'tag' bands visible) as well as to check which proteins remained attached to the beads.

4.4.2 X-ray crystallographic structure of stabilised ring at 2.4 Å

4.4.2.1 Crystallisation of S78C HsPrx3

To probe the molecular alterations of the S78C mutation on protein structure, a crystal structure was solved. Crystallisation of S78C HsPrx3 was successful using a fine screen developed around condition D12 from the MORPHEUS screen (Gorrec, 2009). A rod-shaped crystal (**Figure 4.11**) grew in 3 weeks after initial tray setting of 33 mg/mL cleaved S78C HsPrx3 protein in the B12 condition (0.1 M Tris-bicine, pH 8.9, 15% MPD, 10% PEG1000, 12.5% PEG3350, 0.02 M alcohol additives). An X-ray diffraction data set to a resolution of 2.4 Å was collected for that single crystal.

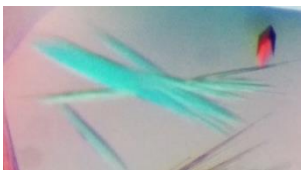

Figure 4.11: The rod-shaped crystal of S78C HsPrx3
Most crystals that grew were needle-like. However, the rod (in pink at top right corner) diffracted and the resulting structure solved at 2.4 Å. These crystals, viewed using a polariser, are normally colourless.

4.4.2.2 Data processing and structure refinement

The X-ray diffraction data were processed and solved as described in **Section 7.8**. The data were processed in the space group I222 and solved by molecular replacement using the monomer from the wild-type HsPrx3 crystal structure as a search model (PDB: 5JCG). Consistent with the wild-type structure, the asymmetric unit contains nine monomers and when all the symmetry equivalent molecules are generated, it reveals an organisation of three, stacked dodecameric rings. This model includes all residues, except for the first four residues belonging to the cleaved tag.

Table 4.4: Data collection and refinement statistics for S78C HsPrx3, PDB: 5UCX

	S78C HsPrx3, PDB: 5UCX
Data collection	
Space group	I222
Cell dimensions	
a, *b*, *c* (Å)	133.4, 167.6, 221.5
α, β, γ(°)	90.0 , 90.0 , 90.0
Resolution (Å)	48.9 - 2.40 (2.46 - 2.40)
R_{pim}	0.117 (0.679)
I/σI	6.4 (1.5)
$CC_{1/2}$	0.980 (0.379)
Completeness (%)	99.9 (99.2)
Redundancy	6.1 (5.6)
Refinement	
Resolution (Å)	2.40
No. unique reflections	91953
R_{work}/ R_{free}	0.194/0.228
No. atoms	
Protein	13640
Water	58
B-factors (Å^2)	
Protein	24
R.m.s deviations	
Bond lengths (Å)	0.01
Bond angles (º)	1.357

There are nine monomers within this crystal lattice.

4.4.2.3 Crystal structure of S78C HsPrx3 at 2.4 Å

The S78C HsPrx3 structure is consistent with that of the wild-type HsPrx3 crystal structure (described in **Section 2.3**). Each monomer possesses a fully folded C-terminus and a reduced Cys_P contained within a fully folded active site. The monomers are arranged as dodecameric rings that are stacked to form short protein tube composed of three rings (**Figure 4.12**). In fact, wild-type HsPrx3 and S78C HsPrx3 are virtually identical proteins on comparison of the monomers, yielding a root mean square deviation of 0.216 Å across 195 equivalent Cα positions. The structural similarities between the wild-type and the S78C mutein are evident when comparing average interface areas: for the A interface 651 $Å^2$ and 654 $Å^2$, and the B interface 1978 $Å^2$ and 1952 $Å^2$, respectively (using PDBePISA; Krissinel *et al*, 2007).

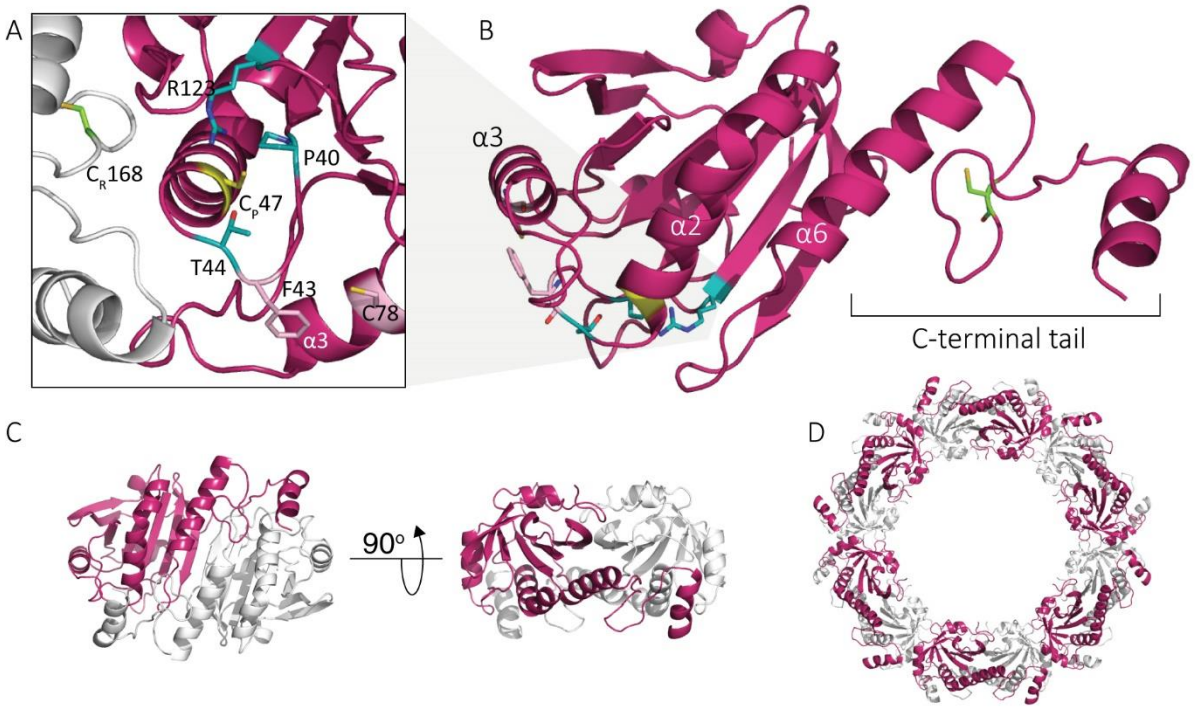

Figure 4.12: S78C HsPrx3 crystal structure
(**A**) The active site is highlighted, with peroxidatic cysteine (C_P47, yellow) and resolving cysteine (C_R168; green) highlighted in the context of other conserved active site residues (teal). The residues, F43 and C78, mentioned at the A interface (pink sticks) are shown to give context to their location with respect to the active site. (**B**) The S78C HsPrx3 monomer with a fully resolved C-terminal tail and important α helices highlighted. The residues in (A) are shown in the context of the entire monomer. (**C**) The monomer further assembles into dimers, which then form dodecameric rings (**D**).

However, there is greater density observed at the position of the mutated cysteine (C78) that clearly accounts for a sulfur atom not present in serine residues (**Figure 4.13**). The C78 residue hydrogen bonds with an equivalent C78 residue on the adjacent monomer across from the dimer-dimer interface, or A interface. As the protein crystals used to generate this structure grew in reducing conditions, it is expected that no disulfide bonds were formed between the C78 residues. The positioning of the apposing C78 residues, with thiols splayed away from each other, also does not appear to support disulfide bond formation. Curiously, the C78 residue stabilises a nearby phenylalanine residue, F43, on the same monomer. Superimposing nine wild-type monomers reveals that F43 can adopt an array of movements at the A interface (**Figure 4.13**), however, in all nine S78C monomers overlaid, the F43 remains resolutely in the same position, where it is able to increase its Pi-Pi interaction with a tryptophan residue, W82, also on the same monomer. Otherwise, the side chains and interactions within the A interface remain the consistent between the wild-type and the S78C mutein.

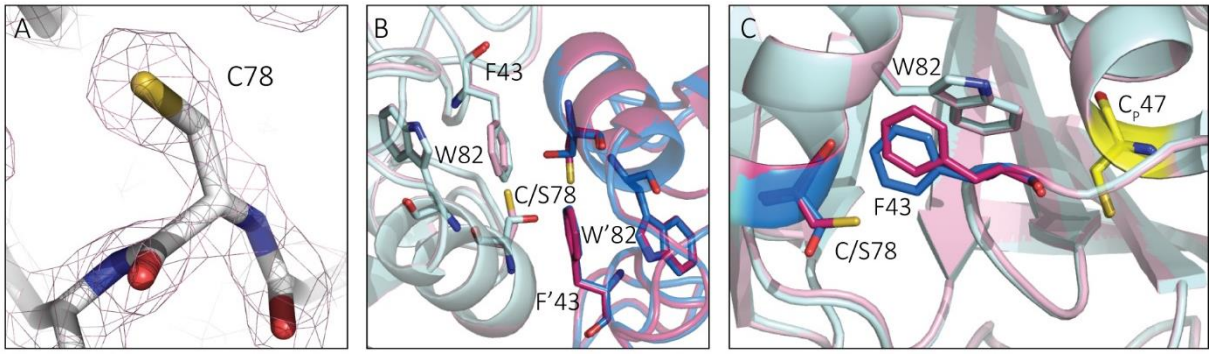

Figure 4.13: C78 residue and A interface interactions

(**A**) A difference density map ($2f_o$-f_c) at 1.2 σ (mesh) with crystal structure model (white) overlaid at residue C78. The thiol fits well within the density, demonstrating a fully reduced C78 residue at the A interface of S78C HsPrx3 protein. (**B**) The A interface of wild-type HsPrx3 (cartoon in blue) superimposed on the A interface of S78C HsPrx3 (cartoon in pink), with key residues highlighted (sticks). Note the differing positioning of the thiol group of the cysteine (in yellow) and that of the hydroxyl group on the serine. (**C**) The superimposed A interface of a monomer of wildtype (blue) and S78C (pink) HsPrx3. The position of the C78 thiol shifts the F43 residue by 1.1 Å closer to W82. The F43 residue in wild-type protein can be seen to adopt a range of positions, however, the S78C mutein has F43 held in a fixed position (pink) forming a compact hydrophobic pocket. The peroxidatic cysteines of wild-type and S78C HsPrx3 (C_P47 residue in yellow) are also overlaid to give a reference for the location of the active site with respect to the A interface.

4.4.3 Quaternary structure characterisation

4.4.3.1 Behaviour of S78C HsPrx3 proteins in solution using SEC-SLS

Although in the crystal structure, S78C HsPrx3 dodecameric rings appear to stack into three rings, in solution at pH 8.0, the majority of S78C muteins are single toroids, similar to their wild-type counterparts (**Figure 4.14**). Interestingly, a small initial peak is observed in the SEC-SLS analysis that corresponds to HMW species of two dodecameric rings. This has been observed for both cleaved and His_6-tagged S78C muteins in solution under both non-reducing and reducing conditions.

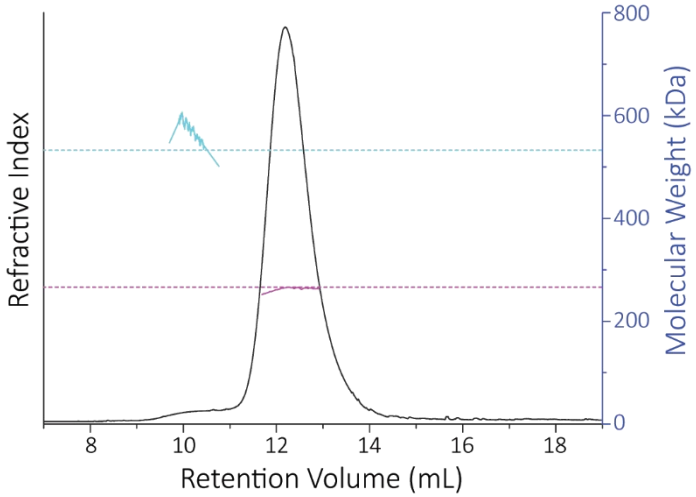

Figure 4.14: S78C HsPrx3 SEC-SLS shows toroids and some stacked toroids
45 µM cleaved S78C HsPrx3 proteins run at 0.4 ml/min in non-reducing conditions. The refractive index (black line) and right-angle light scattering were used to calculate MWs (right axis in blue) of particles in solution. The main protein peak is a dodecameric toroid (~266 kDa) and also a slight peak is noticeable for two stacked rings (~88 kDa). Dotted lines represent theoretical MW for each species.

4.4.3.2 Small angle X-ray scattering analysis of S78C HsPrx3

SAXS analysis of cleaved S78C HsPrx3 proteins verifies the results determined by crystallography as well as the SEC-SLS. Sample and data quality were assessed using Guinier analysis of the SAXS scattering curve at low angles. The linearity of the plot (**Figure 4.15 A**) shows that the scattering of the S78C HsPrx3 is reliable and no sample aggregation or interparticle interference is present (Putnam 2007). Scattering data intensity is plotted along with the real-space pair-wise distance distribution function *P(r)* (**Figure 4.15 B**). The maximum dimension of the scattering particle (D_{max}) was 152 Å as calculated by *AUTOPOROD* (Petoukhov *et al*, 2012). The radius of gyration (R_g) was calculated to be 57 Å, which is in agreement with the Guinier determined R_g at 58 Å. The experimental Porod volume of 418141 nm^3 was used to approximate the MW to be 261 kDa

(Svergun *et al*, 1995), which is slightly smaller than the theoretical MW at 266 kDa. The *P(r)* plot shows two peaks, which indicates that S78C HsPrx3 has a ring shape in solution. In order to compare the solution structure generated from the SAXS data with the crystallographic structure of S78C HsPrx3, *CRYSOL* was used to generate a theoretical scattering plot from the atomic coordinates for a single ring generated from the S78C HsPrx3 crystal structure (PDB: 5UXS). This theoretical scattering fits relatively well with the experimental scattering (chi = 2.77), indicating the ring structure is representative of S78C HsPrx3 proteins in solution. Interestingly, the theoretical Porod volume of 505500 nm^3 is greater than the experimental Porod volume, indicating the solution structure of HsPrx3 may be more compact than in the crystal structure.

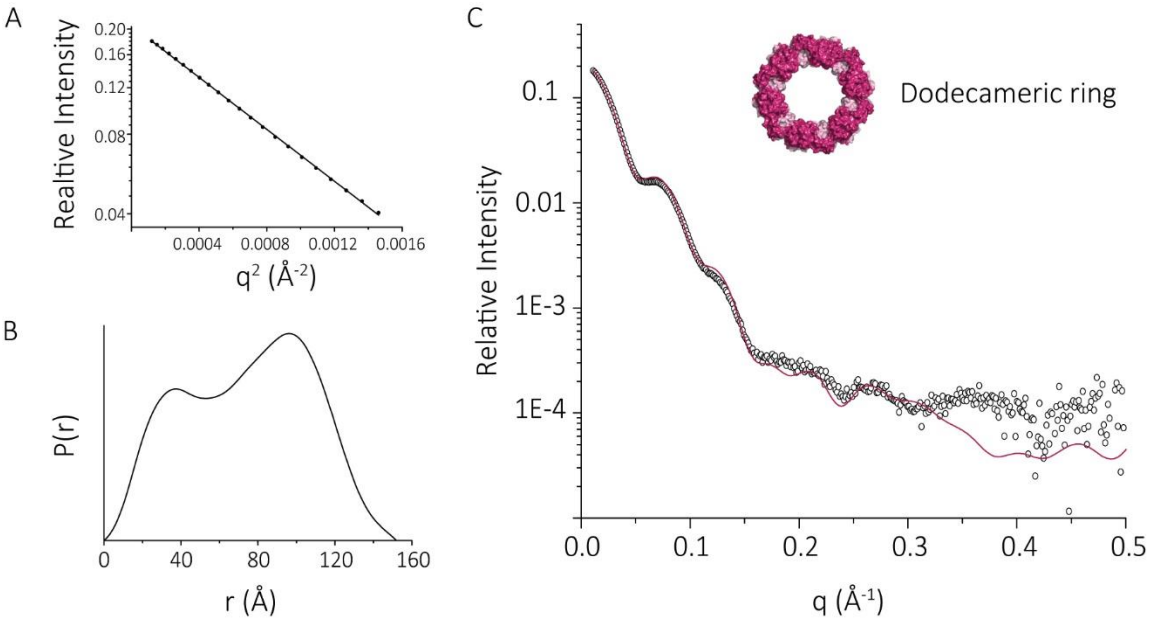

Figure 4.15: S78C HsPrx3 is be dodecameric ring as seen by SAXS
(**A**) The linear Guinier plot as determined using *PRIMUS QT*. (**B**) *P(r)* plot determined using *PRIMUS QT*. (**C**) The experimental scattering profile of S78C HsPrx3 (presented as open circles, o) overlaid with theoretical scattering profiles of the S78C HsPrx3 dodecameric ring (PDB: 5UCX) using *CRYSOL*.

4.4.3.3 Rings are stable under non-reducing conditions as seen via AUC analysis

Oxidants spontaneously dissolve into buffers, and without reducing agents present, a non-reducing buffer will become mildly oxidising (Winterbourn *et al*, 2015). In fact, it can be difficult to keep Prx proteins from oxidising in non-reducing conditions, and this effect is more pronounced in low concentrations of Prxs as a higher percentage of the protein population will become oxidised. In the case of 2-Cys Prxs, such as HsPrx3, oxidation of the protein will cause a change in quaternary structure from a reduced ring into an oxidsed dimer (as outlines in Section 4.1.2). The effect of Prx oxidation in non-reducing conditions can be monitored using the AUC, and this experiment was performed for both 2.3 µM wild-type HsPrx3 and 2.3 µM S78C HsPrx3. The reduced wild-type

HsPrx3 rings, with a peak at 9.8 S, spontaneously oxidise and fall apart into dimers, with a peak at 4.3 S (Figure 4.16). Repeating this experiment with the same conditions using the S78C muteins demonstrated the stability of these toroids, with just a single peak at 9.2 S, which does not dissociate to dimers (Figure 4.16).

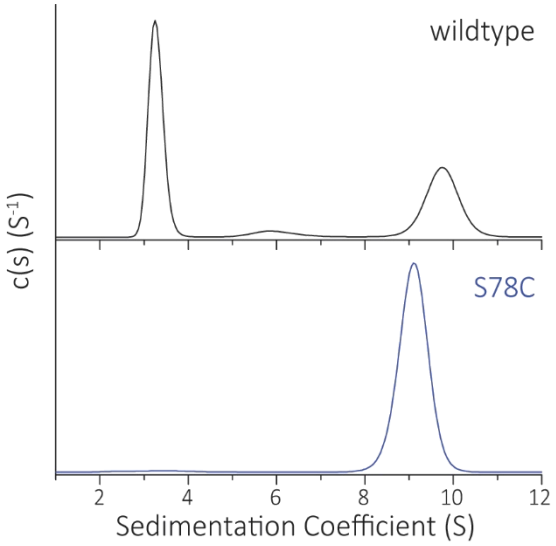

Figure 4.16: AUC showing stabilised S78C HsPrx3 toroids in mildly oxidising non-reducing buffer
The experiment was conducted with 2.3 µM of purified proteins in 20 mM HEPES, 150 mM NaCl without any reducing agents. Data were fitted to a continuous c(s) distribution model at a resolution of 300 and a confidence level of 0.95 using *SEDFIT* (Schuck 2000). Data were fitted with an *s* value ranging between 1 S and 12 S. The fit resulted in a frictional ratio (f/f_0) of 1.17 for wild-type HsPrx3 and 1.36 for S78C HsPrx3.

The difference in sedimentation coefficients between the two different proteins suggests the S78C muetins are smaller than wild-type HsPrx3 proteins. This is consistent with the discrepancies between the Porod volumes from the SAXS data collected. Perhaps stabilised dimer-dimer interface results in a more compact ring structure, as was hypothesised in Wood 2002.

This additional cysteine at the A interface stabilises the toroid form of S78C HsPrx3, resulting in the creation of improved second-generation tectons from a wild-type blueprint.

4.5 Peroxidase activity and quaternary structure

The solution structures of both S75E HsPrx3 and S78C HsPrx3 were established as obligate dimers and stabilised rings, respectively. Competitive assays with horse radish peroxidase (HRP) and catalase were used to probe the effect of these mutations on the peroxidase activity of each mutein. These assays are only accurate for Prxs with reactions rates for H_2O_2 in the same order of magnitude ~ 10^7 $M^{-1}s^{-1}$ as the competing enzymes: HRP and catalase. For slower Prxs, a time course

on an SDS-PAGE gel may be sufficient (Nagy *et al*, 2011). The HRP competitive assay monitors only **Step 1** in **Figure 4.1**, whereas the catalase assay and the SDS-PAGE assay both monitor **Steps 1 to 2**. The sensitive nature of its peroxidase activity, makes it difficult to monitor Prx activity as precautions must be made to ensure proteins are fully reduced and are not oxidised by other factors outside their intended substrate (Winterbourn *et al*, 2016).

4.5.1 The S75E dimer can still react with H_2O_2

An optimised HRP competition assay (**Section 7.10**) enabled the generation of more data points with smaller errors for the determination of activity of Prx proteins, with every attempt made to optimise human error. The assay is finical, making it imperative to have wild-type HsPrx3 as a control protein in every experiment. The second order rate of reaction of wild-type HsPrx3 towards H_2O_2, under the optimised conditions of this assay, was (4.7 ± 0.2) x 10^7 $M^{-1}s^{-1}$ (**Figure 4.17**). This rate of reaction is similar to those reported in the literature for HsPrx3 at 2 x 10^7 $M^{-1}s^{-1}$ (Cox *et al*, 2009b, Nagy *et al*, 2011).

A comparison of the rate of reactions between wild-type protein and the muteins, S75E HsPrx3 and S78C HsPrx3 (**Figure 4.17**), reveals interesting results. Stabilised ring, S78C HsPrx3, shows comparable activity to wild-type protein, with a rate of (4.0 ± 0.5) x 10^7 $M^{-1}s^{-1}$. The error is the standard deviation for triplicates for each data point. The resulting activity assay data points plot as a slight curve, rather than a straight line, making it difficult to fit a linear line for the reaction rate. This curve in data points is indicative of slight background oxidation of S78C HsPrx3. Nonetheless, the reaction rates of S78C HsPrx3 and wild-type HsPrx3 are not unambiguously different.

Despite its lack of ability to form rings, the S75E dimer retains its ability to react with H_2O_2, but at a relatively slower rate of 1.1 ± 0.1 x 10^7 $M^{-1}s^{-1}$. Although this rate is four times slower than the wild-type reactivity, the rate of S75E HsPrx3 is still two orders of magnitude higher than the AhpC dimer mutant (Parsonage *et al*, 2005). The HRP competitive assay can overestimate reaction rates for peroxidases whose activity is <10^6 $M^{-1}s^{-1}$, making it too slow to reliably compete with HRP (Winterbourn *et al*, 2016). Therefore, an SDS-PAGE reaction was carried out (**Section 7.10.2**) for a more accurate assessment of the lower reactivity of S75E dimer mutein towards H_2O_2.

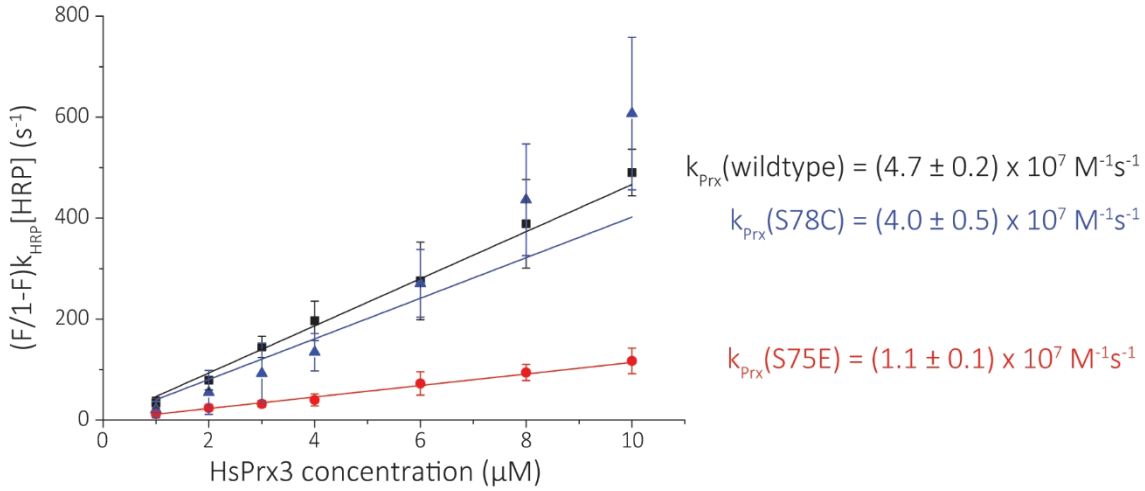

Figure 4.17: HRP competitive assay for HsPrx3 muteins
As described in **Section 7.10.1**, each experiment was performed as triplicates and the errors on the pseudo-second order rates, k_{Prx}, are standard deviations from within this triplicate. Plot shows HsPrx3 concentrations against the approximated "first order" relative rate of HRP disappearance at 403 nm. The k_{Prx} is calculated from the gradient of a linear line of best fit to the data points. Lines of best fit do not fit the data points of S78C HsPrx3 proteins, which seem to curve.

4.5.2 Catalase competitive assays to assess Prx reactivity towards H_2O_2

The catalase competitive assay was used to probe the order of magnitude of reactivity of HsPrx3 proteins towards H_2O_2 (Cox *et al*, 2009b; Nagy *et al*, 2011; **Section 7.10.2**). The catalase competitive assay, although not as quantitative as the HRP competitive assays, gives an easy visual confirmation of the relative actives of HsPrx3 proteins to catalase enzymes. These experiments were performed in collaboration with Alexander Peskin (School of Medicine, University of Otago, Christchurch). Protein samples were reduced with 500 mM DTT for 30 minutes, and these samples were run on the LC-MS to ascertain populations of reduced and oxidised proteins for comparison to the SDS-PAGE gels.

Human catalase reacts with H_2O_2 at a rate constant of 3×10^7 $M^{-1}s^{-1}$ (Dunford, 1999). Catalase is introduced at increasing concentrations to a constant mix of 10 µM H_2O_2 and 10 µM HsPrx3 protein. The resulting formation of disulfide bond upon HsPrx3 oxidation was monitored using a non-reducing SDS-PAGE gel. In fact, these SDS-PAGE gels are able to resolve populations of not only reduced HsPrx3 monomers and oxidised dimers, but also between different types of oxidised dimer: where either one or two disulfide bonds are formed (as observed in S78C hsPrx3 gel as a band doublet; **Figure 4.18**). These results corroborate the HRP activity assay in that the S78C HsPrx3 proteins remains similarly active to the wild-type HsPrx3, at a rate range both in 10^7 $M^{-1}s^{-1}$.

The results for S75E HsPrx3 suggests that that rate of reaction is in fact much lower than was indicated by the HRP assay. So an SDS-PAGE based assay was used on S75E HsPrx3 to determine its activity towards H_2O_2 (Nagy *et al*, 2011).

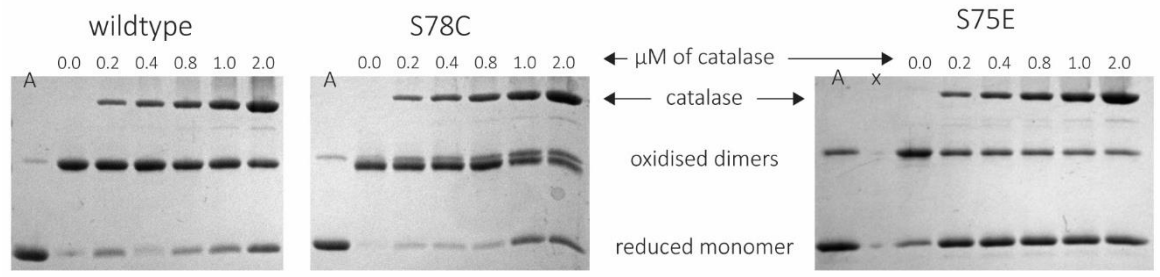

Figure 4.18: Catalase competition assay on non-reducing SDS-PAGE gel
SDS-PAGE gel shows distinct populations for reduced monomers, oxidised dimer (sometimes a doublet) as well as the increasing concentrations of catalase. Proteins were reduced using 500 mM DTT for 30 minutes (lane A in all gels), yet oxidised dimer bands can be seen in all gels. See **Section 7.10.2** for more details on experimental set up. Briefly, 5 µM H_2O_2 and 5 µM HsPrx3 were used for the catalase reactions. Assay buffer composed of 20 mM HEPES (pH 8.0), 150 mM NaCl was freshly made and purged with argon or nitrogen gas before each experiment. The concentration of catalase is varied from 0, 0.2, 0.4, 0.8, 1 and 2 µM. Both wild-type HsPrx3 and S78C HsPrx3 react in the range of 10^7 $M^{-1}s^{-1}$ as interpreted visually by the intensity of bands on the gel (that is at 2 µM, human catalase can out compete both proteins to about 50% of wild-type protein or S78C mutein). S75E mutein, on the other hand is completely out-competed by human catalase, indicating the slower rate of reaction for this dimer mutant.

4.5.3 The SDS-PAGE assay for slow peroxidases, such as S75E HsPrx3

In contrast to the rates derived from the HRP competitive assay, the rate of reaction of the S75E mutein with H_2O_2, at ~10^4 $M^{-1}s^{-1}$, is three orders of magnitude slower than that of wild-type HsPrx3. In order to get a better estimate of the second order rate of reaction of S75E, time course experiments were performed while monitoring the decrease in reduced protein populations, which is indicated by the formation of a dimer protein band on a non-reducing SDS-PAGE gel (Nagy *et al*, 2011; **Section 7.10.3**). These results indicate S75E HsPrx3 has a rate of reaction of ~3.35 x 10^4 $M^{-1}s^{-1}$ (**Figure 4.19**), which is one order of magnitude slower than the reported rates for the dimer AhpC proteins (Parsonage *et al*, 2005).

Despite incubation of S75E HsPrx3 with DTT for 30 min, it can be seen on the SDS-PAGE gels that S75E muteins do not become fully reduced, with a population of ~10% oxidised dimers at 44 kDa. This strange, but reproducible, observation could account for the lack of crystallisation of this protein, as this dimer is a mixed population of oxidised and reduced protein. The SDS-PAGE assay takes into account this subpopulation of already oxidised dimers.

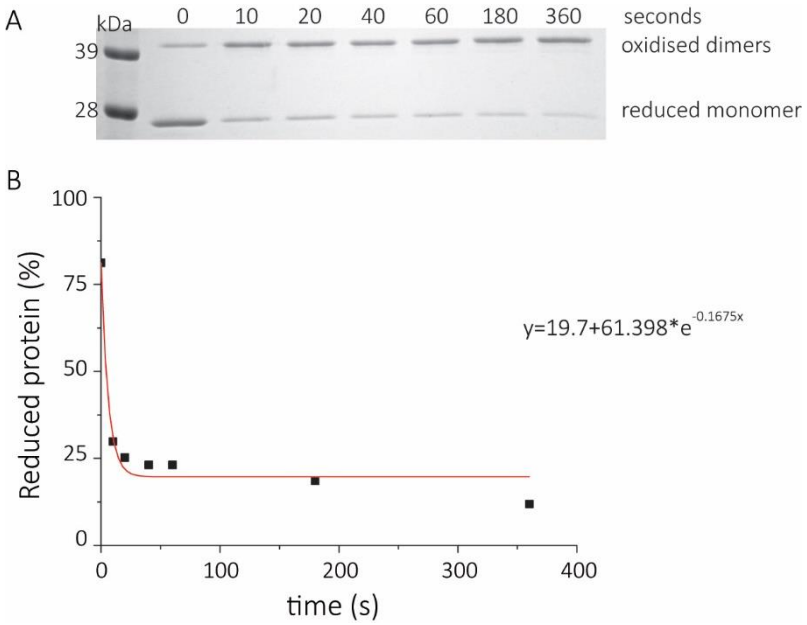

Figure 4.19: Rate of reaction of S75E HsPrx3

Rate of reaction of S75E mutein is slow enough that it can be monitored on the SDS-PAGE gel. To diminish the presence of stubborn oxidised dimers, S75E HsPrx3 was incubated with 10 mM DTT for 2 h, yet the oxidised dimers remain! Catalase was used in this experiment as a means to quench the reaction between S75E mutein and H_2O_2. Relative intensities of protein bands on SDS-PAGE gel (above) were calculated and percentage of reduced protein was plotted against time. Data points were fitted to an exponential equation and the pseudo-first order rate of reduction was corrected for by [H_2O_2] to give a rate of 4.35 x 10^4 $M^{-1}s^{-1}$. Ideally the exponential fit for this graph could do with more data points that covered the range of the curve.

4.5.4 Summarizing the variety of assays used and their results

These activity assay results for the various HsPrx3 muteins (summarized in **Table 4.5**) gives a good indication of their peroxidase activity towards H_2O_2 within the context of the wider Prx literature. It is important to note that the HRP competitive assay monitors the disappearance of H_2O_2 (Step 1 of the catalytic cycle, **Figure 4.1**), whereas the catalase and SDS-PAGE assays monitors the formation of the disulfide bond (Step 2 of the catalytic cycle). Other more comprehensive, newly developed assays can provide a more detailed overview of individual rates of reaction for each step along the entire catalytic cycle, such as the stopped flow fluorescence technique (Parsonage *et al*, 2015).

Table 4.5: Summary of reaction rates for HsPrx3 towards H_2O_2.

HsPrx3	Rate of reactivity ($M^{-1}s^{-1}$)
Wild-type	(4.7 ± 0.2) x 10^7 [a]
S78C – stabilised ring	(4.0 ± 0.5) x 10^7 [a]
S75E – dimer	3.35 x 10^4 [b]

[a] results from the HRP competitive assay

[b] results derived from the SDS-PAGE assay with H_2O_2

4.6 Discussion

4.6.1 Evolutionary advantages of oligomerisation: why would you put a ring on it?

The formation of a dodecameric ring is key for maximal peroxidase activity of HsPrx3 towards H_2O_2. The dimer-dimer interactions that form the ring, serve to stabilise a loop that connects to the active site, similar to what was shown with StAhpC (Parsonage *et al*, 2005). In the case of HsPrx3, there is no significant increase in peroxidase activity observed for the stabilised ring mutein, S78C, compared with the wild-type HsPrx3 (Table 4.5), as detected by both the HRP competitive assay and the catalase assay. In contrast, the dimeric S75E mutein is three orders of magnitude less active towards H_2O_2, compared with the wild-type HsPrx3. This demonstrates the importance of protein oligomerisation in conferring HsPrx3 with greater sensitivity for the reduction of its substrate, H_2O_2, enabling it to perform its diverse cellular functions as the minder of the mitochondrial redox landscape.

Interestingly, the dimeric PrxQ from *Xylella fastidiosa*, can also react with H_2O_2 at a similar rate of 10^7 $M^{-1}s^{-1}$, indicating that ringed structures are not necessary in order for the high reaction rates with H_2O_2, but rather a fully folded active site. Nor does switching from ring formations to dimeric species required for optimal activity, as observed in the 2-Cys Prx, human Prx4 (HsPrx4), where the stabilised ring remains as rings even after reacting with H_2O_2 at 2 x 10^7 $M^{-1}s^{-1}$ (Wang *et al*, 2012). Therefore it is unknown how quaternary structure switching from reduced ring to oxidised dimers is physiologically relevant, but it is tempting to hypothesise that this switching behaviour could be crucial for the other currently unknown functions of these 2-Cys Prxs in a wider cellular context, beyond their peroxidase function. This is especially relevant in eukaryotes where Prxs control levels of H_2O_2, which is not just a detrimental oxidant, but also an important signalling molecule for cellular processes (see Section 1.4.2).

Quaternary structural changes could also transiently reveal binding sites for other proteins. As oxidised dimers, it was reasoned that Prx active sites are more accessible for recycling enzymes, such as thioredoxin (Wood *et al*, 2003a). It is curious that the rate of reaction of S75E muteins with H_2O_2 occurs at ~10^4 $M^{-1}s^{-1}$, making this peroxidase slower than the predicted recycling rates of thioredoxin, at 10^6 $M^{-1}s^{-1}$ (Cox *et al*, 2010). The partial uncoiling of the α2 helix, observed in response to other chemical stressors, has also revealed binding sites for other proteins. For instance, the crystal structure of HsPrx1 bound to sulfiredoxin showed local unwinding of the α2

helix exposing the Cys_P to the sulfiredoxin active site (Jonsson *et al*, 2009). Currently, there have been very few studies for binding partners of Prxs, in general, and especially in the context of quaternary structural switching. The dimeric S75E HsPrx3 and stabilised S78C HsPrx3 rings could be suitable protein candidates used to probe protein associations of HsPrx3, especially *in vivo*.

In certain Prxs, protein concentration plays a critical role in protein oligomerisation, such as for the formation of the decameric rings of AhpC. Reduced enzyme was decameric, whereas disulfide bonded dimers were dimers at low concentration but decamers at high concentration (Wood *et al*, 2002). The HsPrx3 concentrations used within the HRP competitive assay range from being 12-100 fold less than the expected cellular concentrations (125 µM HsPrx3 in the mitochondria – Cox *et al*, 2009a). However, the AUC results sit within this lower protein concentration range, thus giving an insight into the oligomeric states of each protein. Concentration-dependent oligomerisation has not been investigated in-depth, and can be further explored for influencing ring formation. Especially for S75E, there seems to occasionally be a tetrameric species at higher concentrations >45 µM, whereas cleaved S78C also seems to spontaneously stack into double rings on the SEC-SLS.

4.6.2 Mixed population of hard-to-reduce dimer: ideas for diffractive crystals

The S75E HsPrx3 mutein is folded and has a solution quaternary structure analogous to that of a dimeric wild-type HsPrx3 (Section 4.3). With the understanding that the dimer-dimer interface has been disrupted, it is possible to imagine the active site becoming destabilised or more flexible, preventing fast substrate binding, However, a high resolution structure of S75E HsPrx3 is required to analyse any changes to the precise molecular interactions that result from the mutation, which could be responsible for its lowered, but still moderate, activity towards H_2O_2.

In all S75E HsPrx3 protein preparations, there is a small subpopulation of non-reducible dimers often observed as a 50 kDa protein band on a reducing SDS-PAGE gel (such as in Figure 4.3). This heterogeneous mix of oxidised and reduced protein could be the underlying cause for the complications in growing protein crystals. Other Prxs have also been reported to be difficult to reduce, and cannot be reduced by the reductants, such as DTT or TCEP, but only by using thioredoxin (Horta *et al*, 2010; Winterbourn *et al*, 2016). Using thioredoxin could also be a means to successfully reduce S75E HsPrx3 for future experiments, such as X-ray crystallography. Without a higher resolution structure of this protein, it is difficult to rule out whether the S75E mutation

has destabilised the overall protein structure in some way to cause it not to reduce. Conversely, in order to create a homogenous population of protein, S75E HsPrx3 could also be systematically oxidised prior to crystallisation. It is tempting to speculate that the S75E mutein crystals, which took 12 months to appear, were perhaps only able to grow due to the slow oxidation of the protein population over time.

At protein concentrations higher than 45 µM, a small population of S75E mutein dimers further associate as observed in both AUC and SEC-SLS. Although, yet to be definitively examined, it is unlikely further dimer-dimer associations occur via the A interface due to the charge-charge repulsion introduced by the glutamic acid. Instead, it is exciting to speculate that the dimer-dimer associations may be occurring via a different interface, such as the one which initiates catenane formation as those observed in BtPrx3 protein (Cao *et al*, 2005). Mutations of key residues at this putative interface would be required to fully investigate this idea.

Curiously, the lower reactivity of S75E HsPrx3 towards H_2O_2 occurs within the same range as several other dimeric Prxs, which is a testament to the well conserved peroxidatic active site within the Prx superfamily. As covered in Section 1.4.1, ancestral Prx subfamilies contain proteins that dimerise through the A interface, and most exhibit lowered rates of reaction towards H_2O_2 that range from 10^4-10^5 $M^{-1}s^{-1}$ (Perkins *et al*, 2015). While most of these Prxs are confined to bacterial and archaeal hosts, the Prx5 subfamily can also be found in mammalian systems – an example of which is human Prx5 (HsPrx5), which is also localised to the mitochondria. HsPrx5 has been found to preferentially decompose peroxynitrite at 10^6-10^7 $M^{-1}s^{-1}$, and also reacts with H_2O_2 at 10^5 $M^{-1}s^{-1}$ (Knoops *et al*, 2007). HsPrx3 is also known to react with other hydroperoxides, but at a much lower rate (Peskin *et al*, 2010), perhaps, now that the conformational changes of the S75E mutein is no longer constricted by adjacent dimers, it would be interesting to test its ability to react with other organic hydroperoxides.

4.6.3 Cysteine-stabilised phenylalanine gate is key for maintenance of the ring form in certain Prxs

The AUC experiments demonstrate that S78C HsPrx3 is a stabilised ring in non-reducing conditions, when wild-type HsPrx3 rings dissociate. It is striking how a single point mutation to introduce the cysteine residue can have such a profound effect on the quaternary structure of HsPrx3. Although it is one of the least abundant, cysteines are also one of the most highly conserved residues within functional sites of proteins (Marino *et al*, 2010). There is a strong selective pressure to keep cysteines buried as they not well tolerated on solvent exposed surfaces, and due to this, many buried cysteines are classified as hydrophobic (Poole, 2015). Cysteine residues have a large van der Waals radius and are more hydrophobic than serine residues, which could lead to tighter associations at the A interface (Lee *et al*, 2007). Therefore, the properties of cysteine residues lends themselves towards stabilising protein-protein interactions.

Alternatively, the stabilisation of flexible loop regions at the dimer-dimer interface can also act to promote ring formation (Morais *et al*, 2015). Upon examining the crystal structure of S78C HsPrx3, there is a notable shift in the surrounding residues of the A interface, which may contribute to the resulting stabilisation of HsPrx3 ring structure. It is revealed that the C78 residue stabilises the movements of the F43 sidechain, which is part of loop that connects to the active site (Figure 4.12 A and 4.13 C). C78 holds the aryl ring of F43 over the indolic ring of W82 at a distance of 4.49 Å, enabling potential π- π interactions to occur. The stabilisation of this loop region connected to the active site prevents large conformational changes that cause the dodecameric ring to dissociate.

These large conformational changes are observed in a similar scenario, where a cysteine residue stabilises the A interface for another typical 2-Cys Prx, human Prx1 (HsPrx1). HsPrx1 has a conserved cysteine residue (C83) at a homologous position to the S78 residue in HsPrx3, which confers ring stabilisation in non-reducing buffers (Figure 5 in Lee *et al*, 2007). Much like in the case of S78C HsPrx3, the C83 residues do not form a disulfide bond between the equivalent C83 on the adjacent dimer (Matsumura *et al*, 2008), instead the interface is stabilised by hydrophobic and van der Waals forces. The stabilisation of the equivalent phenylalanine, F48, is observed, along with a fully folded active site, in all ten monomers of the crystal structure of *Rattus norvegicus* Prx1 (RtPrx1) (also known as heme-binding protein 23 (HBP23); PDB 2z9s; Matsumura *et al*, 2008). The mutation of C83 into a serine (C83S Prx1) disrupts the decameric ring stability, and the region containing F48 shows large conformational changes; this is observed in both dimeric crystal structures available of RtPrx1 (PDB: 1QQ2; Hirotsu *et al*, 1999) and HsPrx1 (PDB: 4XCS; Cho *et al*,

2015). These conformational changes are striking, with the tryptophan W87 (equivalent to W82 in HsPrx3) completely displacing the F48 residue as the active site is unfurled (**Figure 4.20**). This altered arrangement, along with similar observations in the HsPrx3 crystal structures, supports a new hypothesis that ring destabilisation begins with a locally unfolded active site whereby a disulfide bond can form, but it is the further unwinding of the α2 helix as well as the loop connecting with α2 that actually pries the dimers apart.

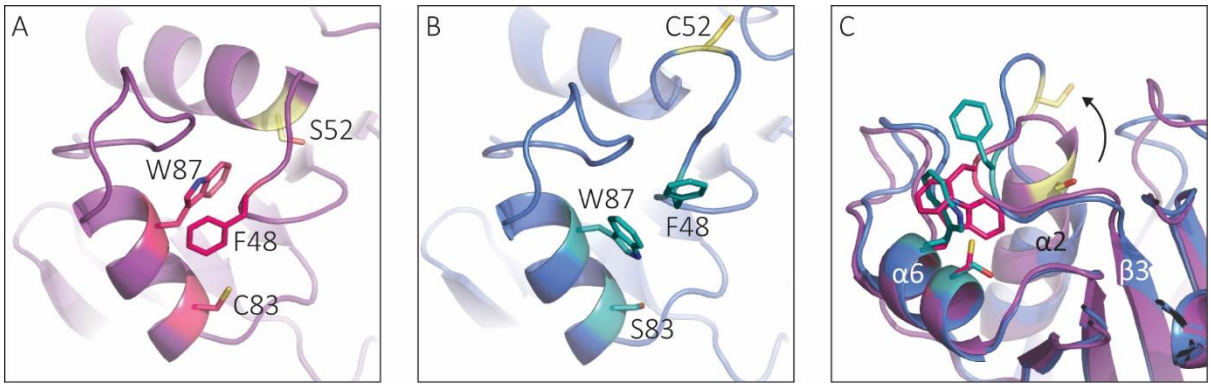

Figure 4.20: A interface of HsPrx1 proteins.
(**A**) C52S RtPrx1 forms a decameric ring (Matsumura *et al*, 2008) and the residues within the A interface are highlighted: the mutated serine (yellow) and key residues (pink). The cysteine residue acts to stabilise F48 and W87. This is monomer A, but is representative of all chains in the dodecameric ring (PDB: 2Z9S). (**B**) The equivalent view on the dimeric C83S RtPrx1 (Hirotsu *et al*, 1999). The residues F48 and W87 are both flipped out allowing for an extension of the active site loop (**C**), which would hinder decameric ring formation.

The idea that ring destabilisation can occur in two steps, is supported by several crystal structures of 2-Cys Prxs adopting decameric or dodecameric ring forms, despite having locally unfolded active sites with a disulfide bond between the Cys_P and Cys_R (**Figure 4.21**; Kitano *et al*, 2005; Parsonage *et al*, 2005; Cao *et al*, 2015). The crowded environs of crystallisation would influence the equilibrium between ring and dimeric quaternary structures to favour ring formation, even if they do not appear to do so in solution. An example of this is the BtPrx3 crystal structure where certain oxidised dimers, that normally would dissociate in solution, are assembled as dodecameric rings (PDB: 3MH4; Cao *et al*, 2015). The introduction of the cysteine in the S78C HsPrx3 mutein stabilises this region without the requirement for molecular crowding in crystal conditions. Therefore S78C HsPrx3 may remain as stabilised rings in solution even after disulfide bonds are introduced; this is supported by the catalase assay results (**Figure 4.18**) as well as the AUC analysis (**Figure 4.16**).

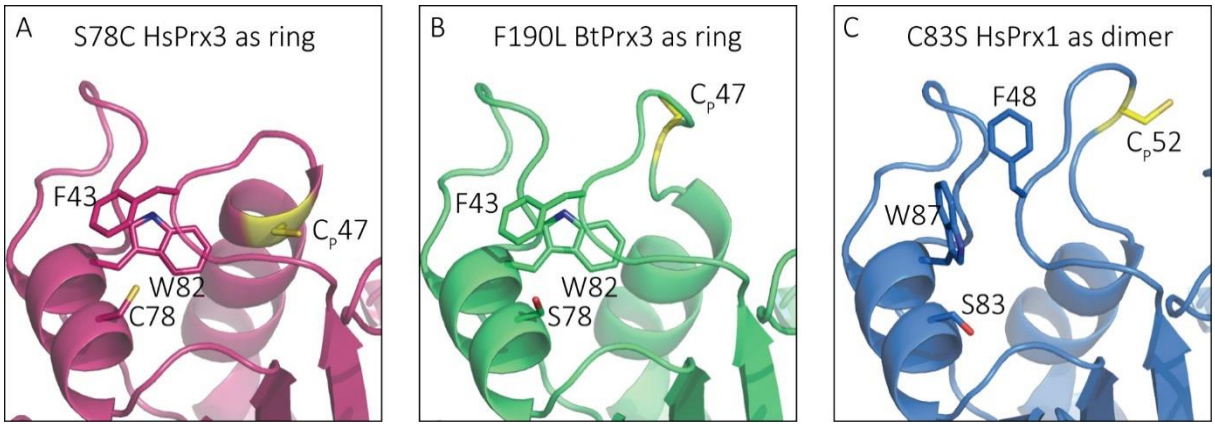

Figure 4.21: The possible mechanism by which ring stabilisation and destabilisation occurs
The peroxidatic cysteine (C_P, a yellow stick) is a reference to highlight the active site local unfolding (**B**), and further unfolding (**C**) that is associated with complete ring dissociation. The A interface of S78C HsPrx3 (**A**) with C78 holding F43 in place over the W82 residue (PDB: 5UXC). A similar interaction is observed at the A interface of F190L BtPrx3 (**B**; PDB: 4MH3; Parsonage *et al*, 2015) where the active site is also locally unfolded with C_P47 disulfide bonded with Cys_R (not shown). The A interface of the C83S HsPrx1 (**C**; PDB: 1QQ2; Hirotsu *et al*, 1999) show the flipped side chains of W87 and F48 as well as the complete unwinding of active site loops, where C_P52 is disulfide bonded with Cys_R (not shown).

Of course, to test the importance of both phenylalanine and tryptophan residues for loop region stabilisation, point mutations where the aromatic side chains are removed, such as replacing these residues systematically with alanine, must be performed on the S78C HsPrx3. On the other hand, if the cysteines residues act to simply form hydrophobic interactions that force the A interface together, it would be interesting to mutate S78 to hydrophobic residue, such as threonine, to test this idea. A rationale for this could be that in HsPrx4, the naturally stable decameric 2-Cys Prx, there are threonine residues (T155) in this position that interact together to form hydrophobic pocket (Cao *et al*, 2011).

4.7 Summary

With just one point mutation, the switches in quaternary structure, between dimer and rings, can be removed, demonstrating the ease at which HsPrx3 protein tectons can be manipulated to create or limit assemblies. The quaternary structures of two muteins were examined using solution characterisation techniques such as SAXS, SEC-SLS and AUC, to reveal the creation of an obligate dimer (S75E HsPrx3) and a stabilised ring (S78C HsPrx3). Activity assays were used to probe the reactivity of these proteins towards H_2O_2.

The circular dichroism spectrum of S75E HsPrx3 protein correlated with that of a folded protein, and the SAXS scattering plot was representative of a dimeric HsPrx3 species. Surprisingly, this obligate dimer was shown to be minimally active towards H_2O_2, implying that the formation of the A interface is not critical, but acts to stabilises the active site to allow for the fast reaction of Cys_P with H_2O_2. The fact that peroxidase activity is a feature of both dimeric and ring structures suggests that oligomerisation could also have other yet unknown biological function, such as the accessibility of different protein binding partners to HsPrx3 during these different oligomeric states.

The crystal structure of S78C HsPrx3 revealed a non-covalently linked toroid structure with an intriguing phenylalanine-tryptophan gate which stabilises the A interface. The activity of this protein is comparable to wild-type HsPrx3, which is in contrast to the ring stabilisation of His_6-tagged HsPrx3, suggesting that there are two mechanisms for ring stabilisation at play. The creation of S78C HsPrx3 has resulted in more stable, non-covalently linked tectons with which future functional devices can be formed from.

Chapter 5: Towards functionalisable peroxiredoxin tectons

5.1 Introduction

5.1.1 Functionalised protein nanotubes in nanotechnology

The inherent biocompatibility and ease of creating proteins that self-assemble into nanotubes makes them promising components of future nanodevices (Section 1.3.3.4). The creation of large structures enables a greater surface area for functionalisation. The functionalisation of these various types of nanotubes exploit both internal and external surfaces and often fall into two categories: either with the biomineralisation of metal ions to create nanowires (Yemini *et al*, 2004), or by attaching functional moieties onto the nanotube scaffold (Miller *et al*, 2007; Nam *et al*, 2006). Being able to control tube lengths enables the generation of templates of certain lengths and this can be engineered into protein sequences with the addition of cysteine residues (Miranda *et al*, 2009; Ballister *et al*, 2008). Future applications of these nanodevices are far reaching and range from microelectronics (Nam *et al*, 2006) to sensors (Kong *et al*, 2000).

Peroxiredoxins (Prxs) have both redox-sensitive control of toroid self-assembly, as well as pH-sensitive control of toroid stacking, making these proteins uniquely versatile scaffolds on which new functionalities can be engineered (Phillips, 2014; Phillips *et al*, 2014). The creation of Prx-based smart materials harnesses the desirable properties of these protein nanotubes for novel applications in nanotechnology.

5.1.2 Various reactions of functionalised protein tectons

Some reliable methods for immobilisation of biomolecules onto solid surfaces include: adsorption, direct covalent attachment, or non-covalent interaction between a cargo and an appropriately derivatised surface (Putzbach and Ronkainen, 2013). These techniques can be limited by the lack of control of molecular orientation between two reactants, with deleterious results arising if reactions occur near or at protein active sites, or reaction conditions causing denaturation of proteins (Moses and Moorhouse, 2007). Nonetheless, the reactive chemistries of amino acid

sidechains that cover the surface of self-assembling protein structures provide a versatile foundation for functionalising these architectures for nanotechnological applications. Widely used methods to functionalise protein surfaces include engineering amino acid tags onto the ends of the protein sequences (Section 5.1.2.1), or exploiting naturally available reactive amino acids, such as lysine and cysteine residues, and engineering these strategically onto the protein surface (Section 5.1.2.2). Alternatively, synthetic amino acids with novel chemistries can be incorporated into the protein sequence (Section 5.1.2.3).

5.1.2.1 N- and C-terminal attachments

N- and C-terminal attachments are usually engineered peptide tags that are able to bind to metal ions, such as poly-histidine tags (Ardini *et al*, 2014), or those that are recognised by specific enzymes, such as sortase (Witte *et al*, 2013). Occasionally these peptide additions can affect protein expression by inadvertently disrupting protein folding (Rumlová *et al*, 2001; Fonda *et al*, 2002), as well as the quaternary structure self-assembly of the modified protein, such as described in Section 2.1.3.4. Poly-histidine tags (His_6-tags) coordinate metal ions and this non-covalent attachment has been routinely exploited for recombinant protein purification (Nilsson *et al*, 1997). The metal coordination ability of His_6-tags enables them to bind to nanoparticle cargoes, e.g. His_6-tagged SmPrx1 proteins were able to coordinate gold nanoparticles to form 'nano-peapods' as a first step towards creating protein-blueprinted nanowires (Ardini *et al*, 2014). In the case of HsPrx3, the N- and C-termini protrude in useful locations away from the main protein folds that dictate its quaternary structure, with the N-termini located inside the ring and the C-termini projects outwards away from the ring. This increases the probability that Prx scaffolds are amenable to derivatisation.

5.1.2.2 Bioconjugation through surface lysine, cysteine, and tyrosine residues

Similar to the addition of tags, exploiting pre-existing amino acid chemistries, such as those of lysine, cysteine or tyrosine residues, is an easy and reliable means to functionalise a protein nanostructure (Figure 5.1; Thordarson *et al*, 2006). In particular, the reactive primary amine sidechain of lysine residues can react selectively with a variety of moieties. Protein nanowires, made from human serum albumin, were functionalised using lysine residues that react with an NHS-biotin (Omichi *et al*, 2014). These attached biotins were then bound to avidin proteins allowing for control of nanowire size, and also enabled the assembly of an array of proteins onto the surface of the protein nanowires. The positions of the lysine residues were not specific, resulting in a coating of this nanowire with other proteins as a proof of concept to show these

nanowires are versatile platforms for surface functionalisation. Both, the wide range of reactions available and their infrequent appearance on protein surfaces, make cysteine residues appealing canonical amino acids for bioconjugation reactions that can be synthesised onto proteins (Poole, 2015). Utilising cysteine chemistry is a less viable option for functionalising HsPrx3 proteins, however, due to the crucial active site cysteine residues that control HsPrx3 quaternary structure.

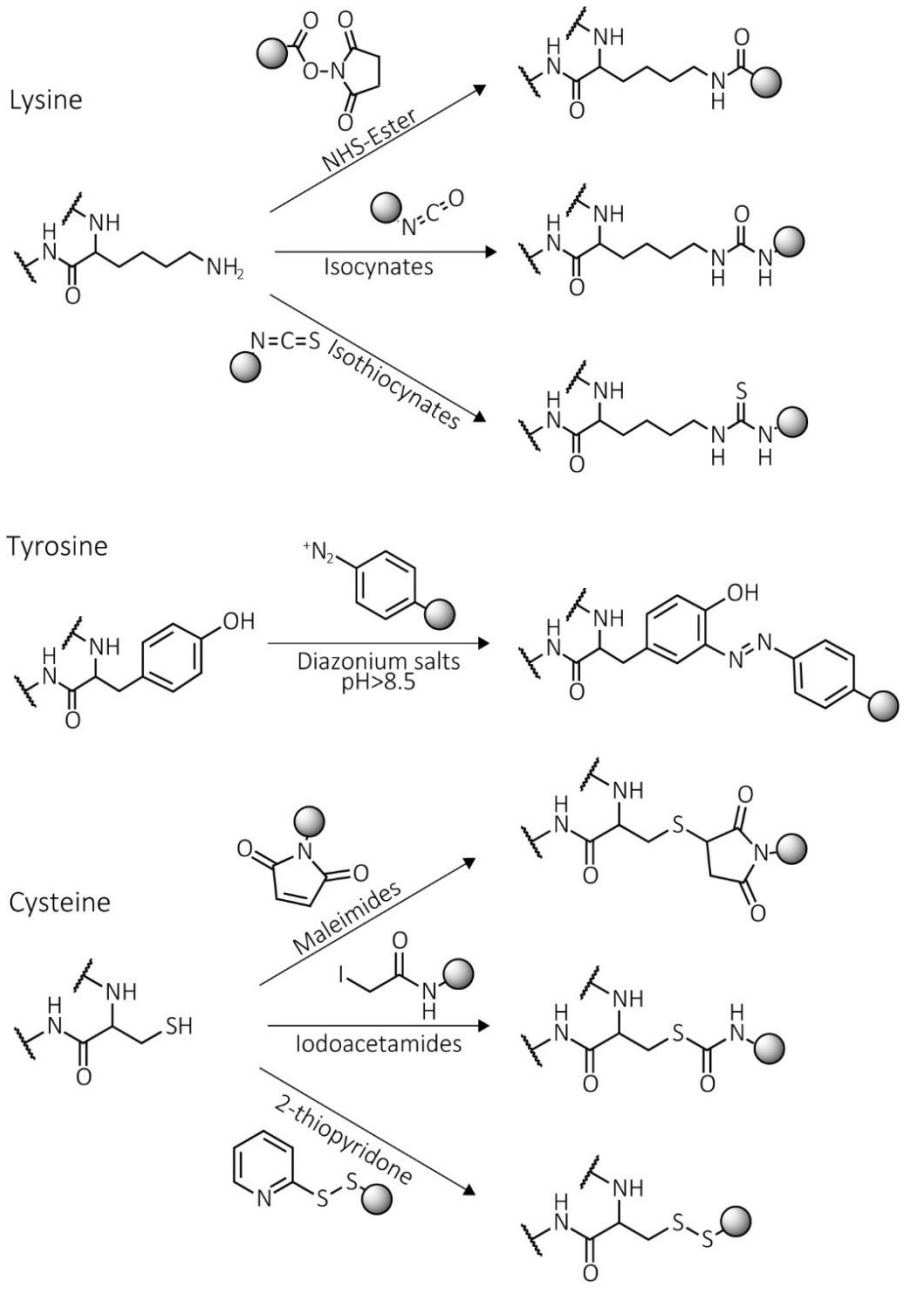

Figure 5.1: Bioconjugation reactions of lysine, tyrosine and cysteine surface residues
Various bioconjugation reactions can target a variety of moieties (grey balls) onto certain amino acid residues, such as lysine, tyrosine and cysteine residues, present on protein surfaces (left). Attachable moieties can vary in their properties, enabling the attachment of new function onto protein surfaces.

5.1.2.3 Click chemistry: introduction of azide groups onto protein surfaces

Another means of attaching functionalities to protein structures is through introducing covalent interactions created by click chemistry (Dieterich and Link, 2009). This is where highly energetic small unit reactants are able to generate products in a reliable and selective process and can be used to achieve chemo-selective ligations between a reactive unit on a cargo and its reaction partner, whether it be a modified or synthetic amino acid, located on a protein surface. In theory, these orientation-specific reactions enable precise spatial control of each cargo attached onto the protein surface (Best, 2009).

Canonical amino acids, such as lysine residues, on protein surfaces have been modified to enable click chemistry reactions (Wang *et al*, 2003). The surface lysine residues of cowpea mosaic virus particles were modified into reactive alkynes that were able to perform click chemistry reactions with azide-coupled folic acid-PEG conjugates, thereby permitting these modified nano-cages to be directed towards tumour cells (Destito *et al*, 2007). Again, this process of modifying canonical amino acids depends on their location within a protein sequence, with lysine residues being abundant surface residues (Baud and Karlin, 1999). The specific location of reactive surface residues, therefore, must be engineered into the protein sequence without causing disruption of folding or quaternary structure assembly.

The use of synthetic amino acids, or unnatural amino acids (UAAs), provide a specific means to directly functionalise a protein surface. The techniques of incorporating UAAs have been developed for protein-protein interactions and can be performed in a variety of protein expression systems to be explored in Section 5.1.3. UAAs have been used to bio-orthogonally label proteins to probe subtle protein-protein interactions that occur within a cell (Dieterich *et al*, 2006). It has also been used as an *in vivo* tool for adding small fluorescent tags onto proteins of interest or cells themselves to monitor their migration within a system (Yoon *et al*, 2016). Bio-orthogonal labelling has vastly expanded in the last decade with new synthetic amino acids as well as improved methods for incorporating them into the protein.

There are multiple methods to bio-orthogonally label proteins and each varies in its range of reaction rates and catalytic requirements. There have been many reviews on this topic (Lang and Chin, 2014, Neumann, 2012) revealing that the most common reactive species that can undergo multiple bio-orthogonal reactions is the azide group (Figure 5.2). In fact, the paradigm of all click reactions is the Cu(I)-catalysed cycloaddition between azides and terminal alkyne (called CuAAC). An alternative is to use strain-promoted cyclooctyne derivatives that react with azides (called

SPAAC). Azides are also able to undergo Staudinger ligations with phosphines, which is an oxidation-sensitive reaction. The most reactive reactions for azides start with CuAAC at ~10^2 $M^{-1}s^{-1}$, then SPAAC at ~10^{-1} $M^{-1}s^{-1}$, followed by the Staudinger ligation at ~10^{-1} $M^{-1}s^{-1}$.

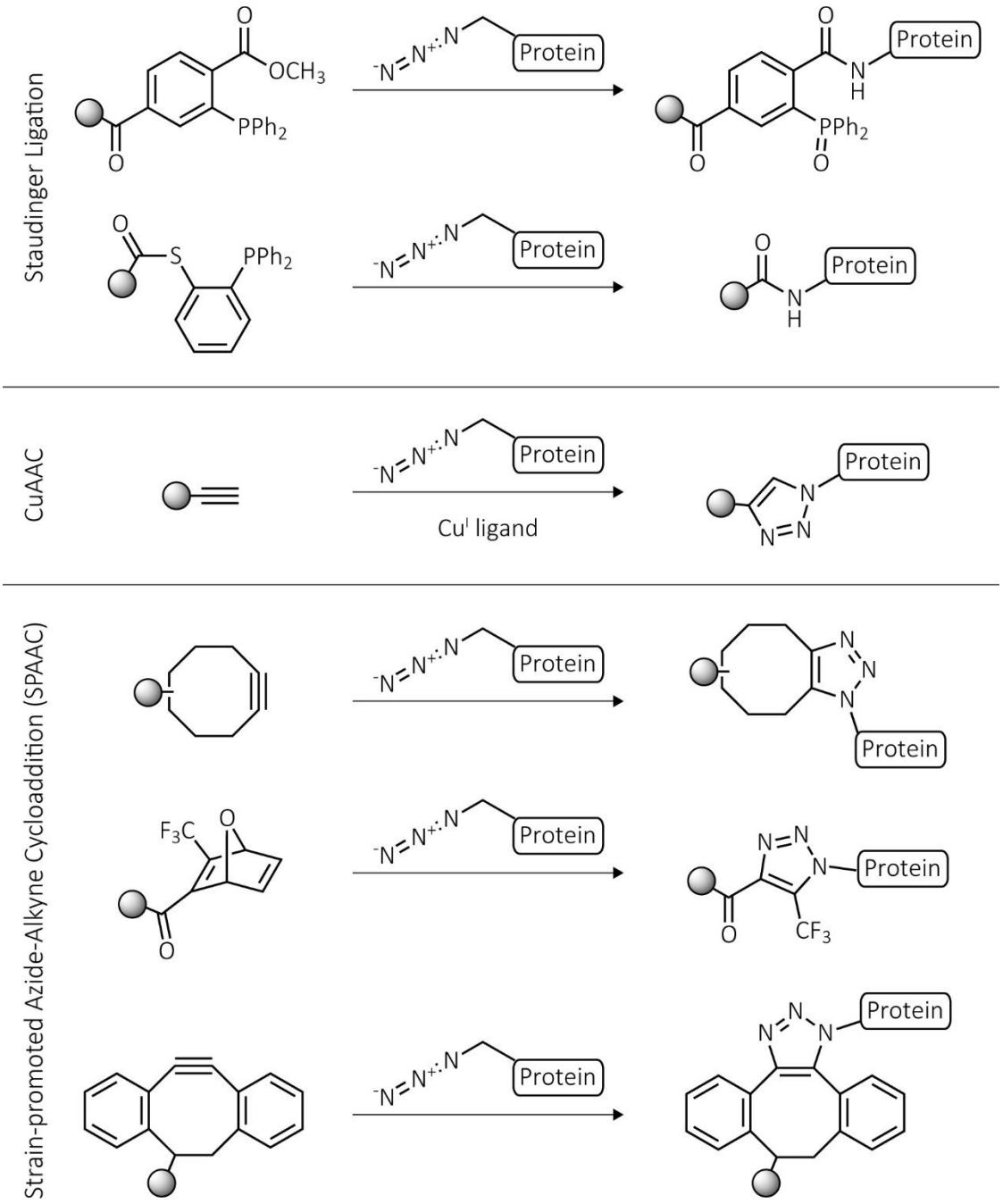

Figure 5.2: Click reactions with azides

Azide groups are able to react with a variety of molecules, some of which are shown here. They fall into three classes of reactions: Staudinger ligations, Copper-catalysed azide-alkyne cycloaddition (CuAAC) and strain-promoted azide-alkyne cycloaddition (SPAAC). Attachable moieties are represented as grey balls. Diagram is adapted from van Berkel *et al*, 2011.

Another property of azide groups is their photoreactivity, where UV light can activate the azide group onto a highly reactive nitrene that is able to react with a variety of compounds from water to the amide backbone of proteins (Scheme 11.29 in Gritsan and Platz, 2010). This has been used as a means to probe intra-protein interactions *in vivo* (Wang *et al*, 2014; Shao *et al*, 2015; Reddington *et al*, 2015).

In this thesis, azides were chosen as the click reactive unit of interest, not only for their capacity to react with numerous click partners, but also for their biocompatibility with biological samples. Incorporating azide groups onto HsPrx3 protein surfaces will expand the functionalisable potential of this tecton.

5.1.3 Creating azide-functionalised protein tectons

Biomolecules - such as proteins, nucleic acids, lipids and glycans - can be modified with small clickable units (Sletten and Bertozzi, 2009) which can covalently ligate with various complementary molecules tagged with functional units such as fluorophores, ligands, or affinity tags (Moses *et al*, 2007). In this case, proteins are the target biomolecule and ways to attach clickable units onto proteins to generate functionalisable tectons include:

1) Modifying existing canonical amino acids to act as clickable units (Section 5.1.2.2 – where the moiety in Figure 5.1 would be an azide group). However, this technique relies on amino acids already present in the protein sequence to react with clickable molecules (Thordarson *et al*, 2006).

2) Clickable units can be incorporated using enzymes, such as sortase, to modify engineered peptide tags (Witte *et al*, 2013). This technique is more specific but is restricted to modifications at the C- or N-terminal ends of proteins.

3) Incorporating UAAs that contain a clickable moiety into protein sequences. The variety of methods to do this often involve fooling the cellular protein expression machinery to make the modified protein, including: *in vitro* protein expression (Smolskaya *et al*, 2013), and *in vivo* protein expression in mammalian cells, yeast, insect cells, and *E. coli* (Berg *et al*, 2014; Lancia *et al*, 2014). Specific UAA incorporation into protein sequences offers the greatest flexibility for engineered functionalisation of protein tectons; however, not all methods of incorporation were created equal. The following explores why this might be the case.

5.1.4 Fooling *E. coli* protein expression machinery to create modified protein tectons

As covered in Section 1.3.2.1, *E. coli* protein translation is orchestrated by a variety of protein complexes that ensure amino acids are assembled in the correct order, according to a DNA blueprint, to create a peptide chain that will eventually fold into functional structures. This complex system, having evolved over millions of years, has been rewired in order to incorporate UAAs into proteins (Alberts *et al*, 2002).

5.1.4.1 Auxotrophic bacterial strains: Substituting pre-existing amino acids with UAA

Auxotrophic bacteria for certain amino acids have been used for decades to incorporation of UAAs, such as selenomethionine, for introducing heavy atoms into protein crystals (Budisa *et al*, 1995). This technique replaces the original amino acid with a similar UAA to globally modify the proteins produced by *E. coli*. As a result, yields are small and the UAAs that can be utilised are limited to those that are very similar to the original amino acid (Budisa, 2004). One of the major advantages of the global replacement of an amino acid is the ease of incorporating multiple UAAs into the same protein (Merkel *et al*, 2010). Methionine analogues, L-azidohomoalanin (AHA) and L-homopropargylglycine (HPG), have been incorporated successfully into protein N-termini using auxotrophic *E. coli* deficient in methionine, M15MA (Wang *et al*, 2008).

5.1.4.2 Expanding the genetic code: orthogonal tRNA synthetases and tRNA

The most robust and well-studied technique of incorporating UAAs is through the addition of orthogonal translational machinery that recognises the UAA and incorporates this into a degenerate stop codon in an *E. coli* expression system. These orthogonal methods have also been developed beyond their *E. coli* origins, to other *in vivo* expression systems such as mammalian cells (Schmied *et al*, 2014), yeast (Shao *et al*, 2015) and *C. elegans* (Parrish *et al*, 2012).

The *E. coli* UAA incorporation methods will be the focus of this chapter, and the requirements are:

- Aminoacyl-tRNA synthetases that only aminoacylate desired tRNAs with the correct UAA;
- Unique tRNA-codon pairs that recognise an *E. coli* stop codon, usually the amber codon (*UAG* on an mRNA) as it rarely terminates an essential gene and is the least used stop codon in *E. coli* (~7 %) (Nakamura *et al*, 2010; Xie and Schultz, 2005);
- An UAA that is not a substrate for endogenous synthetases.

For UAA incorporation within *E. coli,* the most popular orthogonal tRNA/synthetase pairs originate from an archaea, *Methanococcus jannaschii*. In particular, the tyrosine residues of *M. jannaschii* are introduced at the *UAG* codon (Wang *et al*, 2001), and this has been exploited for the introduction of tyrosine-like UAAs into the amber codons of *E. coli* (Young *et al*, 2011). Directed evolution of these orthogonal tRNA/synthetase pairs within *E. coli* have increased the yields of recombinant proteins (Amiram *et al*, 2015; Ryu and Schultz, 2006; Chatterjee *et al*, 2013). These directed evolution experiments involve introducing random mutations to the orthogonal protein translation machinery. Inserting a stop codon in the middle of an essential gene (such as antibiotic resistance) ensures that gene expression must occur in order for full length protein production, which enables cells to survive a round of selection containing the antibiotic (Chin *et al*, 2002; Santoro *et al*, 2002).

There are many types of UAAs that can take part in click chemistry reactions, but a combination of commercially available products (p-azidophenylalanine) and well established methods guides this choice to use *E. coli* expression systems with orthogonal aminoacyl-tRNA synthetases (MjaaRS) and tRNA from *M. jannaischii* (Chatterjee *et al*, 2013). A promising method, chosen for its ease of integration into the current protein expression system, involves the use of a pUltra plasmid that encodes for orthogonal transitional machinery, as well as a pET protein expression vector both transformed inside BL21 (DE3) *E. coli* cells (Figure 5.3).

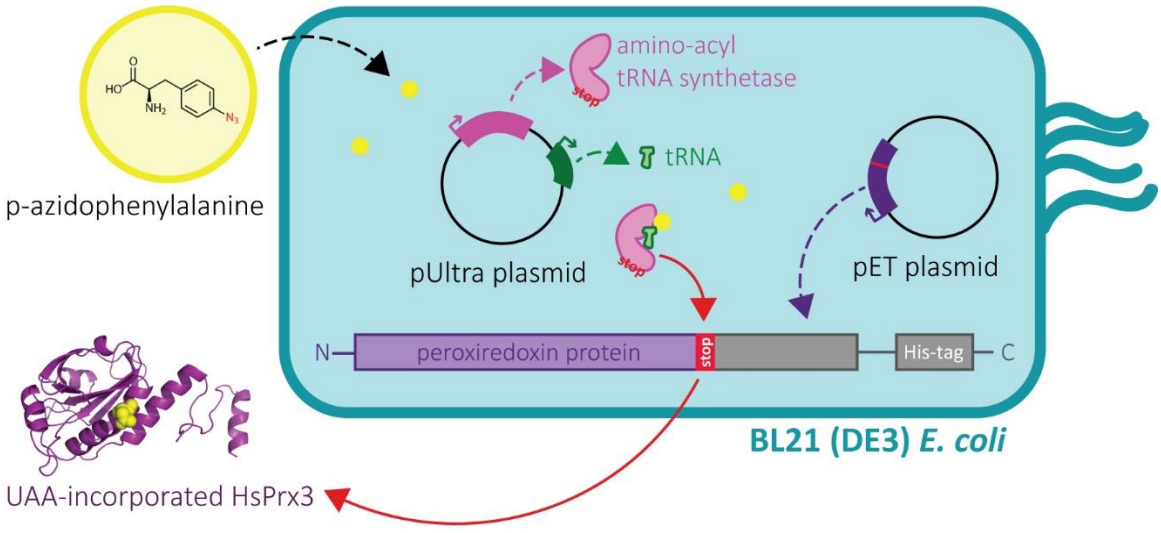

Figure 5.3: Using pUltra and pET plasmids to generate UAA incorporated proteins
A cartoon representation of the p-azidophenylalanine being incorporated into protein sequences using the *E. coli* expression system described in Chatterjee *et al*, 2013.

5.1.5 Chapter overview

HsPrx3 proteins can be manipulated to form several switchable nano-architectures. By incorporating UAAs into specific locations on HsPrx3 protein surfaces, hotspots for functionalisation via covalent attachments can be engineered to make these modified tectons even more appealing for nanotechnological applications.

The UAA, p-azidophenylalanine (pAzF), was chosen for its commercial availability and wealth of literature on methods for its incorporation into recombinant proteins expressed in *E. coli*. pUltra was designed from the available literature to include sequences that encode orthogonal tRNA synthetases and tRNA from *M. jannaschii* (Chatterjee *et al*, 2013, Guo *et al*, 2009, Chin *et al*, 2002). The MjaaRS/tRNA pair recognise pAzF and incorporates this UAA into a strategically placed amber stop codon with the protein sequence. Various UAA mutein constructs based on HsPrx3 with either C-terminal (pET11a) or N-terminal (pET28a) histidine tags were designed and explored as part of research towards creating functionalisable HsPrx3 tectons.

5.2 Making the pUltra plasmid

5.2.1 Plasmid re-design

At the time of this research, the pUltra plasmid was not commercially available so the plasmid design was based on literature from the Schultz group (Chatterjee *et al*, 2013, Guo *et al*, 2009, Chin *et al*, 2002). Epoch Lifesciences were employed to synthesise the pUltra plasmid described in Chatterjee *et al*, 2013; however, the resulting plasmid is not exactly the same as in this paper. These differences are explained below.

The pUltra plasmid (**Figure 5.4**) is based on a commercially available plasmid, pCDF-1b, which is compatible with *E. coli* BL21 (DE3) protein expression systems. pCDF-1b has an origin of expression, *CloDF13*, that causes the BL21 (DE3) host to produce this plasmid in high copy numbers (Stuitje *et al*, 1981; Camps, 2010). The high copy number plasmids, rather than low copy number plasmids, should in theory also result in more plasmid products synthesised (explained in **Section 5.1.4**). The expression of these plasmids are not intended to overwhelm the BL21 (DE3) cells, because it will disrupt normal cellular amber codon function (Chatterjee *et al*, 2013).

The pUltra plasmid encodes genes for orthogonal translation machinery derived from *M. jannaschii.* These include the genes of the MjaaRS (optimised for *E. coli* protein expression) and the corresponding tRNA pair, which were evolved for recognition of pAzF and its incorporation into the amber stop codon (Guo *et al*, 2009, Chin *et al*, 2002). The *tacI* promoter sequence and *rrnB* terminator sequence (t1) were incorporated either side of the MjaaRS gene (de Boer *et al*, 1983, Orosz *et al*, 1991). The *E. coli proK* promoter and terminator as well as the Fis binding site were incorporated either side of the $tRNA^{pAzF}_{CUA.}$ (Neidhardt, 1996).

The evolved MjaaRS protein sequence with evolved residues highlighted (Chin *et al*, 2002):

MDEFEMIKRNTSEIISEEELREVLKKDEKSATIGFEPSGKIHLGHYLQIK
KMIDLQNAGFDIIILLADLHAYLNQKGELDEIRKIGDYNKKVFEAMGLKA
KYVYGSNFQLDKDYTLNVYRLALKTTLKRARRSMELIAREDENPKVAEVI
YPIMQVNPLHYQGVDVAVGGMEQRKIHMLARELLPKKVVCIHNPVLTGLD
GEGKMSSSKGNFIAVDDSPEEIRAKIKKAYCPAGVVEGNPIMEIAKYFLE
YPLTIKRPEKFGGDLTVNSYEELESLFKNKELHPMRLKNAVAEELIKILE
PIRKRL

The DNA sequence for orthogonal tRNA chosen for the most efficient pAzF incorporation into amber stop codons (Guo *et al*, 2009):

CCCGCCTTAGTTCAG-AGGGCAGAACGGCGGACTCTAAATCCGCATGGCA

CGGGTTCAAATCCCGTAGGCGGGACCA

Both of these sequences, corresponding promotors and terminators, as well as part of the lacI repressor gene were synthesised as one synthetic construct (Epoch Lifesciences). This construct was then inserted into the *MluI* and *AvrII* restriction sites within pCDF-1b. The resulting pUltra plasmid, at 4590 base pairs (**Figure 5.4**), is 387 base pairs smaller than the one described in Chatterjee *et al*, 2013.

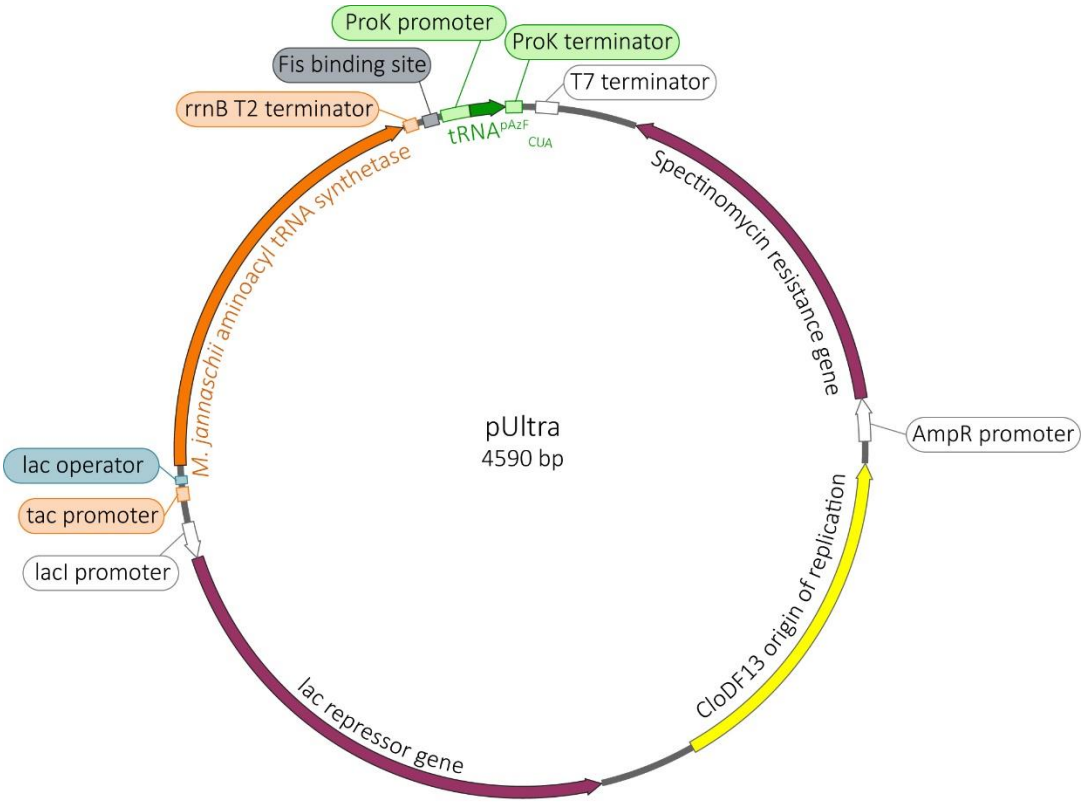

Figure 5.4: pUltra plasmid based on pCDF-1b
Open reading frames encoding the tRNA (green) and tRNA synthesase (orange) are on a plasmid with a spectinomycin resistance gene. Descriptions of various components of this plasmid can be found in the text. The plasmid design is based on Chatterjee *et al*, 2013.

5.2.2 Plasmid verification

The production of MjaaRS and corresponding tRNA were difficult to verify because expression of both gene products were not expected to be extraordinarily high. The presence of the tRNA was never directly verified. Control trial expressions using BugBuster were performed for MjaaRS (as per Section 7.3.1), and the resulting soluble and insoluble protein fractions were run on an SDS-PAGE gel (Figure 5.5). The appearance of bands ~30-35 kDa (indicated by arrows; Figure 5.5) could be indicative of MjaaRS expression. Direct verification of MjaaRS was not possible as antibodies for this particular protein were not available for Western blot analysis.

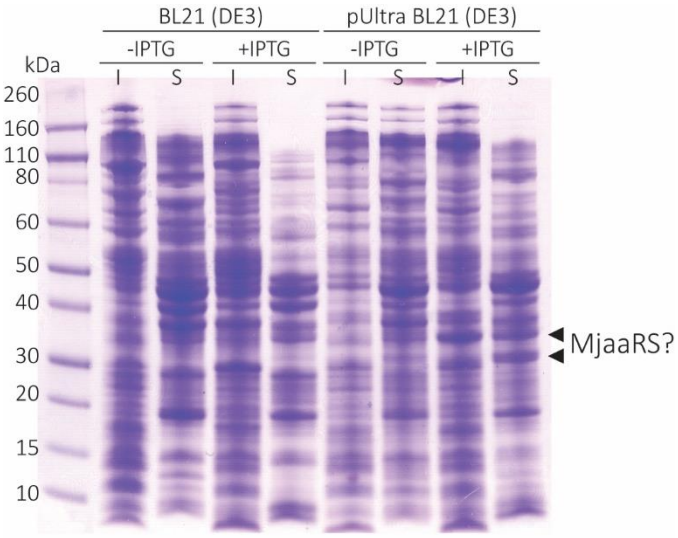

Figure 5.5: SDS-PAGE for trial expressions of pUltra plasmid versus BL21 (DE3)
A comparison of the total protein samples from BL21 (DE3) cells with and without the transformation of pUltra plasmid. Both insoluble (I) and soluble (S) fractions were run side-by-side from samples taken before and after protein expression induction (indicated as -IPTG and +IPTG, respectively). The appearance of different bands (indicated by triangles) at ~30-35 kDa could indicate the presences of MjaaRS protein, which has an expected MW of 34.8 kDa.

5.3 Unnatural amino acid muteins: design and strategy

5.3.1 Designing the functionalisable tecton: positions of UAA incorporation on protein surface

The amber stop codon (*tag*) was engineered to specific locations within the HsPrx3 gene sequence to target the orthogonal protein translation machinery for UAA incorporation at those sites. Aryl amino acids that resemble p-AzF, such as tyrosine and phenylalanine residues, on the HsPrx3 protein surface were chosen in order minimise any disturbances to the protein structure. The amino acid locations of these aryl amino acids can be visualised using the crystal structure (**Figure 5.6**). The resulting mutant protein constructs were called: Y10*tag*, Y160*tag* and F190*tag* HsPrx3.

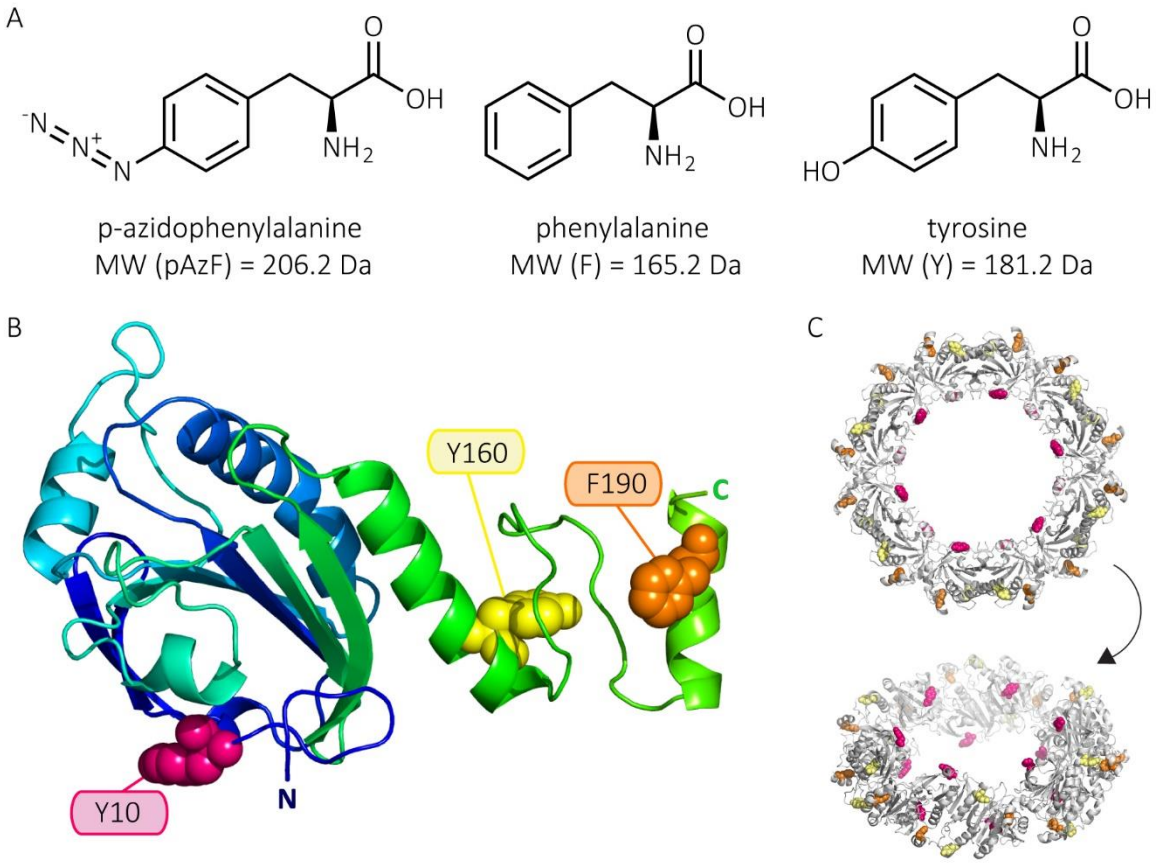

Figure 5.6: Inserting p-azidophenylalanine (pAzF) into HsPrx3
(**A**) A comparison of the structures of aryl amino acid residues: p-azidophenylalanine (pAzF), tyrosine (Y) and phenylalanine (F). (**B**) The locations of the aryl residues Y10, Y160 and F190 on the HsPrx3 monomer (PDB: 5JCG). The peptide backbone of the HsPrx3 monomer is represented as a cartoon with the N-terminus (blue) and C-terminus (green) highlighted on a colour gradient. (**C**) The locations of residues Y10, Y160 and F190 in relation to the HsPrx3 protein ring, with the same residue colouring as in (B).

5.3.2 Dissolving p-azidophenylalanine into growth media

Three methods for dissolving commercially available pAzF, a white powder, into a solution were tested and the resulting pH change of unbuffered growth media, LB, upon addition of dissolved pAzF was monitored (**Table 5.1**). 1 M NaOH was chosen as the preferred method of dissolving pAzF as the powder dissolved quickly (Lancia 2014, Berg 2014). The resulting minimal change to the pH of the growth media would mean *E. coli* cells would also not be stressed due to acidification when growing in LB (Sezonov *et al*, 2007). Growth of bacterial cultures to high density, such as those found in protein expression, acidifies surrounding media and can cause a switch in cellular protein expression of the bacteria to adapt to the acidic environment (Castanie-Cornet *et al*, 1999). Hence, buffered growth media, such as terrific broth or Magnificent Broth™, were used to avoid these issues and to achieve higher cell densities. In order to avoid photo-activating the azide group (Gritsan *et al*, 2010), all tubes containing pAzF were wrapped in aluminium foil and large flasks of media were kept away from windows.

Table 5.1: Solvents and dissolving methods of pAzF.

Dissolving method	Solubility of 1M pAzF	pH of LB (normally pH 7.0)
1 M NaOH[a]	✓✓	7.5
80% acetic acid[b]	✓	5.5
Sonication into LB	✓	7.0

[a] Berg 2014
[b] http://www.scbt.com/datasheet-289923.html
[a,b] first dissolved pAzF in solvent, then added to LB
✓ - incompletely dissolved, can still see some precipitates
✓✓ - completely dissolved

5.4 Rationale and design of UAA HsPrx3 C-terminal His_6-tagged proteins

5.4.1 Wild-type HsPrx3 C-terminal His_6-tag protein expression and purification

Expressing C-terminal His_6-tag proteins, with a strategically placed amber stop codon at the desired location for UAA incorporation, allowed for the easy selection of full length proteins with incorporated UAAs, as these would be the only amino acid sequences ending in a His_6-tag. However, the previously described wild-type HsPrx3 construct (**Section 2.2**) was N-terminally His_6-

tagged (WT-Nter), so the expression for wild-type C-terminal His_6-tagged HsPrx3 (WT-Cter) protein also needed to be verified.

The WT-Cter protein gene was inserted into a pET-11a plasmid (Epoch Lifesciences). The expected MW for a full length His_6-tagged, monomeric protein is 23503.6 Da. The amino acid sequence, where the wild-type HsPrx3 protein (pink) with the residues of interest highlighted in yellow, rTEV protease cleavage site (green), and the His_6-tag (blue), are detailed as follows:

APAVTQHAPYFKGTAVVNGEFKDLSLDDFKGKYLVLFFYPLDFTFVCPTE
IVAFSDKANEFHDVNCEVVAVSVDSHFSHLAWINTPRKNGGLGHMNIALL
SDLTKQISRDYGVLLEGSGLALRGLFIIDPNGVIKHLSVNDLPVGRSVEE
TLRLVKAFQYVETHGEVCPANWTPDSPTIKPSPAASKEYFQKVNQMENLY
FQGGTHHHHHH

5.4.1.1 The initial purification

The expression and purification of WT-Cter was performed almost exactly as was done for WT-Nter (**Sections 7.3 and 7.4**). The major difference was the use of lower imidazole concentrations in the wash buffer: at 10 mM as opposed to 25 mM. The lower imidazole concentration was to account for any altered affinity towards Ni^{2+} caused by the change in histidine tag location.

The resulting purity of WT-Cter proteins, after the usual purification protocol (**Section 7.4**), was poor, as assessed using SDS-PAGE gels. This can be accounted for by the lack of overexpressed WT-Cter protein (despite a large protein band at ~23 kDa in fraction 1; **Figure 5.7**), and non-specific binding of *E. coli* lysate onto the HisTrap FF column. There was a large band at ~23 kDa in fraction 11, which suggests that WT-Cter may be expressed, but optimisation was required to improve the purification of this protein. Disturbingly, fraction 11 corresponded to the elution volume for dimeric HsPrx3 protein, hinting that the C-terminal His_6-tag was preventing dimer-dimer associations, as there have been reports of His_6-tags affecting protein oligomerisation (Amor-Mahjoub *et al*, 2006; Majorek *et al*, 2014; Fonda *et al*, 2002). There was also a ~23 kDa band in fraction 7. However, the band only occasionally appeared in the purification of this protein (compare with fraction 7 in **Figure 5.9**).

In order to check for the expression of the C-terminal His_6-tag, a Western blot was performed using anti-His_6-tag antibodies, to detect the presence of the protein purification tag (**Figure 5.7 D**). The positive control was of the N-terminally His_6-tagged HsPrx3 which has an expected MW 2 kDa higher than C-terminal His_6-tagged HsPrx3.

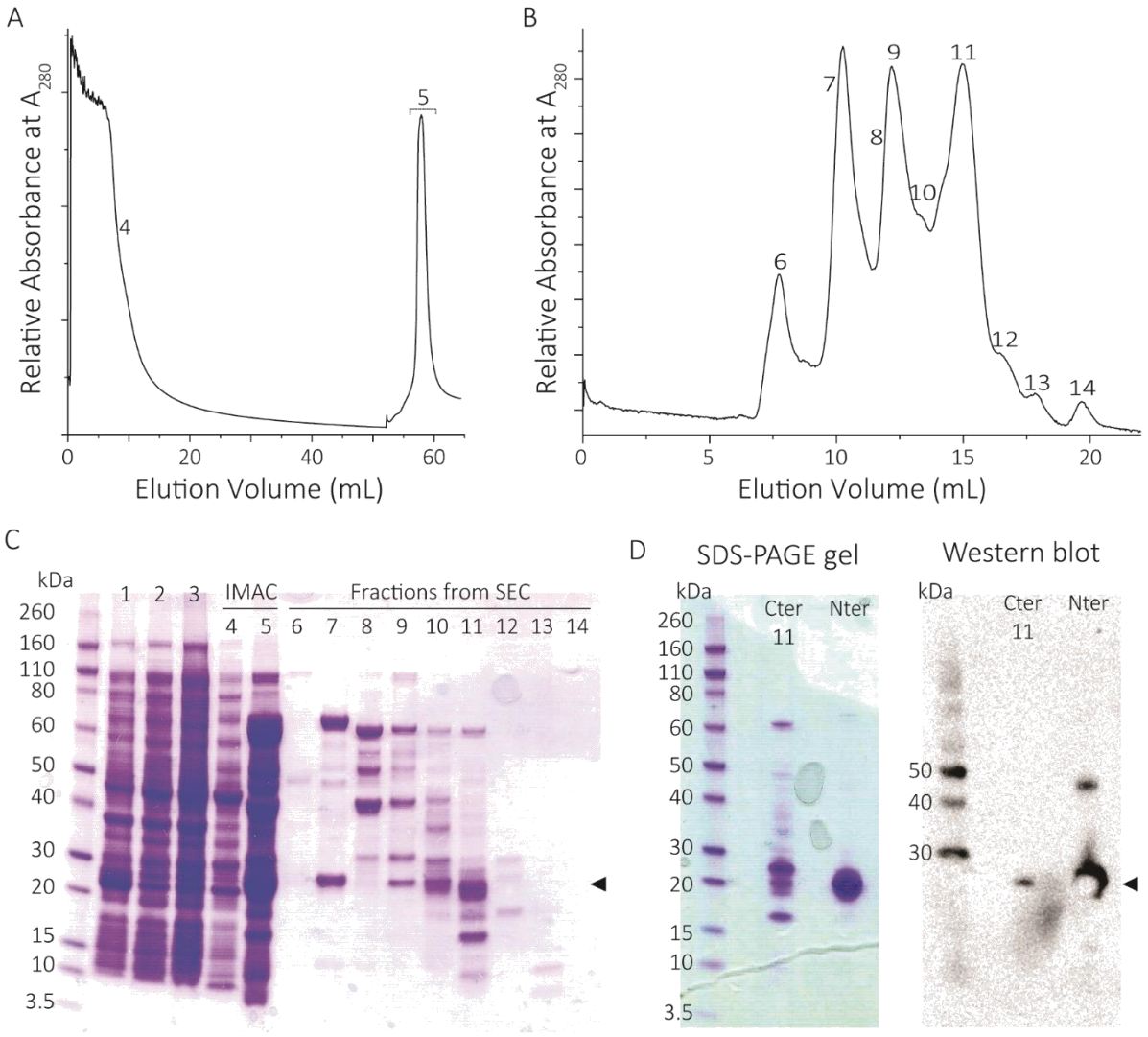

Figure 5.7: The initial purification of WT-Cter protein

(**A**) Chromatogram showing the IMAC purification with the fraction numbers corresponding to the SDS-PAGE gel in C. The elution buffer was flowed through the column at ~52 mL, eluting proteins off the nickel column. (**B**) Chromatogram showing the SEC purification with fraction numbers corresponding to the gel in C. The SEC column was a HiLoad 13300. (**C**) SDS-PAGE gel showing proteins present in each of the purification steps. The Novex MW ladder was used as a standard in the first lane. Gel numberings are as follows: 1 – total proteins in *E.coli* lysate; 2 – soluble protein in lysate; 3 – proteins that did not bind to IMAC column; 4 – proteins eluted after 10 mM imidazole wash; 5 – Pooled IMAC elution; fractions 6 to 14 correspond to proteins that elute off the SEC column. (**D**) Western blot of fraction 11 and the corresponding SDS-PAGE gel. A light band at ~23 kDa shows in Western blot, indicating that anti-His_6-tag is bound to the proteins in both fraction 11 for WT-Cter and for WT-Nter. Ideally, fraction 7 should have also been tested for His_6-tag presence. The Western blot also detected a trace dimer band for WT-Nter (~50 kDa).

5.4.1.2 Optimisation of wild-type HsPrx3 purification conditions

In order to increase the cell density of bacteria to increase yields of WT-Cter protein, the growth media was changed from LB to buffered terrific broth (TB; **Table 7.1** in **Section 7.2.1**). The bacterial cells were grown in 500 mL TB to an OD_{600} ~ 1.7 before induction of protein expression. Otherwise,

expression conditions were kept the same as previously (**Section 7.3.2**). Some adjustments were made to the compositions of the purification buffers for WT-Cter proteins (compare **Table 5.2** with **Table 7.8**). Adjusting solution pH from 8.0 to 7.0 was reported to stabilise the formation of Prx rings (Morais *et al*, 2015), so all of the purification buffers were made to 7.0 to encourage the protein ring formation. The use of phosphine reducing agent, TCEP, was avoided as it reacts with azide groups.

Table 5.2: Purification buffers for UAA protein purifications

Buffer	Composition
IMAC buffer A	20 mM HEPES, pH 7.0; 150 mM NaCl; 10 mM imidazole
IMAC buffer B	20 mM HEPES, pH 7.0; 150 mM NaCl; 500 mM imidazole
SEC buffer C	20 mM HEPES, pH 7.0; 150 mM NaCl

In order to improve the purity of the resulting protein band, a concentration gradient of imidazole in the IMAC wash as well as in the elution buffer as used to wash off non-specifically bound proteins. The gradient elution resulted in two peaks being purified (**Figure 5.8**). The resulting ~23 kDa band in pool B (Fractions 13 and 14 in **Figure 5.8**) appears more pure compared with elution fractions from previous purifications (Fraction 5 in **Figure 5.7**), suggesting that wash and elution imidazole gradients were effective in removing non-specifically bound proteins.

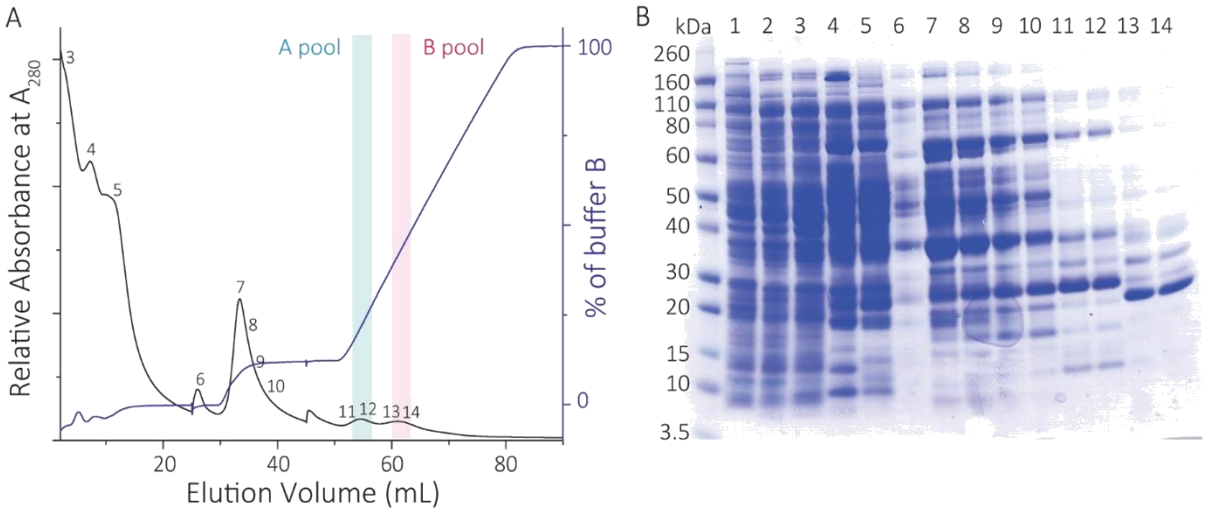

Figure 5.8: Chromatogram of IMAC purification of WT-Cter and corresponding SDS-PAGE gel
(**A**) The IMAC chromatogram shows the percentage of elution buffer (buffer B) being flowed through the IMAC column. A small gradient wash of ~10% elution buffer eluted off many non-specifically bound proteins. The gradient elution of proteins from the IMAC column resulted in two peaks, both of which were pooled and run separately on a SEC. (**B**) The corresponding SDS-PAGE gel of each of IMAC fractions. The Novex MW ladder was used as a standard. Gel numberings are as follows: 1 – total proteins in *E. coli* lysate; 2 – soluble protein in lysate; 3 to 14 are the fractions that correspond to the IMAC chromatogram.

The pooled elution peaks, A and B, were separately passed through a SEC column as an additional purification step. The SEC chromatgram and corresponding SDS-PAGE gel for pool A and B are very similar, so only pool B data are shown (**Figure 5.9**). Despite the lowered pH of purification buffers, at pH 7.0, ringed species were not detected, instead the major peak eluted off the SEC column corresponded to that of dimeric proteins. At this point, it could not be ruled out that WT-Cter were oxidised dimers as there were no reducing agents in the buffers, or that the C-terminal His_6-tag effected the protein quaternary structure (as was observed in the WT-Nter constructs).

Concentrating SEC fractions 9 to 12, although not completely pure, gave a protein expression yield of 5 mg per L of culture, which is 20 fold lower than WT-Nter protein expression. Fraction 11 from the SEC purification step was diluted into 100% acetonitrile and run on an LC-MS with the resulting mass of 23523 ± 20 Da, with the expected mass (23503.6 Da) being within this error.

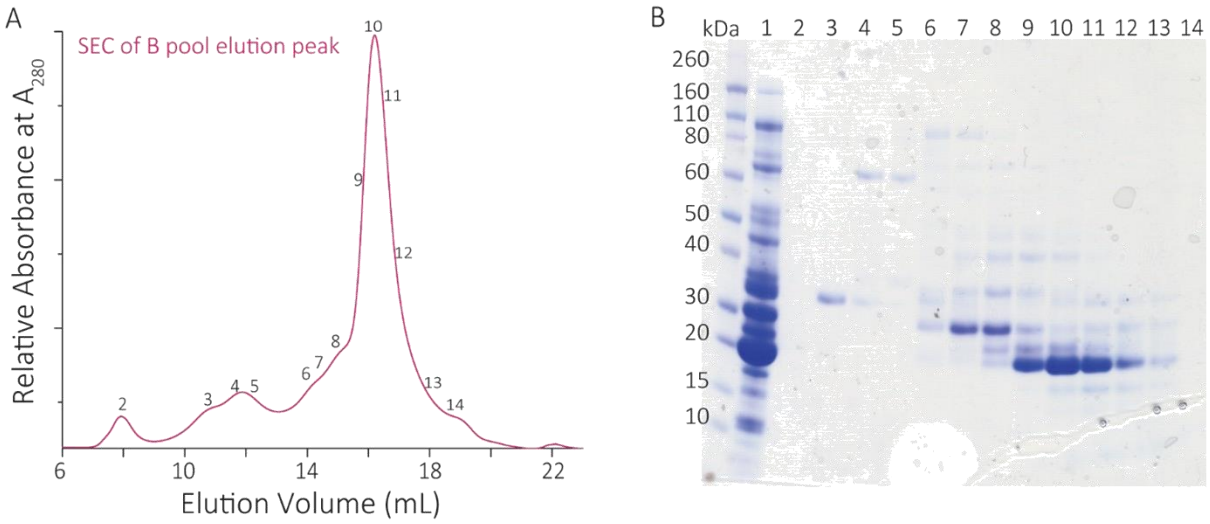

Figure 5.9: SEC and corresponding SDS-PAGE gel of IMAC elution pool B of WT-Cter
SEC chromatogram (**A**) and corresponding SDS-PAGE gel (**B**), with numbers corresponding to the fractions on the SEC. Gel lane numberings are as follows: 1 – total proteins in *E. coli* lysate; 2 to 14 correspond to the SEC chromatogram.

A Western blot was performed for the main peaks of the SEC for both pool A and B (**Figure 5.10**). A C-terminal His_6-tag specific antibody was used to identify the presence of C-terminal specific histidine tags. The protein bands from pool B emit a chemiluminescent signal, indicating that these samples contain C-terminal His_6-tags. The chemiluminescence detection is an indirect detection method that involves signal amplification via secondary antibodies; meaning quantification of proteins from this signal is difficult and often unreliable (Bell, 2016).

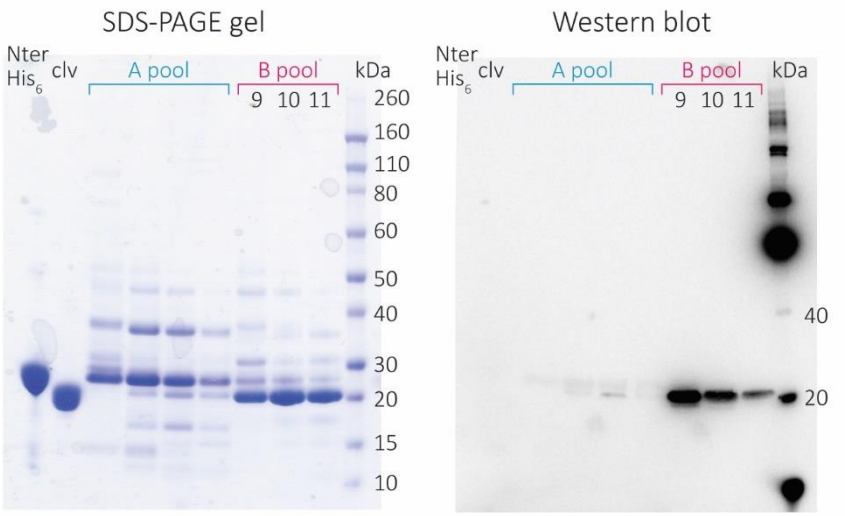

Figure 5.10: Western blot of WT-Cter SEC purification fractions using C-terminal His_6-tag antibody
An SDS-PAGE gel and corresponding Western plot of SEC fractions over the largest peak from the A pool and B pool of the WT-Cter purifications. For the Western blot, an antibody against C-terminal His_6-tag was used, with N-terminally His_6-tagged protein (Nter His_6) as well as cleaved HsPrx3 protein (clv) as negative controls. Only B pool fractions 9-11 (numbers corresponding to Figure 5.9) had chemiluminescent bands, with only faint bands detected for the A pool fractions.

Despite improvements in purity of the resulting protein, it was concerning that the yield for the C-terminal His_6-tagged wild-type HsPrx3 was 20 fold lower than the N-terminally His_6-tagged, as UAA incorporation is also expected to result in lower full length protein yields. Nonetheless, having the ability to quickly select for incorporation of UAAs made using C-terminally His_6-tagged constructs worth pursuing as a viable method to make full length UAA incorporated proteins. So, forging onwards, mutants were designed.

5.4.2 Test expressing unnatural amino acid muteins

The wild-type HsPrx3 C-terminal His_6-tagged pET11a construct was mutated by inserting amber stop codons, nucleic acids '*tag*', onto relevant positions within the HsPrx3 gene that encode for residues: Y10, Y160, F190 (Section 5.3.1). The resulting muteins are called Y10*tag*, Y160*tag* and F190*tag* and their expected truncated and full length MWs are as follows:

Table 5.3: Molecular weight of C-terminal His_6-tagged constructs

HsPrx3 C-terminal His_6-tag	Theoretical molecular weights (Da)	
	Truncated	Full length (with pAzF incorporation*)
Wild-type (WT-Cter)	n/a	23503.6
Y10*tag*-Cter	891.0	23528.6 *
Y160*tag*-Cter	17537.1	23528.6 *
F190*tag*-Cter	20794.7	23544.6 *

Chemically competent pUltra BL21 (DE3) cells were transformed with each of the pET11a plasmids (Section 7.2.6) and test expressions for these proteins were performed. Standard test expression conditions (Section 7.3.1) were insufficient for the observation of protein bands on the SDS-PAGE. Cobalt beads were used to isolate full length proteins from the lysate; however, this also did not yield any noticeable protein bands when the elution fractions were run on a gel (data not shown). Therefore, 250 mL TB bacterial cultures was used for trial expressions using BugBuster for cell lysis. The TB growth medium was necessary to increase the cell density in order for any overexpression bands to be observable (Figure 5.11). Intriguingly, overexpression of truncated Y160*tag*-Cter and F190*tag*-Cter was observed to be produced in abundance as indicated by large protein bands (circled in red, Figure 5.11; compared MWs on Table 5.3). The overexpression of truncated Y160*tag*-Cter resulted in large bands in the insoluble fraction, perhaps due to the misfolding of partially expressed protein. On the other hand, overexpressed protein bands were observed in the soluble fraction for the F190*tag*-Cter construct; this is consistent with other C-terminally truncated Prxs (Cha *et al*, 2000, Koo *et al*, 2002; Cao *et al*, 2011; König *et al*, 2013). In all of the test expression gels, there were no notable full length protein bands expressed.

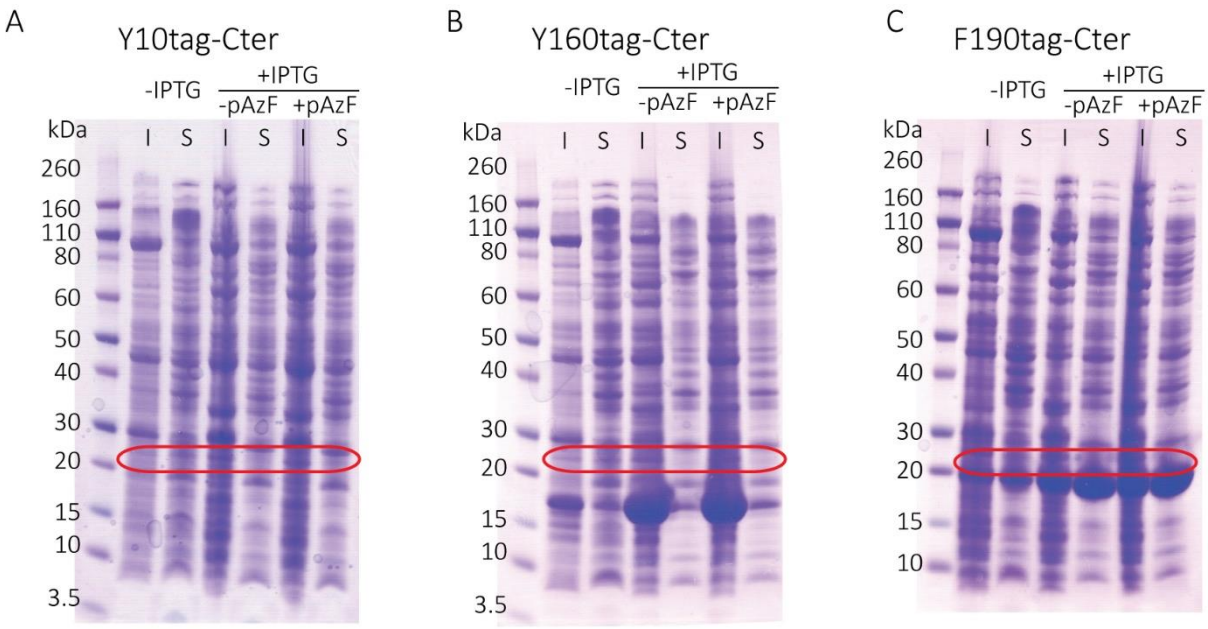

Figure 5.11: SDS-PAGE gels of the expression trials for UAA muteins expressed in 250 mL TB
The absence of full length protein overexpression was indicated by the lack of an obvious protein band at ~ 23 kDa, which is the expected monomeric MW for each of these constructs. However, there are notable overexpression bands for truncated constructs, Y160*tag*-Cter and F190*tag*-Cter (red circles). The gel labels for all gels are as follows. The Novex molecular weight protein ladder was run in the first lane. Insoluble fractions (I) and soluble fractions (S) were run side-by-side as a comparison for any soluble overexpressed bands. All gels show samples without induction of protein expression (-IPTG) and with induction of protein expression (+IPTG) in the absence (-pAzF) or presence (+pAzF) of p-azidophenylalanine.

In order to detect the presence of full length protein, bacterial growth culture volumes were increased again to 500 mL buffered TB to achieve even higher cell density and favour the likelihood of full length protein production. Since over expression for full length proteins is unlikely, IMAC purifications for proteins with His_6-tags were done to isolate UAA incorporated protein away from other *E. coli* proteins within the lysate.

Similar to what was observed in the above test expression, the attempted large-scale expression of Y160*tag*-Cter and F190*tag*-Cter constructs resulted in the abundant expression of truncated species. These truncated proteins eluted off the IMAC, but were unable to be easily separated from any potential full length protein, so focus was shifted to optimising and purifying Y10*tag*-Cter proteins.

5.4.3 Optimising Y10*tag*-Cter protein expression and purification

In order to generate sufficient full length proteins for detection on a SDS-PAGE gel, larger expression cultures were used. Y10*tag*-Cter pET11a pUltra BL21 (DE3) cells were grown in 500 mL TB at 37 °C, 180 rpm until the cell density reached OD_{600} = 1.7-2.2. A final concentration of 1 mM pAzF was then added to the culture 10 min prior to induction of protein expression via the addition of 1 mM IPTG (final concentration) to cooled bacterial cultures. The culture was then incubated at 18 °C, 180 rpm for 20 h.

The purification conditions of Y10*tag*-Cter protein was the same as that of WT-Cter protein (**Section 5.4.1**), resulting in similar purification chromatograms and gels (compare Y10*tag*-Cter **Figure 5.13** with WT-Cter **Figure 5.9**). The LC-MS results also confirmed the mass of Y10*tag*-Cter being at 23500 ± 20 kDa, indicating expression of full length protein.

The Western blott results, however, revealed something troubling about the Y10-Cter protein purification. Firstly, although a C-terminal His_6-tag specific antibody was used, the positive control band of WT-Cter only chemiluminesced faintly. This was perhaps due to the degradation of the denatured WT-Cter protein sample stored in SDS-PAGE loading dye at 4 °C for a couple of months. Secondly, two protein bands were detected across the main SEC protein peak in fractions 6 – 9 (**Figure 5.12**). The lower MW chemiluminescent protein band at ~20 kDa does not match the truncated MW of Y10*tag*-Cter, which is not expected to appear on SDS-PAGE gels (**Table 5.3**). Again, this SEC peak occurred in the dimer elution region, despite the pH of purification buffers were kept at 7.0. Hence, the removal of the C-terminal His_6-tag (**Section 7.5.3.2**) was predicted to restore the

protein ring oligomerisation ability of HsPrx3. Cleavage of the C-terminal His_6-tag for both Y10*tag*-Cter and WT-Cter were unsuccessful, although, it cannot be ruled out that the C-terminal His_6-tag could be binding to the protein surface and occluding the rTEV protease. A negative control grown in 500 mL TB, without the addition pAzF, also yielded a 23 kDa protein band when eluted after the IMAC run, and this prompted deeper investigation into whether the correct full length protein was being produced at all.

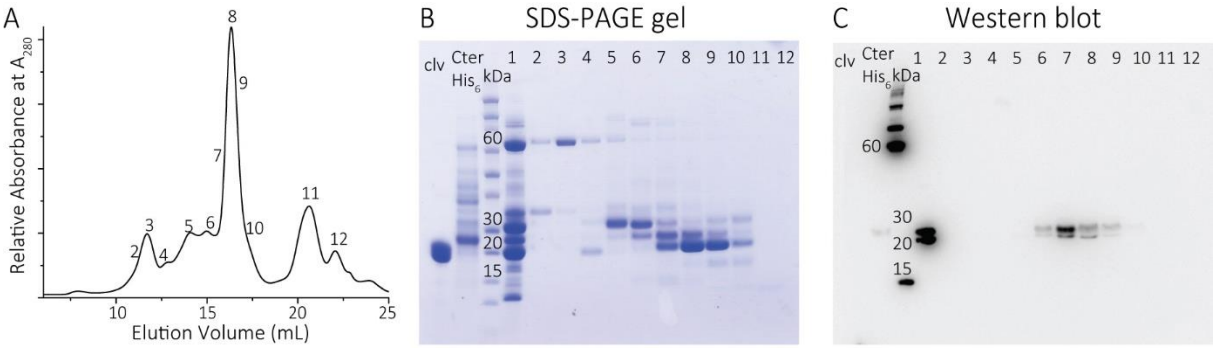

Figure 5.12: Purification of Y10*tag*-Cter with SEC chromatogram and correlating protein bands on the SDS-PAGE as well as Western blot.
(**A**) Chromatogram of SEC purification step with numbers corresponding to the fractions run on the following SDS-PAGE gel and Western blot. (**B**) SDS-PAGE gel with cleaved wild-type HsPrx3 (clv) as a negative control and WT-Cter fraction 11 (Cter His_6) as a positive control for the Western blot below. The Novex MW ladder with some relevant protein bands labelled with corresponding MW in kDa. Gel fractions are as follows: 1 – total loaded protein onto SEC; 2 to 12 – fractions that correspond to the SEC chromatogram above. (**C**) Western blot using antibodies that detect and bind to C-terminal His_6-tags. Interestingly, there are two bands that chemiluminescence at ~25 kDa and a lower band at ~20 kDa. These bands are located in the highest SEC peak. Disturbingly, the positive control for WT-Cter only chemiluminesced faintly.

5.4.4 Top-down MS/MS reveals purification of incorrect protein

The numerous inconsistencies with these C-terminally His_6-tagged UAA protein purifications warranted scepticism over the true identity of this low-yield full length protein that eluted off the SEC column as a dimer without a cleavable His_6-tag. Top-down MS/MS was used to investigate this supposed WT-Cter protein (performed by Martin Middleditch and Leo Payne of the Mass Spectrometry Centre, Auckland Science Analytical Services, University of Auckland, New Zealand).

Purified WT-Cter protein solution, similar to that of fraction 11 in **Figure 5.9**, was analysed by LC-MS to reveal a population of three proteins with MW of 25308.48 Da, 23550 Da and 23639.91 Da. Top-down MS/MS was then employed to sequence the first few amino acids at the C-terminal region of this protein, enabling the identification of this protein as an *E coli* cyclic AMP-activated

global transcriptional regulator (CRP) at 23509.23 Da (**Figure 5.13**). This provided an unambiguous, if disappointing, resolution to the observed discrepancies in protein purification.

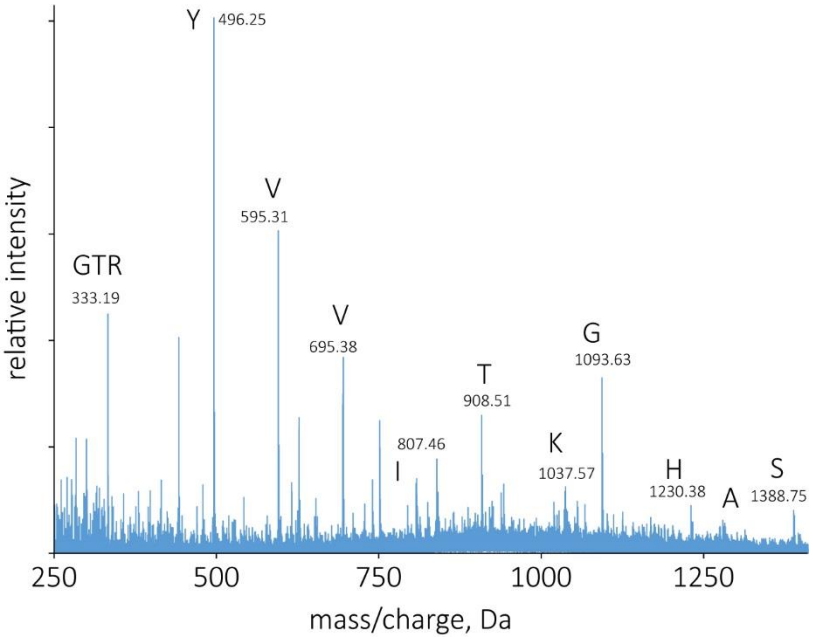

Figure 5.13: Top-down MS/MS spectra of protein C-terminus reveals it is not HsPrx3 protein
The C-terminal peptide Y ion series reveals an amino acid sequence of SAHGKTIVVYGTR. This sequence corresponds to a protein called cyclic AMP-activated global transcriptional regulator (CRP), which was presumably purified from the *E. coli* lysate. Graph was adapted from one supplied from Martin Middleditch.

CRP protein had been shown to readily attach itself onto IMAC columns without a histidine tag (Wickstrum and Egan, 2002). It contains six histidine residues in its sequence, some of which are partly solvent exposed on the CRP crystal structure. The authors also speculate that three of these histidine residues (at positions 17, 19 and 21) were located in a 'stripe' along the surface of CRP approximately opposite to DNA binding site. Perhaps, this 'stripe' of histidine residues could have given a false-positive hit in promiscuous antibody binding from C-terminal histidine tag antibody.

5.5 HsPrx3 N-terminal His_6-tagged protein expression

Although less elegant, N-terminal His_6-tagged wild-type HsPrx3 (WT-Nter) protein expression gives consistently high protein yields (as described in **Section 2.2**). The resulting decrease in yield expected for UAA incorporated proteins should still result in sufficient viable full length proteins for downstream applications. The N-terminal His_6-tag purifies both truncated proteins and full length UAA incorporated proteins, necessitating the careful separation of these species.

5.5.1 Expression trials of the HsPrx3 constructs: Y10*tag*-Nter, Y160*tag*-Nter, F190*tag*-Nter

With the same rationale as in **Section 5.3.1**, an amber stop codon (nucleic acid sequence 'tag') was designed into the Y10, Y160, F190 amino acid sequence positions of wild-type HsPrx3 proteins (**Table 5.4**). This generated three separate new constructs where the HsPrx3 gene was in a pET-28a vector with kanamycin resistance (Epoch Lifesciences). Note that this is a different vector from the previously mentioned N-terminal His_6-tagged constructs, chosen for their difference in antibiotic selection (kanamycin as opposed to ampicillin), to avoid ampicillin degradation throughout the experiment (Hou and Poole, 1969; Robinson-Fuentes *et al*, 1997). This plasmid was transformed into chemically competent pUltra BL21 (DE3) cells (**Section 7.2.6**) and protein expression trials were carried out (**Section 7.3.1**).

Table 5.4: Molecular weights of N-terminal His_6-tagged HsPrx3 constructs

HsPrx3 N-terminal His_6-tag	Theoretical molecular weights (Da)	
	Truncated	Full length (with pAzF incorporation*)
Wild-type (WT-Nter)	n/a	25322.7
Y10*tag*-Nter	4811.4	25347.7 *
Y160*tag*-Nter	21457.5	25347.7 *
F190*tag*-Nter	24577.92	25363.7 *

A SDS-PAGE gel was used to ascertain the insoluble and soluble proteins for the test expression of each construct (**Figure 5.14**). Yet again, the abundant expression of truncated protein species for both the Y160*tag*-Nter and F190-Nter constructs were observed (compare Nter constructs **Figure 5.14** with the Cter constructs **Figure 5.11**). However, full length protein bands at ~25 kDa were not observed for either the Y10*tag*-Nter construct or the Y160*tag*-Nter construct. In the case of F190*tag*-Nter, it is especially difficult to discern truncated from full length proteins using an SDS-PAGE gel. Small-scale test expressions involving cobalt beads for purification were also investigated, but yielded similar inconclusive results as full length protein bands were faint.

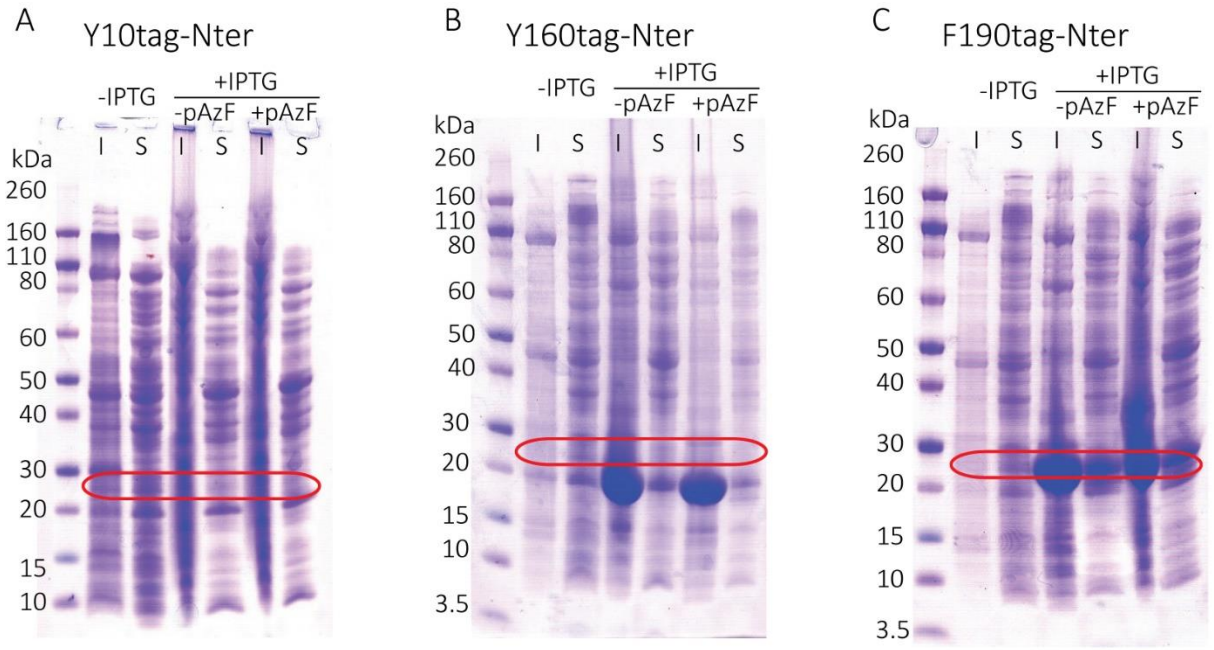

Figure 5.14: SDS-PAGE gels showing test expression of N-terminally His_6-tagged UAA muteins
The absence of full length protein overexpression was indicated by the lack of an obvious protein band at ~ 25 kDa for the Y10*tag*-Nter and Y160*tag*-Nter constructs. However, there are notable overexpression bands for truncated constructs, Y160*tag*-Cter and F190*tag*-Cter, in the insoluble fraction (red circles). Curiously, a ~25 kDa band in the soluble fraction of the F190-tag test expression was observed, in both the presence and absence of p-AzF, which indicated that full length and truncated proteins were indistinguishable on the gel. The labels for all gels are as follows: the Novex molecular weight protein ladder was run in the first lane. Insoluble fractions (I) and soluble fractions (S) were run side-by-side for comparison of any soluble overexpressed bands. All gels show samples without induction of protein expression (-IPTG) and with induction of protein expression (+IPTG) in the absence (-pAzF) or presence (+pAzF) of p-azidophenylalanine.

The Y10*tag*-Nter construct was chosen as the best option for optimising UAA incorporation into HsPrx3 proteins as the expression of Y10-Nter full length proteins would be distinct from its truncated species, which are too small to appear on an SDS-PAGE gel. In order to establish whether or not full length proteins are expressed, even at low levels, medium-scale test preparations of Y10*tag*-Nter were performed.

5.5.2 Full length protein bands and expression optimisation of Y10*tag*-Nter constructs

A variety of bacterial growth conditions were explored in parallel to improve the expression of full length Y10*tag*-Nter proteins. The standard preparation for all growth conditions were as follows (based on Section 7.3.1): 250 mL of TB growth media was used to grow the bacterial cultures of Y10*tag*-Nter pUltra BL21 (DE3) until an optical density of OD_{600} = 2.0 was reached. At this point, 1 mM pAzF (final concentration) was added to cooled cultures 10 min prior to protein expression

induction via the addition of 1 mM IPTG (final concentration). Proteins were expressed for a default temperature and time of 18 °C and 20 h, after which the cells were spun down and lysed using a sonicator (Section 7.3.3.1). In contrast to previous protein purifications, the IMAC was performed using 1 mL HisTrap FF columns to decrease the overt non-specific binding of *E. coli* lysate proteins onto the nickel beads. The IMAC purification buffers, bar the addition of TCEP, and protein purification protocol were kept the same as for WT-Nter protein (Table 7.8; Section 7.4). The protein peaks eluted from the IMAC column were pooled and loaded onto a SEC column. Fractions from the SEC were run on a gel, and it is only then that possible full length HsPrx3 bands of ~25 kDa may appear in the elution volume of ringed proteins. This is a simple way to effectively deduce whether the HsPrx3 protein is folded correctly and are still able to oligomerise into rings.

5.5.2.1 Magnificent Broth™ produces more full length protein than terrific broth

Both terrific broth (TB) and Magnificent Broth™ (MB) are rich growth media that are buffered to sustain higher densities of *E. coli* cells (OD_{600} 1.7-2.0 as opposed to OD_{600} 0.5-0.7 for LB) without detrimental acidification of the bacterial culture. Prior to this experiment, purifications with either TB or MB were performed on four separate occasions, with similar results to those detailed below.

Successful expression was indicated by the presence of faint ~25 kDa bands detected using the SDS-PAGE gel. These so called 'promising bands' occurred at the elution volumes expected for HsPrx3 rings (circled in red Figure 5.15). Bacterial cultures in TB seem to produce some full length protein bands, but this was a reduced amount compared with cells grown in MB. Without the addition of pAzF, the negative control cultures for both TB and MB consistently had no visible bands in this region (Figure 5.15 C). Note that the SEC chromatographs all have similar profiles, despite differences in bacterial cultures. Across all different conditions, the relative size of the peak that contained fractions 6-9, which correspond to the elution volumes HsPrx3 rings, does not correlate to how much full length protein is expressed, as these fractions also contain another protein at ~ 70 kDa (red arrow heads in Figure 5.15).

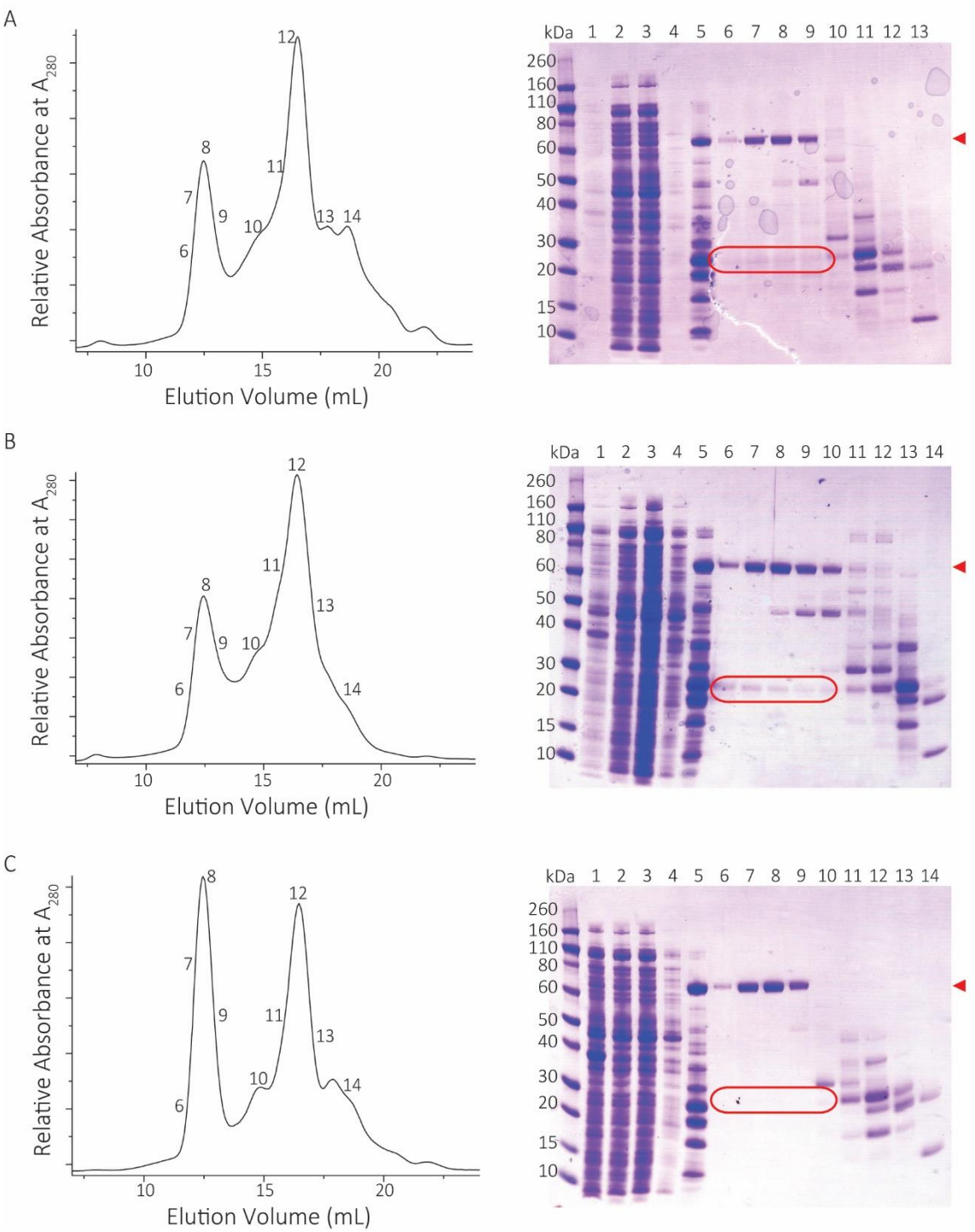

Figure 5.15: Magnificent Broth™ expresses the 'promising band' indicating potential full length protein expression

SEC chromatograms and the corresponding SDS-PAGE gels for cultures grown in TB with added pAzF (**A**), cultures grown in MB with added pAzF (**B**), and cultures grown in MB without pAzF (**C**). In all of the sets of SBS-PAGE gels, the numbering of the fractions are the same. Each gel contains a Novex MW protein ladder as a standard followed by these fractions: 1 – total protein lysate; 2 – soluble proteins; 3 – proteins that did not attach to IMAC column; 4 – proteins that were washed off IMAC column at 25mM imidazole; 5 – the total protein loaded onto the SEC column; 6 to 13 or 14 correspond to the fractions from the SEC. The location of the ~25 kDa promising band (red circle) and contaminating ~70 kDa *E. coli* protein (red arrow head) are highlighted.

5.5.2.2 Other approaches to improve expression

Since expression using MB was successful, this was the growth media used for the following optimisation of Y10*tag*-Nter full length protein production. Three angles of attack for improving full length protein expression included:

- The removal of antibiotics from large expression cultures. Kanamycin resistance can occur in buffered cell cultures containing phosphate (such as TB and MB), which could cause a loss of the pET28a plasmid (Sinha, 1984; Studier, 2005). An alternative and parallel theory was that antibiotics used, spectinomycin and kanamycin, both disrupt the ribosome of cells (Wilson, 2014). Therefore, decreasing the protein production load on cells by removing antibiotics in the large bacterial cultures, may encourage the bacterial cells to be less stressed and to produce more full length proteins.
- Changing the protein expression conditions from 18 °C, 20 h to 37 °C, 5h. The shorter protein expression time window leads to lowered cell density, which resulted in no detectable expression of the full length band at 37 °C.
- The final pAzF concentrations added to the growth media was increased from 1 mM to 5 mM, in order to encourage greater incorporation into the protein sequence and the subsequent production of full length proteins. There was no notable increase in production of the promising protein band.

5.5.3 Large-scale expressions of Y10*tag*-Nter: promising initial results for UAA incorporation

The expression of Y10*tag*-Nter protein was achieved using 1 L of MB with the cell culture density reaching OD_{600} ~2.2 before the addition 1 mM pAzF to flasks about 10 minutes before the induction of protein expression using 1 mM IPTG. These flasks were grown at 18 °C for 36 h. Two 1 mL HisTrap FF columns were used for IMAC purification as per **Section 5.5**. The elution peak from the IMAC column was pooled and concentrated to 500 µL for injection into SEC column. Samples from the SEC purification step were run on a reducing SDS-PAGE gel, and a promising band was observed in fractions 9-11 (**Figure 5.16**) with a MW of ~25 kDa that corresponds to full length Y10*tag*-Nter protein. From this purification, ~ 100 µg of pure protein was obtained per L of culture.

LC-MS of fraction 9 showed that the MW of multiple species that range from 50537-50668 Da, indicating not only do these MWs match closely with the theoretical MW of full length proteins, but also these proteins ionised as dimer on the LC-MS. Since these SEC fractions do not contain

reducing agents, the presence of oxidised full length proteins, such that monomers are covalently linked by disulfide bonds, is possible. As a quick indicator of the expression of full length Y10-Nter protein, a Western blot was performed to detect the presence of histidine tags using anti-His_6-tag antibody. Although these results were treated with scepticism, chemiluminescence was detected in only the protein bands present in the SEC elution fractions that were predicted to contain rings (Fractions 9-11 in **Figure 5.16 D**).

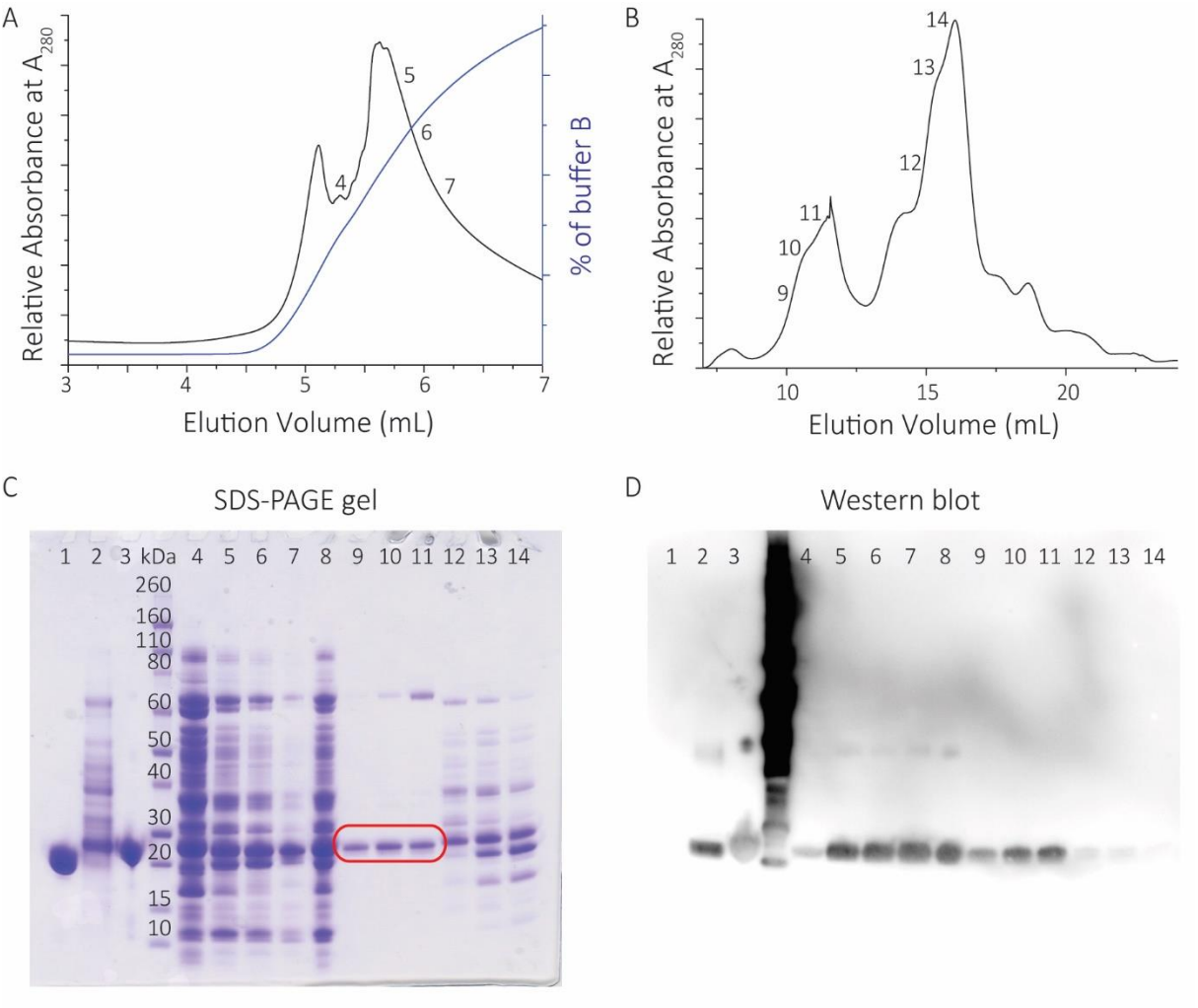

Figure 5.16: Expression and purification of Y10*tag*-Nter HsPrx3
(**A**) Chromatogram showing the IMAC purification with the fraction numbers corresponding to the SDS-PAGE gel in C. The elution buffer was flowed through the column at ~4 mL, eluting proteins off the Ni-column. (**B**) Chromatogram showing the SEC purification with fraction numbers corresponding to the gel in C. The SEC column was a HiLoad 13300. (**C**) SDS-PAGE gel showing: 1 – cleaved wild-type (WT) HsPrx3 protein; 2 – 'WT-Cter' protein, actually CRP; 3 – WT-Nter protein as a positive control for His_6-tags; MW ladder in kDa; 4 to 7 – fractions corresponding to IMAC chromatogram; 8 – pooled proteins loaded onto SEC; 9 to 14 - protein fractions eluted from the SEC purification step. The promising band (red circle) is highlighted. (**D**) Western blot of the above SDS-PAGE gel showing chemiluminescent signal for both positive controls and the ~25 kDa bands in the IMAC fractions as well as for the SEC fractions, which correspond to ring elution volumes.

The results from the LC-MS and Western blots suggested the presence of His_6-tagged full length proteins that can oligomerise to form dimers and rings. Although this is reminiscent of HsPrx3 proteins, these techniques to not directly confirm the protein identity or the successful incorporation of pAzF into the protein structure. For this, peptide MS was employed to probe the incorporation of pAzF into position Y10 of HsPrx3 protein (in collaboration with Martin Middleditch and Leo Payne from the Mass Spectrometry Facility, University of Auckland).

The gel bands from fraction 10 and 11 were cut out, destained and then digested with the proteases: gluC and trypsin. These enzymes cleave the protein into peptides of known length, and this sample was sprayed onto the QTOF instrument. The resulting peptide population included peptides with position Y10 completely skipped as well as heavily modified peptides (Table 5.5). With the expected mass difference between F and pAzF being +41 Da, the additional mass detected suggests the possibility of pAzF incorporation followed by its reaction with some other small molecule. Further discussion for this puzzling result is presented in Section 5.6.4. The same analysis was performed on WT-Nter protein, and there was only a single population of peptide with a tyrosine residue incorporated in position 10, as would be expected for wild-type protein.

Table 5.5: Peptide MS results for Y10*tag*-Nter promising protein gel band

Peptide sequence	Ratio as detected
NLYFQGIDPFTAPAVTQHAP-K	1
NLYFQGIDPFTAPAVTQHAPF(+148.058 Da)K	2
NLYFQGIDPFTAPAVTQHAPF(+114.070 Da)K	0.28

This is a promising result of possible pAzF incorporation into HsPrx3 proteins. However, due to time restraints, this project was continued by another PhD student in the lab.

5.6 Discussion

5.6.1 Overview

The generation of UAA incorporated full length proteins involves a complex orchestration of a variety of protein making machinery. The various factors which influenced the success of UAA incorporation will be discussed in the following sections. These previous attempts at producing UAA incorporated proteins has revealed important details about the system that must be further explored in order to improve yields. Firstly, it is important to base UAA incorporation on a protein that can be easily expressed in large quantities. This was not the case for WT-Cter constructs (Section 5.6.2), but could have been achievable for WT-Nter (Section 5.6.4). Despite these setbacks, this process stream-lined a production flow chart (Figure 5.17 in Section 5.6.3) which could be used to guide future purifications of UAA incorporated proteins. Secondly, fundamental validation of protein expression from pUltra and assessment of UAA incorporation efficiency of protein machinery were not carried out (Section 5.6.5). Nor were the pAzF residues checked for their viability for incorporation (Section 5.6.6). Other factors that influenced the success of pUltra incorporation will also be discussed for future consideration (Section 5.6.7). Lastly suggestions for future work (Section 5.6.8) places onus on exploring other systems for functionalisation of HsPrx3 protein tectons.

5.6.2 Why was wild-type HsPrx3 C-terminal His_6-tagged not expressed?

The failed purification of C-terminal His_6-tag wild-type (WT-Cter) HsPrx3 was in stark contrast to the success of expression and purification of WT-Nter proteins, and could have been attributed to two main factors. Firstly, the expression vector was changed from pET151-D-TOPO (for WT-Nter) to pET11a, and perhaps this was a contributing factor for the 'low yields' of full length protein detected by sensitive/promiscuous Western blots. The lack of overexpression of WT-Cter was at odds with the observation that truncated Y160*tag*-Cter and F190*tag*-Cter expressed so abundantly (Figure 5.11 in Section 5.4.2). These overexpressed bands were observed in the insoluble fraction, possibly due to incomplete protein folding because of their truncated amino acid sequences. Truncated F190*tag*-Cter, however, was also overexpressed in the soluble fraction, which suggests that expressing WT-Cter HsPrx3 proteins should be possible. Perhaps the lowering of the pH of purification buffers in order to shift the oligomeric state of HsPrx3 proteins from dimers to rings (Morais *et al*, 2015) was the critical flaw. This lowered pH may have exacerbated the false-positive result of the appearance CRP protein, by stabilising this protein in solution as its pI is 8.38. Whereas,

at this lowered pH of 7.0, the full length WT-Cter construct, with a pI of 7.09, could have been destabilised. This could have also been the cause of the disappearing 'promising band' at ~23 kDa when comparing fraction 7 in **Figure 5.7** (pH 8.0) and **Figure 5.9** (pH 7.0).

5.6.3 Improving the systematic detection of full length HsPrx3 proteins

The current system for detection of full length HsPrx3 proteins involves the following steps (**Figure 5.17**). Using indirect techniques, such as TEV cleavage or Western blots, to verify the presence of HsPrx3 may be useful as an initial indication of possible success, but peptide MS must be done for direct confirmation of protein sequences.

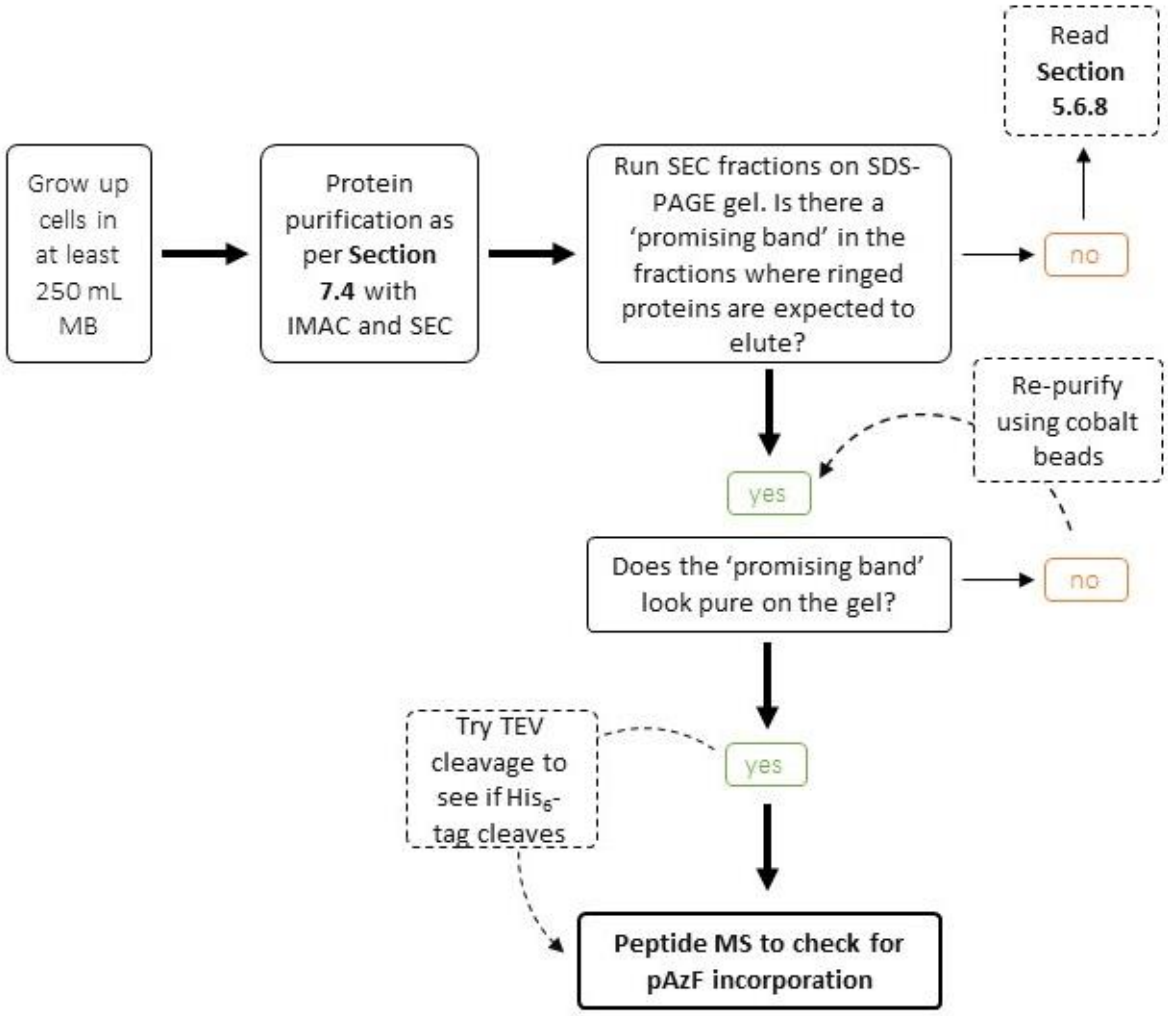

Figure 5.17: Flow chart of UAA incorporation process showing key steps and checks
It is important to have sufficient cell density in order to detect full length protein bands, hence 250 mL MB should be used for all test purifications. The purification steps should follow that of WT-Nter constructs (**Section 7.4**) as this process will select for full length and fully folded proteins that are able to still form ringed quaternary structures. Despite all promising indications on gels, peptide MS must be performed to unequivocally identify the presence of pAzF in HsPrx3 protein.

This method for selecting optimal expression conditions for UAA incorporated proteins is somewhat laborious as it involves working with large culture volumes and long purification steps. Although the use of peptide MS is essential for verification of the correct product, it is expensive, therefore possible improvements can be made (Table 5.6).

Table 5.6: Suggestions for improved detection of UAA incorporation

Method	Comments
Testing for peroxidase activity	Testing whole cell lysate for peroxidase activity will not be accurate due to other peroxidases present, so purification of protein is required. This method, although faster than peptide MS/MS, is indirect.
rTEV protease for cleavage of His_6-tags	Although an indirect method, this could be a fast and inexpensive way to quickly check for full length HsPrx3 protein production. The addition of reducing agents in order to do this will also reduce the azide group, rendering it unable to perform further click reactions. This technique would not be useful for N-terminal His_6-tagged constructs with larger truncated proteins compared to Y10*tag*-Nter.
rTEV protease to cleave off a fluorescent tag	Same as above, but even faster detection results as no purification would be required.
Purification of pAzF-incorporated proteins using alkene resin	UAA incorporation can be directly assessed, however, these reactions are not easily reversible so this method could only be used for the initial screen.

5.6.4 Possible reasons for the puzzling results from the large-scale Y10*tag*-Nter expressions

The full length Y10*tag*-Nter constructs produced had unexpected incorporations or skipping of residues that occurred at the Y10 amino acid position (Section 5.5.3). This mixed population of full length HsPrx3 protein with the skipped Y10 residues and the additional mass, were in contrast to the single population of WT-Nter proteins detected using peptide MS. The WT-Nter construct used for this comparison was generated from a pET151-D-TOPO plasmid. An important control expression of WT-Nter produced from the pET24a plasmid, the plasmid containing the Y10*tag*-Nter

construct, was never performed. Although it is unlikely to be an explanation for these puzzling observations, this needs to be verified as the change in plasmid (from pET151-D-TOPO) could have had an unknown effect on overall protein expression. It is curious that MB growth media seemed better at producing full length proteins compared with cells grown in TB (Figure 5.15 in Section 5.5.2.1). As the composition of MB is propriety, it is not possible to examine what factors within this media that could cause greater expression of full length proteins. However, in both growth media, greater cell density and longer expression times produced more full length protein, although this did not necessarily mean pAzF was correctly incorporated as an active functional moiety.

The increase in unexpected mass of 148 Da and 114 Da for the peptide sequence suggests that the azide group may have reacted with some other species, as this was not an observation for the WT-Nter control proteins. This suggests that some pAzF residues may have been incorporated and then reacted with some other small molecule, which is a possibility due to the long protein production time. Section 5.6.6 explores pAzF accessibility and reactivity. This is a promising result that warrants further investigation into how yields for these species can be increased.

The low levels of UAA incorporation and subsequent occasional production of full length HsPrx3 monomers could have consequences for protein folding and stability. HsPrx3 proteins are never found as monomeric proteins in solution, as they form homodimers immediately after synthesis from the ribosome. Therefore, due to a lack of a partnering monomer, the occasional full folded UAA incorporated Y10*tag*-Nter monomer may become unfolded and insoluble. Again, the production of full length proteins is expected to occur at low levels, so any HsPrx3 protein bands in the insoluble fraction will not be overexpressed and may not be distinguishable from other *E. coli* proteins. Perhaps the parallel synthesis of full length WT-Nter monomers could be used to encourage pAzF incorporation into soluble full length HsPrx3 proteins. On this note, exploring F190*tag*-Nter as an option for pAzF incorporation may be a viable option, considering the truncated F190*tag*-Nter protein is mostly soluble, providing monomers to which UAA incorporated HsPrx3 can bind.

5.6.5 pUltra – how this can be improved?

Although some promising results indicate Y10*tag*-Nter constructs were being made, an attributing factor to the poor incorporation of pAzF into HsPrx3 could have been the use of the designed pUltra plasmid (Section 5.3.1) which was smaller by 387 base pairs compared to the commercially

available equivalent. It must be assessed whether using the original commercial pUltra, which was only available recently, will result in better UAA incorporation into the HsPrx3 protein gene. Despite being based on the literature (described in Section 5.3.1), the expression outputs from pUltra, both the *M. jannaschii* aminoacyl-tRNA synthetase and the reciprocating tRNA, should have also been verified in-house.

5.6.6 Exploring pAzF reactivity and accessibility to the protein sequence

The reactivity of pAzF and, therefore, also its accessibility to the amber stop codon both play defining roles in the success and efficiency of UAA incorporation. The azide group in pAzF was partly chosen for its specific reactivity towards chemical groups not normally present in biological situations (Figure 5.2), enabling its synthesis in *E. coli* (Chatterjee *et al*, 2013). However, azides are also photoreactive: upon exposure to UV light, a highly reactive nitrene is generated which can react with an assortment of compounds, including protein backbones (Gritsan *et al*, 2010). Despite best efforts to avoid exposure to UV light, some pAzF may have cross-linked, rendering it unrecognisable to the protein translation machinery. It has also been shown that sample preparation can reduce the pAzF residue into p-amino-L-phenylalanine (pAmF: 180 Da) (Shao *et al*, 2015; Chin *et al*, 2003). This lack of azide group will render the protein no longer able to perform click chemistry.

It is plausible that remaining viable pAzF residues had been incorporated sparingly into other amber stop codon sites within the *E. coli* genome hence the extremely low yields of full length proteins observed for the Y10*tag*-Nter construct. However, if this deleterious incorporation of UAAs into random amber stop codons had occurred, bacterial growth rates would have been expected to stall during the protein expression. This was not evident as bacterial pellets from cultures with and without pAzF addition were of similar weights/sizes. This suggests that the pAzF was not particularly accessible to incorporation. It is uncertain whether pAzF reacted with anything in the various growth medium, rendering the UAA unrecognisable by the protein translation machinery. The puzzling results for the full length Y10*tag*-Cter constructs, with added unexpected mass, support this hypothesis. As a future experiment, small volumes of this UAA should be mixed with all the solutions used throughout protein expression and purification in order to see if it is being modified in anyway using LC-MS.

5.6.7 Future factors to consider for *in vivo* incorporation of pAzF into HsPrx3 using *E. coli* methods

The titration of plasmid copy numbers containing the orthogonal translation machinery, such as for the predecessor plasmids to pUltra, were a contributing factor towards improving modified protein yields, with higher copy number resulting in higher full length protein production (Ryu *et al*, 2006; Young *et al*, 2010; Chatterjee *et al*, 2013). In fact, a recent paper divorces copy number of plasmids from the efficiency of UAA incorporation in order to directly improve the efficiency of UAA incorporation by the orthogonal tRNA/synthetase pair (Amiram *et al*, 2015). The translational machinery genes were embedded into the *E. coli* genome and produced at endogenous levels. Directed evolution experiments were performed to select for more efficient orthogonal tRNA/synthetase pairs to incorporate UAAs, as opposed to having this effect through increased copies of the tRNA/synthetase pairs themselves. An improved plasmid was derived based on this paper, called pUltramate, where the sequences of improved MjaaRS and tRNA have been incorporated into the pUltra plasmid.

The location of the amber stop codon with the protein gene can influence the ability for the protein translation machinery to incorporate the UAA (Pott *et al*, 2014). Not only can certain nucleic acid sequences cause the ribosome to skip more (Weiss *et al*, 1987; Farabaugh and Björk, 1999), but certain residues surrounding the amber codon can influence the efficiency of UAA incorporation (Pott *et al*, 2014). The incorporation of UAA to the amber stop codon must compete with the release factor protein binding to the ribosome at the stop codon and signalling the subunits to disassemble. Mutants of this release factor protein (Schmied *et al*, 2014) and even its deletion from the *E. coli* genome (Zheng *et al*, 2016) have both resulted in higher UAA incorporation efficiency. Cell lines with deleted release factor genes are now also available for purchase and could be viable future option for the improved incorporation of UAA into proteins. Another improvement on the efficiency of UAA incorporation was by the synthetic evolution of a ribosome that can decode quadruplet codons (Neumann *et al*, 2010). These ribosomes work with the orthogonal protein translation machinery to assign the blank codons to certain UAA, including pAzF. This technique was used to probe the intra-protein crosslinking, but has also been adapted for fluorescently labelling proteins (Wang *et al*, 2014), and could very well be adapted to functionalising protein tectons.

Position of the UAA on a protein can affect its folding, and this has implications on its efficiency of incorporation (Arpino *et al*, 2015), with the most efficient UAA incorporations occurring at

positions where native sidechains are buried. This poses a problem for applications as exposed functional groups are desired for further reactions for functionalisation of protein tectons. It is likely that the location optimisation of UAA incorporation needs to be protein specific, and therefore, this must be done for HsPrx3.

5.6.8 Back to the drawing board?

It is clear that *in vivo* UAA incorporation using *E. coli* is still an evolving field of research. It will be interesting to see how these techniques improve over time to accommodate other proteins outside of the regularly used GFP. With the end goal of functionalising HsPrx3 in mind, it may be more efficient to delay efforts to explore more reliable methods for generating proteins with functionalisable chemistries. HsPrx3 remains a versatile protein tecton that can tolerate amino acid substitutions and redesigns, and so utilising its surface chemistries may be the most viable route in order to achieve functionalisable tectons. The modification of canonical amino acids (such as lysine residues in Section 5.1.2), where a mutant tecton with just a single lysine designed onto the protein surface would make HsPrx3 a great functionalisable tecton, assuming this mutant still retains its ability to form complex quaternary structures. NHS-PEG_4-azides are readily commercially available and can be used to react with these primary amines, with an end result similar to the aims of this chapter.

5.7 Summary

Chapter 5 introduces an attempt at progressing the work from the previous chapters onwards from the characterisation of HsPrx3 as a potential tecton for nanotechnology, towards the use of this tecton for applications. The functionalisation of HsPrx3 was the key goal of this chapter and, with only partial success in the expression of Y10*tag*-Nter constructs, there are many avenues left to be explored (detailed in Section 5.6) for functionalising this protein tecton.

Chapter 6: Conclusions and future perspectives

6.1 Overview

Proteins that self-assemble into a variety of structures make great tectons for nanotechnology. Human peroxiredoxin 3 (HsPrx3) is one such protein, self-assembling from dimers into ringed-shaped architectures, which can further stack to form protein tubes. Part of this thesis explored the self-assembly of HsPrx3, not only informing how to control the creation of these structures, with implications for its use in future applications, but also expanding on the knowledge of its biological function. This is evident in Chapter 2, where the first crystal structure of HsPrx3 in a stacked conformation was used as a blueprint for engineering new functions, as well as a basis for creating a novel hypothesis for its biological role, where the stacking of HsPrx3 rings is representative of a self-chaperoning function. Native mass spectrometry (nMS) analysis of HsPrx3 at pH 4.0 revealed the self-assembling mechanism of protein tubes as non-commutative (Chapter 3). The redox-influenced association of protein dimers into dodecameric toroids was also examined and muteins were engineered to disrupt this assembly, creating a stabilised toroid and a minimally active obligate dimer (Chapter 4). Having gained a deeper understanding of HsPrx3 self-assembly, the next step was to functionalise the protein surface with novel chemistries (Chapter 5). An unnatural amino acid (UAA), p-azidophenylalanine, was chosen for *in vivo* incorporation into HsPrx3 *via* an *E. coli* expression system. Although, not entirely successful, this marks a promising initial venture at functionalising HsPrx3. A visual overview of this thesis (Figure 5.1) highlights some of these key findings. The following sections will explore the future perspectives of each of these results.

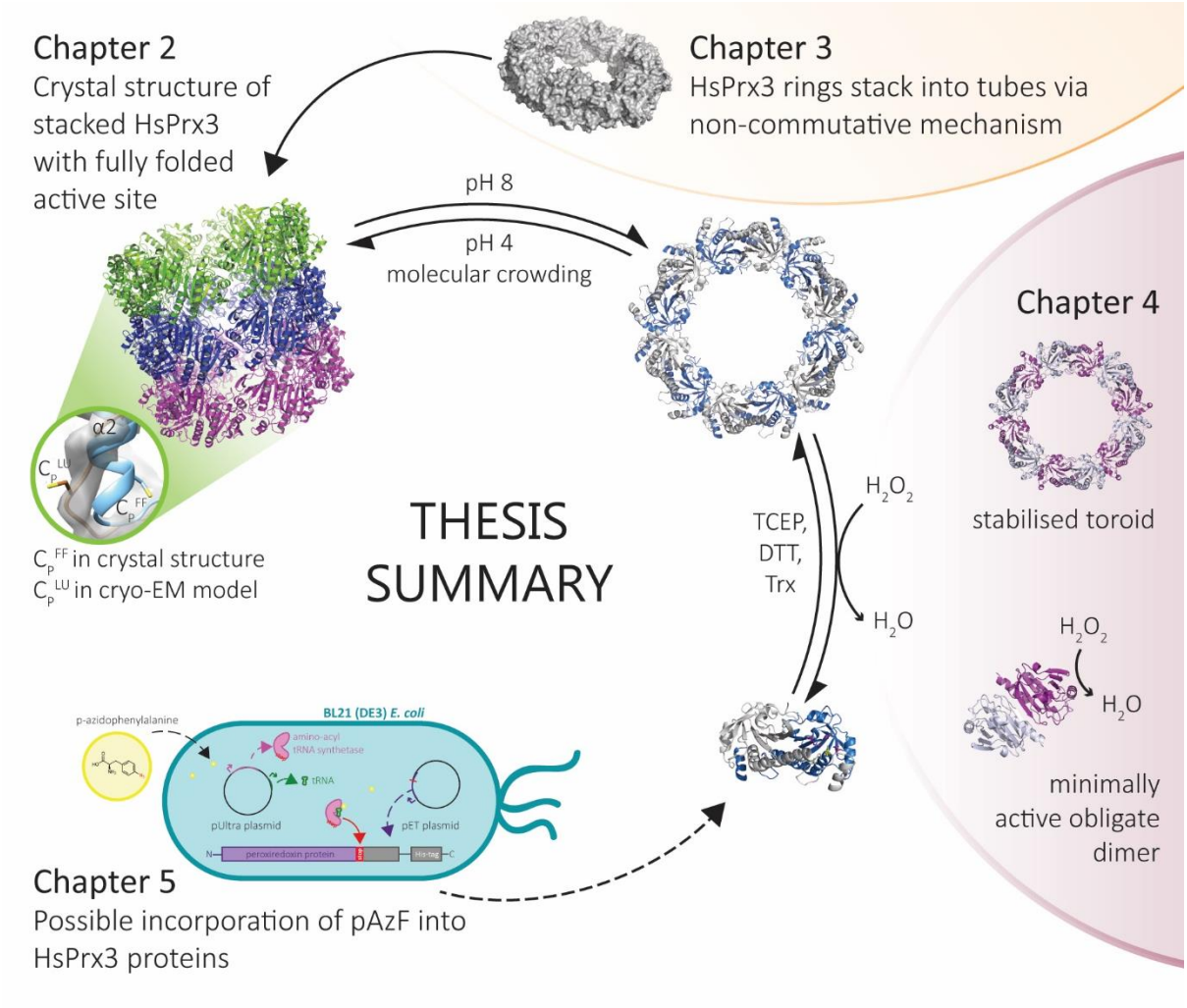

Figure 6.1: Summary diagram of the results achieved in the context of chapters within this thesis
The catalytic cysteine in the fully folded (C_P^{FF}) and locally unfolded conformation (C_P^{LU}).

6.2 Future perspectives

6.2.1 Examining the *in vivo* relevance of HsPrx3 high molecular weight structures

Despite the various hypothesises that HsPrx3 ring stacking serves a chaperoning function, whether it be as a molecular chaperone or a self-chaperone (**Section 2.4.3**), the *in vivo* relevance of HsPrx3 ring stacking has yet to be ascertained. New developments in cryo-tomography, a technique for *in situ* visualisation of proteins, could be used to address this in mammalian mitochondria. A similar study was performed in yeast mitochondrial matrix for the crystalline structures of aldehyde dehydrogenase, Ald4p (Fukuda *et al*, 2015, Misonou *et al*, 2014). It would not only be interesting to see whether these stacked Prx structures exist at all, but also the conditions *in vivo*, that would induce their formation.

6.2.2 Surveying the quaternary structure of hyperoxidised Prxs

There are numerous examples of muteins with their stacked ring formation attributed to amino acid substitutions that mimic the hyperoxidised state (Section 2.1.3.2). However, hyperoxidised Prxs have only been shown to form spherical protein balls (Jang *et al*, 2004), or single ring chaperone species (Teixeira *et al*, 2015), with no direct link between hyperoxidised Prx to the formation of stacked ring protein tubes. Recent developments by Poynton *et al*, suggest that the quaternary structure of HsPrx3 is significantly impacted upon the formation of a sulfenic acid at Cys_P, resulting in the preferential formation of dimers and even unstable monomeric species. Crystallisation of the hyperoxidised HsPrx3 would provide clues as to how this modification to Cys_P can alter the protein quaternary structure.

6.2.3 Controlling protein tube lengths

The associations described for the R interface of the HsPrx3 crystal structure (Section 2.3.4) also need to be experimentally verified by introducing point mutations to critical residues, such as H164. In the case of H164, it is proposed that lowered pH increases its positive charge causing Prx stacks to associate. So mutating the H164 residue into a positively charged amino acid, such as lysine, could result in better electrostatic interactions at the R interface. It is important to note that HsPrx3 have the same R interfaces at the top and bottom of the rings; so rather than capping the tubes, having more stabilised stacks could shift the equilibrium of protein tube formation. In fact, mutations to the R interface interactions could be a viable means to control HMW tube lengths for applications in nanotechnology. Further investigations are required into how salts can affect the formation of large HsPrx3 protein tubes. This could be an easy means to control tube lengths without having to engineer new enzymes.

The most promising results for controlling protein tube lengths is to use His_6-tagged wild-type HsPrx3 to alter the equilibrium of tube formation to get smaller stacks of HsPrx3 (Section 3.3). It would be interesting to test different ratios of His_6-tagged versus cleaved proteins at pH 4.0 using the nMS set up as well as the AUC to probe if the lengths of the protein tube population were changed.

Another means to control tube lengths would be to create protein caps that limit the growth of the protein tubes, like that of Hcp1 ring proteins (Ballister *et al*, 2008). This could separate the inner tube space from the outside, creating a nano-container with variable lengths and different

sized inner volumes. These protein caps could be based on HsPrx3, perhaps the His_6-tagged variety can cap the end of HsPrx3 protein tubes by also binding to a nanoparticle, such as for the nano-peapods described (Ardini *et al*, 2014).

6.2.4 Beyond the non-commutative mechanism: probing dimer swapping between rings

Although the mechanism of HsPrx3 tube formation at pH 4.0 was found to be non-commutative, the kinetics of self-assembly has yet to be explored as it occurs on a time scale < 60 seconds. In order to probe this phenomenon, a stopped flow instrument set up can be used to lower solution pH incrementally prior to protein injection into the nMS instrument.

With the aim of investigating dimer subunit swapping between cleaved and His_6-tagged wild-type HsPrx3 protein rings at pH 8.0, these proteins were mixed together and sprayed onto the nMS (Section 3.3.1). Other homooligomers spontaneously associate and dissociate, swapping subunits between each HMW species within seconds to minutes (Sobott *et al*, 2002; Aquilina *et al*, 2005; Benesch *et al*, 2010). Dimer subunit swapping does not occur for this particular HsPrx3 mixture, but this could be a result of using stabilised His_6-tagged wild-type HsPrx3 rings (Section 3.4.2). Alternatively, to truly test for subunit swapping, labelling proteins with heavy carbon or nitrogen would result in comparable cleaved wild-type protein species with which to mix (Rutsdottir *et al*, 2017), and the mass difference between labelled and unlabelled proteins can be detected using nMS.

6.2.5 Pinpointing a threshold H_2O_2 concentration that destabilises the protein ring

Although formation of the disulfide bond between two Prx monomers in a homodimer is known to destabilise the formation of the A interface, leading to Prx ring dissociation, the question arises of how many disulfide bonds does it take to disrupt a ring? The dissociation of reduced wild-type HsPrx3 rings can be monitored by nMS in real-time during increasing exposure to H_2O_2, with stabilised S78C HsPrx3 rings as a control. From Prx protein crystal structures (Cao *et al*, 2015) and the stabilised S78C HsPrx3 mutein, it seems possible that HsPrx3 protein rings can remain intact even after disulfide bond formation (Section 4.6.3). Perhaps a threshold concentration of H_2O_2 in which the rings dissociate. This again, links the oligomerisation of Prxs to another yet unknown

cellular function, and would be crucial knowledge with regards to protein ring stability that could influence the use of these proteins as tectons for nanotechnology.

6.2.6 Disentangling the redox switch as a means to use HsPrx3 as a cancer therapeutic

As a crucial cellular peroxidase, HsPrx3 has been linked to a variety of cancers (Li *et al*, 2015; Section 1.5.3.3), and so disrupting the toroidal structure may be a means to design therapeutics against this highly abundant human protein. That is, drugs that disrupt oligomerisation of HsPrx3 can be used to improve the efficacy of other chemotherapies by temporarily impairing HsPrx3 function, and by removing one of the pathways a cancer cell uses to circumvent cell death. Mouse experiments have been shown to survive Prx3 knockouts (Li *et al*, 2007; Zhang *et al*, 2016). However, cancer cells may not be able to tolerate its unusually highly oxidative environments and can undergo cell death mediated by reactive oxygen species (Song *et al*, 2011; Mishra *et al*, 2015).

6.2.7 Towards functionalising HsPrx3 tectons

The study of HsPrx3 structures and examination of their self-assembly concerned the first three results chapters, with Chapter 5 as a first survey of functionalising HsPrx3 tectons for applications beyond its original biological function. The incorporation of an UAA into specific locations of the protein would provide novel reactive groups, such as azides, with which to perform click chemistry. The suggestions for future troubleshooting of this were discussed in Section 5.6.

In the course of functionalising HsPrx3, it is important to meld the novel characteristics of HsPrx3 as a tecton with any of its future functions. The reversible assembly of HsPrx3 protein structures, via an environmental trigger such as changes on pH or presence of H_2O_2, can enable these proteins to act as switchable scaffolds. Enzymes can be tethered to the outer surface of HsPrx3 rings and these rings can be assemble into tubes. The enzyme-decorated tubes act as a biological scaffold for a cascade of reactions. Alternatively, the central cavity of HsPrx3 protein tubes can act as nano-tunnel within which small enzymatic cascades can occur, like an 'enzymatic highway' where substrates can be channelled for different metabolic pathways (Dueber *et al*, 2009; Glover and Clark, 2016). The specific spatial separation between each stacked ring provides exquisite patterning at the nano-scale, which can be tuned to separate of fluorophores for complex fluorescence resonance energy transfer cascades (Buckhout-White *et al*, 2014). Conductive polymers, on the other hand, could be used to embellish the outer surface of protein tubes bound

with metal ions/nanoparticles in the central cavity, increasing the conductive properties of protein nanowires (Abdallh *et al*, 2014).

Overall, this thesis enriches our understanding of the versatile nature of HsPrx3 protein as self-assembling building blocks, with implications for its biological role as well as its for future applications in bionanotechnology.

Chapter 7: Materials and methods

7.1 Reagents and chemicals

Unless otherwise stated, all chemicals were obtained from Sigma-Aldrich (Auckland, New Zealand), or Invitrogen (Victoria, Australia). 0.22 µm filtration devices used in this thesis included Corning® Costar® Spin-X® centrifuge tube filters (ThermoFisher Scientific) and ReliaPrep™ Syringe Filters 0.22 µm PES (Ahlstrom). Sodium dodecyl sulfate polyacrylamide gel electrophoresis (SDS-PAGE) gels, MES running buffers and Novex® protein molecular weight ladders were all supplied by Invitrogen. Chromatography media were obtained as pre-packed columns or loose gels from GE Healthcare Lifesciences (Auckland, New Zealand). Purified water from a MilliQ system (Millipore) was used throughout.

The centrifuges used were Eppendorf 5810R (fixed angle rotor F-34-6-38) and Sorvall RC6 plus (rotor F10S6x500Y). The spectrophotometers used were Cary 4000 UV-Vis spectrophotometer (Varian) used for checking protein concentration for crystallography and Spectramax M5 (Molecular Devices) that are able to hold microplates for assays as well as cuvettes for checking optical density of bacterial cultures.

7.2 Molecular Biology and DNA manipulation

7.2.1 Growth media

All media and equipment for bacterial culture were sterilised by autoclaving prior to use. All bacterial work was carried out under sterile conditions using an updraft generated by a flame, and standard aseptic technique was employed (Bykowski and Stevenson, 2005).

All components of media in Table 7.1 were dissolved in MilliQ water before being sterilised by autoclaving. When required and immediately before use, appropriate antibiotics were added to media, which was cooled below 50 °C. This is especially important when making LB agar, as agar must be heated to melt all solids and then cooled prior to addition of antibiotics, before being poured into Petri dishes to set.

Table 7.1

Media	Composition
LB medium (Bertani, 1951)	bacto-tryptone (10 g/L), yeast extract (5 g/L), NaCl (10 g/L)
LB agar	LB medium + 1.5% agar
TB medium	bacto-tryptone (10 g/L), yeast extract (5 g/L) buffered with 1M potassium phosphate, pH 7.2
Magnificent Broth™	unsure because propriety (MacConnell Research)

7.2.2 Antibiotics and other media additives

All antibiotics used were sterilised by passing the solution through a 0.22 µm filter and stored as 1000x stock solutions at -20 °C. The working concentrations (Table 7.2) were used to select for appropriate bacterial strains. Stock isopropyl-β-D-thiogalactopyranoside (IPTG) was made up to a concentration of 1 M and added to media at a 1/4000 dilution to give a working concentration of 0.25 mM.

Table 7.2

Antibiotic	Working concentration (µg/mL)	Solvent to dissolve
Ampicillin	100	MilliQ water
Chloramphenicol	50	100% ethanol
Kanamycin	50	MilliQ water
Spectinomycin	50	MilliQ water

7.2.3 Protein expression genes and plasmids

Epoch Biolabs (Sugar Land, Texas, USA) were employed to perform all the molecular biology required for this work. The human peroxiredoxin 3 (HsPrx3) gene was originally obtained from Mark Hampton in the Christchurch School of Medicine, and subsequently cloned into a pET151-D-TOPO vector (Novagen, 1999) by Pam Zhu in the Gerrard laboratory. This plasmid was sent to Epoch Biolabs for further DNA manipulations. All of the subsequent subcloning of HsPrx3 gene variants into new pET vectors was performed by Epoch Biolabs (**Tables 7.3 - 7.5**).

Table 7.3: Protein names with the corresponding amino acid sequences, as single letter identifiers, designed to be expressed from the pET 151-D-TOPO (ampicillin resistance). The following features are coloured as follows: histidine tag (pink), linker region (blue), TEV protease cleavage site (green); native protein sequence (black). Mutated residues are highlighted in yellow.

Wild-type HsPrx3 N-terminal His_6-tag (WT-Nter)	MHHHHHHGKPIPNPLLGLDSTENLYFQGIDPFT APAVTQHAPYFKGTAVVNGEFKDLSLDDFKGKYLVLFFYPLDFTFVCPTE IVAFSDKANEFHDVNCEVVAVSVDSHFSHLAWINTPRKNGGLGHMNIALL SDLTKQISRDYGVLLEGSGLALRGLFIIDPNGVIKHLSVNDLPVGRSVEE TLRLVKAFQYVETHGEVCPANWTPDSPTIKPSPAASKEYFQKVNQ
S75E HsPrx3	MHHHHHHGKPIPNPLLGLDSTENLYFQGIDPFT APAVTQHAPYFKGTAVVNGEFKDLSLDDFKGKYLVLFFYPLDFTFVCPTE IVAFSDKANEFHDVNCEVVAVSVDEHFSHLAWINTPRKNGGLGHMNIALL SDLTKQISRDYGVLLEGSGLALRGLFIIDPNGVIKHLSVNDLPVGRSVEE TLRLVKAFQYVETHGEVCPANWTPDSPTIKPSPAASKEYFQKVNQ
S78C HsPrx3	MHHHHHHGKPIPNPLLGLDSTENLYFQGIDPFT APAVTQHAPYFKGTAVVNGEFKDLSLDDFKGKYLVLFFYPLDFTFVCPTE IVAFSDKANEFHDVNCEVVAVSVDSHFCHLAWINTPRKNGGLGHMNIALL SDLTKQISRDYGVLLEGSGLALRGLFIIDPNGVIKHLSVNDLPVGRSVEE TLRLVKAFQYVETHGEVCPANWTPDSPTIKPSPAASKEYFQKVNQ

Table 7.4: Protein names with the corresponding amino acid sequences, as single letter identifiers, designed to be expressed from the pET 11a (ampicillin resistance). The following features are coloured as follows: histidine tag (pink), linker region (blue), TEV protease cleavage site (green); native protein sequence (black). Mutated residues are highlighted in yellow, with a dash (-) indicating the presences of the "tag" amber stop codon.

Wild-type HsPrx3 C-terminal His_6-tag (WT-Cter)	M APAVTQHAPYFKGTAVVNGEFKDLSLDDFKGKYLVLFFYPLDFTFVCPTE IVAFSDKANEFHDVNCEVVAVSVDSHFSHLAWINTPRKNGGLGHMNIALL SDLTKQISRDYGVLLEGSGLALRGLFIIDPNGVIKHLSVNDLPVGRSVEE TLRLVKAFQYVETHGEVCPANWTPDSPTIKPSPAASKEYFQKVNQ MENLYFQGGTHHHHHH

Y10*tag* HsPrx3 C-terminal His_6-tag Y10*tag*-Cter	M APAVTQHAP-FKGTAVVNGEFKDLSLDDFKGKYLVLFFYPLDFTFVCPTE IVAFSDKANEFHDVNCEVVAVSVDSHFSHLAWINTPRKNGGLGHMNIALL SDLTKQISRDYGVLLEGSGLALRGLFIIDPNGVIKHLSVNDLPVGRSVEE TLRLVKAFQYVETHGEVCPANWTPDSPTIKPSPAASKEYFQKVNQ MENLYFQGGTHHHHHH
Y160*tag* HsPrx3 C-terminal His_6-tag Y160*tag*-Cter	M APAVTQHAPYFKGTAVVNGEFKDLSLDDFKGKYLVLFFYPLDFTFVCPTE IVAFSDKANEFHDVNCEVVAVSVDSHFSHLAWINTPRKNGGLGHMNIALL SDLTKQISRDYGVLLEGSGLALRGLFIIDPNGVIKHLSVNDLPVGRSVEE TLRLVKAFQ-VETHGEVCPANWTPDSPTIKPSPAASKEYFQKVNQ MENLYFQGGTHHHHHH
F190*tag* HsPrx3 C-terminal His_6-tag F190*tag*-Cter	M APAVTQHAPYFKGTAVVNGEFKDLSLDDFKGKYLVLFFYPLDFTFVCPTE IVAFSDKANEFHDVNCEVVAVSVDSHFSHLAWINTPRKNGGLGHMNIALL SDLTKQISRDYGVLLEGSGLALRGLFIIDPNGVIKHLSVNDLPVGRSVEE TLRLVKAFQYVETHGEVCPANWTPDSPTIKPSPAASKEY-QKVNQ MENLYFQGGTHHHHHH

Table 7.5: Protein names with the corresponding amino acid sequences, as single letter identifiers, designed to be expressed from the pET 24a (kanamycin resistance). The following features are coloured as follows: histidine tag (pink), linker region (blue), TEV protease cleavage site (green); native protein sequence (black). Mutated residues are highlighted in yellow, with a dash (-) indicating the presences of the "tag" amber stop codon.

Y10*tag* HsPrx3 N-terminal His_6-tag (Y10*tag*-Nter)	MHHHHHHGKPIPNPLLGLDSTENLYFQGIDPFT APAVTQHAP-FKGTAVVNGEFKDLSLDDFKGKYLVLFFYPLDFTFVCPTE IVAFSDKANEFHDVNCEVVAVSVDSHFSHLAWINTPRKNGGLGHMNIALL SDLTKQISRDYGVLLEGSGLALRGLFIIDPNGVIKHLSVNDLPVGRSVEE TLRLVKAFQYVETHGEVCPANWTPDSPTIKPSPAASKEYFQKVNQ
Y160*tag* HsPrx3 N-terminal His_6-tag (Y160*tag*-Nter)	MHHHHHHGKPIPNPLLGLDSTENLYFQGIDPFT APAVTQHAPYFKGTAVVNGEFKDLSLDDFKGKYLVLFFYPLDFTFVCPTE IVAFSDKANEFHDVNCEVVAVSVDSHFSHLAWINTPRKNGGLGHMNIALL SDLTKQISRDYGVLLEGSGLALRGLFIIDPNGVIKHLSVNDLPVGRSVEE TLRLVKAFQ-VETHGEVCPANWTPDSPTIKPSPAASKEYFQKVNQ
F190*tag* HsPrx3 N-terminal His_6-tag (F190*tag*-Nter)	MHHHHHHGKPIPNPLLGLDSTENLYFQGIDPFT APAVTQHAPYFKGTAVVNGEFKDLSLDDFKGKYLVLFFYPLDFTFVCPTE IVAFSDKANEFHDVNCEVVAVSVDSHFSHLAWINTPRKNGGLGHMNIALL SDLTKQISRDYGVLLEGSGLALRGLFIIDPNGVIKHLSVNDLPVGRSVEE TLRLVKAFQYVETHGEVCPANWTPDSPTIKPSPAASKEY-QKVNQ

7.2.4 Bacterial strains

The *E. coli* bacterial strains used for plasmid propagation (Table 7.6) and protein expression (Table 7.7) are described below. These cells were all propagated from the original commercial stock (Life Technologies) and made chemically competent in-house (Section 7.2.5). All bacteria were snap frozen using liquid nitrogen and stored at -80 °C.

Table 7.6: The *E. coli* strains used for plasmid propagation. *originally purchased from Stratagene.

E. coli strain	Genotype	Antibiotic resistance
XL1Blue*	*recA1 endA1 gyrA96 thi-1 hsdR17 supE44 relA1 lac* [F' *proAB lacI*^{q}*ZΔM15* Tn10 (Tet^{r})]	tetracycline
DH5α	F^{-} Φ80*lac*ZΔM15 Δ(*lac*ZYA-*arg*F) U169 *rec*A1 *end*A1 *hsd*R17 (rK–, mK+) *pho*A *sup*E44 λ– *thi*-1 *gyr*A96 *rel*A1	none

Table 7.7: The *E. coli* strains used as expression hosts for protein production. These cells contain a gene for T7 RNA polymerase making them compatible with pET vectors (Section 7.2.3) for protein over expression. Specifically, BL21 (DE3) cells were transformed with pET 11a and pET 24a vectors, whereas Rosetta (DE3) cells were transformed with pET 151-D-TOPO vectors. Rosetta (DE3) cells contains a pRARE plasmid, with chloramphenicol resistance, that encodes for tRNA synthetases found in human protein production for codons that are not often used in *E. coli.*

E. coli strain	Genotype	Antibiotic resistance
BL21 (DE3)	F' *ompT hsdS$_B$* (r_B^- m_B^-) *gal dcm* (DE3)	None
Rosetta (DE3)	F' *ompT hsdS$_B$* (r_B^- m_B^-) *gal dcm* (DE3) pRARE (Cam^{R})	Chloramphenicol

7.2.5 Chemically competent cell preparation

All chemically competent cell strains were prepared using a modified $CaCl_2$ method (Chan *et al*, 2013). Thawed bacterial stocks were plated on LB agar and incubated at 37 °C for 16-20h to allow for colonies to form. A single colony was picked and transferred into 10 mL LB media and this seed culture was incubated for 16-20h at 37 °C, 180 rpm. 50 mL LB was inoculated with 500 µL seed culture, and bacteria cells were grown at 37 °C, 180 rpm until OD_{600}= 0.4-0.6 (as measured on Spectramax M5 spectrophotometer), when the cells were rapidly cooled on ice, and were kept on ice for the rest of the preparation. Bacterial cells were spun down at 4 °C, 3000 xg for 5 min. Supernatant was carefully discarded, and cells were gently resuspended in 25 mL ice-cold 0.1 M $CaCl_2$. Resuspended cells were incubated on ice for 1 h, then centrifuged at 4000 xg, 8 min, 4 °C. The supernatant was carefully removed and cells were resuspended in ice-cold 0.1 M $CaCl_2$, 15% (v/v) glycerol. 100 µL aliquots were snap frozen using liquid nitrogen and stored at -80 °C.

Both the cells stocks used to generate new competent cells, as well as the freshly made competent cells were plated on LB agar containing the range of antibiotics used routinely in the lab. These act as controls to ensure no contaminating cells were present before or after this protocol.

7.2.6 Bacterial transformation protocol for chemically competent cells

50 µL aliquots of competent cells were thawed on ice before the additions of approximately 100 ng plasmid DNA. The DNA and cells were incubated on ice for 5 min, before heat shock treatment at 42 °C for 90 s, after which they were immediately transferred back onto ice. 350 µL LB medium was added and the cells were incubated at 37 °C, 200 rpm for at least 30 minutes to allow time for the transformed bacteria to express their antibiotic resistance genes. 30 µL recovered cells were spread onto LB agar plates containing appropriate selection antibiotics. The plates were incubated at 37 °C for 16-20 h, when colonies appeared, indicating successfully transformed cells.

7.2.7 Plasmid propagation and isolation from *E. coli*

All plasmids were amplified by transforming the desired DNA plasmids into either chemically competent XL1Blue or DH5α cells (Section 7.2.6). A single colony was picked and grown in 10 mL LB media containing appropriate antibiotics for 16-20h at 37 °C, 200 rpm. Plasmids were isolated from this bacterial cell culture using a commercial kit (QIAprep Spin Miniprep kit, QIAGEN) according to manufacturer's instructions. The plasmids were collected in the supplied elution buffer and stored at -20 °C.

7.3 Recombinant protein expression in *E.coli*

7.3.1 Small-scale test expressions for optimising protein expression

Chemically competent cells, either BL21 (DE3) or Rosetta (DE3) cells, were freshly transformed with the desired pET plasmid (Section 7.2.6; Table 7.7). The protocol for a standard expression is as follows. A single colony was picked and grown in 10 mL LB media containing appropriate antibiotics for 16-20h at 37 °C, 200 rpm. 20 mL LB was inoculated with 500 µL seed culture, and bacteria cultures were grown at 37 °C, 180 rpm until OD_{600}= 0.4-0.6. Protein production was induced upon the addition of 1mM IPTG (final concentration). The conditions that were varied, including protein expression conditions, are detailed in Table 7.8.

Table 7.8

Conditions varied	How it was varied?
Growth media used	See Table 7.1 for full list, otherwise specified in figure legends
Final IPTG concentrations	Ranged from 0.2 – 1 mM
Protein expression temperature and times	Flasks cooled before incubating cell culture at the following temperatures/time: 18 °C for 16-20 h; 37 °C for 3-5 h; 28 °C for 16 h

Cells were harvested via centrifugation at 4 °C, 5000 xg for20 min. Cells were lysed either using BugBuster® (Merck Millipore; as per manufacturer's instructions) or using sonication (Section 7.3.3). Total lysate was spun at 4 °C, 20000 xg for 15 min to separate out soluble and insoluble fractions, which were run on an SDS-PAGE gel (Section 7.6.2) to discern proteins present in each fraction. 8M urea was added to insoluble pellets to solubilise proteins to ensure distinct bands were seen on SDS-PAGE gel.

7.3.2 Large-scale expression of proteins

This is the established standard protocol for N-terminally His_6-tagged wild-type HsPrx3 protein expression. Chemically competent cells, either BL21 (DE3) or Rosetta (DE3) cells, were freshly transformed with the desired pET plasmid (Section 7.2.6; Table 7.7). A single colony was picked and grown in 10 mL LB media containing appropriate antibiotics for 16-20h at 37 °C, 200 rpm. 500 mL LB was inoculated with 5 mL seed culture, and bacteria cultures were grown at 37 °C, 180 rpm until OD_{600}= 0.4-0.6. Flasks containing bacterial cultures were cooled to at least room temperature before protein production was induced upon the addition of 1mM IPTG (final concentration).

Induced bacteria were incubated with shaking at 200 rpm at 18 °C for 16-20h. Cells were harvested by centrifugation at 5000 xg for 20 minutes into pellets. The supernatant was carefully discarded and cell pellets were resuspended in buffer A (Table 7.9 in Section 7.4.1) before further lysis, or storage at -20 °C until use.

7.3.2.1 The expression of unnatural amino acid proteins

The method development, detailed in Chapter 5, uses H-4-Azido-Phe-OH reagent (Bachem F3075).

7.3.3 Cell Lysis

All cell lysis was performed either on ice or at 4 °C. Methods of cell lysis were chosen depending on the size of each protein preparation. BugBuster® or sonication using the smallest probe were employed for lysis of trail expressions. Large pellets of bacterial cells were lysed using sonication with the larger probe or the cell disruptor.

7.3.3.1 BugBuster® protein extraction reagent

BugBuster® protein extraction reagent was used, according to the manufacturer's instructions, to resuspend small cell pellets from the small-scale protein test expressions. This reagent was used for a high-throughput check for overexpression of desired proteins in cell lysates. It was important to follow these instructions to achieve complete cell lysis, otherwise soluble proteins may incorrectly appear in the insoluble fraction. Sometimes the protein of interest was unstable in the presence of BugBuster®, causing these proteins to precipitate and appear insoluble, when they might not be in the correct buffer conditions. Therefore, sonication was the preferred method for cell lysis, after overexpression of protein bands was established using BugBuster®.

7.3.3.2 Sonication

Cell pellets were thawed and resuspended in approximately 3 mL/g of cell pellet in buffer A (Table 7.9). Proteolytic activity was inhibited by the addition of 1 cOmplete™, EDTA free protease inhibitor tablet per 50 mL of cell resuspension. Sonication with either the micro-probe for volumes < 5 mL, or the large probe for volumes > 50 mL. Sonication occurred on ice using a UP200S Ultrasonic Processor (Hielscher) at 65% amplitude, 0.5 s on, 0.5 s off, for 15 min.

7.3.3.3 Cell disruptor

Cell pellets were thawed and resuspended in approximately 5 mL/g of cell pellet in buffer A (**Table 7.9**). Proteolytic activity was inhibited by the addition of 1 cOmplete™, EDTA free protease inhibitor tablet per 50 mL of cell resuspension. The mechanical cell disruptor (Microfluidics™) was washed and equilibrated with buffer A before the addition of resuspended cell solution.

7.4 Protein purification

7.4.1 Buffers and equipment

The following chromatographic techniques were performed using AKTA protein purification systems, peristaltic pumps and gravity flow methods. The standard purification buffers used for N-terminally His_6-tagged wild-type HsPrx3 protein are listed in **Table 7.9**. Protein purification procedures can be conducted at 4 °C or 25 °C with similar yields in pure protein. Prior to any procedure, all columns and resins used in gravity flow were pre-equilibrated with at least three column volumes of initial purification buffer. Prior to sample being loaded onto any columns, they were passed through a 0.22 µm filter.

Table 7.9

Buffer	Composition
IMAC buffer A	20 mM HEPES, pH 8.0; 150 mM NaCl; 25 mM imidazole
IMAC buffer B	20 mM HEPES, pH 8.0; 150 mM NaCl; 500 mM imidazole
SEC buffer C	20 mM HEPES, pH 8.0; 150 mM NaCl; 2 mM TCEP
Storage buffer D	20 mM HEPES, pH 8.0; 150 mM NaCl; 2 mM TCEP; 5% glycerol

7.4.2 Immobilised affinity chromatography (IMAC)

Since recombinant HsPrx3 proteins are His_6-tagged, immobilised affinity chromatography (IMAC) was used as the initial purification step for these proteins. Bacterial lysate was loaded through either a 1 mL or 5 mL HisTrap FF column using a peristaltic pump. Columns were washed with at least five column volumes of buffer A (**Table 7.9**), before buffer B was used to elute off proteins remaining attached to the Ni^{2+} column. Fractions corresponding to any 280 nm absorbance peaks were analysed by SDS-PAGE for protein of interest prior to being pooled.

7.4.3 Preparative size exclusions chromatography (SEC)

Depending on the amount of protein to be loaded onto the SEC column, either a HiLoad Superdex200 16/60 120 mL or Superdex200 10/300GL 24 mL columns were used for size exclusion chromatography. Pooled proteins were concentrated to either 500 µL or 2 mL and injected into pre-equilibrated 24 mL or 120 mL columns, respectively. Eluted fractions corresponding to the 280 nm absorbance peak were analysed by SDS-PAGE for protein of interest prior to being pooled.

Purified His_6-tagged HsPrx3 proteins were either concentrated (Section 7.5.2) and then stored (Section 7.5.1) for later use, or the His_6-tag was removed using rTEV protease (Section 7.5.3).

7.5 Other protein manipulations

7.5.1 Protein storage and handling

Freshly purified proteins, whether it be His_6-tagged or cleaved protein, were kept in storage buffer D (Table 7.9) and flash frozen using liquid nitrogen and stored at -80 °C. Proteins could be buffer exchanged into storage buffer D, but often 50% glycerol stock was added directly into the purified protein mix to a final concentration of approximately 5%.

As a general rule, it was best to use freshly thawed proteins for every experiment. These proteins were buffer exchanged into fresh buffer required for the particular experiment (Section 7.5.2). However, purified proteins could be kept at 4 °C under reducing conditions (buffer C, Table 7.9) for a few hours without detrimental effects to quaternary structure or function.

7.5.2 Concentrating proteins and buffer exchange

In order to concentrate purified proteins, Vivaspin® centrifugal spin concentrators with PES membranes at the appropriate molecular weight cut off were used (Sartorius).

Spin concentrators were also a method used for buffer exchange, where samples were concentrated then diluted with the new buffer and re-concentrated repetitively. This method took time for viscous solutions at high protein concentration and was not particularly effective for low concentrations of protein, as protein can become attached to the spin filter membrane.

Buffer exchange for small volumes of protein solution from 0.5 – 2 mL was achieved using Slide-a-Lyzer™ MINI dialysis buttons with the correct molecular weight cut off (ThermoFisher Scientific). These buttons were placed in at least 1 L of new buffer and left for at least 3 h with stirring of buffer. Dialysis overnight was done to achieve complete buffer matching of proteins to the new buffer.

Complete buffer exchange was also be achieved using the SEC column (Section 7.4.3). Micro Bio-Spin™ P6 Gel disposable buffer exchange columns (Bio-Spin6 columns, BioRad) were pre-equilibrated with buffer of interest, and buffer exchange performed according to manufacturer's instructions. Buffer exchange using Bio-Spin6 columns was a fast process, and was used in both native mass spectrometry (Chapter 3) and for the activity assays (Chapter 4, Section 4.5).

7.5.3 His_6-tag removal using recombinant TEV protease

7.5.3.1 rTEV protease expression and purification

Recombinant tobacco etch virus (rTEV) protease was purified using a modified method inspired by Blommel and Fox, 2007. pRK793 encodes for the rTEV protease gene with a C-terminal His_6-tag, followed by a TEV cleavage site, then an MBP-tag, which was co-expressed to improve solubility of the rTEV-MBP construct (Blommel *et al*, 2007). Glycerol stocks of *E. coli* BL21 RILP transformed with pRK793 were plated onto LB agar containing kanamycin and chloramphenicol. Seed cultures and large-scale protein expression was performed (Section 7.3.2), followed by cell lysis by sonication (Section 7.3.3.2), with the following modifications of buffers (Table 7.10). In order to remove insoluble proteins and cell debris, the lysate was spun at 18000 xg, 30 min, 4 °C. The supernatant, or soluble protein, was incubated at 4 °C for at least 5 h to allow self-cleavage of rTEV-MBP construct and the separation of MBP from the rTEV-His_6-tag. Successful self-cleavage was determined by SDS-PAGE gel before proceeding. rTEV protease was purified from the soluble lysate using IMAC (Section 7.4.2), and then buffer exchanged using SEC into rTEV storage buffer (Table 7.10). The isolation of pure protein was confirmed using SDS-PAGE as a single band at ~ 28 kDa.

Table 7.10: Buffers for rTEV purification

Buffer	Composition
IMAC buffer A –rTEV	20 mM HEPES, pH 8.0; 150 mM NaCl; 25 mM imidazole; 0.3 mM TCEP
IMAC buffer B –rTEV	20 mM HEPES, pH 8.0; 150 mM NaCl; 500 mM imidazole; 0.3 mM TCEP
rTEV storage buffer	20 mM HEPES, pH 8.0; 150 mM NaCl; 5% glycerol; 3 mM TCEP

7.5.3.2 rTEV protease cleavage of His_6-tags from other recombinant proteins

rTEV protease was routinely used to remove the His_6-tags from the HsPrx3 constructs, which all contained rTEV protease cleavage sites between the histidine tags and the protein sequence (Tables 7.3 – 7.5). Purified HsPrx3 proteins in buffer C (Table 7.9), contained the reducing agent, TCEP, required for correct rTEV protease function. Otherwise, buffer exchange of His_6-tagged HsPrx3 into storage buffer (Table 7.9) were required before commencing. rTEV protease and His_6-tagged HsPrx3 proteins were mixed at approximately 1:20 ratio, and incubated at 4 °C for 16-20 h. This protein mix was incubated with Co^{2+} HisPur resin pre-equilibrated with buffer C (Table 7.9) for 5 min at 25 °C. The cleaved protein was in the flow through, whereas the His_6-tagged rTEV and cleaved His_6-tags bound to the resin. It was important to ensure there was sufficient resin to bind rTEV protease and cleaved tags, according to the manufacturer's instructions. The resin was washed with five column volumes of buffer C. The washes and flow through contained only cleaved HsPrx3 protein, verified as single bands at ~23 kDa on SDS-PAGE gels. This protein was then concentrated (Section 7.5.2) to ~ 10 mg/mL before storage (Section 7.5.1).

7.5.4 Testing protein stability in different ammonium acetate concentrations

In order to rapidly test the solubility of HsPrx3 proteins in different ammonium acetate concentrations, a 10 mg/mL aliquot of protein was diluted to 1 in 20 using different concentrations of pH 8.0 ammonium acetate solutions (10 mM, 50 mM, 100 mM and 200 mM). The samples were spun at 20000 xg for 10 minutes to remove precipitated proteins. This was done at 0 h, and also after 5 h and 25 h. 5 µL supernatant was run on an SDS-PAGE gel to visually check amounts of soluble proteins present.

7.6 Protein characterisation

7.6.1 Determination of protein concentration

UV absorbance of aromatic amino acids at 280 nm provides a direct method for quantifying protein concentration, as long as the solution contained pure protein that is not bound to co-factors that adsorb in this region. The UV measurement was routinely done using a Nano-Drop-1000 spectrophotometer. Protein concentrations exceeding 5 mg/mL were diluted to get a more

accurate absorbance reading. The extinction coefficient for each protein was measured using ExPASy ProtParam tool (http://web.expasy.org/protparam/). The Beer-Lambert law was used to convert the absorbance into concentration.

For crystallographic screens, the Cary-4000 spectrophotometer instrument was used for accurate measurements of absorbance at 280 nm of protein solutions. Approximately 150 µL of diluted protein solution was scanned from 230-500 nm, with blank subtraction, to gain a more accurate measurement of absorbance at 280 nm. The absorbance peak was below 1 to ensure that the measurement was in the linear range of the spectrophotometer.

7.6.2 Sodium dodecyl sulfate polyacrylamide gel electrophoresis (SDS-PAGE)

All reagents for SDS-PAGE were supplied by ThermoFisher Scientific (Table 7.11). This technique was routinely used to assess the purity of proteins and their MW. Samples were mixed with 2x loading buffer and heated to 95 °C for 5 min to denature samples. Samples were centrifuged prior to loading onto gels. The gels were run at 165 mV, 275 mA for 35 minutes.

Table 7.11: Reagents used for SDS-PAGE

Components	Details or methods
Gel	Bolt™ 4-12 % Bis-Tris Plus Gels, 10-well or 15 well gels (Invitrogen)
Buffer	Bolt® MES running buffer allows for a separation range of 3.5 kDa to 160 kDa
2x loading buffer stocks (reducing/non-reducing)	For 5 mL of loading buffer: 2.5 mL NuPAGE® LDS Sample Buffer (4x); ± 1 mL 500 mM DTT; making the rest up with MilliQ to 5 mL This buffer was pre-mixed and stored at -20 °C
Molecular weight ladder	Novex® Sharp Pre-stained Protein Standard (Life Technologies)

The gels were stained using Coomassie Blue solution (1 g/L Coomassie R250 in MilliQ with 10% glacial acetic acid and 40% ethanol) for 30 min, before destaining for 1h using the destain solution (MilliQ with 10% glacial acetic acid and 40% ethanol). Complete destaining was achieved when gels are rinsed in MilliQ water overnight. Gels were imaged using a document scanner.

7.6.3 Western blot immunodetection

Western blots were employed to identify the presence of His_6-tags on proteins using a commercially available set up by Invitrogen that enables this to be done within one day. The full list of reagents used is in Table 7.12. Two identical SDS-PAGE gels were run containing the protein of interest (Section 7.6.2). One gel was Coomassie stained to in order to detect other proteins present without a His_6-tag, whereas the other was used for the Western blot. Protein bands were transferred onto PVDF membranes using Program 5 on the iBlot® 2 system according to the manufacturer's instructions. The PVDF membranes were blotted with 4 µL primary antibody and 10 µL secondary antibodies using the iBind™ Flex Western system according to manufacturer's instructions (Table 7.11) – this system also removes the need to wash the membrane repetitively or blot with milk powder. The iBind™ step was left for approximately 6 hours before proceeding to detection.

Table 7.12: Reagents and instruments used for Western blotting

Components	Details or methods (Catalogue number)
Transfer device	iBlot® 2 Gel Transfer Device (IB21001)
Transfer membrane	iBlot® 2 Transfer Stacks, PVDF, mini or regular size depending on number of gels used. (IB24001 or IB24002)
Western blotting device	iBind™ Flex Western Device (SLF2000)
Western blotting reagents	iBind™ Flex Cards (SLF2010); iBind™ Flex Solution Kit (SLF2020)
Chemiluminescence detection kit	Enhanced Chemiluminescence Western Blotting Detection Kit (Amersham; RPN2108)
Primary antibodies	Anti-His_6-tag mouse monoclonal antibody (Abcam; ab18184) Anti-His C-term mouse monoclonal antibody (Invitrogen)
Secondary antibody	Mouse IgG, HRP-linked from sheep (part of Amersham kit)

Chemiluminescence detection was achieved using a Western Blotting Detection Kit (Amersham; RPN2108) according to the manufacturer's instructions. Briefly, equal volumes of Enhanced Chemiluminescence detection solutions 1 and 2 were mixed and 1.5 mL of this mix was used per membrane. This mix is poured onto the membrane and allowed to stand at room temperature for 60 s before an image was taken using the ImageQuant LAS-4000 (Fujifilm) in chemiluminescence mode with a 45 s exposure time.

7.7 Biophysical techniques – solution studies

7.7.1 Circular dichroism

Purified proteins were diluted into MilliQ water to ~ 0.2 mg/mL prior to addition into a 1 mm path length quartz cuvette kept at 20 °C. The Jasco J815 circular dichroism spectrophotometer was used to record wavelength scans between 180 nm and 260 nm in 2 nm increments. The background MilliQ data were subtracted from the sample data, and any data exceeding 600 V was removed. The data were converted to mean residue ellipticity by multiplying with a conversion factor (**Equation 1**) and plotted against wavelength (Greenfield, 2007).

Equation 1:

$$conversion\ factor = \frac{molecular\ weight\ \left(\frac{g}{mol}\right) * protein\ concentration\ (\frac{mg}{ml})}{number\ of\ amino\ acids * path\ length\ (mm)}$$

7.7.2 Analytical size exclusion chromatography with static light scattering (SEC-SLS)

Protein stocks were thawed and buffer exchange into appropriate buffers (**Section 7.5.2**). A Superdex200 Increase 10/300 GL (GE Healthcare) was connected to a Viscotek 302-040 Triple Detector GPC/SEC system (ATA Scientific) operated at 28 °C and equilibrated with said buffer. 100 µL of protein samples were injected into the column and eluted at a flow rate of 0.5 mL/min. The absolute molecular weight was calculated from the refractive index and right-angle light scattering measurements calibrated against bovine serum albumin (BSA) (66.5 kDa, Sigma). BSA was run either side of the protein sample sequence to ensure consistency throughout the sample sequence in experiments which would take a few hours. Calibration and calculations of absolute MWs were done on *OmniSEC* (Malvern Company).

7.7.3 Small angle X-ray scattering (SAXS)

Small angle X-ray scattering (SAXS) data were collected on the SAXS/WAXS beamline (Australian Synchrotron), equipped with a Dectris-Pilatus 1M detector (170 mm × 170 mm, effective pixel size, 172 × 172 µm). The X-ray wavelength was 1.0332 Å and the sample detect distance of 16000 mm

was used, providing a q range of 0.006-0.4 $Å^{-1}$ (where q is the magnitude of the scattering vector, which is related to the scattering angle (2θ) and the wavelength (λ) as follows: $q = (4\pi/\lambda)\sin\theta$). For all proteins analysed, 50 µL of protein sample at approximately 10 mg/mL was injected into a Superdex200 5/150 GL column, pre-equilibrated with buffer. This size exclusion chromatography occurred prior to eluted samples being transferred into 1.5 mm glass capillary, kept at 20 °C, for data collection at 2 second intervals.

Two dimensional intensity plots were radially averaged, normalised to sample transmission, and background subtracted using *Scatterbrain* software (Australian Synchrotron). All subsequent SAXS analyses were performed using the ATSAS version 2.3 software package (Petoukhov *et al*, 2012). *PRIMUS* was used to determine Guinier plots to assess data quality (Konarev *et al*, 2003). *GNOM* was used to perform indirect Fourier transformation of the scattering data to generate the P(r) distribution (Svergun, 1992). *CRYSOL* was used to generate theoretical scattering curves from atomic coordinates, and compared these to the experimental scattering curves (Svergun *et al*, 1995).

7.7.4 Analytical ultracentrifugation (AUC)

Proteins were buffer exchanged into buffer of interest using SEC or Bio-Spin6 columns (Section 7.5.2). 400 µL of reference buffer and 380 µL of sample solutions were loaded into 12 mm double sector cells with quartz or sapphire windows and mounted in an An-60 Ti eight-hole rotor. Larger blank volume was required to accurately place the meniscus of the sample (Cole *et al*, 2008). Sedimentation velocity experiments were performed in an XL1 Analytical Ultracentrifuge (Beckman Coulter; Lebowitz *et al*, 2002). Depending on the protein and the concentrations used, the absorbance optical system was set in the range of 230-285 nm. Initial scans performed at 3000 rpm were used to determine optimal radial settings and wavelengths. Proteins were centrifuged at 20 °C at a various rotor speeds, depending on the size of the sample (Table 7.13). Radial absorbance data were collected at a single wavelength without averaging, using a 0.003 cm step size for a total of at least 70 scans. All data were collected at 20 °C. *SEDINTERP* was used to calculate the partial specific volume of both wild-type and S78C HsPrx3 (0.7423 g/mL and 0.7401 g/mL, respectively), the solvent density (1.006 g/mL) and viscosity (0.01031 poise) (Laue *et al*, 1992). Data were fitted to a continuous c(s) distribution model at a resolution of 300 and a confidence level of 0.95 using *SEDFIT* (Schuck and Rossmanith, 2000). Data was fitted with an *s* value ranging between 2 S and 12 S. The fit resulted in a frictional ratio (f/f_0) of 1.1678 for wild-type HsPrx3 and 1.3634 for S78C HsPrx3.

Table 7.13:

Figure number	Sample name	Rotor speed (rpm)	Wavelength (nm)
Figure 3.2	Cleaved wild-type, pH 8.0	42000	285
Figure 3.6 C	Cleaved wild-type, pH 4.0	30000	285
Figure 3.7 C	His_6-tagged wild-type, pH 4.0	24000	280
Figure 3.11	Cleaved and His_6-tagged wild-type, pH 4.0	24000	280
Figure 4.7	His_6-tagged S75E mutein	50000	280
Figure 4.17	Cleaved S78C mutein	45000	231

7.8 X-ray crystallography

7.8.1 Crystallisation

Crystallisation trials were performed using freshly purified proteins, or thawed proteins that have been subjected to fresh buffer exchange via SEC. Proteins were concentrated to greater than 40 mg/mL (Section 7.5.2), and precise concentration was verified (Section 7.6.1), before dilution to desired concentration ranges. The preparation and incubation of all plates occurred at 20 °C with a relative humidity of 85%.

7.8.1.1 Initial robot screens

Initial protein crystallisation screens were set up as sitting-drop vapour diffusion experiments. Screening was carried out against six sets of 96-conditions (total of 576 conditions) prepared in-house (by Dr Ivan Ivanovich, University of Auckland) based on precipitant solutions from a variety of screens, including: Hampton Sparse Matrix I and II, Hampton MPD, Precipitant Synergy, Clear Strategy, Top67, PEG/pH, PEG/ion, Stura Footprint, and MORPEUS (Moreland *et al*, 2005). The MultiPROBE II HT/EX liquid-handling robot (Perkin-Elmer) was used to dispense 70 µL in-house screen into 96-well Intelli-Plates (Hampton Research; 100 µl/reservoir). The Oryx4 Protein Crystallisation Robot (Douglas Instruments) dispensed protein solutions and mixed this with the reservoir solutions at a 2:1 and 1:1 ratio, with final droplet volumes being 0.45 nL and 0.3 nL respectively. The plates were sealed and monitored for crystal growth. Crystals were observed for wild-type HsPrx3 after 2 weeks resulted in diffraction (Chapter 2).

7.8.1.2 Crystal optimisation: making fine screens

Once a promising crystal was found from this initial screening, optimisation was carried out. Promising conditions were checked for reproducibility by repeating the sitting-drop vapour diffusion experiments manually in CrystalClear P™ strip, with crystallisation buffers taken from the 96-well plates. Often crystals could not be reproducibly grown, as hand pipetting and in-house 96-well plates are not exactly the same as previous plates. In order to explore slight differences in pipetting that could occur when making screen, fine screens were made that had incremental changes to certain precipitant concentrations and pH. In particular, a fine screen was made around condition D12 of the MORPHEUS screen (Gorrec, 2009), which contained 96 slight variations to this condition, and was made up in a 96-well deep-well plate (Appendix B). The same method was used as above to combine protein sample solutions with reservoir solution in a sitting-drop vapour diffusion set up. This yielded diffracting crystals for S78C HsPrx3 after 2 weeks (Chapter 4, Section 4.4.2).

Other methods for crystal optimisation attempted for S75E HsPrx3 included using hanging-drop vapour diffusion in 24-well VDX plates (Hampton Research). Where 2 µL drops were manually set up as 1:1 protein:crystallisation buffer and were equilibrated with 500 µL reservoir solution in sealed wells. However, none of these conditions were fruitful (Chapter 4, Section 4.3.2).

7.8.1.3 Is it salt or protein crystals?

Crystal formation in the initial screens, although promising, does not necessarily mean it is proteinaceous. In fact, salt crystals often appear. The definitive way to test for salt crystals is by observing the crystal diffraction patterns, if the crystals diffract at all. Many crystals especially that of S75E HsPrx3 did not diffract (Chapter 4, Section 4.3.2). In order to rule out salt crystals, Izit Crystal Dye (Hampton Research) was employed to test the nature of crystals. Crystals in question were manipulated and washed twice in reservoir solution, before 0.1 uL of Izit Dye was added to the solution containing washed crystals. The dye is a small molecule that penetrates solvent channels of macromolecular crystals, colouring protein crystals blue and leaves salt crystals colourless. Crystals can also be manipulated, washed in reservoir solutions twice and loaded onto an SDS-PAGE gel for observations of any protein bands (Section 7.6.2). However, since protein crystals are often so small, they would contain low amounts of proteins which result in very faint bands, if any.

7.8.2 Crystal preparation

Crystals were mounted onto cryo-loops (Hampton Research) of appropriate sizes for the crystal of interest and briefly soaked in cryoprotectant solution (usually 20% glycerol added to the reservoir solution) before being flash cooled in liquid nitrogen. Cryo-protectant and rapid flash cooling technique was required in order to prevent build-up of ice crystals that disrupt crystal order. This step was successfully performed by Dr Dave Goldstone for the wild-type HsPrx3 crystal and by Dr Jeremy Keown for the S78C HsPrx3 crystal. Crystals were maintained at -173 °C.

7.8.3 Crystal diffraction and data collections

X-ray diffraction data were collected on the MX2 micro crystallography beamline, equipped with an ADSC Quantum 315r Detector, at the Australian Synchrotron. The beamline was controlled using the Blu-Ice interface and are equipped with SAM loading robots that mounts crystals onto the goniometer under a constant stream of liquid nitrogen (McPhillips *et al*, 2002)

7.8.4 Data processing

MOSFLM was used to index and integrate data (Battye *et al*, 2011). *POINTLESS* was used for unit cell and space group prediction (from CCP4 program suite; Evans, 2006). *AIMLESS* was employed to scale and merge equivalent measurements (Evans, 2011; Evans and Murshudov, 2013). Appropriate high resolution limits were determined by comparing statistical parameters such as R_{merge}, R_{pim}, mean I/σ(I), completeness and $CC^{1/2}$ (Karplus and Diederichs, 2012, Evans, 2006).

As an estimate of the number molecules in the asymmetric unit was obtained using the *MATTHEWS COEFFICIENT* program (Matthews, 1968; Kantardjieff and Rupp, 2003).

7.8.5 Model building and refinement

Molecular replacement was used to estimate the phases from a search model using *Phaser* (McCoy 2007). Structure refinement was performed on *REFMAC5* (Murshudov *et al*, 2011). Iterative improvement of both the map and the model was performed using alternative cycles of refinement and residue-by-residue analysis in *COOT* (Emsley *et al*, 2004). *COOT* was used to manually reposition residues to better fit electron density as well as to check residue identities by exploiting

known sequences of these recombinant proteins. Water molecules were added during a round of refinement on *REFMAC5*, followed by manual assessment for the fit of these waters into the observed spherical density map and whether they had appropriate hydrogen bonding. Following each round of refinement, the output residual factor (R_f) and free residual factor (R_{free}) were both monitored for a decrease, and until no significant reduction (> 0.010) was afforded by subsequent cycles. All final images were generated in *PyMOL* (The PyMOL Molecular Graphics System, Version 1.5.0.4 Schrödinger, LLC).

7.9 Mass spectrometry

7.9.1 Liquid chromatography mass spectrometry (LC-MS)

The masses of purified proteins were confirmed by LC-MS using an Agilent (Santa Clara, CA) 1260 infinity system equipped with an Agilent 6120 quadrupole mass spectrometer using electron spray ionisation in positive mode. Protein samples were mixed with 100% acetonitrile in 1:1 ratio and passed through a 0.22 µm filter (Section on filtration). A reverse phase column, Zorbix 300058-C3 (3.5 µm; 3 x 50 mm) column (Agilent), was pre-equilibrated (5% acetonitrile, 0.1% trifluoroacetic acid) prior to loading 20 µL protein solution onto the column. A linear gradient method was used with 5%-95% acetonitrile, with constant 0.1% trifluoroacetic acid, at a flow rate of 0.3 mL/min. Spectra was recorded and molecular weight was calculated as in “Box 2” from Glish and Vachet, 2003.

7.9.2 Top-down mass spectrometry and peptide mass spectrometry

Both top-down and peptide mass spectrometry were used as more precise checks for protein identity in Chapter 5. Top-down MS/MS allows for sequencing of proteins from the C-terminal end. A solution of purified protein in 20 mM HEPES pH 7.0, 150 mM NaCl was given to Martin Middleditch (Mass Spectrometry Facility, University of Auckland). The samples were run on a Linear Ion Trap- Fourier Transform mass spectrometer (Thermo Finnigan). Peptide mass spectrometry (MS) involves digesting proteins using proteases into peptides and using these peptide fragments to compare with how known protein sequences would fragment. Proteins were run on an SDS-PAGE gel (Section 7.6.2), and the band of interest was cut out and given to Martin Middleditch (Mass Spectrometry Facility, University of Auckland). Gel bands were detained and proteins extracted from the bands. These denatured proteins were digested with trypsin and GluC

proteases and the mix of peptides were examined with the TripleTOF® 6600 (SCIEX). All data analysis for both of these techniques was also performed in collaboration with Martin Middleditch (University of Auckland).

7.9.3 Native mass spectrometry

Native mass spectrometry (nMS) was used in Chapter 3 to probe the oligomeric state of HsPrx3 in the gas phase, and the experiments were performed at the University of Oxford, in collaboration with Prof. Dame Carol Robinson. HsPrx3 proteins were thawed and buffer exchanged into 100 mM ammounium acetate, pH 8.0 or pH 4.0, using a Bio-Spin6 columns (Section 7.5.2), then diluted to ~ 20 µM. Rapid dilution (of 1 in 20 for final concentration of 20 µM monomeric concentration) of concentrated protein at pH 8.0 to pH 4.0 ammonium acetate was also performed, with similar results to using buffer exchange columns. Nanoflow electrospray ionisation mass spectrometry (nESI-MS) was performed on a Synapt HDMS quadrupole time-of-flight mass spectrometer (Waters Corporation, Manchester, U.K.). 20 µM HsPrx3 was introduced to the spectrometer using gold-coated borosilicate capillaries prepared in-house as previously described (Nettleton *et al*, 1998).

Experiments were performed under positive ion mode, with the following instrument parameters: capillary voltage 1.35 kV; sample cone voltage 15 V; extraction cone voltage 1.0 V; source temperature 20 °C; ion trap collision energy 10 V; transfer collision energy 4 V; trap flow 3.5 mL/min (argon gas); ion mobility source 20 mL/min (argon gas); backing pressure 5.0 mBar (nitrogen gas).

Spectra were analysed using *MassLynx* software (Waters) and *UniDec* (Marty *et al*, 2015).

7.10 Peroxidase activity assay

7.10.1 Horse radish peroxidase competitive assay

7.10.1.1 Preparation of the reagents

HsPrx3 was concentrated to at least 20 µM, then reduced using 2 mM β-mercaptoethanol for 30 minutes. The reductant was removed by passing the protein through Bio-Spin6 columns twice (Hugo *et al*, 2009). To avoid oxidant contamination, activity assay buffer had argon gas bubbled through for at least 30 min prior to use, and experiments were performed within the hour of buffer exchange. The final HsPrx3 protein concentration was determined using the Nano-Drop (**Section 7.6.1**). The spectrophotometer was used to determine the concentration of H_2O_2 at a wavelength of 240 nm, ε_{240} = 43.6 $M^{-1}cm^{-1}$ and horse radish peroxidase (HRP) at a wavelength of 403 nm, ε_{403} = 1.02 x 10^7 $M^{-1}cm^{-1}$ (as per Ogusucu *et al*, 2007).

7.10.1.2 The assay

Reaction mixtures contained 10 µM HRP and 8 µM H_2O_2 with varying concentrations of peroxiredoxin (between 1 µM to 10 µM) in 100 mM potassium phosphate, 0.1 mM DTPA, pH 7.5 at 25 °C. Final reaction volume of 250 µL.

The reactions were triplicated in Geunier black well, clear-bottomed 96 well plates. Peroxiredoxin and HRP were pre-mixed, and the reaction was initiated when H_2O_2 was added. The absorbance measurements at 403 nm were taken after 2 minutes using plate reader on the Spectramax M5 spectrophotometer.

7.10.1.3 Data analysis

The HRP concentration was re-checked by dividing by ε_{403} = 1.02 x 10^7, and the values *F* and *1-F* were calculated (**Equation 2**). Along with k_{HRP} = 1.78 x 10^7 $M^{-1}s^{-1}$, the value of $\left(\frac{F}{1-F}\right) k_{HRP}[HRP]$ in s^{-1} can be calculated. The slope of the line derived from $\left(\frac{F}{1-F}\right) k_{HRP}[HRP]$ versus $[Prx]$, gives the second order rate constant, k_{Prx} in $M^{-1}s^{-1}$ (**Equation 2**; **Figure 7.1**). Fitting data points onto a linear plot was achieved using *Origin Pro 8.5* (OriginLab Corporation).

$$\left(\frac{F}{1-F}\right) k_{HRP}[HRP] = k_{Prx}[Prx] \qquad \text{Equation 2}$$

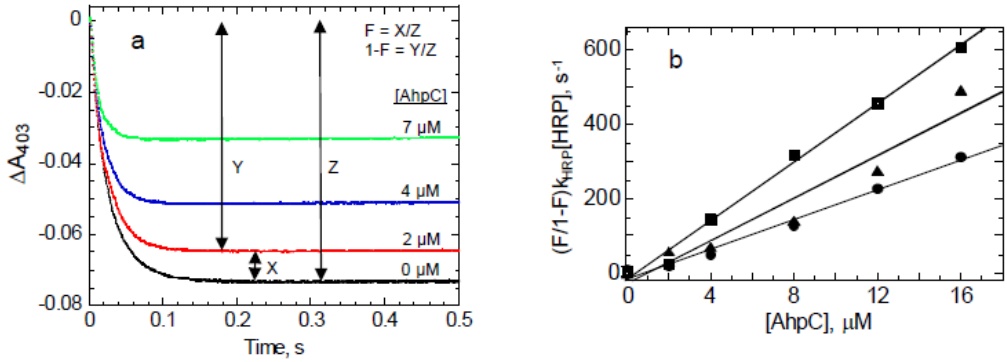

Figure 7.1: Data analysis to derive k_{Prx}

In this case, stop-flow experiments enable sub-second monitoring of reactions and the decrease in absorbance at 403 nm (left). **Equation 2** was used to derive $\left(\frac{F}{1-F}\right) k_{HRP}[HRP]$ in s^{-1} , and this was plotted against Prx concentration in µM (right). From this, a linear best fit line can be plotted, and the gradient is k_{Prx}. These diagrams are from Cox *et al*, 2009b. Permission pending.

7.10.2 Catalase competitive assay using SDS-PAGE

HsPrx3 proteins were incubated with 5 mM DTT for at least 30 min to fully reduce disulphide bonds, before reductant was removed using the Bio-Spin6 columns (**Section 7.5.2**). HsPrx3 and human catalase concentrations were determined using the Lowry assay (**Section 7.6.1**). The spectrophotometer was used to determine the concentration of H_2O_2 at a wavelength of 240 nm, ε_{240} = 43.6 $M^{-1}cm^{-1}$. These experiments were performed at 25 °C and in collaboration with Alexander Peskin (University of Otago).

Visualised using SDS-PAGE gels, human catalase (Sigma) was used to probe the range at which HsPrx3 activity towards H_2O_2 would occur. This was achieved by pre-mixing 5 µM reduced HsPrx3 with a range of human catalase concentrations (0.1, 0.2, 0.4, 0.8, 1.0, 2.0 µM). 5 µM H_2O_2 was added to the pre-mix, the samples mixed vigorously and any free cysteine residues were then capped with 20 µM NEM. Samples were mixed with loading buffer and run on an SDS-PAGE gel (**Section 7.6.2**). Visual inspection of the gels gave an indication of the relative rates of reaction between the catalase and the HsPrx3 in question.

7.10.3 Time course SDS-PAGE assay to monitor slow reaction rates towards H_2O_2

This experiment was used to probe the reaction rate of S75E HsPrx3 in **Chapter 4**. Again, HsPrx3 proteins were incubated with 5 mM DTT for at least 30 min to fully reduce disulphide bonds, before reductant was removed using the Bio-Spin6 columns (**Section 7.5.2**). HsPrx3 and human catalase concentrations were determined using the Lowry assay (**Section 7.6.1**). In this case, the catalase was used to stop the reaction between the slow HsPrx3 and H_2O_2 (Nagy *et al*, 2011). 5 µM H_2O_2 and 5 µM S75E HsPrx3 was used in each reaction, the reaction being stopped after 10, 20, 40, 60, 180 and 360 seconds after mixing. The samples were mixed with loading buffer and run on an SDS-PAGE gel (**Section 7.6.2**). The SDS-PAGE gel allowed the visual monitoring of the disappearance of the reduced monomeric species (Nagy *et al*, 2011).

The band intensities from the scanned gel were assessed using *ImageJ* and plotted, against time, as a percentage decrease when compared to the reduced protein. The data points were fitted in *Origin Pro 8.5* to an exponential equation: $y = A + B * e^{Cx}$, where C gives a pseudo-first order reaction rate in s^{-1}, which is corrected with the concentration of H_2O_2 (in this case, 5 µM) to get a second order reaction rate in $M^{-1}s^{-1}$ (Nagy *et al*, 2011).

References

Abdallh M, Bakir E, Yousif E (2014) Study the electrical conductivity of crosslinked polyester doped with different metal salts. *Journal of Saudi Chemical Society* **18**: 387-391

Adhikari RY, Malvankar NS, Tuominen MT, Lovley DR (2016) Conductivity of individual *Geobacter* pili. *RSC Advances* **6**: 8354-8357

Adimora NJ, Jones DP, Kemp ML (2010) A model of redox kinetics implicates the thiol proteome in cellular hydrogen peroxide responses. *Antioxidants & Redox Signaling* **13**: 731-43

Aeby E, Ahmed W, Redon S, Simanis V, Lingner J (2016) Peroxiredoxin 1 protects telomeres from oxidative damage and preserves telomeric DNA for extension by telomerase. *Cell Reports* **17**: 3107-3114

Afonine PV, Grosse-Kunstleve RW, Echols N, Headd JJ, Moriarty NW, Mustyakimov M, Terwilliger TC, Urzhumtsev A, Zwart PH, Adams PD (2012) Towards automated crystallographic structure refinement with *phenix.refine*. *Acta Crystallographica Section D* **68**: 352-367

Aggeli A, Bell M, Boden N, Keen JN, Knowles PF, McLeish TCB, Pitkeathly M, Radford SE (1997) Responsive gels formed by the spontaneous self-assembly of peptides into polymeric beta-sheet tapes. *Nature* **386**: 259-262

Ahnert SE, Marsh JA, Hernández H, Robinson CV, Teichmann SA (2015) Principles of assembly reveal a periodic table of protein complexes. *Science* **350**

Alberts B, Johnson A, Lewis J, Raff M, Roberts K, Walter P (2002) Molecular biology of the cell. *Garland Science*, New York

Aldaye FA, Sleiman HF (2007) Modular access to structurally switchable 3D discrete DNA assemblies. *J Am Chem Soc* **129**: 13376-13377

Amiram M, Haimovich AD, Fan C, Wang Y-S, Aerni H-R, Ntai I, Moonan DW, Ma NJ, Rovner AJ, Hong SH, Kelleher NL, Goodman AL, Jewett MC, Soll D, Rinehart J, Isaacs FJ (2015) Evolution of translation machinery in recoded bacteria enables multi-site incorporation of nonstandard amino acids. *Nature Biotechnology* **33**: 1272-1279

Amor-Mahjoub M, Suppini JP, Gomez-Vrielyunck N, Ladjimi M (2006) The effect of the hexahistidine-tag in the oligomerization of HSC70 constructs. *Journal of Chromatography B* **844**: 328-34

An BC, Lee SS, Jung HS, Kim JY, Lee Y, Lee KW, Lee SY, Tripathi BN, Chung BY (2015) An additional cysteine in a typical 2-Cys peroxiredoxin of *Pseudomonas* promotes functional switching between peroxidase and molecular chaperone. *FEBS Letters* **589**: 2831-2840

Angeles DC, Gan B-H, Onstead L, Zhao Y, Lim K-L, Dachsel J, Melrose H, Farrer M, Wszolek ZK, Dickson DW, Tan E-K (2011) Mutations in LRRK2 increase phosphorylation of peroxiredoxin 3 exacerbating oxidative stress-induced neuronal death. *Human Mutation* **32**: 1390-1397

Angelucci F, Bellelli A, Ardini M, Ippoliti R, Saccoccia F, Morea V (2015) One ring (or two) to hold them all. On the structure and function of protein nanotubes. *FEBS Journal* **282**: 2827-2845

Angelucci F, Saccoccia F, Ardini M, Boumis G, Brunori M, Di Leandro L, Ippoliti R, Miele AE, Natoli G, Scotti S, Bellelli A (2013) Switching between the alternative structures and functions of a 2-Cys peroxiredoxin, by site-directed mutagenesis. *Journal of Molecular Biology* **425**: 4556-4568

Aoyama S, Shimoike M, Hiratsuka Y (2013) Self-organized optical device driven by motor proteins. *Proc Natl Acad Sci USA* **110**: 16408-16413

Aquilina JA, Benesch JL, Ding LL, Yaron O, Horwitz J, Robinson CV (2005) Subunit exchange of polydisperse proteins: mass spectrometry reveals consequences of a αA-crystallin truncation. *The Journal of Biological Chemistry* **280**: 14485-91

Aran M, Ferrero D, Wolosiuk A, Mora-García S, Wolosiuk RA (2011) ATP and Mg^{2+} promote the reversible oligomerization and aggregation of chloroplast 2-Cys peroxiredoxin. *Journal of Biological Chemistry* **286**: 23441-23451

Ardini M, Giansanti F, Di Leandro L, Pitari G, Cimini A, Ottaviano L, Donarelli M, Santucci S, Angelucci F, Ippoliti R (2014) Metal-induced self-assembly of peroxiredoxin as a tool for sorting ultrasmall gold nanoparticles into one-dimensional clusters. *Nanoscale* **6**: 8052-61

Ardini M, Golia G, Passaretti P, Cimini A, Pitari G, Giansanti F, Leandro LD, Ottaviano L, Perrozzi F, Santucci S, Morandi V, Ortolani L, Christian M, Treossi E, Palermo V, Angelucci F, Ippoliti R (2016) Supramolecular self-assembly of graphene oxide and metal nanoparticles into stacked multilayers by means of a multitasking protein ring. *Nanoscale* **8**: 6739-6753

Arpino JAJ, Baldwin AJ, McGarrity AR, Tippmann EM, Jones DD (2015) In-frame amber stop codon replacement mutagenesis for the directed evolution of proteins containing non-canonical amino acids: identification of residues open to bio-orthogonal modification. *PLOS ONE* **10**: e0127504

Ashkenasy N, Horne WS, Ghadiri MR (2006) Design of self-assembling peptide nanotubes with delocalized electronic states. *Small* **2**: 99-102

Ashmead H (2016) Proteins as building blocks for biological nanomaterials. *University of Canterbury, Christchurch, New Zealand*, https://ir.canterbury.ac.nz/handle/10092/12830

Audette GF, van Schalk EJ, Hazes B, Irvin RT (2004) DNA-binding protein nanotubes: learning from nature's nanotech examples. *Nano Letters* **4**: 1897-1902

Backus EHG, Kuiper JM, Engberts JBFN, Poolman B, Bonn M (2011) Reversible optical control of monolayers on water through photoswitchable lipids. *The Journal of Physical Chemistry B* **115**: 2294-2302

Bai Y, Luo Q, Zhang W, Miao L, Xu J, Li H, Liu J (2013) Highly ordered protein nanorings designed by accurate control of glutathione s-transferase self-assembly. *J Am Chem Soc* **135**: 10966-10969

Balci S, Bittner AM, Hahn K, Scheu C, Knez M, Kadri A, Wege C, Jeske H, Kern K (2006) Copper nanowires within the central channel of tobacco mosaic virus particles. *Electrochimica Acta* **51**: 6251-6257

Ballister ER, Lai AH, Zuckermann RN, Cheng Y, Mougous JD (2008) *In vitro* self-assembly from a simple protein of tailorable nanotubes building block. *Proc Natl Acad Sci USA* **105**: 3733-3738

Baneyx F, Matthaei JF (2014) Self-assembled two-dimensional protein arrays in bionanotechnology: from S-layers to designed lattices. *Current Opinion in Biotechnology* **28**: 39-45

Baneyx F, Mujacic M (2004) Recombinant protein folding and misfolding in *Escherichia coli*. *Nature Biotechnology* **22**: 1399-1408

Banta S (2007) Engineering protein and peptide building blocks for nanotechnology. *J Nanosci Nanotechnol* **7**: 387-401

Baranova E, Fronzes R, Garcia-Pino A, Van Gerven N, Papapostolou D, Pehau-Arnaudet G, Pardon E, Steyaert J, Howorka S, Remaut H (2012) SbsB structure and lattice reconstruction unveil Ca^{2+} triggered S-layer assembly. *Nature* **487**: 119-122

Barranco-Medina S, Lazaro JJ, Dietz KJ (2009) The oligomeric conformation of peroxiredoxins links redox state to function. *FEBS Letters* **583**: 1809-16

Battye TGG, Kontogiannis L, Johnson O, Powell HR, Leslie AGW (2011) iMOSFLM: A new graphical interface for diffraction-image processing with MOSFLM. *Acta Crystallographica Section D* **67**: 271-281

Baud F, Karlin S (1999) Measures of residue density in protein structures. *Proc Natl Acad Sci USA* **96**: 12494-12499

Bell G (2016) Quantifying western blots: none more black. *BMC Biology* **14**: 116

Benesch JLP (2009) Collisional activation of protein complexes: picking up the pieces. *Journal of the American Society for Mass Spectrometry* **20**: 341-348

Benesch JLP, Aquilina JA, Baldwin AJ, Rekas A, Stengel F, Lindner RA, Basha E, Devlin GL, Horwitz J, Vierling E, Carver JA, Robinson CV (2010) The quaternary organization and dynamics of the molecular chaperone HSP26 are thermally regulated. *Chemistry & Biology* **17**: 1008-1017

Berg M, Michalowski A, Palzer S, Rupp S, Sohn K (2014) An *in vivo* photo-cross-linking approach reveals a homodimerization domain of Aha1 in *S. cerevisiae*. *PLOS One* **9**: e89436

Bernstein SL, Dupuis NF, Lazo ND, Wyttenbach T, Condron MM, Bitan G, Teplow DB, Shea JE, Ruotolo BT, Robinson CV, Bowers MT (2009) Amyloid-β 2 protein oligomerization and the importance of tetramers and dodecamers in the aetiology of Alzheimer's disease. *Nature Chemistry* **1**: 326-331

Best MD (2009) Click chemistry and bioorthogonal reactions: unprecedented selectivity in the labeling of biological molecules. *Biochemistry* **48**: 6571-6584

Blommel PG, Fox BG (2007) A combined approach to improving large-scale production of tobacco etch virus protease. *Protein expression and purification* **55**: 53-68

Boileau C, Eme L, Brochier-Armanet C, Janicki A, Zhang CC, Latifi A (2011) A eukaryotic-like sulfiredoxin involved in oxidative stress responses and in the reduction of the sulfinic form of 2-Cys peroxiredoxin in the cyanobacterium *Anabaena* PCC7120. *New Phytologist* **191**: 1108-1118

Boveris A, Chance B (1973) The mitochondrial generation of hydrogen peroxide. General properties and effect of hyperbaric oxygen. *Biochemical Journal* **134**: 707-16

Bozzi M, Mignogna G, Stefanini S, Barra D, Longhi C, Valenti P, Chiancone E (1997) A novel non-heme iron-binding ferritin related to the DNA-binding proteins of the DPS family in *Listeria innocua*. *Journal of Biological Chemistry* **272**: 3259-3265

Braun E, Eichen Y, Sivan U, Ben-Yoseph G (1998) DNA-templated assembly and electrode attachment of a conducting silver wire. *Nature* **391**: 775-778

Brodin JD, Carr JR, Sontz PA, Tezcan FA (2014) Exceptionally stable, redox-active supramolecular protein assemblies with emergent properties. *Proc Natl Acad Sci USA* **111**: 2897-2902

Bromley E, Channon K, Moutevelis E, Woolfson D (2008) Peptide and protein building blocks for synthetic biology: from programming biomolecules to self-organized biomolecular systems. *ACS Chem Biol* **3**: 38-50

Buckhout-White S, Spillmann CM, Algar WR, Khachatrian A, Melinger JS, Goldman ER, Ancona MG, Medintz IL (2014) Assembling programmable FRET-based photonic networks using designer DNA scaffolds. *Nature Communications* **5**: 5615

Budisa N (2004) Prolegomena to future experimental efforts on genetic code engineering by expanding its amino acid repertoire. *Angew Chem-Int Edit* **43**: 6426-6463

Budisa N, Steipe B, Demange P, Eckerskorn C, Kellermann J, Huber R (1995) High-level biosynthetic substitution of methionine in proteins by its analogs 2-aminohexanoic acid, selenomethionine, telluromethionine and ethionine in *Escherichia coli*. *European Journal of Biochemistry* **230**: 788-96

Burgess RR (2009) Chapter 20 protein precipitation techniques. In Methods in Enzymology, pp 331-342

Bykowski T, Stevenson B (2005) Aseptic technique. In Current Protocols in Microbiology, *John Wiley & Sons, Inc.*

Cadenas E, Boveris A, Ragan CI, Stoppani AOM (1977) Production of superoxide radicals and hydrogen-peroxide by NADH-ubiquinone reductase and ubiquinol-cytochrome *c* reductase from beef-heart mitochondria. *Archives of Biochemistry and Biophysics* **180**: 248-257

Camps M (2010) Modulation of ColE1-like plasmid replication for recombinant gene expression. *Recent Patents on DNA & Gene Sequences* **4**: 58-73

Cao Z, Bhella D, Lindsay JG (2007) Reconstitution of the mitochondrial PrxIII antioxidant defence pathway: general properties and factors affecting PrxIII activity and oligomeric state. *Journal of Molecular Biology* **372**: 1022-1033

Cao Z, McGow DP, Shepherd C, Lindsay JG (2015) Improved catenated structures of bovine peroxiredoxin III F190L reveal details of ring-ring interactions and a novel conformational state. *PLOS ONE* **10**: e0123303

Cao Z, Roszak AW, Gourlay LJ, Lindsay JG, Isaacs NW (2005) Bovine mitochondrial peroxiredoxin III forms a two-ring catenane. *Structure* **13**: 1661-4

Cao ZB, Tavender TJ, Roszak AW, Cogdell RJ, Bulleid NJ (2011) Crystal structure of reduced and of oxidized peroxiredoxin IV enzyme reveals a stable oxidized decamer and a non-disulfide-bonded intermediate in the catalytic cycle. *Journal of Biological Chemistry* **286**: 42257-42266

Castanie-Cornet MP, Penfound TA, Smith D, Elliott JF, Foster JW (1999) Control of acid resistance in *Escherichia coli*. *Journal of Bacteriology* **181**: 3525-35

Castro H, Teixeira F, Romao S, Santos M, Cruz T, Florido M, Appelberg R, Oliveira P, Ferreira-da-Silva F, Tomas AM (2011) *Leishmania* mitochondrial peroxiredoxin plays a crucial peroxidase-unrelated role during infection:iInsight into its novel chaperone activity. *PLOS Pathology* **7**: e1002325

Causton HC, Feeney KA, Ziegler CA, O'Neill JS (2015) Metabolic cycles in yeast share features conserved among circadian rhythms. *Current Biology* **25**: 1056-62

Cha M-K, Yun C-H, Kim I-H (2000) Interaction of human thiol-specific antioxidant protein 1 with erythrocyte plasma membrane. *Biochemistry* **39**: 6944-6950

Chae HZ, Kim HJ, Kang SW, Rhee SG (1999) Characterization of three isoforms of mammalian peroxiredoxin that reduce peroxides in the presence of thioredoxin. *Diabetes Research and Clinical Practice* **45**: 101-112

Chan WT, Verma CS, Lane DP, Gan SKE (2013) A comparison and optimization of methods and factors affecting the transformation of *Escherichia coli*. *Bioscience Reports* **33**: 931-U172

Chance B, Sies H, Boveris A (1979) Hydroperoxide metabolism in mammalian organs. *Physiological Reviews* **59**: 527-605

Chang TS, Cho CS, Park S, Yu SQ, Kang SW, Rhee SG (2004) Peroxiredoxin III, a mitochondrion-specific peroxidase, regulates apoptotic signaling by mitochondria. *Journal of Biological Chemistry* **279**: 41975-41984

Chatterjee A, Sun SB, Furman JL, Xiao H, Schultz PG (2013) A versatile platform for single- and multiple-unnatural amino acid mutagenesis in *Escherichia coli*. *Biochemistry* **52**: 1828-1837

Chen Y-J, Groves B, Muscat RA, Seelig G (2015) DNA nanotechnology from the test tube to the cell. *Nature Nanotechnology* **10**: 748-760

Chin JW, Cropp TA, Anderson JC, Mukherji M, Zhang Z, Schultz PG (2003) An expanded eukaryotic genetic code. *Science* **301**: 964-967

Chin JW, Santoro SW, Martin AB, King DS, Wang L, Schultz PG (2002) Addition of p-azido-L-phenylalanine to the genetic code of *Escherichia coli*. *J Am Chem Soc* **124**: 9026-9027

Cho KJ, Park Y, Khan T, Lee J-H, Kim S, Seok JH, Chung YB, Cho AE, Choi Y, Chang T-S, Kim KH (2015) Crystal structure of dimeric human peroxiredoxin-1 C83S mutant. *Bulletin of the Korean Chemical Society* **36**: 1543-1545

Chou TF, So C, White BR, Carlson JCT, Sarikaya M, Wagner CR (2008) Enzyme nanorings. *Acs Nano* **2**: 2519-2525

Chworos A, Severcan I, Koyfman AY, Weinkam P, Oroudjev E, Hansma HG, Jaeger L (2004) Building programmable jigsaw puzzles with RNA. *Science* **306**: 2068-2072

Clark TD, Buehler LK, Ghadiri MR (1998) Self-assembling cyclic β^3-peptide nanotubes as artificial transmembrane ion channels. *J Am Chem Soc* **120**: 651-656

Cole JL, Lary JW, P. Moody T, Laue TM (2008) Analytical ultracentrifugation: sedimentation velocity and sedimentation equilibrium. *Methods in Cell Biology* **84**: 143-179

Comellas-Aragones M, Engelkamp H, Claessen VI, Sommerdijk NAJM, Rowan AE, Christianen PCM, Maan JC, Verduin BJM, Cornelissen JJLM, Nolte RJM (2007) A virus-based single-enzyme nanoreactor. *Nature Nanotechnology* **2**: 635-639

Copley SD, Novak WRP, Babbitt PC (2004) Divergence of function in the thioredoxin fold suprafamily: evidence for evolution of peroxiredoxins from a thioredoxin-like ancestor. *Biochemistry* **43**: 13981-13995

Cowan DA, Fernandez-Lafuente R (2011) Enhancing the functional properties of thermophilic enzymes by chemical modification and immobilization. *Enzyme and Microbial Technology* **49**: 326-346

Cox AG, Pearson AG, Pullar JM, Jonsson TJ, Lowther WT, Winterbourn CC, Hampton MB (2009a) Mitochondrial peroxiredoxin 3 is more resilient to hyperoxidation than cytoplasmic peroxiredoxins. *Biochemical Journal* **421**: 51-8

Cox AG, Peskin AV, Paton LN, Winterbourn CC, Hampton MB (2009b) Redox potential and peroxide reactivity of human peroxiredoxin 3. *Biochemistry* **48**: 6495-501

Cox AG, Winterbourn CC, Hampton MB (2010) Mitochondrial peroxiredoxin involvement in antioxidant defence and redox signalling. *Biochem J* **425**: 313-325

Cunniff B, Newick K, Nelson KJ, Wozniak AN, Beuschel S, Leavitt B, Bhave A, Butnor K, Koenig A, Chouchani ET, James AM, Haynes AC, Lowther WT, Murphy MP, Shukla A, Heintz NH (2015) Disabling mitochondrial peroxide metabolism via combinatorial targeting of peroxiredoxin 3 as an effective therapeutic approach for malignant mesothelioma. *PLOS ONE* **10**: e0127310

Cunniff B, Wozniak AN, Sweeney P, DeCosta K, Heintz NH (2014) Peroxiredoxin 3 levels regulate a mitochondrial redox setpoint in malignant mesothelioma cells. *Redox Biology* **3**: 79-87

Daegelen P, Studier FW, Lenski RE, Cure S, Kim JF (2009) Tracing ancestors and relatives of *Escherichia coli* B, and the derivation of B strains REL606 and BL21(DE3). *Journal of Molecular Biology* **394**: 634-643

de Boer HA, Comstock LJ, Vasser M (1983) The *tac* promoter: A functional hybrid derived from the *trp* and *lac* promoters. *Proc Natl Acad Sci USA* **80**: 21-25

De Stefano L, Vitale A, Rea I, Staiano M, Rotiroti L, Labella T, Rendina I, Aurilia V, Rossi M, D'Auria S (2008) Enzymes and proteins from extremophiles as hyperstable probes in nanotechnology: the use of D-trehalose/D-maltose-binding protein from the hyperthermophilic archaeon *Thermococcus litoralis* for sugars monitoring. *Extremophiles* **12**: 69-73

Destito G, Yeh R, Rae CS, Finn MG, Manchester M (2007) Folic acid-mediated targeting of cowpea mosaic virus particles to tumor cells. *Chemistry & Biology* **14**: 1152-1162

Dgany O, Gonzalez A, Sofer O, Wang W, Zolotnitsky G, Wolf A, Shoham Y, Altman A, Wolf SG, Shoseyov O, Almog O (2004) The structural basis of the thermostability of SP1, a novel plant (*Populus tremula*) boiling stable protein. *Journal of Biological Chemistry* **279**: 51516-51523

Dieterich DC, Link AJ (2009) Click chemistry in protein engineering, design, detection and profiling. In Click Chemistry for Biotechnology and Materials Science, pp 309-325.

Dieterich DC, Link AJ, Graumann J, Tirrell DA, Schuman EM (2006) Selective identification of newly synthesized proteins in mammalian cells using bioorthogonal noncanonical amino acid tagging (BONCAT). *Proc Natl Acad Sci USA* **103**: 9482-9487

Domínguez-Vera JM (2004) Iron(III) complexation of Desferrioxamine B encapsulated in apoferritin. *Journal of Inorganic Biochemistry* **98**: 469-472

Douglas T, Young M (2006) Viruses: making friends with old foes. *Science* **312**: 873-875

Dueber JE, Wu GC, Malmirchegini GR, Moon TS, Petzold CJ, Ullal AV, Prather KLJ, Keasling JD (2009) Synthetic protein scaffolds provide modular control over metabolic flux. *Nature Biotechnology* **27**: 753-759

Dujardin E, Peet C, Stubbs G, Culver JN, Mann S (2003) Organization of metallic nanoparticles using tobacco mosaic virus templates. *Nano Letters* **3**: 413-417

Dunford HB (1999) Heme peroxidases. *John Wiley*

Eakins GL, Pandey R, Wojciechowski JP, Zheng HY, Webb JEA, Valéry C, Thordarson P, Plank NOV, Gerrard JA, Hodgkiss JM (2015) Functional organic semiconductors assembled via natural aggregating peptides. *Advanced Functional Materials* **25**: 5640-5649

Edeling MA, Smith C, Owen D (2006) Life of a clathrin coat: Insights from clathrin and AP structures. *Nature Reviews Molecular Cell Biology* **7**: 32-44

Edgar RS, Green EW, Zhao Y, van Ooijen G, Olmedo M, Qin X, Xu Y, Pan M, Valekunja UK, Feeney KA, Maywood ES, Hastings MH, Baliga NS, Merrow M, Millar AJ, Johnson CH, Kyriacou CP, O'Neill JS, Reddy AB (2012) Peroxiredoxins are conserved markers of circadian rhythms. *Nature* **485**: 459-464

El-Sherbiny IM, Yacoub MH (2013) Hydrogel scaffolds for tissue engineering: progress and challenges. *Global Cardiology Science and Practice* **2013**: 38

Emsley P, Cowtan K (2004) Coot: Model-building tools for molecular graphics. *Acta Crystallographica Section D* **60**: 2126-2132

Esworthy RS, Ho YS, Chu FF (1997) The Gpx1 gene encodes mitochondrial glutathione peroxidase in the mouse liver. *Archives of Biochemistry and Biophysics* **340**: 59-63

Evans P (2006) Scaling and assessment of data quality. *Acta Crystallographica Section D* **62**: 72-82

Evans P (2011) An introduction to data reduction: space-group determination, scaling and intensity statistics. *Acta Crystallographica Section D* **67**: 282-292

Evans PR, Murshudov GN (2013) How good are my data and what is the resolution? *Acta Crystallographica Section D* **69**: 1204-1214

Fang J, Böhringer KF, Achour H (2016) Self-assembly. In Reference Module in Materials Science and Materials Engineering, *Elsevier*

Farabaugh PJ, Björk GR (1999) How translational accuracy influences reading frame maintenance. *The EMBO Journal* **18**: 1427-1434

Farokhzad OC, Langer R (2009) Impact of nanotechnology on drug delivery. *ACS Nano* **3**: 16-20

Feng L, Park SH, Reif JH, Yan H (2003) A two-state DNA lattice switched by DNA nanoactuator. *Angew Chem-Int Edit* **115**: 4478-4482

Ferrer-Sueta G, Manta B, Botti H, Radi R, Trujillo M, Denicola A (2011) Factors affecting protein thiol reactivity and specificity in peroxide reduction. *Chemical Research in Toxicology* **24**: 434-450

Fink AL, Calciano LJ, Goto Y, Kurotsu T, Palleros DR (1994) Classification of acid denaturation of proteins: intermediates and unfolded states. *Biochemistry* **33**: 12504-12511

Finkel T (2011) Signal transduction by reactive oxygen species. *The Journal of Cell Biology* **194**: 7-15

Fischer G, Rossmann M, Hyvönen M (2015) Alternative modulation of protein–protein interactions by small molecules. *Current Opinion in Biotechnology* **35**: 78-85

Fonda I, Kenig M, Gaberc-Porekar V, Pristovaek P, Menart V (2002) Attachment of histidine tags to recombinant tumor necrosis factor-alpha drastically changes its properties. *The Scientific World Journal* **2**: 1312-1325

Franklin RE (1955) Structure of tobacco mosaic virus. *Nature* **175**: 379-381

Fu TJ, Seeman NC (1993) DNA double crossover molecules. *Biochemistry* **32**: 3211-3220

Fukuda Y, Laugks U, Lučić V, Baumeister W, Danev R (2015) Electron cryotomography of vitrified cells with a volta phase plate. *Journal of Structural Biology* **190**: 143-154

Furst EM (2013) Directed self-assembly. *Soft Matter* **9**: 9039-9045

Fuss M, Luna M, Alcántara D, de la Fuente JM, Enríquez-Navas PM, Angulo J, Penadés S, Briones F (2008) Carbohydrate–carbohydrate interaction prominence in 3D supramolecular self-assembly. *The Journal of Physical Chemistry B* **112**: 11595-11600

Gao XY, Matsui H (2005) Peptide-based nanotubes and their applications in bionanotechnology. *Advanced Materials* **17**: 2037-2050

Gerrard JA (2013) Protein nanotechnology: What is it? In Protein Nanotechnology: Protocols, Instrumentation, and Applications, second edition, Gerrard J.A. (ed) pp 1-15. Totowa, NJ: *Humana Press*

Ghadiri MR, Granja JR, Milligan RA, McRee DE, Khazanovich N (1993) Self-assembling organic nanotubes based on a cyclic peptide architecture. *Nature* **366**: 324-327

Gilardi G, Meharenna YT, Tsotsou GE, Sadeghi SJ, Fairhead M, Giannini S (2002) Molecular Lego: design of molecular assemblies of P450 enzymes for nanobiotechnology. *Biosensors & Bioelectronics* **17**: 133-45

Glish GL, Vachet RW (2003) The basics of mass spectrometry in the twenty-first century. *Nature Reviews Drug Discovery* **2**: 140-150

Glover DJ, Clark DS (2016) Protein calligraphy: a new concept begins to take shape. *ACS Central Science* **2**: 438-444

Gonen S, DiMaio F, Gonen T, Baker D (2015) Design of ordered two-dimensional arrays mediated by noncovalent protein-protein interfaces. *Science* **348**: 1365-1368

Goodman RP, Schaap IAT, Tardin CF, Erben CM, Berry RM, Schmidt CF, Turberfield AJ (2005) Rapid chiral assembly of rigid DNA building blocks for molecular nanofabrication. *Science* **310**: 1661-1665

Goodsell DS, Olson AJ (2000) Structural symmetry and protein function. *Annual Review of Biophysics and Biomolecular Structure* **29**: 105-153

Gorrec F (2009) The MORPHEUS protein crystallization screen. *Journal of Applied Crystallography* **42**: 1035-1042

Górzny MŁ, Walton AS, Wnęk M, Stockley PG, Evans SD (2008) Four-probe electrical characterization of Pt-coated TMV-based nanostructures. *Nanotechnology* **19**: 165704

Gough DR, Cotter TG (2011) Hydrogen peroxide: a jekyll and hyde signalling molecule. *Cell Death and Disease* **2**: e213

Gourlay LJ, Bhella D, Kelly SM, Price NC, Lindsay JG (2003) Structure-function analysis of recombinant substrate protein 22 kDa (SP-22). A mitochondrial 2-Cys peroxiredoxin organized as a decameric toroid. *The Journal of Biological Chemistry* **278**: 32631-7

Greenfield NJ (2007) Using circular dichroism spectra to estimate protein secondary structure. *Nature Protocols* **1**: 2876-2890

Griffin MDW, Gerrard JA (2012) The relationship between oligomeric state and protein function. In Protein Dimerization and Oligomerization in Biology, Matthews J.M. (ed) pp 74-90. New York, NY: *Springer New York*

Grishin NV, Phillips MA (1994) The subunit interfaces of oligomeric enzymes are conserved to a similar extent to the overall protein sequences. *Protein Science* **3**: 2455-2458

Gritsan N, Platz M (2010) Photochemistry of azides: the azide/nitrene interface. In Organic Azides, pp 311-372. *John Wiley & Sons, Ltd*

Gross AJ, Haddad R, Travelet C, Reynaud E, Audebert P, Borsali R, Cosnier S (2016) Redox-active carbohydrate-coated nanoparticles: self-assembly of a cyclodextrin–polystyrene glycopolymer with tetrazine–naphthalimide. *Langmuir* **32**: 11939-11945

Grueninger D, Treiber N, Ziegler MOP, Koetter JWA, Schulze M-S, Schulz GE (2008) Designed protein-protein association. *Science* **319**: 206-209

Guo HH, Choe J, Loeb LA (2004) Protein tolerance to random amino acid change. *Proc Natl Acad Sci USA* **101**: 9205-9210

Guo J, Melançon CE, Lee HS, Groff D, Schultz PG (2009) Evolution of amber suppressor tRNAs for efficient bacterial production of proteins containing nonnatural amino acids. *Angew Chem-Int Edit* **48**: 9148-9151

Guo P (2010) The emerging field of RNA nanotechnology. *Nature Nanotechnology* **5**: 833-842

Hall A, Karplus PA, Poole LB (2009) Typical 2-Cys peroxiredoxins - structures, mechanisms and functions. *FEBS Journal* **276**: 2469-2477

Hall A, Nelson K, Poole LB, Karplus PA (2011) Structure-based insights into the catalytic power and conformational dexterity of peroxiredoxins. *Antioxidants & Redox Signaling* **15**: 795-815

Hall A, Parsonage D, Poole LB, Karplus PA (2010) Structural evidence that peroxiredoxin catalytic power is based on transition-state stabilization. *Journal of Molecular Biology* **402**: 194-209

Halley JD, Winkler DA (2008) Consistent concepts of self-organization and self-assembly. *Complexity* **14**: 10-17

Hampton MB, O'Connor KM (2016) Peroxiredoxins and the regulation of cell death. *Molecules and Cells* **39**: 72-76

Han X, Zheng Y, Munro CJ, Ji Y, Braunschweig AB (2015) Carbohydrate nanotechnology: hierarchical assembly using nature's other information carrying biopolymers. *Current Opinion in Biotechnology* **34**: 41-47

Harris JR, Schroder E, Isupov MN, Scheffler D, Kristensen P, Littlechild JA, Vagin AA, Meissner U (2001) Comparison of the decameric structure of peroxiredoxin-II by transmission electron microscopy and X-ray crystallography. *Biochim Biophys Acta* **1547**: 221-234

Harrison PM, Arosio P (1996) Ferritins: Molecular properties, iron storage function and cellular regulation. *Biochim Biophys Acta* **1275**: 161-203

Hartgerink JD, Clark TD, Ghadiri MR (1998) Peptide nanotubes and beyond. *Chem-Eur J* **4**: 1367-1372

Hauser CAE, Zhang S (2010) Nanotechnology: peptides as biological semiconductors. *Nature* **468**: 516-517

Haynes AC, Qian J, Reisz JA, Furdui CM, Lowther WT (2013) Molecular basis for the resistance of human mitochondrial 2-Cys peroxiredoxin 3 to hyperoxidation. *Journal of Biological Chemistry* **288**: 29714-29723

He D, Marles-Wright J (2015) Ferritin family proteins and their use in bionanotechnology. *New Biotechnology* **32**: 651-657

Heddle JG (2008) Protein cages, rings and tubes: useful components of future nanodevices? *Nanotechnology, Science and Applications* **1**: 67-78

Heddle JG, Fujiwara I, Yamadaki H, Yoshii S, Nishio K, Addy C, Yamashita I, Tame JRH (2007) Using the ring-shaped protein TRAP to capture and confine gold nanodots on a surface. *Small* **3**: 1950-1956

Hernandez-Ainsa S, Muus C, Bell NAW, Steinbock LJ, Thacker VV, Keyser UF (2013) Lipid-coated nanocapillaries for DNA sensing. *Analyst* **138**: 104-106

Hirotsu S, Abe Y, Okada K, Nagahara N, Hori H, Nishino T, Hakoshima T (1999) Crystal structure of a multifunctional 2-Cys peroxiredoxin heme-binding protein 23 kDa/proliferation-associated gene product. *Proc Natl Acad Sci USA* **96**: 12333-12338

Ho YS, Magnenat JL, Bronson RT, Cao J, Gargano M, Sugawara M, Funk CD (1997) Mice deficient in cellular glutathione peroxidase develop normally and show no increased sensitivity to hyperoxia. *Journal of Biological Chemistry* **272**: 16644-16651

Hofmann B, Hecht HJ, Flohe L (2002) Peroxiredoxins. *Biological Chemistry* **383**: 347-364

Holmes TC, de Lacalle S, Su X, Liu GS, Rich A, Zhang SG (2000) Extensive neurite outgrowth and active synapse formation on self-assembling peptide scaffolds. *Proc Natl Acad Sci USA* **97**: 6728-6733

Horne WS, Stout CD, Ghadiri MR (2003) A heterocyclic peptide nanotube. *J Am Chem Soc* **125**: 9372-9376

Horta BB, Oliveira MAd, Discola KF, Cussiol JRR, Netto LES (2010) Structural and biochemical characterization of peroxiredoxin Q beta from *Xylella fastidiosa*: catalytic mechanism and high reactivity. *Journal of Biological Chemistry* **285**: 16051-16065

Hou JP, Poole JW (1969) Kinetics and mechanism of degradation of ampicillin in solution. *Journal of Pharmaceutical Sciences* **58**: 447-54

Houseman BT, Mrksich M (2002) Carbohydrate arrays for the evaluation of protein binding and enzymatic modification. *Chemistry & Biology* **9**: 443-54

Hoyle NP, O'Neill JS (2015) Oxidation–reduction cycles of peroxiredoxin proteins and nontranscriptional aspects of timekeeping. *Biochemistry* **54**: 184-193

Huang P-S, Boyken SE, Baker D (2016) The coming of age of *de novo* protein design. *Nature* **537**: 320-327

Huard DJE, Kane KM, Tezcan FA (2013) Re-engineering protein interfaces yields copper-inducible ferritin cage assembly. *Nature Chemical Biology* **9**: 169-176

Hugo M, Turell L, Manta B, Botti H, Monteiro G, Netto LES, Alvarez B, Radi R, Trujillo M (2009) Thiol and sulfenic acid oxidation of AhpE, the one-cysteine peroxiredoxin from *Mycobacterium tuberculosis*: kinetics, acidity constants, and conformational dynamics. *Biochemistry* **48**: 9416-9426

Huh JY, Kim Y, Jeong J, Park J, Kim I, Huh KH, Kim YS, Woo HA, Rhee SG, Lee KJ, Ha H (2012) Peroxiredoxin 3 is a key molecule regulating adipocyte oxidative stress, mitochondrial biogenesis, and adipokine expression. *Antioxidants & Redox Signaling* **16**: 229-43

Ibba M, Soll D (2000) Aminoacyl-tRNA synthesis. *Annual Review of Biochemistry* **69**: 617-50

Ilk N, Egelseer EM, Sleytr UB (2011) S-layer fusion proteins - construction principles and applications. *Current Opinion in Biotechnology* **22**: 824-831

Israelachvili JN (2011) Intermolecular and surface forces. *Academic Press*, Burlington, MA

Jang HH, Lee KO, Chi YH, Jung BG, Park SK, Park JH, Lee JR, Lee SS, Moon JC, Yun JW, Choi YO, Kim WY, Kang JS, Cheong GW, Yun DJ, Rhee SG, Cho MJ, Lee SY (2004) Two enzymes in one: two yeast peroxiredoxins display oxidative stress-dependent switching from a peroxidase to a molecular chaperone function. *Cell* **117**: 625-35

Jeong W, Park SJ, Chang TS, Lee DY, Rhee SG (2006) Molecular mechanism of the reduction of cysteine sulfinic acid of peroxiredoxin to cysteine by mammalian sulfiredoxin. *The Journal of Biological Chemistry* **281**: 14400-7

Ji X-T, Huang L, Huang H-Q (2012) Construction of nanometer cisplatin core-ferritin (NCC-F) and proteomic analysis of gastric cancer cell apoptosis induced with cisplatin released from the NCC-F. *Journal of Proteomics* **75**: 3145-3157

Jonsson P, Jonsson MP, Hook F (2010) Sealing of submicrometer wells by a shear-driven lipid bilayer. *Nano Letters* **10**: 1900-6

Jonsson TJ, Johnson LC, Lowther WT (2009) Protein engineering of the quaternary sulfiredoxin.peroxiredoxin enzyme.substrate complex reveals the molecular basis for cysteine sulfinic acid phosphorylation. *The Journal of Biological Chemistry* **284**: 33305-10

Kagawa W, Kurumizaka H, Ishitani R, Fukai S, Nureki O, Shibata T, Yokoyama S (2002) Crystal structure of the homologous-pairing domain from the human RAD52 recombinase in the undecameric form. *Molecular Cell* **10**: 359-371

Kantardjieff KA, Rupp B (2003) Matthews coefficient probabilities: improved estimates for unit cell contents of proteins, DNA, and protein–nucleic acid complex crystals. *Protein Science* **12**: 1865-1871

Karanicolas J, Corn JE, Chen I, Joachimiak LA, Dym O, Peck SH, Albeck S, Unger T, Hu W, Liu G, Delbecq S, Montelione GT, Spiegel CP, Liu DR, Baker D (2011) A *de novo* protein binding pair by computational design and directed evolution. *Molecular Cell* **42**: 250-60

Karplus PA (2015) A primer on peroxiredoxin biochemistry. *Free Radical Biology & Medicine* **80**: 183-90

Karplus PA, Diederichs K (2012) Linking crystallographic model and data quality. *Science* **336**: 1030-3

Kato (1985) Cylinder protein isolated from rat liver mitochondria. *Zoological Science* **2**: 485-490

Ke C, Destecroix H, Crump MP, Davis AP (2012) A simple and accessible synthetic lectin for glucose recognition and sensing. *Nature Chemistry* **4**: 718-723

Khoshouei M, Radjainia M, Phillips AJ, Gerrard JA, Mitra AK, Plitzko JM, Baumeister W, Danev R (2016) Volta phase plate cryo-EM of the small protein complex Prx3. *Nature Communications* **7**

Kil In S, Lee Se K, Ryu Keun W, Woo Hyun A, Hu M-C, Bae Soo H, Rhee Sue G (2012) Feedback control of adrenal steroidogenesis via H_2O_2-dependent, reversible inactivation of peroxiredoxin III in mitochondria. *Molecular Cell* **46**: 584-594

Kil IS, Ryu KW, Lee SK, Kim JY, Chu SY, Kim JH, Park S, Rhee SG (2015) Circadian oscillation of sulfiredoxin in the mitochondria. *Molecular Cell* **59**: 651-63

Kilic T, Sanglier S, Van Dorsselaer A, Suck D (2006) Oligomerization behavior of the archaeal Sm2-type protein from *Archaeoglobus fulgidus*. *Protein Science* **15**: 2310-2317

Kim SH, Fountoulakis M, Cairns N, Lubec G (2001) Protein levels of human peroxiredoxin subtypes in brains of patients with Alzheimer's disease and Down syndrome. *J Neural Transm Suppl*: 223-35

Kimple ME, Brill AL, Pasker RL (2001) Overview of affinity tags for protein purification. In Current Protocols in Protein Science, *John Wiley & Sons, Inc.*

King NP, Sheffler W, Sawaya MR, Vollmar BS, Sumida JP, André I, Gonen T, Yeates TO, Baker D (2012) Computational design of self-assembling protein nanomaterials with atomic level accuracy. *Science* **336**: 1171-1174

Kitano K, Kita A, Hakoshima T, Niimura Y, Miki K (2005) Crystal structure of decameric peroxiredoxin (AhpC) from *Amphibacillus xylanus*. *Proteins: Structure, Function and Genetics* **59**: 644-647

Knez M, Bittner AM, Boes F, Wege C, Jeske H, Maiβ E, Kern K (2003) Biotemplate synthesis of 3-nm nickel and cobalt nanowires. *Nano Letters* **3**: 1079-1082

Knoops B, Argyropoulou V, Becker S, Fert L, Kuznetsova O (2016) Multiple roles of peroxiredoxins in inflammation. *Molecules & Cells* **39**: 60-64

Knoops B, Loumaye E, Van Der Eecken V (2007) Evolution of the peroxiredoxins. *Sub-cellular Biochemistry* **44**: 27-40

Konarev PV, Volkov VV, Sokolova AV, Koch MHJ, Svergun DI (2003) PRIMUS: a Windows PC-based system for small-angle scattering data analysis. *Journal of Applied Crystallography* **36**: 1277-1282

Kong J, Franklin NR, Zhou CW, Chapline MG, Peng S, Cho KJ, Dai HJ (2000) Nanotube molecular wires as chemical sensors. *Science* **287**: 622-625

König J, Galliardt H, Jütte P, Schäper S, Dittmann L, Dietz K-J (2013) The conformational bases for the two functionalities of 2-cysteine peroxiredoxins as peroxidase and chaperone. *Journal of Experimental Botany* **64**: 3483-3497

Konstas K, Langford SJ, Latter MJ (2010) Advances towards synthetic machines at the molecular and nanoscale level. *International Journal of Molecular Sciences* **11**: 2453-2472

Koo KH, Lee S, Jeong SY, Kim ET, Kim HJ, Kim K, Song K, Chae HZ (2002) Regulation of thioredoxin peroxidase activity by C-terminal truncation. *Archives of Biochemistry and Biophysics* **397**: 312-318

Krissinel E, Henrick K (2007) Inference of macromolecular assemblies from crystalline state. *Journal of Molecular Biology* **372**: 774-797

Kristensen P, Rasmussen DE, Kristensen BI (1999) Properties of thiol-specific anti-oxidant protein or calpromotin in solution. *Biochemical and Biophysical Research Communications* **262**: 127-131

Kuchler A, Yoshimoto M, Luginbuhl S, Mavelli F, Walde P (2016) Enzymatic reactions in confined environments. *Nature Nanotechnology* **11**: 409-420

Kumara MT, Srividya N, Muralidharan S, Tripp BC (2006) Bioengineered flagella protein nanotubes with cysteine loops: self-assembly and manipulation in an optical trap. *Nano Letters* **6**: 2121-2129

Kwon J, Lee S-R, Yang K-S, Ahn Y, Kim YJ, Stadtman ER, Rhee SG (2004) Reversible oxidation and inactivation of the tumor suppressor PTEN in cells stimulated with peptide growth factors. *Proc Natl Acad Sci USA* **101**: 16419-16424

Lai Y-T, Reading E, Hura GL, Tsai K-L, Laganowsky A, Asturias FJ, Tainer JA, Robinson CV, Yeates TO (2014) Structure of a designed protein cage that self-assembles into a highly porous cube. *Nature Chemistry* **6**: 1065-1071

Lancia JK, Nwokoye A, Dugan A, Joiner C, Pricer R, Mapp AK (2014) Sequence context and crosslinking mechanism affect the efficiency of *in vivo* capture of a protein-protein interaction. *Biopolymers* **101**: 391-397

Lang K, Chin JW (2014) Bioorthogonal reactions for labeling proteins. *ACS Chemical Biology* **9**: 16-20

Larkin MA, Blackshields G, Brown NP, Chenna R, McGettigan PA, McWilliam H, Valentin F, Wallace IM, Wilm A, Lopez R, Thompson JD, Gibson TJ, Higgins DG (2007) Clustal W and Clustal X version 2.0. *Bioinformatics* **23**: 2947-2948

Laue TM, Shah BD, Ridgeway TM, Pelletier SL (1992) Computer-aided interpretation of analytical sedimentation data for proteins. In Analytical Ultracentrifugation in Biochemistry and Polymer Science, Harding S.E., Rowe A.J., Horton J.C. (eds) pp 90-125. Cambridge: *The Royal Society of Chemistry*

Laursen BS, Sørensen HP, Mortensen KK, Sperling-Petersen HU (2005) Initiation of protein synthesis in bacteria. *Microbiology and Molecular Biology Reviews* **69**: 101-123

Lawson DM, Artymiuk PJ, Yewdall SJ, Smith JMA, Livingstone JC, Treffry A, Luzzago A, Levi S, Arosio P, Cesareni G, Thomas CD, Shaw WV, Harrison PM (1991) Solving the structure of human H ferritin by genetically engineering intermolecular crystal contacts. *Nature* **349**: 541-544

Lebowitz J, Lewis MS, Schuck P (2002) Modern analytical ultracentrifugation in protein science: a tutorial review. *Protein Science* **11**: 2067-2079

Lee EM, Lee SS, Tripathi BN, Jung HS, Cao GP, Lee Y, Singh S, Hong SH, Lee KW, Lee SY, Cho J-Y, Chung BY (2015) Site-directed mutagenesis substituting cysteine for serine in 2-Cys peroxiredoxin (2-Cys PrxA) of *Arabidopsis thaliana* effectively improves its peroxidase and chaperone functions. *Annals of Botany* **116**: 713-725

Lee S-R, Kwon K-S, Kim S-R, Rhee SG (1998) Reversible inactivation of protein-tyrosine phosphatase 1B in A431 cells stimulated with epidermal growth factor. *Journal of Biological Chemistry* **273**: 15366-15372

Lee W, Choi KS, Riddell J, Ip C, Ghosh D, Park JH, Park YM (2007) Human peroxiredoxin 1 and 2 are not duplicate proteins: the unique presence of Cys83 in Prx1 underscores the structural and functional differences between Prx1 and Prx2. *The Journal of Biological Chemistry* **282**: 22011-22

Legault J, Carrier C, Petrov P, Renard P, Remacle J, Mirault ME (2000) Mitochondrial Gpx1 decreases induced but not basal oxidative damage to mtDNA in T47D cells. *Biochemical and Biophysical Research Communications* **272**: 416-422

Lehn J-M (2002) Toward complex matter: supramolecular chemistry and self-organization. *Proc Natl Acad Sci USA* **99**: 4763-4768

Lehn J-M (2007) From supramolecular chemistry towards constitutional dynamic chemistry and adaptive chemistry. *Chemical Society Reviews* **36**: 151-160

Levy ED, Erba EB, Robinson CV, Teichmann SA (2008) Assembly reflects evolution of protein complexes. *Nature* **453**: 1262-1265

Li L (2016) The relevance of mammalian peroxiredoxins to the gametogenesis, embryogenesis, and pregnancy outcomes. *Reproductive Sciences* **24**: 812-817

Li L, Shoji W, Oshima H, Obinata M, Fukumoto M, Kanno N (2008) Crucial role of peroxiredoxin III in placental antioxidant defense of mice. *FEBS Letters* **582**: 2431-2434

Li L, Shoji W, Takano H, Nishimura N, Aoki Y, Takahashi R, Goto S, Kaifu T, Takai T, Obinata M (2007) Increased susceptibility of MER5 (peroxiredoxin III) knockout mice to LPS-induced oxidative stress. *Biochemical and Biophysical Research Communications* **355**: 715-721

Li L, Yu A-Q (2015) The functional role of peroxiredoxin 3 in reactive oxygen species, apoptosis, and chemoresistance of cancer cells. *Journal of Cancer Research and Clinical Oncology* **141**: 1-7

Li X, Gao H, Uo M, Sato Y, Akasaka T, Feng Q, Cui F, Liu X, Watari F (2009) Effect of carbon nanotubes on cellular functions *in vitro*. *J Biomed Mater Res A* **91**: 132-9

Li XM, Fan YB, Watari F (2010) Current investigations into carbon nanotubes for biomedical application. *Biomedical Materials* **5**: 22001

Lim JM, Lee KS, Woo HA, Kang D, Rhee SG (2015) Control of the pericentrosomal H_2O_2 level by peroxiredoxin I is critical for mitotic progression. *The Journal of Cell Biology* **210**: 23-33

Linko V, Ora A, Kostiainen MA (2015) DNA nanostructures as smart drug-delivery vehicles and molecular devices. *Trends in Biotechnology* **33**: 586-94

Littlejohn J (2012) Peroxiredoxins: a model for a self-assembled nanoscale system. *University of Canterbury*, *Christchurch, New Zealand*

Lowther WT, Haynes AC (2011) Reduction of cysteine sulfinic acid in eukaryotic typical 2-Cys peroxredoxins by sulfiredoxin. *Antioxidants & Redox Signaling* **15**: 99-109

MacDiarmid CW, Taggart J, Kerdsomboon K, Kubisiak M, Panascharoen S, Schelble K, Eide DJ (2013) Peroxiredoxin chaperone activity is critical for protein homeostasis in zinc-deficient yeast. *Journal of Biological Chemistry* **288**: 31313-31327

Majorek KA, Kuhn ML, Chruszcz M, Anderson WF, Minor W (2014) Double trouble: Buffer selection and His-tag presence may be responsible for non-reproducibility of biomedical experiments. *Protein Science* **23**: 1359-68

Malcos JL, Hancock WO (2011) Engineering tubulin: microtubule functionalization approaches for nanoscale device applications. *Appl Microbiol Biotechnol* **90**: 1-10

Malmstrom J, Wason A, Roache F, Yewdall NA, Radjainia M, Wei S, Higgins MJ, Williams DE, Gerrard JA, Travas-Sejdic J (2015) Protein nanorings organized by poly(styrene-block-ethylene oxide) self-assembled thin films. *Nanoscale* **7**: 19940-19948

Malvankar NS, Vargas M, Nevin KP, Franks AE, Leang C, Kim BC, Inoue K, Mester T, Covalla SF, Johnson JP, Rotello VM, Tuominen MT, Lovley DR (2011) Tunable metallic-like conductivity in microbial nanowire networks. *Nature Nanotechnology* **6**: 573-579

Manea F (2015) Engineering synthetic Lsm rings for applications in nanotechnology. *Macquarie University, Sydney, Australia*, http://hdl.handle.net/1959.14/1075221

Manevich Y, Reddy KS, Shuvaeva T, Feinstein SI, Fisher AB (2007) Structure and phospholipase function of peroxiredoxin 6: identification of the catalytic triad and its role in phospholipid substrate binding. *Journal of Lipid Research* **48**: 2306-2318

Mao CD, Sun WQ, Seeman NC (1997) Assembly of Borromean rings from DNA. *Nature* **386**: 137-138

Mao CD, Sun WQ, Shen ZY, Seeman NC (1999) A nanomechanical device based on the B-Z transition of DNA. *Nature* **397**: 144-146

Marino SM, Gladyshev VN (2010) Cysteine function governs its conservation and degeneration and restricts its utilization on protein surfaces. *Journal of Molecular Biology* **404**: 902-916

Marsh JA, Teichmann SA (2015) Structure, dynamics, assembly, and evolution of protein complexes. In Annual Review of Biochemistry, pp 551-575.

Marty MT, Baldwin AJ, Marklund EG, Hochberg GKA, Benesch JLP, Robinson CV (2015) Bayesian deconvolution of mass and ion mobility spectra: from binary interactions to polydisperse ensembles. *Analytical Chemistry* **87**: 4370-4376

Mashaghi A, Swann M, Popplewell J, Textor M, Reimhult E (2008) Optical anisotropy of supported lipid structures probed by waveguide spectroscopy and its application to study of supported lipid bilayer formation kinetics. *Analytical Chemistry* **80**: 3666-3676

Mashaghi S, Jadidi T, Koenderink G, Mashaghi A (2013) Lipid nanotechnology. *International Journal of Molecular Sciences* **14**: 4242-82

Matsumura S, Uemura S, Mihara H (2004) Fabrication of nanofibers with uniform morphology by self-assembly of designed peptides. *Chem-Eur J* **10**: 2789-2794

Matsumura T, Okamoto K, Iwahara SI, Hori H, Takahashi Y, Nishino T, Abe Y (2008) Dimer-oligomer interconversion of wild-type and mutant rat 2-Cys peroxiredoxin. *Journal of Biological Chemistry* **283**: 284-293

Matsushima S, Ide T, Yamato M, Matsusaka H, Hattori F, Ikeuchi M, Kubota T, Sunagawa K, Hasegawa Y, Kurihara T, Oikawa S, Kinugawa S, Tsutsui H (2006) Overexpression of mitochondrial peroxiredoxin-3

prevents left ventricular remodeling and failure after myocardial infarction in mice. *Circulation* **113**: 1779-1786

Matthews BW (1968) Solvent content of protein crystals. *Journal of Molecular Biology* **33**: 491-497

Mazzini A, Polverini E, Parisi M, Sorbi RT, Favilla R (2007) Dissociation and unfolding of bovine odorant binding protein at acidic pH. *Journal of Structural Biology* **159**: 82-91

McCoy AJ, Grosse-Kunstleve RW, Adams PD, Winn MD, Storoni LC, Read RJ (2007) Phaser crystallographic software. *Journal of Applied Crystallography* **40**: 658-674

McMillan RA, Paavola CD, Howard J, Chan SL, Zaluzec NJ, Trent JD (2002) Ordered nanoparticle arrays formed on engineered chaperonin protein templates. *Nature Materials* **1**: 247-252

McPhillips TM, McPhillips SE, Chiu H-J, Cohen AE, Deacon AM, Ellis PJ, Garman E, Gonzalez A, Sauter NK, Phizackerley RP, Soltis SM, Kuhn P (2002) Blu-ice and the distributed control system: software for data acquisition and instrument control at macromolecular crystallography beamlines. *Journal of Synchrotron Radiation* **9**: 401-406

Medalsy I, Dgany O, Sowwan M, Cohen H, Yukashevska A, Wolf SG, Wolf A, Koster A, Almog O, Marton I, Pouny Y, Altman A, Shoseyov O, Porath D (2008) SP1 protein-based nanostructures and arrays. *Nano Letters* **8**: 473-7

Meissner U, Schroder E, Scheffler D, Martin AG, Harris JR (2007) Formation, TEM study and 3D reconstruction of the human erythrocyte peroxiredoxin-2 dodecahedral higher-order assembly. *Micron* **38**: 29-39

Melis Sardan E, Goksu C, Mohammad Aref K, Mustafa OG (2016) Self-assembled peptide nanostructures for functional materials. *Nanotechnology* **27**: 402002

Merkel L, Schauer M, Antranikian G, Budisa N (2010) Parallel incorporation of different fluorinated amino acids: on the way to “teflon” proteins. *ChemBioChem* **11**: 1505-1507

Miller RA, Presley AD, Francis MB (2007) Self-assembling light-harvesting systems from synthetically modified tobacco mosaic virus coat proteins. *J Am Chem Soc* **129**: 3104-3109

Miranda FF, Iwasaki K, Akashi S, Sumitomo K, Kobayashi M, Yamashita I, Tame JR, Heddle JG (2009) A self-assembled protein nanotube with high aspect ratio. *Small* **5**: 2077-84

Mishra M, Jiang H, Wu L, Chawsheen HA, Wei Q (2015) The sulfiredoxin-peroxiredoxin (Srx-Prx) axis in cell signal transduction and cancer development. *Cancer Letters* **366**: 150-9

Misonou Y, Kikuchi M, Sato H, Inai T, Kuroiwa T, Tanaka K, Miyakawa I (2014) Aldehyde dehydrogenase, Ald4p, is a major component of mitochondrial fluorescent inclusion bodies in the yeast *Saccharomyces cerevisiae*. *Biology Open* **3**: 387-396

Moon JC, Hah YS, Kim WY, Jung BG, Jang HH, Lee JR, Kim SY, Lee YM, Jeon MG, Kim CW, Cho MJ, Lee SY (2005) Oxidative stress-dependent structural and functional switching of a human 2-Cys peroxiredoxin isotype II that enhances HeLa cell resistance to H_2O_2-induced cell death. *The Journal of Biological Chemistry* **280**: 28775-84

Moon JC, Kim GM, Kim E-K, Lee HN, Ha B, Lee SY, Jang HH (2013) Reversal of 2-Cys peroxiredoxin oligomerization by sulfiredoxin. *Biochemical and Biophysical Research Communications* **432**: 291-295

Morais MAB, Giuseppe PO, Souza TACB, Alegria TGP, Oliveira MA, Netto LES, Murakami MT (2015) How pH modulates the dimer-decamer interconversion of 2-Cys peroxiredoxins from the Prx1 subfamily. *Journal of Biological Chemistry* **290**: 8582-8590

Moreland N, Ashton R, Baker HM, Ivanovic I, Patterson S, Arcus VL, Baker EN, Lott JS (2005) A flexible and economical medium-throughput strategy for protein production and crystallization. *Acta Crystallographica Section D* **61**: 1378-1385

Morgan B, Van Laer K, Owusu TNE, Ezerina D, Pastor-Flores D, Amponsah PS, Tursch A, Dick TP (2016) Real-time monitoring of basal H_2O_2 levels with peroxiredoxin-based probes. *Nature Chemical Biology* **12**: 437-443

Moses JE, Moorhouse AD (2007) The growing applications of click chemistry. *Chemical Society Reviews* **36**: 1249-1262

Mougous JD, Cuff ME, Raunser S, Shen A, Zhou M, Gifford CA, Goodman AL, Joachimiak G, Ordoñez CL, Lory S, Walz T, Joachimiak A, Mekalanos JJ (2006) A virulence locus of *Pseudomonas aeruginosa* encodes a protein secretion apparatus. *Science* **312**: 1526-1530

Mu Y, Lian F-M, Teng Y-B, Ao J, Jiang Y-L, He Y-X, Chen Y, Zhou C-Z, Chen X (2013) The N-terminal β-sheet of peroxiredoxin 4 in the large yellow croaker *Pseudosciaena crocea* is involved in its biological functions. *PLOS ONE* **8**: e57061

Murphy MP (2009) How mitochondria produce reactive oxygen species. *Biochemical Journal* **417**: 1-13

Murshudov GN, Skubak P, Lebedev AA, Pannu NS, Steiner RA, Nicholls RA, Winn MD, Long F, Vagin AA (2011) REFMAC5 for the refinement of macromolecular crystal structures. *Acta Crystallographica Section D* **67**: 355-367

Murshudov GN, Vagin AA, Dodson EJ (1997) Refinement of macromolecular structures by the maximum-likelihood method. *Acta Crystallographica Section D* **53**: 240-255

Nadeau PJ, Charette SJ, Toledano MB, Landry J (2007) Disulfide bond-mediated multimerization of Ask1 and its reduction by thioredoxin-1 regulate H_2O_2-induced c-Jun NH_2-terminal kinase activation and apoptosis. *Molecular Biology of the Cell* **18**: 3903-3913

Nagy P, Karton A, Betz A, Peskin AV, Pace P, O'Reilly RJ, Hampton MB, Radom L, Winterbourn CC (2011) Model for the exceptional reactivity of peroxiredoxins 2 and 3 with hydrogen peroxide a kinetic and computational study. *Journal of Biological Chemistry* **286**: 18048-18055

Nakamura T, Kado Y, Yamaguchi T, Matsumura H, Ishikawa K, Inoue T (2010) Crystal structure of peroxiredoxin from *Aeropyrum pernix* K1 complexed with its substrate, hydrogen peroxide. *Journal of Biochemistry* **147**: 109-115

Nam KT, Kim D-W, Yoo PJ, Chiang C-Y, Meethong N, Hammond PT, Chiang Y-M, Belcher AM (2006) Virus-enabled synthesis and assembly of nanowires for lithium ion battery electrodes. *Science* **312**: 885-888

Neidhardt FC (1996) *Escherichia coli* and *Salmonella*: Cellular and molecular biology. *ASM Press*

Nel A, Madler L, Velegol D, Xia T, Hoek E, Somasundaran P, Klaessig F, Castranova V, Thompson M (2009) Understanding biophysicochemical interactions at the nano-bio interface. *Nature Materials* **8**: 543 - 557

Nelson KJ, Knutson ST, Soito L, Klomsiri C, Poole LB, Fetrow JS (2011) Analysis of the peroxiredoxin family: using active-site structure and sequence information for global classification and residue analysis. *Proteins: Structure, Function, and Bioinformatics* **79**: 947-964

Nettleton EJ, Sunde M, Lai Z, Kelly JW, Dobson CM, Robinson CV (1998) Protein subunit interactions and structural integrity of amyloidogenic transthyretins: evidence from electrospray mass spectrometry. *Journal of Molecular Biology* **281**: 553-64

Neumann CA, Krause DS, Carman CV, Das S, Dubey DP, Abraham JL, Bronson RT, Fujiwara Y, Orkin SH, Van Etten RA (2003) Essential role for the peroxiredoxin Prdx1 in erythrocyte antioxidant defence and tumour suppression. *Nature* **424**: 561-565

Neumann H (2012) Rewiring translation – genetic code expansion and its applications. *FEBS letters* **586**: 2057-2064

Neumann H, Wang K, Davis L, Garcia-Alai M, Chin JW (2010) Encoding multiple unnatural amino acids via evolution of a quadruplet-decoding ribosome. *Nature* **464**: 441-444

Nikolajski M, Adams GG, Gillis RB, Besong DT, Rowe AJ, Heinze T, Harding SE (2014) Protein–like fully reversible tetramerisation and super-association of an aminocellulose. *Scientific Reports* **4**: 3861

Nilsson J, Ståhl S, Lundeberg J, Uhlén M, Nygren P-å (1997) Affinity fusion strategies for detection, purification, and immobilization of recombinant proteins. *Protein Expression and Purification* **11**: 1-16

Noh YH, Baek JY, Jeong W, Rhee SG, Chang T-S (2009) Sulfiredoxin translocation into mitochondria plays a crucial role in reducing hyperoxidized peroxiredoxin III. *Journal of Biological Chemistry* **284**: 8470-8477

Nonn L, Berggren M, Powis G (2003) Increased expression-of mitochondrial peroxiredoxin-3 (thioredoxin peroxidase-2) protects cancer cells against hypoxia and drug-induced hydrogen peroxide-dependent apoptosis. *Molecular Cancer Research* **1**: 682-689

Nooren IMA, Thornton JM (2003) Structural characterisation and functional significance of transient protein–protein interactions. *Journal of Molecular Biology* **325**: 991-1018

Noy A, Artyukhin AB, Huang S-C, Martinez JA, Misra N (2011) Functional integration of membrane proteins with nanotube and nanowire transistor devices. In Bioconjugation Protocols: Strategies and Methods, Mark S.S. (ed) pp 533-552. Totowa, NJ: *Humana Press*

O'Donoghue P, Ling J, Wang Y-S, Soll D (2013) Upgrading protein synthesis for synthetic biology. *Nature Chemical Biology* **9**: 594-598

Ogusucu R, Rettori D, Munhoz DC, Netto LE, Augusto O (2007) Reactions of yeast thioredoxin peroxidases I and II with hydrogen peroxide and peroxynitrite: rate constants by competitive kinetics. *Free Radical Biology & Medicine* **42**: 326-34

Olmedo M, O'Neill JS, Edgar RS, Valekunja UK, Reddy AB, Merrow M (2012) Circadian regulation of olfaction and an evolutionarily conserved, non-transcriptional marker in *Caenorhabditis elegans*. *Proc Natl Acad Sci USA* 109: 20479-20484

Omichi M, Asano A, Tsukuda S, Takano K, Sugimoto M, Saeki A, Sakamaki D, Onoda A, Hayashi T, Seki S (2014) Fabrication of enzyme-degradable and size-controlled protein nanowires using single particle nano-fabrication technique. *Nature Communications* 5

Orosz A, Boros I, Venetianer P (1991) Analysis of the complex transcription termination region of the *Escherichia coli* rrnB gene. *European Journal of Biochemistry* 201: 653-659

Orrenius S (2007) Reactive oxygen species in mitochondria-mediated cell death. *Drug Metabolism Reviews* 39: 443-455

Oyelaran O, Gildersleeve JC (2009) Glycan arrays: Recent advances and future challenges. *Current Opinion in Chemical Biology* 13: 406-413

Pace PE, Peskin AV, Han MH, Hampton MB, Winterbourn CC (2013) Hyperoxidized peroxiredoxin 2 interacts with the protein disulfide-isomerase ERp46. *Biochemical Journal* 453: 475-485

Padilla JE, Colovos C, Yeates TO (2001) Nanohedra: using symmetry to design self assembling protein cages, layers, crystals, and filaments. *Proc Natl Acad Sci USA* 98: 2217-2221

Painter AJ, Jaya N, Basha E, Vierling E, Robinson CV, Benesch JLP (2008) Real-time monitoring of protein complexes reveals their quaternary organization and dynamics. *Chemistry & Biology* 15: 246-253

Panfili E, Sandri G, Ernster L (1991) Distribution of glutathione peroxidases and glutathione-reductase in rat-brain mitochondria. *FEBS Letters* 290: 35-37

Park SH, Pistol C, Ahn SJ, Reif JH, Lebeck AR, Dwyer C, LaBean TH (2006) Finite-size, fully addressable DNA tile lattices formed by hierarchical assembly procedures. *Angew Chem-Int Edit* 45: 735-739

Parlea L, Puri A, Kasprzak W, Bindewald E, Zakrevsky P, Satterwhite E, Joseph K, Afonin KA, Shapiro BA (2016) Cellular delivery of RNA nanoparticles. *ACS Combinatorial Science* 18: 527-547

Parrish AR, She X, Xiang Z, Coin I, Shen Z, Briggs SP, Dillin A, Wang L (2012) Expanding the genetic code of *Caenorhabditis elegans* using bacterial aminoacyl-tRNA synthetase/tRNA pairs. *ACS Chemical Biology* 7: 1292-1302

Parsonage D, Nelson KJ, Ferrer-Sueta G, Alley S, Karplus PA, Furdui CM, Poole LB (2015) Dissecting peroxiredoxin catalysis: separating binding, peroxidation, and resolution for a bacterial AhpC. *Biochemistry* 54: 1567-1575

Parsonage D, Youngblood DS, Sarma GN, Wood ZA, Karplus PA, Poole LB (2005) Analysis of the link between enzymatic activity and oligomeric state in AhpC, a bacterial peroxiredoxin. *Biochemistry* 44: 10583-92

Peptu CA, Ochiuz L, Alupei L, Peptu C, Popa M (2014) Carbohydrate based nanoparticles for drug delivery across biological barriers. *Journal of Biomedical Nanotechnology* 10: 2107-2148

Perkins A, Nelson KJ, Parsonage D, Poole LB, Karplus PA (2015) Peroxiredoxins: guardians against oxidative stress and modulators of peroxide signaling. *Trends in Biochemical Sciences* **40**: 435-445

Perkins A, Nelson KJ, Williams JR, Parsonage D, Poole LB, Karplus PA (2013) The sensitive balance between the fully folded and locally unfolded conformations of a model peroxiredoxin. *Biochemistry* **52**: 8708-8721

Perkins A, Parsonage D, Nelson KJ, Ogba OM, Cheong PH, Poole LB, Karplus PA (2016) Peroxiredoxin catalysis at atomic resolution. *Structure* **24**: 1668-1678

Peskin AV, Cox AG, Nagy P, Morgan PE, Hampton MB, Davies MJ, Winterbourn CC (2010) Removal of amino acid, peptide and protein hydroperoxides by reaction with peroxiredoxins 2 and 3. *Biochemical Journal* **432**: 313-321

Peskin AV, Low FM, Paton LN, Maghzal GJ, Hampton MB, Winterbourn CC (2007) The high reactivity of peroxiredoxin 2 with H_2O_2 is not reflected in its reaction with other oxidants and thiol reagents. *Journal of Biological Chemistry* **282**: 11885-11892

Petoukhov MV, Franke D, Shkumatov AV, Tria G, Kikhney AG, Gajda M, Gorba C, Mertens HDT, Konarev PV, Svergun DI (2012) New developments in the atsas program package for small-angle scattering data analysis. *Journal of Applied Crystallography* **45**: 342-350

Petrovska I, Nüske E, Munder MC, Kulasegaran G, Malinovska L, Kroschwald S, Richter D, Fahmy K, Gibson K, Verbavatz J-M, Alberti S (2014) Filament formation by metabolic enzymes is a specific adaptation to an advanced state of cellular starvation. *eLife* **3**: e02409

Phalen TJ, Weirather K, Deming PB, Anathy V, Howe AK, van der Vliet A, Jonsson TJ, Poole LB, Heintz NH (2006) Oxidation state governs structural transitions in peroxiredoxin II that correlate with cell cycle arrest and recovery. *The Journal of Cell Biology* **175**: 779-89

Phillips AJ (2014) Structural characterisation of proteins from the peroxiredoxin family. *University of Canterbury, Christchurch, New Zealand*, http://ir.canterbury.ac.nz/handle/10092/9371

Phillips AJ, Littlejohn J, Yewdall NA, Zhu T, Valéry C, Pearce FG, Mitra AK, Radjainia M, Gerrard JA (2014) Peroxiredoxin is a versatile self-assembling tecton for protein nanotechnology. *Biomacromolecules* **15**: 1871-1881

Pieters BJGE, van Eldijk MB, Nolte RJM, Mecinovic J (2016) Natural supramolecular protein assemblies. *Chemical Society Reviews* **45**: 24-39

Piñeyro MaD, Pizarro JC, Lema F, Pritsch O, Cayota A, Bentley GA, Robello C (2005) Crystal structure of the tryparedoxin peroxidase from the human parasite *Trypanosoma cruzi*. *Journal of Structural Biology* **150**: 11-22

Poole LB (2015) The basics of thiols and cysteines in redox biology and chemistry. *Free Radical Biology and Medicine* **80**: 148-157

Poole LB, Nelson KJ (2016) Distribution and features of the six classes of peroxiredoxins. *Molecules & Cells* **39**: 53-59

Pope B, Kent HM (1996) High efficiency 5 min transformation of *Escherichia coli*. *Nucleic Acids Research* **24**: 536-537

Portillo-Ledesma S, Sardi F, Manta B, Tourn MV, Clippe A, Knoops B, Alvarez B, Coitiño EL, Ferrer-Sueta G (2014) Deconstructing the catalytic efficiency of peroxiredoxin-5 peroxidatic cysteine. *Biochemistry* **53**: 6113-6125

Pott M, Schmidt MJ, Summerer D (2014) Evolved sequence contexts for highly efficient amber suppression with noncanonical amino acids. *ACS Chemical Biology* **9**: 2815-2822

Poynton RA, Peskin AV, Haynes AC, Lowther WT, Hampton MB, Winterbourn C (2016) Kinetic analysis of structural influences on the susceptibility of peroxiredoxins 2 and 3 to hyperoxidation. *Biochemical Journal* **473**: 411-421

Pukala TL, Ruotolo BT, Zhou M, Politis A, Stefanescu R, Leary JA, Robinson CV (2009) Subunit architecture of multiprotein assemblies determined using restraints from gas-phase measurements. *Structure* **17**: 1235-1243

Pum D, Toca-Herrera JL, Sleytr UB (2013) S-layer protein self-assembly. *International Journal of Molecular Sciences* **14**: 2484-2501

Putnam CD, Hammel M, Hura GL, Tainer JA (2007) X-ray solution scattering (SAXS) combined with crystallography and computation: defining accurate macromolecular structures, conformations and assemblies in solution. *Quarterly Reviews of Biophysics* **40**: 191-285

Putzbach W, Ronkainen N (2013) Immobilization techniques in the fabrication of nanomaterial-based electrochemical biosensors: a review. *Sensors* **13**: 4811

Radjainia M, Venugopal H, Desfosses A, Phillips Amy J, Yewdall NA, Hampton Mark B, Gerrard Juliet A, Mitra Alok K (2015) Cryo-electron microscopy structure of human peroxiredoxin-3 filament reveals the assembly of a putative chaperone. *Structure* **23**: 912-920

Randall LM, Ferrer-Sueta G, Denicola A (2013) Chapter three - peroxiredoxins as preferential targets in H_2O_2-induced signaling. In Methods in Enzymology, Enrique C., Lester P. (eds) pp 41-63. *Academic Press*

Ravichandran R (2009) Nanotechnology-based drug delivery systems. *Nanobiotechnology* **5**: 17-33

Reches M, Gazit E (2006) Controlled patterning of aligned self-assembled peptide nanotubes. *Nature Nanotechnology* **1**: 195-200

Reddington SC, Baldwin AJ, Thompson R, Brancale A, Tippmann EM, Jones DD (2015) Directed evolution of GFP with non-natural amino acids identifies residues for augmenting and photoswitching fluorescence. *Chemical Science* **6**: 1159-1166

Rego JM, Lee J-H, Lee DH, Yi H (2013) Biologically inspired strategy for programmed assembly of viral building blocks with controlled dimensions. *Biotechnology Journal* **8**: 237-246

Rhee SG (2011) Multiple functions of peroxiredoxins: Peroxidases, sensors and regulators of the intracellular messenger H_2O_2, and protein chaperones. *Antioxidants & Redox Signaling* **15**: 781-794

Rhee SG (2016) Overview on peroxiredoxin. *Molecules & Cells* **39**: 1-5

Rhee SG, Chae HZ, Kim K (2005) Peroxiredoxins: a historical overview and speculative preview of novel mechanisms and emerging concepts in cell signaling. *Free Radical Biology & Medicine* **38**: 1543-52

Rhee SG, Kang SW, Chang TS, Jeong W, Kim K (2001) Peroxiredoxin, a novel family of peroxidases. *IUBMB Life* **52**: 35-41

Rhee SG, Kil IS (2016) Mitochondrial H_2O_2 signaling is controlled by the concerted action of peroxiredoxin III and sulfiredoxin: linking mitochondrial function to circadian rhythm. *Free Radical Biology and Medicine* **99**: 120-127

Robinson-Fuentes VA, Jefferies TM, Branch SK (1997) Degradation pathways of ampicillin in alkaline solutions. *Journal of Pharmacy and Pharmacology* **49**: 843-851

Rosano GL, Ceccarelli EA (2014) Recombinant protein expression in *Escherichia coli*: advances and challenges. *Frontiers in Microbiology* **5**: 172

Rothbauer M, Küpcü S, Sticker D, Sleytr UB, Ertl P (2013) Exploitation of S-layer anisotropy: pH-dependent nanolayer orientation for cellular micropatterning. *ACS Nano* **7**: 8020-8030

Rothemund PWK (2006) Folding DNA to create nanoscale shapes and patterns. *Nature* **440**: 297-302

Rothemund PWK, Ekani-Nkodo A, Papadakis N, Kumar A, Fygenson DK, Winfree E (2004) Design and characterization of programmable DNA nanotubes. *J Am Chem Soc* **126**: 16344-16352

Rother M, Nussbaumer MG, Renggli K, Bruns N (2016) Protein cages and synthetic polymers: a fruitful symbiosis for drug delivery applications, bionanotechnology and materials science. *Chemical Society Reviews* **45**: 6213-6249

Rumlová M, Benedíková J, Cubínková R, Pichová I, Ruml T (2001) Comparison of classical and affinity purification techniques of Mason-Pfizer monkey virus capsid protein: the alteration of the product by an affinity tag. *Protein Expression and Purification* **23**: 75-83

Ruotolo BT, Giles K, Campuzano I, Sandercock AM, Bateman RH, Robinson CV (2005) Evidence for macromolecular protein rings in the absence of bulk water. *Science* **310**: 1658-1661

Rutsdottir G, Härmark J, Weide Y, Hebert H, Rasmussen MI, Wernersson S, Respondek M, Akke M, Højrup P, Koeck PJB, Söderberg CAG, Emanuelsson C (2017) Structural model of dodecameric heat-shock protein HSP21 - flexible N-terminal arms interact with client proteins while C-terminal tails maintain the dodecamer and chaperone activity. *Journal of Biological Chemistry* **292**: 8103-8121

Ryadnov M, Woolfson D (2003) Engineering the morphology of a self-assembling protein fibre. *Nature Materials* **2**: 329 - 332

Ryadnov MG (2007) A self-assembling peptide polynanoreactor. *Angew Chem-Int Edit* **46**: 969-972

Ryu J, Park CB (2010) High stability of self-assembled peptide nanowires against thermal, chemical, and proteolytic attacks. *Biotechnology and Bioengineering* **105**: 221-230

Ryu YH, Schultz PG (2006) Efficient incorporation of unnatural amino acids into proteins in *Escherichia coli*. *Nature Methods* **3**: 263-265

Saccoccia F, Di Micco P, Boumis G, Brunori M, Koutris I, Miele AE, Morea V, Sriratana P, Williams DL, Bellelli A, Angelucci F (2012) Moonlighting by different stressors: crystal structure of the chaperone species of a 2-Cys peroxiredoxin. *Structure* **20**: 429-39

Sakata E, Stengel F, Fukunaga K, Zhou M, Saeki Y, Förster F, Baumeister W, Tanaka K, Robinson Carol V (2011) The catalytic activity of Ubp6 enhances maturation of the proteasomal regulatory particle. *Molecular Cell* **42**: 637-649

Salgado EN, Ambroggio XI, Brodin JD, Lewis RA, Kuhlman B, Tezcan FA (2010) Metal templated design of protein interfaces. *Proc Natl Acad Sci USA* **107**: 1827-1832

Sano KI, Shiba K (2003) A hexapeptide motif that electrostatically binds to the surface of titanium. *J Am Chem Soc* **125**: 14234-14235

Santo-Domingo J, Demaurex N (2012) The renaissance of mitochondrial pH. *The Journal of General Physiology* **139**: 415-423

Santoro SW, Wang L, Herberich B, King DS, Schultz PG (2002) An efficient system for the evolution of aminoacyl-tRNA synthetase specificity. *Nature Biotechnology* **20**: 1044-1048

Saviano M, Zaccaro L, Lombardi A, Pedone C, Diblasio B, Sun XC, Lorenzi GP (1994) A structural 2-ring version of a tubular stack of β-rings in crystals of a cyclic D,L-hexapeptide. *J Incl Phenom Mol Recogn Chem* **18**: 27-36

Schäfer J, Höbel S, Bakowsky U, Aigner A (2010) Liposome–polyethylenimine complexes for enhanced DNA and siRNA delivery. *Biomaterials* **31**: 6892-6900

Schmied WH, Elsässer SJ, Uttamapinant C, Chin JW (2014) Efficient multisite unnatural amino acid incorporation in mammalian cells via optimized pyrrolysyl tRNA synthetase/tRNA expression and engineered ERF1. *J Am Chem Soc* **136**: 15577-15583

Schroder E, Littlechild JA, Lebedev AA, Errington N, Vagin AA, Isupov MN (2000) Crystal structure of decameric 2-Cys peroxiredoxin from human erythrocytes at 1.7 Å resolution. *Structure with Folding & Design* **8**: 605-615

Schuck P, Rossmanith P (2000) Determination of the sedimentation coefficient distribution by least-squares boundary modeling. *Biopolymers* **54**: 328-341

Seebach D, Matthews JL, Meden A, Wessels T, Baerlocher C, McCusker LB (1997) Cyclo-β-peptides: Structure and tubular stacking of cyclic tetramers of 3-aminobutanoic acid as determined from powder diffraction data. *Helvetica Chimica Acta* **80**: 173-182

Seeman NC (2003) DNA in a material world. *Nature* **421**: 427-431

Seeman NC (2005) Structural DNA nanotechnology. In Nanobiotechnology Protocols, Rosenthal S.J., Wright D.W. (eds) pp 143-166. Totowa, NJ: *Humana Press*

Seo MS, Kang SW, Kim K, Baines IC, Lee TH, Rhee SG (2000) Identification of a new type of mammalian peroxiredoxin that forms an intramolecular disulfide as a reaction intermediate. *Journal of Biological Chemistry* **275**: 20346-20354

Sezonov G, Joseleau-Petit D, D'Ari R (2007) *Escherichia coli* physiology in Luria-Bertani broth. *Journal of Bacteriology* **189**: 8746-8749

Shao N, Singh NS, Slade SE, Jones AME, Balasubramanian MK (2015) Site specific genetic incorporation of azidophenylalanine in *Schizosaccharomyces pombe*. *Scientific Reports* **5**: 17196

Sharon M, Robinson CV (2007) The role of mass spectrometry in structure elucidation of dynamic protein complexes. *Annual Review of Biochemistry* **76**: 167-193

Shenton W, Douglas T, Young M, Stubbs G, Mann S (1999) Inorganic-organic nanotube composites from template mineralization of tobacco mosaic virus. *Advanced Materials* **11**: 253-256

Shigehara K, Kudoh H, Sakai T, Osada Y, Murakami Y, Shikinaka K (2013) Thermoresponsive synthetic polymer–microtubule hybrids. *Langmuir* **29**: 11786-11792

Shih WM, Quispe JD, Joyce GF (2004) A 1.7-kilobase single-stranded DNA that folds into a nanoscale octahedron. *Nature* **427**: 618-621

Shiloach J, Fass R (2005) Growing *E. coli* to high cell density—a historical perspective on method development. *Biotechnology Advances* **23**: 345-357

Simmel FC (2009) Bioelectronics: wiring-up ion channels. *Nature Physics* **5**: 783-784

Sinclair JC, Davies KM, Venien-Bryan C, Noble MEM (2011) Generation of protein lattices by fusing proteins with matching rotational symmetry. *Nature Nanotechnology* **6**: 558-562

Singleton MR, Wentzell LM, Liu Y, West SC, Wigley DB (2002) Structure of the single-strand annealing domain of human RAD52 protein. *Proc Natl Acad Sci USA* **99**: 13492-13497

Sinha RP (1984) Effect of buffering media with phosphates on antibiotic resistance of lactic *Streptococci*. *Applied and Environmental Microbiology* **47**: 1175-1177

Sletten EM, Bertozzi CR (2009) Bioorthogonal chemistry: Fishing for selectivity in a sea of functionality. *Angew Chem-Int Edit* **48**: 6974-6998

Smith AM (2015) Interaction of metal ions with proteins as a source of inspiration for biomimetic materials. In Functional Metallosupramolecular Materials, pp 1-31. *The Royal Society of Chemistry*

Smolskaya S, Zhang ZJ, Alfonta L (2013) Enhanced yield of recombinant proteins with site-specifically incorporated unnatural amino acids using a cell-free expression system. *PLOS ONE* **8**: e68363

Sobott F, Benesch JL, Vierling E, Robinson CV (2002) Subunit exchange of multimeric protein complexes. Real-time monitoring of subunit exchange between small heat shock proteins by using electrospray mass spectrometry. *The Journal of Biological Chemistry* **277**: 38921-9

Sobotta MC, Liou W, Stocker S, Talwar D, Oehler M, Ruppert T, Scharf AN, Dick TP (2015) Peroxiredoxin-2 and STAT3 form a redox relay for H_2O_2 signaling. *Nature Chemical Biology* **11**: 64-70

Soito L, Williamson C, Knutson ST, Fetrow JS, Poole LB, Nelson KJ (2011) PREX: Peroxiredoxin classification index, a database of subfamily assignments across the diverse peroxiredoxin family. *Nucleic Acids Research* **39**: D332-7

Song I-S, Kim H-K, Jeong S-H, Lee S-R, Kim N, Rhee BD, Ko KS, Han J (2011) Mitochondrial peroxiredoxin III is a potential target for cancer therapy. *International Journal of Molecular Sciences* **12**: 7163-7185

Staiano M, Baldassarre M, Esposito M, Apicella E, Vitale R, Aurilia V, D'Auria S (2010) New trends in bionanotechnology: stable proteins as advanced molecular tools for health and environment. *Environmental Technology* **31**: 935-942

Stasiak AZ, Larquet E, Stasiak A, Müller S, Engel A, Van Dyck E, West SC, Egelman EH (2000) The human RAD52 protein exists as a heptameric ring. *Current Biology* **10**: 337-340

Steinmetz NF, Lomonossoff GP, Evans DJ (2006) Decoration of cowpea mosaic virus with multiple, redox-active, organometallic complexes. *Small* **2**: 530-533

Stillman TJ, Upadhyay M, Norte VA, Sedelnikova SE, Carradus M, Tzokov S, Bullough PA, Shearman CA, Gasson MJ, Williams CH, Artymiuk PJ, Green J (2005) The crystal structures of *Lactococcus lactis* MG1363 DPS proteins reveal the presence of an N-terminal helix that is required for DNA binding. *Molecular Microbiology* **57**: 1101-1112

Studier FW (2005) Protein production by auto-induction in high density shaking cultures. *Protein Expression and Purification* **41**: 207-234

Stuitje AR, Spelt CE, Veltkamp E, Nijkamp HJJ (1981) Identification of mutations affecting replication control of plasmid Clo DF13. *Nature* **290**: 264-267

Stura EA, Nemerow GR, Wilson IA (1992) Strategies in the crystallization of glycoproteins and protein complexes. *Journal of Crystal Growth* **122**: 273-285

Subramani K, Khraisat A, George A (2008) Self-assembly of proteins and peptides and their applications in bionanotechnology. *Current Nanoscience* **4**: 201-207

Svergun D (1992) Determination of the regularization parameter in indirect-transform methods using perceptual criteria. *Journal of Applied Crystallography* **25**: 495-503

Svergun D, Barberato C, Koch MH (1995) CRYSOL - a program to evaluate X-ray solution scattering of biological macromolecules from atomic coordinates. *Journal of Applied Crystallography* **28**: 768-773

Szabó KÉ, Line K, Eggleton P, Littlechild JA, Winyard PG (2009) Structure and function of the human peroxiredoxin-based antioxidant system: The interplay between peroxiredoxins, thioredoxins, thioredoxin reductases, sulfiredoxins and sestrins. In Redox Signaling and Regulation in Biology and Medicine, pp 143-179. *Wiley-VCH Verlag GmbH & Co. KGaA*

Tairum Jr CA, de Oliveira MA, Horta BB, Zara FJ, Netto LES (2012) Disulfide biochemistry in 2-Cys peroxiredoxin: Requirement of Glu50 and Arg146 for the reduction of yeast Tsa1 by thioredoxin. *Journal of Molecular Biology* **424**: 28-41

Takahashi Y, Ueno A, Mihara H (2002) Amyloid architecture: complementary assembly of heterogeneous combinations of three or four peptides into amyloid fibrils. *ChemBioChem* **3**: 637-642

Tamerler C, Sarikaya M (2009) Molecular biomimetics: Nanotechnology and bionanotechnology using genetically engineered peptides. *Philosophical Transactions of the Royal Society A* **367**: 1705-1726

Teixeira F, Castro H, Cruz T, Tse E, Koldewey P, Southworth DR, Tomás AM, Jakob U (2015) Mitochondrial peroxiredoxin functions as crucial chaperone reservoir in *Leishmania infantum*. *Proc Natl Acad Sci USA* **112**: E616-E624

Thielges MC, Chung JK, Axup JY, Fayer MD (2011) Influence of histidine tag attachment on picosecond protein dynamics. *Biochemistry* **50**: 5799-805

Thordarson P, Droumaguet B, Velonia K (2006) Well-defined protein–polymer conjugates: synthesis and potential applications. *Applied Microbiology & Biotechnology* **73**: 243-254

Toledano MB, Bo HB (2016) Microbial 2-Cys peroxiredoxins: insights into their complex physiological roles. *Molecules & Cells* **39**: 31-39

Trujillo M, Ferrer-Sueta G, Thomson L, Flohé L, Radi R (2007) Kinetics of peroxiredoxins and their role in the decomposition of peroxynitrite. In Peroxiredoxin Systems: Structures and functions, Flohé L., Harris J.R. (eds) pp 83-113. Dordrecht: *Springer Netherlands*

Tsai C-J, Zheng J, Alemán C, Nussinov R (2006) Structure by design: from single proteins and their building blocks to nanostructures. *Trends in Biotechnology* **24**: 449-454

Tsukamoto H, Kawano MA, Inoue T, Enomoto T, Takahashi RU, Yokoyama N, Yamamoto N, Imai T, Kataoka K, Yamaguchi Y, Handa H (2007) Evidence that SV40 VP1-DNA interactions contribute to the assembly of 40-nm spherical viral particles. *Genes to Cells* **12**: 1267-1279

Turrens JF (1997) Superoxide production by the mitochondrial respiratory chain. *Bioscience Reports* **17**: 3-8

Usui K, Maki T, Ito F, Suenaga A, Kidoaki S, Itoh M, Taiji M, Matsuda T, Hayashizaki Y, Suzuki H (2009) Nanoscale elongating control of the self-assembled protein filament with the cysteine-introduced building blocks. *Protein Science* **18**: 960-969

van Vught R, Pieters RJ, Breukink E (2014) Site-specific functionalization of proteins and their applications to therapeutic antibodies. *Comput Struct Biotechnol J* **9**: e201402001

van Berkel SS, van Eldijk MB, van Hest JCM (2011) Staudinger ligation as a method for bioconjugation. *Angew Chem-Int Edit* **50**: 8806-8827

Venkatesan BM, Bashir R (2011) Nanopore sensors for nucleic acid analysis. *Nature Nanotechnology* **6**: 615-624

Vilaplana F, Gilbert RG (2010) Characterization of branched polysaccharides using multiple-detection size separation techniques. *Journal of Separation Science* **33**: 3537-54

Vivancos AP, Castillo EA, Biteau B, Nicot C, Ayté J, Toledano MB, Hidalgo E (2005) A cysteine-sulfinic acid in peroxiredoxin regulates H_2O_2-sensing by the antioxidant Pap1 pathway. *Proc Natl Acad Sci USA* **102**: 8875-8880

Wallace DC (1999) Mitochondrial diseases in man and mouse. *Science* **283**: 1482-1488

Wallace Edward WJ, Kear-Scott Jamie L, Pilipenko Evgeny V, Schwartz Michael H, Laskowski Pawel R, Rojek Alexandra E, Katanski Christopher D, Riback Joshua A, Dion Michael F, Franks Alexander M, Airoldi Edoardo M, Pan T, Budnik Bogdan A, Drummond DA (2015) Reversible, specific, active aggregates of endogenous proteins assemble upon heat stress. *Cell* **162**: 1286-1298

Wang A, Nairn NW, Johnson RS, Tirrell DA, Grabstein K (2008) Processing of N-terminal unnatural amino acids in recombinant human interferon-β in *Escherichia coli*. *ChemBioChem* **9**: 324-330

Wang K, Sachdeva A, Cox DJ, Wilf NW, Lang K, Wallace S, Mehl RA, Chin JW (2014) Optimized orthogonal translation of unnatural amino acids enables spontaneous protein double-labelling and FRET. *Nature Chemistry* **6**: 393-403

Wang L, Brock A, Herberich B, Schultz PG (2001) Expanding the genetic code of *Escherichia coli*. *Science* **292**: 498-500

Wang Q, Chan TR, Hilgraf R, Fokin VV, Sharpless KB, Finn MG (2003) Bioconjugation by copper(I)-catalyzed azide-alkyne [3 + 2] cycloaddition. *J Am Chem Soc* **125**: 3192-3193

Wang WX, Pelah D, Alergand T, Shoseyov O, Altman A (2002) Characterization of SP1, a stress-responsive, boiling-soluble, homo-oligomeric protein from aspen. *Plant Physiology* **130**: 865-75

Wang X-y, Wang H-j, Li X-q (2013) Peroxiredoxin III protein expression is associated with platinum resistance in epithelial ovarian cancer. *Tumor Biology* **34**: 2275-2281

Wang X, Wang L, Wang Xe, Sun F, Wang Cc (2012) Structural insights into the peroxidase activity and inactivation of human peroxiredoxin 4. *Biochemical Journal* **441**: 113-118

Wason A (2014) Investigation of Lsm proteins as scaffolds in bionanotechnology. *University of Canterbury, Christchurch, New Zealand*, http://hdl.handle.net/10092/10065

Watabe S, Hiroi T, Yamamoto Y, Fujioka Y, Hasegawa H, Yago N, Takahashi SY (1997) SP-22 is a thioredoxin-dependent peroxide reductase in mitochondria. *European Journal of Biochemistry* **249**: 52-60

Watanabe M, Mishima Y, Yamashita I, Park S-Y, Tame JRH, Heddle JG (2008) Intersubunit linker length as a modifier of protein stability: crystal structures and thermostability of mutant TRAP. *Protein Science* **17**: 518-526

Weiss RB, Dunn DM, Atkins JF, Gesteland RF (1987) Slippery runs, shifty stops, backward steps, and forward hops: -2, -1, +1, +2, +5, and +6 ribosomal frameshifting. *Cold Spring Harbor Symposia on Quantitative Biology* **52**: 687-693

Wendell D, Jing P, Geng J, Subramaniam V, Lee TJ, Montemagno C, Guo P (2009) Translocation of double-stranded DNA through membrane-adapted phi29 motor protein nanopores. *Nature Nanotechnology* **4**: 765-772

Whitesides GM, Grzybowski B (2002) Self-assembly at all scales. *Science* **295**: 2418-2421

Whitesides GM, Lilburn JE, Szajewski RP (1977) Rates of thiol-disulfide interchange reactions between mono- and dithiols and Ellman's reagent. *The Journal of Organic Chemistry* **42**: 332-338

Wickstrum JR, Egan SM (2002) Ni^{+}-affinity purification of untagged camp receptor protein. *BioTechniques* **33**: 728-730

Wilson DN (2014) Ribosome-targeting antibiotics and mechanisms of bacterial resistance. *Nature Reviews Microbiology* **12**: 35-48

Winfree E, Liu FR, Wenzler LA, Seeman NC (1998) Design and self-assembly of two-dimensional DNA crystals. *Nature* **394**: 539-544

Winterbourn CC (2008) Reconciling the chemistry and biology of reactive oxygen species. *Nature Chemical Biology* **4**: 278-286

Winterbourn CC (2013) The biological chemistry of hydrogen peroxide. In Methods in Enzymology, pp 3-25.

Winterbourn CC, Hampton MB (2015) Redox biology: signaling via a peroxiredoxin sensor. *Nature Chemical Biology* **11**: 5-6

Winterbourn CC, Metodiewa D (1999) Reactivity of biologically important thiol compounds with superoxide and hydrogen peroxide. *Free Radical Biology and Medicine* **27**: 322-328

Winterbourn CC, Peskin AV (2016) Kinetic approaches to measuring peroxiredoxin reactivity. *Molecules & Cells* **39**: 26-30

Witte MD, Theile CS, Wu T, Guimaraes CP, Blom AEM, Ploegh HL (2013) Production of unnaturally linked chimeric proteins using a combination of sortase-catalyzed transpeptidation and click chemistry. *Nature Protocols* **8**: 1808-1819

Woo HA, Yim SH, Shin DH, Kang D, Yu DY, Rhee SG (2010) Inactivation of peroxiredoxin I by phosphorylation allows localized H_2O_2 accumulation for cell signaling. *Cell* **140**: 517-28

Wood ZA, Poole LB, Hantgan RR, Karplus PA (2002) Dimers to doughnuts: Redox-sensitive oligomerization of 2-cysteine peroxiredoxins. *Biochemistry* **41**: 5493-5504

Wood ZA, Poole LB, Karplus PA (2003a) Peroxiredoxin evolution and the regulation of hydrogen peroxide signaling. *Science* **300**: 650-3

Wood ZA, Schroder E, Robin Harris J, Poole LB (2003b) Structure, mechanism and regulation of peroxiredoxins. *Trends in Biochemical Sciences* **28**: 32-40

Xiao K, Malvankar NS, Shu C, Martz E, Lovley DR, Sun X (2016) Low energy atomic models suggesting a pilus structure that could account for electrical conductivity of geobacter *Sulfurreducens pili*. *Scientific Reports* **6**

Xie J, Schultz PG (2005) An expanding genetic code. *Methods (San Diego, Calif)* **36**: 227-238

Yamada S, Pokutta S, Drees F, Weis WI, Nelson WJ (2005) Deconstructing the cadherin-catenin-actin complex. *Cell* **123**: 889-901

Yan H, Zhang X, Shen Z, Seeman NC (2002) A robust DNA mechanical device controlled by hybridization topology. *Nature* **415**: 62-65

Yeates TO (2011) Nanobiotechnology: protein arrays made to order. *Nature Nanotechnology* **6**: 541-2

Yemini M, Reches M, Rishpon J, Gazit E (2004) Novel electrochemical biosensing platform using self-assembled peptide nanotubes. *Nano Letters* **5**: 183-186

Yin P, Hariadi RF, Sahu S, Choi HMT, Park SH, LaBean TH, Reif JH (2008) Programming DNA tube circumferences. *Science* **321**: 824-826

Yoon HI, Yhee JY, Na JH, Lee S, Lee H, Kang S-W, Chang H, Ryu JH, Lee S, Kwon IC, Cho YW, Kim K (2016) Bioorthogonal copper free click chemistry for labeling and tracking of chondrocytes *in vivo*. *Bioconjugate Chemistry* **27**: 927-936

Yoshimura H (2006) Protein-assisted nanoparticle synthesis. *Colloids and Surfaces A: Physicochemical and Engineering Aspects* **282–283**: 464-470

Yoshizawa K, Mishima Y, Park S-Y, Heddle JG, Tame JRH, Iwahori K, Kobayashi M, Yamashita I (2007) Effect of N-terminal residues on the structural stability of recombinant horse L-chain apoferritin in an acidic environment. *The Journal of Biochemistry* **142**: 707-713

Young DD, Young TS, Jahnz M, Ahmad I, Spraggon G, Schultz PG (2011) An evolved aminoacyl-tRNA synthetase with atypical polysubstrate specificity. *Biochemistry* **50**: 1894-1900

Young M, Willits D, Uchida M, Douglas T (2008) Plant viruses as biotemplates for materials and their use in nanotechnology. *Annu Rev Phytopathol* **46**: 361-84

Young TS, Ahmad I, Yin JA, Schultz PG (2010) An enhanced system for unnatural amino acid mutagenesis in *E. coli*. *Journal of Molecular Biology* **395**: 361-374

Yurke B, Turberfield A, Mills A, Simmel F, Neumann J (2000) A DNA-fuelled molecular machine made of DNA. *Nature* **406**: 605-608

Yusko EC, Johnson JM, Majd S, Prangkio P, Rollings RC, Li J, Yang J, Mayer M (2011) Controlling protein translocation through nanopores with bio-inspired fluid walls. *Nature Nanotechnology* **6**: 253-260

Zeida A, González Lebrero MC, Radi R, Trujillo M, Estrin DA (2013) Mechanism of cysteine oxidation by peroxynitrite: an integrated experimental and theoretical study. *Archives of Biochemistry and Biophysics* **539**: 81-86

Zhang F, Nangreave J, Liu Y, Yan H (2014) Structural DNA nanotechnology: state of the art and future perspective. *J Am Chem Soc* **136**: 11198-11211

Zhang K, Wang Z, Liu X, Yin C, Basit Z, Xia B, Liu W (2012) Dissection of influenza a virus M1 protein: pH-dependent oligomerization of N-terminal domain and dimerization of C-terminal domain. *PLOS ONE* **7**: e37786

Zhang Y-G, Wang L, Kaifu T, Li J, Li X, Li L (2016) Accelerated decline of physical strength in peroxiredoxin-3 knockout mice. *Experimental Biology and Medicine* **241**: 1395-1400

Zhang Y, Orner BP (2011) Self-assembly in the ferritin nano-cage protein superfamily. *International Journal of Molecular Sciences* **12**: 5406-21

Zhang Y, Seeman NC (1994) Construction of a DNA-truncated octahedron. *J Am Chem Soc* **116**: 1661-1669

Zheng Y, Lajoie MJ, Italia JS, Chin MA, Church GM, Chatterjee A (2016) Performance of optimized noncanonical amino acid mutagenesis systems in the absence of release factor 1. *Molecular BioSystems* **12**: 1746-1749

Zhou C, Yu B, Yang X, Huo T, Lee LJ, Barth RF, Lee RJ (2010a) Lipid-coated nano-calcium-phosphate (LNCP) for gene delivery. *International Journal of Pharmaceutics* **392**: 201-208

Zhou M, Robinson CV (2010b) When proteomics meets structural biology. *Trends in Biochemical Sciences* **35**: 522-529

Zimmerberg J, Kozlov MM (2006) How proteins produce cellular membrane curvature. *Nature Reviews Molecular Cell Biology* **7**: 9-19

Zlotnick A, Francis S, Lee L, Wang J-Y (2015) Self-assembling virus-like and virus-unlike particles. In Viral Nanotechnology, pp 13-26. *CRC Press*

Appendix A

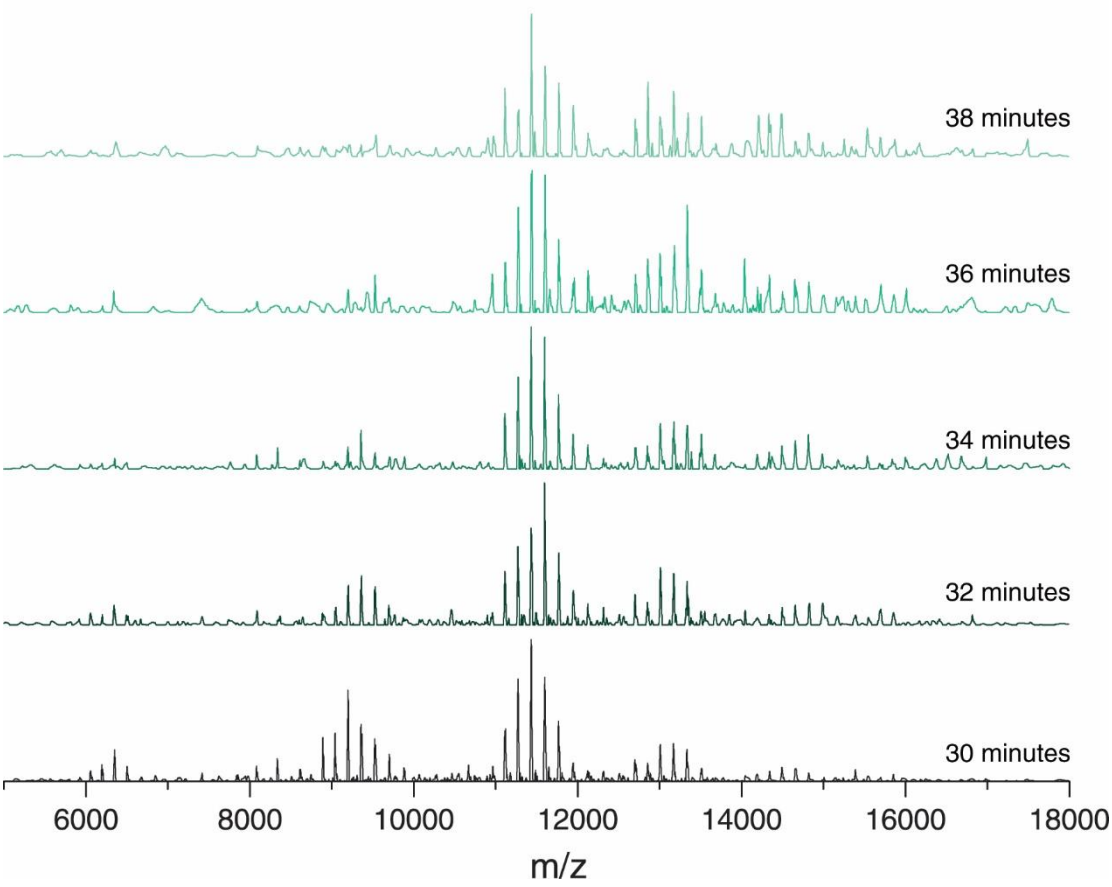

Changes in population of HsPrx3 stacks as seen for changes in real-time MS spectra

Mass spectrum of 20 µM cleaved HsPrx3 in 100 mM ammonium acetate, pH 4.0, ionised in positive ion mode recorded over time. Each spectra was taken at a certain time point between 30 and 38 minutes after the sample was initally sprayed into the spectrophotometer. Similar to **Figure 3.**6, these spectra also show the characteristic distinct charge state series for each discrete HMW HsPrx3 stacked species. The intensities of the charge state series can change over time. In this case, the peaks with m/z ranging from 6000 to 8000, corresponding to single and double rings, decrease as time progresses. This could be a result of variations in complex needle chemistries that occur as protein solutions become ionised overtime.

Appendix B

From Section 7.8.1.2, the fine screen conditions that resulted in the diffracting protein crystal of S78C HsPrx3 protein was based around the D12 condition from the MORPHEUS screen (0.1 M tris-bicine at pH 8.5, 12.5% PEG1000, 12.5% PEG3350, 12.5% MPD, 0.02M alcohol additives).

The concentrations of the alcohol additives (0.02 M) and buffer (0.1 M) were kept constant throughout the fine screen. Whereas, the solution pH was varied at increments of pH 7.7, 8.1, 8.5, and 8.7 (according to Gorrec, 2009) for each set of the concentration variations for the PEG1000, PEG3500 and MPD components. The final concentrations of each of these components were as follows:

	1	2	3
A	10% PEG1000 10% PEG3500 10% MPD	10% PEG1000 10% PEG3500 12.5% MPD	10% PEG1000 10% PEG3500 15% MPD
B	10% PEG1000 12.5% PEG3500 10% MPD	10% PEG1000 12.5% PEG3500 12.5% MPD	10% PEG1000 12.5% PEG3500 15% MPD
C	12.5% PEG1000 10% PEG3500 10% MPD	12.5% PEG1000 10% PEG3500 12.5% MPD	12.5% PEG1000 10% PEG3500 15% MPD
D	12.5% PEG1000 12.5% PEG3500 10% MPD	12.5% PEG1000 12.5% PEG3500 12.5% MPD	12.5% PEG1000 12.5% PEG3500 15% MPD
E	12.5% PEG1000 15% PEG3500 10% MPD	12.5% PEG1000 15% PEG3500 12.5% MPD	12.5% PEG1000 15% PEG3500 15% MPD
F	15% PEG1000 10% PEG3500 10% MPD	15% PEG1000 10% PEG3500 12.5% MPD	15% PEG1000 10% PEG3500 15% MPD
G	15% PEG1000 12.5% PEG3500 10% MPD	15% PEG1000 12.5% PEG3500 12.5% MPD	15% PEG1000 12.5% PEG3500 15% MPD
H	15% PEG1000 15% PEG3500 10% MPD	15% PEG1000 15% PEG3500 12.5% MPD	15% PEG1000 15% PEG3500 15% MPD